

# Exclusive Observables to NLO and Low $x$ PDF Phenomenology at the LHC

Thesis submitted in accordance with the requirements of  
the University of Liverpool for the degree of Doctor of Philosophy  
by

**Christopher Alexander Flett**

May 2021

# Declaration

I hereby declare that the work presented in this thesis is the result of my own research activities unless reference to others is given. None of this material has been previously submitted to this or any other university. All work presented here was carried out in the Theoretical Physics Division of the Department of Mathematical Sciences, University of Liverpool, U.K. during the period of October 2016 until September 2020.

Contributions to this work have been previously published or are awaiting publication elsewhere in:

- **C. A. Flett**, S. P. Jones, A. D. Martin, M. G. Ryskin and T. Teubner, “Towards a determination of the low  $x$  gluon via exclusive  $J/\psi$  production,” PoS **DIS2019** (2019) 053, [arXiv:1907.06471 [hep-ph]].
- **C. A. Flett**, S. P. Jones, A. D. Martin, M. G. Ryskin and T. Teubner, “How to include exclusive  $J/\psi$  production data in global PDF analyses,” Phys. Rev. D **101** (2020) 094011, [arXiv:1908.08398 [hep-ph]].
- **C. A. Flett**, S. P. Jones, A. D. Martin, M. G. Ryskin and T. Teubner, “Exclusive production of heavy quarkonia as a probe of the low  $x$  and low scale gluon PDF,” PoS **LC2019** (2020) 040, [arXiv:1912.09128 [hep-ph]].
- **C. A. Flett**, A. D. Martin, M. G. Ryskin and T. Teubner, “Very low  $x$  gluon density determined by LHCb exclusive  $J/\psi$  data,” Phys. Rev. D **102** (2020) 114021, [arXiv:2006.13857 [hep-ph]].
- **C. A. Flett**, J. A. Gracey, S. P. Jones and T. Teubner, “Exclusive heavy vector meson electroproduction to NLO in collinear factorisation,” [arXiv:2105.07657 [hep-ph]]. *Submitted to Journal of High Energy Physics*

- É. Chapon et al., “Perspectives for quarkonia studies at the High-Luminosity LHC,” [arXiv:2012.14161 [hep-ph]]. *Review prepared for submission to Progress in Particle and Nuclear Physics*

# Abstract

At present, the Parton Distribution Functions (PDFs) for the quarks and gluons of QCD extracted in global fitting analyses suffer from large uncertainties, particularly at low  $x$  and low scales. This is mainly a reflection of the lack of experimental data constraints in this kinematical regime. In this thesis, due to its enhanced sensitivity to the gluon PDF, we will study the exclusive production of heavy vector mesons  $V$ , measured recently in ultra peripheral  $pp$  collisions at the LHC,  $pp \rightarrow p + V + p$ , as a means to reliably constrain, probe and determine the gluon PDF in the very low  $x$  domain.

With the advent of new and improved colliders on the horizon, PDF phenomenology is becoming more and more important at low  $x$  as particle collision energies increase. The data for the exclusive production of the  $J/\psi$  meson from LHCb, specifically, will be promoted as being at the frontier of new low  $x$  and low scale gluon PDF constraints, providing the driving force in allowing this kinematic regime to start, and ultimately become, an area of precision physics.

Using a fully furnished prediction for exclusive  $J/\psi$  photoproduction within the collinear factorisation framework at NLO, a low  $x \sim 10^{-5}$  and low scale  $\mu^2 \sim 2.4 \text{ GeV}^2$  gluon PDF is obtained within a statistical reweighting framework using existing HERA and LHC exclusive data. The significance of this result for low  $x$  global gluon PDF extractions is quantified.

Finally, we build and use a computational workhorse to extract the exclusive *electro* production of heavy vector mesons to NLO in collinear factorisation. This completes the  $Q^2$  phase space for this observable and provides a calculation that is on solid grounds with regards to the applicability of the factorisation ansatz.

# Acknowledgements

I would like to extend my thanks and greatest gratitude to my supervisor, Thomas Teubner, for his guidance and direction over the past four years and for always being ready to answer my many questions about all things particle physics.

Sincere thanks to my collaborators Alan Martin and Misha Ryskin for driving forward the phenomenological aspect of the work and for their kind hospitality at the IPPP on my few trips to Durham. I am also grateful to Stephen Jones for a fruitful collaboration from start to finish of my PhD and for the productive onsite meetings at the MPI and CERN. Thanks to all the academic staff and fellow PhD students at the University of Liverpool for making my experience a pleasant one. In particular, to John Gracey for acquaintance with `FORM` and `REDUZE` in my first two years and for always having his door open and being happy to chat at any time. I acknowledge the computing support from Steve Downing, too.

I'd also like to express my appreciation to the administration staff for their copious organisation of my conference and summer school visits, particularly in my third year. I have learnt a lot and benefited from these wider activities.

Special thanks to Jean Philippe-Lansberg for invitations to speak at the new 'Quarkonia As Tools' workshop series in the French Alps in my third and fourth year and to University of Milan for an invited seminar. I am grateful for the opportunity to present and to receive an external outlook on my work outside of Liverpool and my immediate collaboration. Learning to ski was a perk on the side. It was a privilege to also speak in front of the LHCb collaboration in the main CERN auditorium. Thanks to Ronan McNulty for his continuous encouragement to make predictions using their data.

The support of an STFC studentship, as well as the subsistence payment organised by Ian Jack during my writing up period, helped a great deal financially and I'm thankful to have received this funding.

---

Finally, I'd like to thank all my friends and family, especially to Mum, Dad, Brother and Sister. I appreciate your unconditional love and everything that you do. Of all the friends and teachers I've had in my life, you have been the best. I love you all very much.

# Contents

<b>Abstract</b>	<b>i</b>
<b>Acknowledgements</b>	<b>ii</b>
<b>Contents</b>	<b>vi</b>
<b>List of Figures</b>	<b>x</b>
<b>List of Tables</b>	<b>xi</b>
<b>1 Introduction</b>	<b>1</b>
1.1 Overview . . . . .	1
1.2 Structure of the thesis . . . . .	4
<b>2 Preliminaries</b>	<b>6</b>
2.1 Observables from Perturbative QCD . . . . .	6
2.2 Global PDF analyses . . . . .	11
2.3 Generalised Parton Distribution Functions . . . . .	15
2.3.1 Introduction . . . . .	15
2.3.2 Symmetries and evolution . . . . .	18
2.3.3 The Shuvaev Transform . . . . .	20
2.4 Loop calculation toolbox . . . . .	25
2.5 Taming of $\overline{\text{MS}}$ exclusive $J/\psi$ production at NLO . . . . .	27
2.5.1 Treatment of double logarithmic contributions . . . . .	29
2.5.2 Treatment of double counting power corrections . . . . .	32

---

<b>3</b>	<b>How to include exclusive <math>J/\psi</math> production data in global PDF analyses</b>	<b>36</b>
3.1	Introduction . . . . .	37
3.2	Notation and collinear factorisation . . . . .	39
3.2.1	Non-Relativistic QCD (NRQCD) . . . . .	40
3.3	Connecting exclusive production to the PDFs . . . . .	42
3.4	Description of exclusive $J/\psi$ photoproduction data . . . . .	48
3.4.1	Real part correction . . . . .	48
3.4.2	Restoring the $t$ dependence . . . . .	50
3.4.3	HERA data . . . . .	51
3.4.4	LHCb data . . . . .	54
3.5	Towards the bigger picture . . . . .	59
3.6	Summary . . . . .	61
<b>4</b>	<b>A low <math>x</math> determination of the gluon PDF via exclusive <math>J/\psi</math> production</b>	<b>63</b>
4.1	Introduction . . . . .	63
4.2	Ansatz for the low $x$ gluon . . . . .	64
4.3	Determination of the low $x$ gluon from $J/\psi$ data . . . . .	66
4.3.1	Description of the $J/\psi$ data . . . . .	66
4.3.2	The alternative double-log parametrisation . . . . .	73
4.3.3	Is there evidence of saturation from exclusive $J/\psi$ data? . . . . .	74
4.3.4	Note on higher-twist contributions . . . . .	75
4.4	Comparison with low $x$ gluons from $D$ -meson data . . . . .	76
4.5	Reweighting of NNPDF3.0 gluon via exclusive $J/\psi$ data . . . . .	78
4.6	Summary . . . . .	82
<b>5</b>	<b>Exclusive HVM electroproduction in collinear factorisation at NLO</b>	<b>83</b>
5.1	Introduction . . . . .	83
5.2	Notation and collinear factorisation . . . . .	86
5.2.1	Kinematics and set-up . . . . .	86
5.2.2	HVM and GPD spin projections . . . . .	90
5.2.3	Lorentz-invariant tensor decomposition . . . . .	91
5.3	Overview of calculation . . . . .	95
5.4	LO results . . . . .	96
5.5	NLO results . . . . .	98



---

5.5.1	Linear Reduction . . . . .	98
5.5.2	Integral Reduction . . . . .	102
5.5.3	Quark subprocess . . . . .	104
5.5.4	Gluon subprocess . . . . .	107
5.6	UV renormalisation and mass factorisation . . . . .	117
5.7	High-energy limit . . . . .	122
5.8	Comparison with literature . . . . .	124
5.9	Summary . . . . .	125
<b>6</b>	<b>Conclusions</b>	<b>127</b>
<b>A</b>	<b>Conventions and Properties</b>	<b>130</b>
A.0.1	Sudakov Decomposition . . . . .	130
A.0.2	Polylogarithms . . . . .	131
A.0.3	Trace identities . . . . .	132
<b>B</b>	<b>Resummation in the <math>(x, Q^2)</math> plane</b>	<b>134</b>
<b>C</b>	<b>GPD Singlet Evolution Kernels</b>	<b>137</b>
<b>D</b>	<b>HVM Auxiliary Topologies</b>	<b>139</b>
	<b>Bibliography</b>	<b>145</b>

# List of Figures

2.1	Comparison of NLO gluon PDFs obtained in the NNPDF3.0, MMHT14 and CT14 [38, 40, 42] global analyses at scale $Q = 1.55$ GeV, close to the input scale of the assumed DGLAP evolution. Plot generated within APFEL [146, 147].	13
2.2	Ratios $xg_{\text{CT14}}/xg_{\text{NNPDF3.0}}$ and $xg_{\text{MMHT14}}/xg_{\text{NNPDF3.0}}$ of NLO gluon PDFs taken from [38, 40, 42] at a fixed scale $Q = 1.55$ GeV. Plot generated within APFEL [146, 147].	14
2.3	Parametrisation of the plus component of the hadronic and partonic momenta used in this work.	16
2.4	$\overline{\text{MS}}$ scale variations of $\text{Im } A/W^2$ at LO (black) and NLO (blue) generated using CTEQ6.6 global partons at $\mu_F^2 = \mu_R^2 = 1.2, 2.4, 4.8$ GeV <sup>2</sup> . $\text{Im } A$ is the imaginary part of the amplitude. Plot adapted from [102].	28
2.5	Lower part of Feynman diagrams for exclusive $J/\psi$ production. Left panel: LO contribution evaluated at $\mu_F$ . Right panel: Division of cells at factorisation scale $\mu_F$ allows for a shifting of terms with virtualities $\mu < \mu_F$ between LO and NLO.	30
2.6	Different choices of the factorisation scale $\mu_{F_i}$ allow for different division of cells between the parton evolution and the hard matrix element. The uppermost gluon (labelled red) may not be absorbed into the parton evolution in this scale-shifting approach, described in the text.	31
2.7	Two cut diagrams contributing to the imaginary part of the NLO quark coefficient function. The corresponding cut diagrams for the NLO gluon coefficient function can be obtained by replacing the light quark line by gluons. All permutations of the gluons to the heavy quarks are implicit.	34

2.8	LO and LO+NLO contributions to the imaginary part of the $\gamma p \rightarrow V + p$ amplitude as a function of the $\gamma p$ centre-of-mass energy, $W$ , with $\mu_F = m_c$ before (upper panel) and after (lower panel) the double counting correction has been implemented, as explained in the text. The dashed, continuous and dot-dashed (red) curves correspond to three choices of the factorisation scale $\mu_f$ : namely $\mu_f^2 = 2m_c^2$ , $m_c^2$ , $Q_0^2$ , respectively, where $m_c^2 = M_\psi^2/4 = 2.4 \text{ GeV}^2$ . Here $Q_0 = 1.3 \text{ GeV}$ is the starting scale of the input NLO PDFs from CTEQ6.6 [41] which were used. The dotted black curve is the LO contribution. Plots adapted from [107]. . . . .	35
3.1	(a) LO contribution to $\gamma p \rightarrow V + p$ . (b) NLO quark contribution. For these graphs all permutations of the parton lines and couplings of the gluon lines to the heavy-quark pair are to be understood. Here the momentum $P \equiv (p+p')/2$ and $l$ is the loop momentum. Note that the momentum fractions of the left and right input partons are $x = X + \xi$ and $x' = X - \xi$ respectively; for the gluons coupled directly to the on-shell heavy-quark pair, we have $x' \ll x$ and so $x \simeq 2\xi$ . . . . .	44
3.2	The gluon LO+NLO and quark NLO contributions to the imaginary part of the $\gamma p \rightarrow J/\psi + p$ amplitude for two different choices of the factorisation scale $\mu_f^2 = \mu_R^2 = m_c^2$ , $2m_c^2$ shown by the continuous and dashed curves respectively. CT14 NLO global PDFs [42] are used and the 'optimal' scale $\mu_F = m_c$ is chosen. . . . .	47
3.3	The gluon LO + NLO amplitude, $A_g^{(0)} + A_g^{(1)}$ (solid lines) and the full amplitude, $A_g^{(0)} + A_g^{(1)} + A_q^{(1)}$ (dashed lines) for three global parton sets with all scales set at the 'optimal' value, $\mu_0 = m_c$ . The inclusion of the quark NLO contribution is negligible for the large range of $W$ we consider. . . . .	48
3.4	The enhancement $(1 + \rho^2)$ at the cross section level due to the real part correction, $\rho$ , given over the range of $W$ considered. . . . .	50
3.5	The $\gamma p \rightarrow J/\psi + p$ data obtained at HERA [126, 127, 128, 129] and LHCb [47, 48] compared with the predictions obtained using the NLO PDFs taken from three different sets of global partons [38, 40, 42] with $\mu_f = m_c$ (solid lines). The dashed line for the CT14 prediction, corresponding to $\mu_f^2 = 2m_c^2$ , is added to demonstrate the scale stability of our NLO predictions; but note that our optimal choice $\mu_f^2 = m_c^2$ agrees better with the HERA data. . . . .	52

- 
- 3.6 Cross section predictions evaluated with  $Q_0^2 = \mu_F^2 = 1.2 m_c^2$  fixed and variations  $\mu_f^2 = \mu_R^2 \in \{1.2, 2.4, 3.6\} \cdot m_c^2$  using CTEQ6.6 partons [41]. A good scale stability is observed over the entire HERA energy range considered. . . . . 53
- 3.7 The two diagrams describing exclusive  $J/\psi$  production at the LHC. The left diagram, the  $W_+$  component, is the major contribution to the  $pp \rightarrow p + J/\psi + p$  cross section for a  $J/\psi$  produced at large rapidity  $Y$ . Thus such data allow a probe of very low  $x$  values,  $x \sim M_\psi \exp(-Y)/\sqrt{s}$ ; recall that for two-gluon exchange we have  $x \gg x'$ . The  $q_T$  of the photon is very small and so the photon can be considered as a real on-mass-shell particle. . . . . 55
- 3.8 The ultraperipheral exclusive  $J/\psi$  production process with rescattering corrections. The blue shaded segment represents interactions between so-called spectator partons in the protons, contributing to the eikonal survival factor,  $S_{eik}^2$ . The red shaded segment represents interactions between spectator partons in one proton and the partons (gluon or quark) in the hard process evolution ladder, contributing to the enhanced survival factor,  $S_{enh}^2$ . The enhanced rescattering effects are highly suppressed in comparison with those entering the eikonal contribution. . . . . 57
- 3.9 The central scale prediction  $\sigma$  for a given global input set of NLO partons, here NNPDF3.0 [38], together with its  $1\sigma$  (shaded) error band show that the current PDF uncertainties are much greater than the experimental uncertainty and the scale variations of the theoretical result. For comparison we also show the NNPDF3.1 [39] predictions, indicated by the dotted lines but with the error band unshaded; in this case the  $\sigma + \delta\sigma$  upper limit follows the HERA data for  $x > 10^{-3}$  while for smaller  $x$  it widens to encompass the data. The exclusive  $J/\psi$  data are therefore in a position to improve the global PDF analyses at low  $x$ . . . . . 60
- 4.1 LO and NLO cross section predictions obtained using the central values of the existing global partons from [42]. Dashed (dotted) lines correspond to the scale choices  $\mu_f^2 = \mu_R^2 = m_c^2$  ( $\mu_f^2 = \mu_R^2 = 2m_c^2$ ) with  $\mu_F = Q_0 = m_c$  fixed. . . . . 67

---

4.2	The description of the $J/\psi$ photoproduction HERA [126, 127, 128, 129] and LHCb [47, 48] data based on using the central value of the global gluon PDF from the three global parton analyses [38, 40, 42] for $x > 0.001$ . The solid red, blue and green lines show the central power fit predictions while the dotted lines show the $\pm 1\sigma$ boundaries, using the errors of the parameters in Table 4.1. We also show by dashed lines the cross section predictions obtained using the current central values of the global gluons for all $x$ . . . . .	69
4.3	The cross-hatched region shows the range of behaviour of the low $x$ NLO gluon determined by fitting to exclusive $J/\psi$ data using ansatz eqn. (4.3) with $xg^{\text{global}}$ taken from NNPDF3.0 [38], MMHT14 [40] or CT14 [42] parton sets. The shaded blue area is the NNPDF3.0 global gluon PDF error band. . . . .	72
4.4	(a) The global gluon PDF, $xg(x, \mu^2)$ , at the matching point $x = 0.001$ and $\mu^2 = 2.4 \text{ GeV}^2$ , (b) the global gluon PDF, $xg(x, \mu^2)$ , at the matching point $x = 0.001$ and $\mu^2 = 2.4 \text{ GeV}^2$ after fitting to HERA+LHCb exclusive $J/\psi$ data. Note that the errors shown on the right hand side are those obtained by propagating the $1\sigma$ experimental data errors to our result, but do not account for theoretical uncertainties. . . . .	73
4.5	Comparison of the low $x$ behaviour of the NLO gluon density $xg(x, \mu^2)$ at $\mu^2 = 2.4 \text{ GeV}^2$ obtained from exclusive $J/\psi$ data and from inclusive $D$ -meson data, see text for details. . . . .	78
4.6	The lower and upper bands are, respectively, the cross section predictions obtained using NNPDF3.0 and NNPDF3.1 global partons constrained by the $D$ -meson LHCb data [122, 174]. The latter includes low $x$ resummation effects. The shaded blue band is the cross section prediction obtained based on our reweighting of the NNPDF3.0 NLO global gluon via the exclusive $J/\psi$ data. The experimental data points are presented as in Fig. 4.2. . . . .	79
5.1	Schematic representation of HVM electroproduction. . . . .	86
5.2	The kinematics of quark and gluon initiated processes. Massive quark lines are indicated in bold. . . . .	89
5.3	The six gluon LO diagrams. . . . .	97
5.4	The six NLO quark subprocess diagrams. . . . .	105
5.5	The NLO gluon subprocess diagrams. . . . .	112

# List of Tables

3.1	HERA data selection for exclusive $J/\psi$ photoproduction. 49 data points are considered with $x \gtrsim 5 \times 10^{-3}$ . . . . .	54
3.2	Rapidity gap survival factors $S^2$ for exclusive $J/\psi$ production, $pp \rightarrow p+J/\psi+p$ , in each $J/\psi$ rapidity $Y$ bin, as measured by the LHCb. For each $pp$ centre of mass energy, 7 TeV and 13 TeV, we give the survival probability for each of the two independent $\gamma p \rightarrow J/\psi p$ subprocesses at $\gamma p$ centre of mass energies $W_{\pm}$ . . . . .	56
4.1	The values of $\lambda$ and $n$ obtained from fits to the $J/\psi$ data using three sets of global partons. The respective values of the total $\chi^2_{\min}$ (and $\chi^2_{\min}/\text{d.o.f}$ ) for 45 data points are also shown. . . . .	68
4.2	Individual $\chi^2_{\min}$ contributions due to HERA ( $N_{\text{dat}} = 25$ ), LHCb-14 ( $N_{\text{dat}} = 10$ ) and LHCb-18 ( $N_{\text{dat}} = 10$ ) data for the three global parton sets. . . . .	70
D.1	NAT assignment to each quark and gluon Feynman diagram. The ‘LQ’ quark diagrams refer to those where the photon attaches to the light quark line. . . .	144

---

*For Nana*

# Chapter 1

## Introduction

### 1.1 Overview

The exploration of the inner structure of the proton has long been at the forefront of the field of Collider Phenomenology. With increasingly bigger and better collider machines over the years, the field has fast evolved into one of precision physics, allowing for the constituent quark and gluon valence and sea content of the proton to be understood and unravelled to the highest level. Practically, the internal structure of the proton is encoded into Parton Distribution Functions (PDFs), non-perturbative and rigourously defined entities in Quantum Field Theory that provide part of the input to the Collinear Factorisation theorems of Quantum Chromodynamics (QCD). Developed in 1973 [1], QCD is the theory of strong interactions of quarks and gluons based on the non-abelian SU(3) gauge group and forms one of the pillars of the Standard Model of Particle Physics. The PDFs may be interpreted as the underlying probability densities,  $xf_i(x, Q^2)$ , for a certain partonic species  $i$  within the proton to have a longitudinal momentum fraction  $x$  at a given probing resolution scale,  $Q^2$ . As of now, with the high abundance and statistical quality of collider data collected in the LHC era of high-energy physics, there is a need for the theory activities to have similar precision to results from experiment. To date, PDF extractions at next-to-leading order (NLO) and next-to-next-to-leading order (NNLO) in the systematic expansion in the QCD strong coupling,  $\alpha_s$ , have become the norm and have provided for an exciting phenomenological platform of interaction between the theory and experimental communities.

The first results on PDF phenomenology were, for the most part, greatly centered



on collider measurements deemed to be of an *inclusive* nature. Deep Inelastic Scattering (DIS) is the iconic inclusive process where the proton substructure was first revealed by an experiment at SLAC in 1969, which directly detected the constituent quark via a highly virtual electromagnetic probe [2]. The information from the lepton scattering in a DIS event allows one to measure the structure functions of the proton, which depend on the PDFs. Over the years, a wealth of DIS data with a wide kinematic coverage in the  $(x, Q^2)$  plane was collected and analysed from many different experimental machines and collaborations to better ascertain the PDFs. The logic was that the inclusive DIS structure function observables,  $F_2^p$ , provided the cleanest and most straightforward access to these objects. Initial fixed target data from e.g. NMC and SLAC were garnered but it was not until the advent of the HERA  $ep$  linear collider and the H1, ZEUS and HERMES experiments that the frontier in collider kinematics was extended to much lower  $x$  and much higher  $Q^2$ . The most important result from HERA is arguably the observation of a relatively steep rise in the DIS proton structure function at low  $x$ , attributed to an increase in the gluon density [3, 4].

Together with DIS data, the HERA collider reported measurements on a plethora of other high-energy physics phenomena, including inclusive jet production, Drell-Yan and heavy vector boson production as well as, notably, *diffractive* events [5, 6], discussed below. While the DIS data from HERA provided for a relatively reliable and precise extraction of the quark densities, the gluon density was still largely left in the dark for  $x \lesssim 0.001$  and  $Q^2 \lesssim 20 \text{ GeV}^2$  [7]. This is mainly a reflection of the fact that, within the Parton Model, there is no direct coupling of the gluon to the proton-resolving probe in DIS events, and few observables where the initial partonic subprocess is instead driven by gluons. Constraint on the gluon density at larger  $x \gtrsim 0.001$ , besides DIS [8], came from high- $p_T$  inclusive dijet and prompt photon production [9]. In both cases, the initiating partons are gluons. In the intermediate regime,  $10^{-4} < x < 10^{-3}$ , the data from open charm production and *diffractive*  $J/\psi$  production, the latter of which were part of a class of events that comprised  $\sim 5 - 10\%$  of DIS signatures reported at HERA, served as further probes of the gluon distribution [10]. The gluon density was also determined in this regime and at even smaller  $x$  qualitatively via the derivative  $\partial F_2^p / \partial \ln Q^2$ , however, beyond  $x \sim 10^{-4}$ , the region was engulfed in a huge band of uncertainty with no constraining data resulting in a gluon density that is, for all intents and purposes, unknown. See [4, 11] for reviews on the state of affairs of high-energy phenomenology at the start of the new millennium.

Small  $x$  PDF phenomenology is now kinematically accessible in the LHC era of collider

physics due to greater centre-of-mass energies,  $\sqrt{s}$ , of the colliding protons, allowing for the data on open charm and diffractive  $J/\psi$  production to extend to unprecedented values down to  $x \sim 3 \times 10^{-6}$ . In this thesis, we will consider the *exclusive* production of heavy vector mesons  $V$  mediated by  $\gamma p$  (photoproduction) and  $\gamma^* p$  (electroproduction) hard scatterings,

$$\gamma(\gamma^*) + p \longrightarrow V + p, \quad V = J/\psi, \psi(2S), \Upsilon. \quad (1.1)$$

These are a specific class of diffractive events mentioned above in which the proton  $p$  remains intact and the final state kinematics are fully specified, with no exchange of quantum numbers between the initial and final states [10]. They constituted around 5% of the low  $x$  events in bins of  $Q^2 \geq 10 \text{ GeV}^2$  at HERA [12, 13, 14] and were characterised by the presence of a rapidity gap, a term first coined by Bjorken in 1993 [15], corresponding to a domain in the detector devoid of activity between the final state products. At the LHC, these hard scatterings instead drive the ultraperipheral central exclusive production of the vector mesons,

$$p + p \longrightarrow p + V + p, \quad V = J/\psi, \psi(2S), \Upsilon. \quad (1.2)$$

The ‘+’ signs on the right hand side denote the rapidity gap either side of the vector meson. Generally, exclusive processes allow for further tests of broad aspects of QCD and hadron spectroscopy, as well as constraining the Beyond-the-Standard-Model (BSM) phase space. Here, we are interested in the aspect of exclusive processes that allow for increased sensitivity to the gluon PDF at low  $x$  and low  $Q^2$ .

The cross section susceptibility of exclusive  $J/\psi$  production to the *square* of the gluon density,  $xg(x, Q^2)$ , at leading-order (LO) in the QCD strong coupling  $\alpha_s$  is what makes it an attractive observable to study. The demand of exclusivity results in a  $t$ -channel two-gluon exchange interaction (the pomeron), where a photon fluctuates into a  $c\bar{c}$  heavy quark pair and is subsequently projected onto the outgoing colourless hadronic state that is the  $J/\psi$ . The utility of  $p + p \rightarrow p + J/\psi + p$  as a probe of the low  $x$  domain was first described in [16]. There, the exclusive cross section for the hard quasi-elastic subprocess  $\gamma^* p \rightarrow J/\psi p$ , which drives the  $pp$  initiated reaction, was derived in the leading-log( $Q^2$ )-approximation (LL<sub>Q</sub>A) of perturbative QCD (pQCD). This is equivalent to the LO result in conventional collinear factorisation and showcased the dependence of the process on the

square of the gluon distribution. In 1993, Ryskin [16] showed that

$$\frac{d\sigma}{dt}(\gamma^* p \rightarrow J/\psi p)|_{t=0} = \frac{\Gamma_{ee} M_\psi^3 \pi^3}{48\alpha} \left(1 + \frac{Q^2}{M_\psi^2}\right) \left[\frac{\alpha_s(\bar{Q}^2)}{\bar{Q}^4} xg(x, \mu_F^2)\right]^2, \quad (1.3)$$

with the electromagnetic coupling constant  $\alpha = 1/137$ ,  $\mu_F^2 \sim \bar{Q}^2 = (Q^2 + M_\psi^2)/4$ , where  $Q^2$  is the photon virtuality, and  $M_\psi$  and  $\Gamma_{ee}$  the mass and electronic decay width of the  $J/\psi$  meson, respectively. Unlike in DIS where one makes an inclusive cut over all final state configurations, here we resolve a particular direction in the final state phase space corresponding to the outgoing vector meson. This maximally breaks the collinear factorisation theorems [17] but, by introducing so-called Generalised Parton Distribution Functions (GPDs), we can maintain this formulation and persist in the use of collinear factorisation, albeit with the GPDs as our non-perturbative input. Recall also that, while in DIS there is no leading order contribution involving gluons in the corresponding hard scattering, here we have a  $t$ -channel *two-gluon* exchange at LO that provides for the increased sensitivity to the gluon PDF. However, this well-defined extraction of the final state comes at a price - one must introduce additional ingredients into the quantum field theory description of the underlying process amplitude amounting to GPDs, as mentioned above, as well as non-perturbative matrix elements that characterise the dynamics of the  $c\bar{c} \rightarrow V$  transition vertex. In the case of  $J/\psi$  production, as we will see, non-relativistic QCD (NRQCD) comes as a powerful tool but largely these non-perturbative objects need to be extracted or fixed via the available data and outside the theory toolbox. The PDFs, for example, may be extracted through a so-called global analysis, as discussed in Chapter 2, introducing additional model parametrisations or dealt with as a free parameter in some simultaneous fit. The extent to which these objects introduce a further uncertainty into a given calculation framework, thereby detracting from an otherwise robust extraction of nucleon structure, remains an area of active research.

## 1.2 Structure of the thesis

A broad discussion in Chapter 2 of the elements constituting the theoretical and phenomenological backbone that underlies our work is given. Amongst them, we systematically explore the state-of-the-art of GPD phenomenology and an important simplification that may be made at small  $x$  - a critical ingredient in the description of exclusive  $J/\psi$

production. We then describe the recent new-and-improved theoretical result for the  $J/\psi$  production based on a low- $x$  resummation and low- $Q$  power subtraction.

In Chapter 3 we show, for the first time, the impact that the exclusive  $J/\psi$  LHCb data has on the behaviour of the low  $x$  and low  $Q^2$  gluon PDF within the collinear factorisation framework at NLO, and that the exclusive  $J/\psi$  data from HERA can be successfully described within this set-up by the global partons. We show the dramatic distinguishing effect these LHCb data have on determining the gluon PDF at low  $x$ . Furthermore, it is the first time that this newly refined framework within collinear factorisation at NLO has been used to produce cross section level results. The chapter also includes a thorough analysis of our predictions accounting for the uncertainty of the global partons, requiring complete sets of central GPD and associated error grids to be produced.

In Chapter 4, having promoted the data as a serious and viable means to probe the low- $x$  regime, we show quantitatively the effect that including the exclusive  $J/\psi$  data from LHCb has on a global fit through a Bayesian statistical reweighting procedure. The results allow one, for the first time, to reliably include the  $J/\psi$  photoproduction data in a fixed order NLO fitting machinery. We substantiate these findings by performing a fit to the exclusive data in which the gluon density rises as a pure power, allowing conclusions to be made regarding the onset of gluon saturation.

Finally, in Chapter 5, we build and use a computational workhorse to enable the calculation of exclusive electroproduction of heavy vector mesons to NLO in collinear factorisation. This extends the photoproduction computation of Ivanov et al. [18], allowing for an additional mass scale provided by the photon virtuality,  $Q^2 \neq 0$ , and proceeds by means of integral reduction to extract  $\overline{\text{MS}}$  transverse and longitudinal NLO coefficient functions.

Our conclusions and possible future investigative avenues are detailed and summarised in Chapter 6.

## Chapter 2

# Preliminaries

In this chapter, we will present the concepts and underlying formalisms used throughout this thesis. We begin these preliminaries with an exposition of collinear factorisation in Section 2.1, the basis of all work presented here, and give an overview of parton distribution functions in the context of global analyses in Section 2.2. Then, in Section 2.3, we provide an introduction to the generalised parton distribution function and emphasise the utility of the Shuvaev transform as a means to relate the conventional parton distribution function to a generalised counterpart for low values of the momentum fraction. We highlight the importance of automated Feynman integral reduction tools, employed in this work, in Section 2.4 and end, in Section 2.5, with a discussion of the exclusive  $J/\psi$  production process within the collinear factorisation framework and the far-reaching benefits a treatment of double logarithmic contributions and a double counting carries.

### 2.1 Observables from Perturbative QCD

Smaller and smaller distance scales of the proton may be unravelled through larger and larger momentum scales of cleanly interacting probes at colliders. Inclusive DIS exposed the proton as a complicated sea of constituent quarks and gluons, aptly named partons, at sufficiently large energies of neutral electromagnetic and charged electroweak probes. The interaction of such a probe carrying a virtuality  $Q^2$  allows for a coarse-graining of the matter content, resolving its underlying structure at lengths of  $1/Q$ . With such resolving capabilities available at colliders past and present, the probe is effectively interacting at the constituent level of the colliding matter and gives rise to the so-called ‘Parton Model’

of sub-atomic particle interactions.

Within the framework of collinear factorisation [17], the observables,  $O_a$ , of high-energy physics phenomena are expressed as a convolution of a process dependent, perturbatively calculable *coefficient function*,  $C_{a,j}$ , and a universal parton distribution function (PDF),  $xf_j$ ,<sup>1</sup>

$$O_a(x, Q^2) = (C_{a,j} \otimes xf_j)(x). \quad (2.2)$$

Here,  $x$  is the fraction of (plus-component) momentum of the parent hadron carried by the parton. The coefficient functions are calculated by replacing the hadronic state with an *on-shell* parton  $j$ , in line with the ‘Parton Model’, and evaluated systematically in powers of the QCD strong coupling,  $\alpha_s$ , so that

$$C_{a,j} = \sum_n \left( \frac{\alpha_s}{4\pi} \right)^n C_{a,j}^n. \quad (2.3)$$

Beyond the leading power in this expansion, unphysical divergences manifest themselves in loop momentum integrals as ultraviolet (UV) high energy singularities or originate in phase space configurations where on-shell partons may go collinear, leading to infrared (IR) mass and collinear singularities. Yet, experimentally measurable quantities, which these objects are used to make predictions for, are finite. In a programme of renormalisation, these divergences are removed order by order in  $\alpha_s$ , to render meaningful theory predictions that can be compared to experiment.

In this work, we counteract these divergences using dimensional regularisation in  $d = 4 - 2\epsilon$  space-time dimensions, where  $\epsilon$  is small. This amounts to a shift from the physical  $d = 4$  space-time to one where the aforementioned divergences instead appear on an analytic level as simple poles in the regulator  $\epsilon$ . From explicit power counting in the mass dimensionality of the quark and gluon field and coupling content within the QCD Lagrangian, one can infer that the QCD strong coupling is dimensionless in  $d = 4$ . To maintain this in  $d = 4 - 2\epsilon$ , we introduce an arbitrary scale  $\mu_0^2$ . Explicitly, a given observ-

---

<sup>1</sup>The symbol  $\otimes$  denotes a Mellin convolution. The  $N$ th Mellin moment of a single variable function  $f(x)$  is defined as the integral transform

$$f^N := \int_0^1 dx x^{N-1} f(x) \quad (2.1)$$

to Mellin space. In this space, these convolutions appear as simple products but they will not be discussed in this work.

able,  $O_a(x, Q^2)$ , written in the collinear factorisation scheme is then

$$O_a(x, Q^2) = \left( \hat{C}_{a,j} \left( \hat{\alpha}_s, \frac{Q^2}{\mu_0^2}, \epsilon \right) \otimes x \hat{f}_j \right) (x). \quad (2.4)$$

Hats denote unrenormalised, or bare, quantities so that e.g.  $\hat{\alpha}_s$  represents the bare QCD strong coupling.

The removal of UV divergences proceeds through the renormalisation of the strong coupling constant. We introduce the renormalisation constant for the strong coupling,  $Z_{\alpha_s}$ , and the renormalisation scale,  $\mu_R^2$ , and write

$$\hat{\alpha}_S = \hat{\alpha}_s \mu_0^{2\epsilon}, \quad \alpha_S = \alpha_s \mu_R^{2\epsilon} \quad \text{and} \quad \hat{\alpha}_S = Z_{\alpha_s} \alpha_s \mu_R^{2\epsilon}, \quad (2.5)$$

so that

$$\hat{\alpha}_s = Z_{\alpha_s} \alpha_s \left( \frac{\mu_R^2}{\mu_0^2} \right)^\epsilon. \quad (2.6)$$

Setting  $\mu_0^2 = \mu_R^2$  for notational convenience gives,

$$O_a(x, Q^2) = \left( \hat{C}_{a,j} \left( \alpha_s(\mu_R^2), \frac{Q^2}{\mu_R^2}, \epsilon \right) \otimes x \hat{f}_j \right) (x). \quad (2.7)$$

The remaining divergences correspond to initial state mass singularities (collinear divergences) and are dealt with via mass factorisation, whereby they are absorbed into the PDFs. The bare coefficient functions factorise<sup>2</sup> into a piece that is finite as the  $d \rightarrow 4$  ( $\epsilon \rightarrow 0$ ) physical dimensionality is restored, and a piece that contains the divergences parametrised by explicit poles in  $\epsilon$ . This separation occurs at a factorisation scale  $\mu_F^2$ , and the manner in which one makes this split is dependent on the choice of factorisation scheme, see below. In this way, we obtain,

$$O_a(x, Q^2) = \left( C_{a,i}^{\text{sch}} \left( \alpha_s(\mu_R^2), \frac{Q^2}{\mu_R^2}, \frac{\mu_F^2}{\mu_R^2}, \epsilon \right) \otimes Z_{ij}^{\text{sch}} \left( \alpha_s(\mu_R^2), \frac{\mu_F^2}{\mu_R^2}, \frac{1}{\epsilon} \right) \otimes x \hat{f}_j \right) (x), \quad (2.8)$$

where  $Z_{ij}^{\text{sch}}$  is a scheme dependent IR renormalisation matrix and  $i, j$  run over the partons. After this separation, the  $C_{a,i}^{\text{sch}}$  ( $Z_{ij}^{\text{sch}}$ ) factors admit a Taylor (Laurent) series in  $\epsilon$ . The  $Z_{ij}^{\text{sch}}$  factors therefore carry the diverging terms, made explicit in its functional dependence. As

---

<sup>2</sup>Factorisation has been proven to hold for only a certain class of observables. In some cases, this factorisation is only *assumed* or posited to hold. See [17] for a summary of QCD factorisation theorems.

the bare PDFs,  $x\hat{f}_j$ , are unmeasurable quantities, we can absorb the mass divergences within the  $Z_{ij}^{\text{sch}}$  factors into them. The scheme dependent and renormalised PDFs are then

$$xf_i^{\text{sch}}(x, \mu_F^2, \alpha_s(\mu_R^2)) = Z_{ij}^{\text{sch}} \left( \alpha_s(\mu_R^2), \frac{\mu_F^2}{\mu_R^2}, \frac{1}{\epsilon} \right) \otimes x\hat{f}_j, \quad (2.9)$$

and therefore

$$O_a(x, Q^2) = \left( C_{a,i}^{\text{sch}} \left( \alpha_s(\mu_R^2), \frac{Q^2}{\mu_R^2}, \frac{\mu_F^2}{\mu_R^2}, \epsilon \right) \otimes xf_i^{\text{sch}}(x, \mu_F^2, \alpha_s(\mu_R^2)) \right) (x). \quad (2.10)$$

Equation (2.10) is now finally a convolution of finite quantities and, after sending  $\epsilon \rightarrow 0$ , can be used to produce numerical predictions for experimental observables. The  $C_{a,i}^{\text{sch}}$  encode the hard process dynamics and can be computed in perturbation theory. The  $xf_i^{\text{sch}}$  parametrise the non-perturbative soft physics and can be extracted from experiment, see Section. 2.2. We reiterate that, as the index  $a$  is not carried by the PDF, it is a universal quantity. The terms contributing to  $O_a(x, Q^2)$  at the leading power in  $\alpha_s$  are called leading-order (LO). Those at the next to leading power are the next-to-leading-order (NLO) contributions and so on. The PDFs admit a probabilistic interpretation at LO in the ‘Parton Model’.

In the Minimal Subtraction (MS) scheme, the  $Z_{ij}^{\text{sch}}$  contain *only* the terms proportional to  $1/\epsilon$ . In this scheme, the strong coupling renormalisation constant

$$Z_{\alpha_s}^{\text{MS}} = 1 - \frac{1}{\epsilon} \beta_0 \alpha_s + \mathcal{O}(\alpha_s^2), \quad (2.11)$$

where  $\beta_0$  is the leading order coefficient of the  $\beta$ -function<sup>3</sup>. Substitution of eqn. (2.11) into eqn. (2.6), together with an expansion in  $\epsilon$  to  $\mathcal{O}(\epsilon)$  inclusive, gives the relation between the bare coupling and the renormalised coupling to  $\mathcal{O}(\alpha_s^2)$  accuracy in the MS scheme. This

---

<sup>3</sup>The running of the strong coupling constant  $\alpha_s$ , a feature inherent in QCD by virtue of its asymptotic freedom proven by Gross & Wilczek [19, 20] and independently Politzer [21] in 1973, is given by the  $\beta$ -function. In QCD, this admits the perturbative expansion [21, 22, 23, 24, 25],

$$\beta(\alpha_s) = -\alpha_s \sum_{n=0}^{\infty} \beta_n \left( \frac{\alpha_s}{4\pi} \right)^{n+1}, \quad (2.12)$$

where  $\beta_0 = 11 - 2/3 N_f$ , with  $N_f$  the number of quarks with mass much smaller than the scale  $\mu_R$ .



is,

$$\hat{\alpha}_s = \alpha_s \left( 1 - \alpha_s \beta_0 \left( \frac{1}{\epsilon} + \ln \left( \frac{\mu_R^2}{\mu_0^2} \right) \right) \right) + \mathcal{O}(\alpha_s^3). \quad (2.13)$$

Here, however, we will use the Modified Minimal Subtraction ( $\overline{\text{MS}}$ ) scheme where additional factors of the Euler-Mascheroni constant,  $\gamma_E$ , and  $\ln(4\pi)$ , which appear in dimensionally regularised loop integrals, are absorbed in the redefinition,

$$\frac{1}{\hat{\epsilon}} = \frac{1}{\epsilon} + \gamma_E - \ln(4\pi). \quad (2.14)$$

In the  $\overline{\text{MS}}$  scheme, we therefore have

$$\hat{\alpha}_s = \alpha_s \left( 1 - \alpha_s \beta_0 \left( \frac{1}{\hat{\epsilon}} + \ln \left( \frac{\mu_R^2}{\mu_0^2} \right) \right) \right) + \mathcal{O}(\alpha_s^3). \quad (2.15)$$

The coefficient  $\beta_0$  appearing in eqn. (2.11) is scheme independent and therefore unaffected in this scheme transformation.

The evolution of the  $\overline{\text{MS}}$  PDFs,  $xf_i(x, \mu_F^2, \alpha_s)$ , in the scale  $\mu_F^2$  is given by, from eqn. (2.9),

$$\mu_F^2 \frac{d}{d\mu_F^2} xf_i = \mu_F^2 \frac{d}{d\mu_F^2} Z_{ij} \otimes x\hat{f}_j = \mu_F^2 \frac{d}{d\mu_F^2} Z_{ik} \otimes \left( Z_{kj}^{-1} \otimes xf_j \right) = P_{ij} \otimes xf_j, \quad (2.16)$$

where

$$P_{ij}(x, \alpha_s) = \left( \mu_F^2 \frac{d}{d\mu_F^2} Z_{ik} \otimes Z_{kj}^{-1} \right) (x, \alpha_s) \quad (2.17)$$

are the  $\overline{\text{MS}}$  collinear splitting kernels of QCD. Eqn. (2.16) is the DGLAP equation [26, 27, 28] for the PDF  $xf_i$ , giving its evolution from some initial energy scale  $\mu_{F_1}^2$  to some final scale  $\mu_{F_2}^2$ . The  $P_{ij}$  are known to NNLO in the literature [29, 30] and calculable within pQCD. The DGLAP equation provides the resummation of  $\ln(\mu_{F_2}^2/\mu_{F_1}^2)$  terms at each order in  $\alpha_s$ . See Appendix B for another evolution equation, the BFKL equation, as well as an introduction to resummation in the  $(x, Q^2)$  plane.

Note that an all order computation would allow for the cancellation of all explicit instances of  $\mu_R^2$  and  $\mu_F^2$  on the r.h.s of eqn. (2.10). In practice, however, this is not feasible and conceptually ill-defined due to the asymptotic character of pQCD. Equation (2.10) is therefore truncated at a particular order in  $\alpha_s$  with some residual dependence on the (unphysical) renormalisation and factorisation scales remaining. In a scale fixing approach,

one tries to find a sensible, physically motivated choice of scale so as to mimic the missing higher order contributions. For single scale processes, such as DIS, the ‘optimal’ scale choice is typically set to the energy scale of the process,  $\mu_R^2 = \mu_F^2 \sim Q^2$ . However, this provides for one strategy only, and it is ambiguous as to whether one should finally choose  $Q^2$ ,  $Q^2/2$  or  $2Q^2$ , for example.

We end this section by noting that the Operator Product Expansion (OPE) [31, 32, 33] allows one to formally expand general operator interactions, in a given quantum field theory, as a series of matrix elements of local operators with multiplicative coefficient functions. The OPE, as applied to QCD, identifies the Mellin moments of the non-perturbative PDFs with the local operators of this expansion [34]. The operators are ordered in powers of the scale  $1/Q^2$ , introduced above. The leading, or so-called leading-twist<sup>4</sup>, term in this series dominates for large  $Q^2$  and is equivalent to the leading contribution in the mainstream approach of collinear factorisation.

## 2.2 Global PDF analyses

Parton distribution functions,  $xf(x, Q^2)$  are the non-perturbative input into the conventional collinear factorisation theorems. While their evolution in the scale  $Q$  is known from the DGLAP equations of pQCD [26, 27, 28], see Section 2.1, their  $x$  dependence cannot be extracted from first principles, but from experiment, requiring an interplay between the experimental and theoretical communities. There has been progress on the frontier of lattice QCD too as an independent, but complementary, means to extract the PDFs [35].

The increasing availability of high-precision experimental measurements from the Jefferson lab, HERA, RHIC, the Tevatron and, the LHC, together with theoretical advances in pQCD past the naive LO QCD parton model has meant in some cases an extraction of PDFs at the percent level [36, 37]. There are a variety of different PDF-fitting collaborations providing so-called *global PDF analyses*, which all maintain the same conceptual basis but differ in their mode of extraction and employment of methods to determine the PDFs. Their results are publicly available as interpolation grids in  $x$  and  $Q^2$ , typically up to and including NNLO, and are organised into a central member set together with  $\mathcal{O}(100 - 1000)$  one-sigma variation error sets provided in Hessian eigenvector and/or Monte-Carlo replica format. In this work, we will refer to the PDFs pertaining to the

---

<sup>4</sup>By twist of an operator, we mean the difference of its dimension and spin.

NNPDF [38, 39], MMHT [40] and CT [41, 42] collaborations. Although recently there was reported evidence for BFKL dynamics already at play at HERA energies [43], the DGLAP formalism has remained the mainstream, with all global fitting groups using the conventional DGLAP collinear factorisation formalism to extract process independent PDFs while retaining a degree of uniqueness in their method of approach. In light of [43], the NNPDF collaboration have, in addition, released PDF sets supplemented with small  $x$  BFKL resummation. We will consider these in Chapter 4.

The various groups are largely in agreement in their approaches but can differ in the choice of data included in their fit via e.g. imposition of kinematic cuts, the treatment of data uncertainties and of heavy quark thresholds as well as the input parametrisation at some  $Q_0$ . The input distribution,  $xf(x, Q_0^2)$ , at some starting scale  $Q_0^2 \sim 1 - 2 \text{ GeV}^2$  is the DGLAP initial condition and is typically parametrised independently by each group with some  $x$  dependence that describes the expected small  $x$  and large  $x$  behaviour of the PDF. Typically it is the case, however, that different parametrisation forms lead to successful fits of the data for a wide range of  $x$ . An attempt to remove this parametrisation bias is given by the Monte-Carlo approach of NNPDF which use a Neural Network framework to bypass the reliance on a specific ansatz for the input distribution - all structures are implicitly taken into account in their sampling of the space of possible functional forms.

Generally speaking, it is desired that the functional form for the input distribution, with a given number of free parameters  $\{a_i\}$ , has enough flexibility and freedom to describe the high energy physics data for a wide range of  $x$ . This form may be evolved via DGLAP to any given scale,  $Q$ , to allow calculation of observables and compare with data. Practically, evolution codes such as `QCDNUM` [44] automate this procedure and numerically solve the DGLAP equations on a discrete grid in  $x$  and  $Q^2$ . The input distributions typically involve admixtures of small  $x$  and large  $x$  behaviour, with intermediate behaviours characterised by additional multiplicative polynomials or exponential structures. The precise form depends on the global fitting group and can generically be expressed as

$$xf(x, Q_0^2) = x^{a_1} (1 - x)^{a_2} P(x, \{a_3, a_4, \dots\}), \quad (2.18)$$

where  $\{a_i\}$  are the free parameters to be determined and the function  $P$  is responsible for the behaviour between the low  $x$  sea and large  $x$  valence regimes (described here by parameters  $a_1$  and  $a_2$  respectively). The MMHT14 PDFs [40], for example, have refined the input parametrisations used by the MSTW collaboration [45] with incorporation of

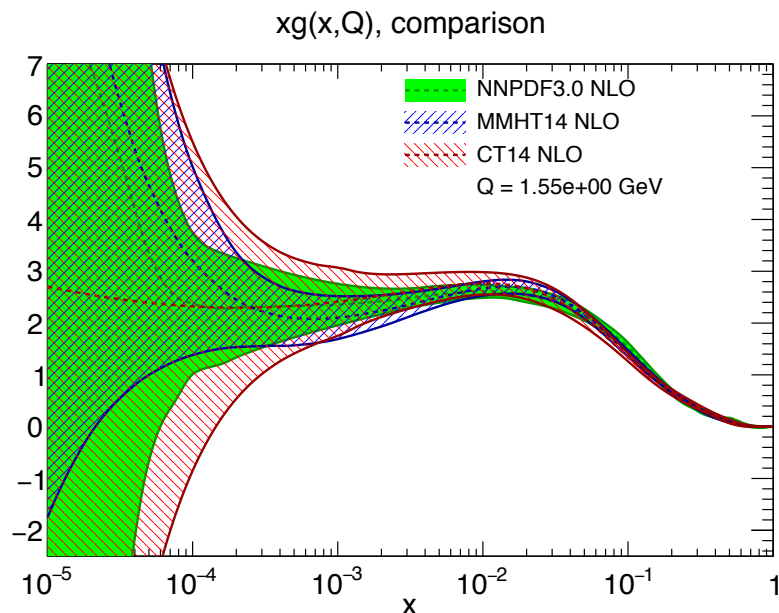


Figure 2.1: Comparison of NLO gluon PDFs obtained in the NNP3.0, MMHT14 and CT14 [38, 40, 42] global analyses at scale  $Q = 1.55 \text{ GeV}$ , close to the input scale of the assumed DGLAP evolution. Plot generated within APFEL [146, 147].

Chebyshev polynomial forms.

In Fig. 2.1, we show a comparison of NLO gluon PDFs obtained from the global analyses NNP3.0 [38], MMHT14 [40] and CT14 [42] at a low scale  $Q = \mathcal{O}(m_c)$ , where  $m_c \sim 1.5 \text{ GeV}$ .<sup>5</sup> In the small  $x$  domain, the gluon PDF dominates. In this regime, the parametrisations of the gluon density all boil down to a simple power law  $xg \sim x^{-\lambda}$  with  $\lambda > 0$ . In global analyses to date, there is a lack of experimental data probing the low  $x$  domain,  $x < 10^{-3}$ . This comes hand in hand with theoretical complications at low  $x$  too, such as the possible necessity of BFKL dynamics and low  $x$  resummation together with the eventual onset of gluon saturation and recombination effects. As such, the PDFs that are extracted in this kinematic regime are poorly understood and have large uncertainty bands. Additionally some PDFs are consistent with decreasing or vanishing gluon densities and are therefore arguably unphysical.

<sup>5</sup>Note that the NNP3 collaboration have published a more up to date global analysis PDF set, NNP3.1 [39]. However, in this work we largely use its predecessor v3.0 and make comparisons between NNP3.0, MMHT14 and CT14 because they are based on similar data constraints and released around the same time. There exist also CT18 PDFs [46] but these, to date, have not been published.

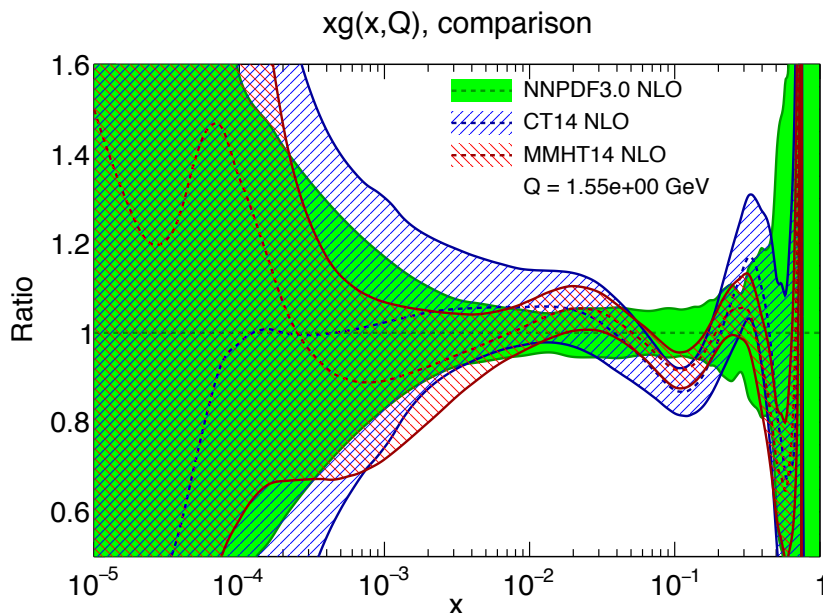


Figure 2.2: Ratios  $xg_{\text{CT14}}/xg_{\text{NNPDF3.0}}$  and  $xg_{\text{MMHT14}}/xg_{\text{NNPDF3.0}}$  of NLO gluon PDFs taken from [38, 40, 42] at a fixed scale  $Q = 1.55 \text{ GeV}$ . Plot generated within APFEL [146, 147].

The relatively recent measurement of central exclusive photoproduction of heavy vector mesons  $V = J/\psi, \psi(2S)$  via ultraperipheral  $pp$  collisions at the LHCb [47, 48] allows kinematic coverage down to  $x \sim \text{few units of } 10^{-6}$  and is a serious candidate to allow for the extraction of a low scale (around the input scale,  $Q_0 \sim 1 - 2 \text{ GeV}$ ) and low  $x$  gluon PDF.

In this thesis, we will explain why the  $J/\psi$  photoproduction data are in a comfortable position to be included in future global analyses, emphasising their utility and constraining power in this low  $x$  and low  $Q$  part of the  $(x, Q)$  phase space. We will quantify the effect that these data would have in a full fitting machinery through performing a reweighting procedure based on a Bayesian statistics framework.

A useful way to compare the different PDF sets is to take one set as a reference and produce ratios of the others relative to this. Fig. 2.2 applies this procedure to the data in Fig. 2.1. Note that current PDF uncertainties in the valence regime,  $x \gtrsim 0.1$ , are also rather sizeable. The origin of the error in the large  $x$  regime is different to that at small  $x$  and important in e.g. BSM searches and PDF flavour separation. We will not, however, discuss this issue here, but see [49, 50] where this is detailed further. In this work we

will also not discuss nuclear PDFs, the non-perturbative input used to describe particle formation via heavy-ion collisions at e.g. RHIC and the LHC [51, 52, 53]. These collisions are regarded as more forthcoming signatures in the search for the saturation momentum,  $Q_s$ , due to the enhancement from the atomic number of the colliding nuclei,  $A^{1/3}$ , but the corresponding PDFs are currently poorer constrained.

## 2.3 Generalised Parton Distribution Functions

### 2.3.1 Introduction

The conventional collinear factorisation theorems used within the Parton Model to describe inclusive processes, like DIS, implicitly integrate out the partonic transverse degrees of freedom perpendicular to the direction of the nucleon and the hard scattering is initiated by partons moving in a single space dimension, collinear to the parent nucleon. In less inclusive processes, the interaction is no longer described on a two-dimensional plane spanned by the directions of the incoming and outgoing electron, as in DIS, but instead, a resolved final state defines another direction which need not, in some frame, lie in this plane. This introduces some transversity in the final state in which a factorisation into objects containing only collinear degrees of freedom will not do. Such processes may instead be described by a factorisation into so-called off-forward distributions, where the transverse degrees of freedom of the partons are then imprinted onto final state hadrons.

In this work, we will be concerned with the Generalised Parton Distribution (GPD), a specific off-forward parton distribution function first introduced more than 20 years ago by Mueller et al. [54], Ji [55, 56] and Radyushkin [57, 58] depending on  $x$ , the longitudinal momentum fraction carried by the parton as well as a skewing parameter  $\xi$  and  $t$ -channel momentum transfer squared  $t = \Delta^2$  that account for the additional transverse kinematics. In Fig. 2.3, we follow the symmetric set up of Ji [59] and introduce a light-cone coordinate system. In this system, a generic four-vector  $v^\mu = (v^0, v^1, v^2, v^3)$  is expressed in the form  $v^\mu = (v^+, v_\perp, v^-)$  via the transformation equations

$$v^\pm = \frac{1}{\sqrt{2}} (v^0 \pm v^3) \quad \text{and} \quad v_\perp = (v^1, v^2). \quad (2.19)$$

The input and output momenta for two partons are  $x = X + \xi$  and  $x' = X - \xi$  with respect to the average incoming proton plus momentum  $P^+ = (p^+ + p'^+)/2$ . Here,  $p^\mu = (1 + \xi)P^\mu$

and  $p'^\mu = (1 - \xi)P^\mu$  are the incoming and outgoing proton momenta respectively and the momentum transfer  $\Delta^\mu = (\Delta^+, \Delta_\perp, \Delta^-) = (p' - p)^\mu$ , where  $\Delta^+ = -2\xi P^+$  contains the longitudinal momentum asymmetry,

$$\xi = \frac{p^+ - p'^+}{p^+ + p'^+}, \quad (2.20)$$

parametrising the skewness of the active parton along the light-cone direction.

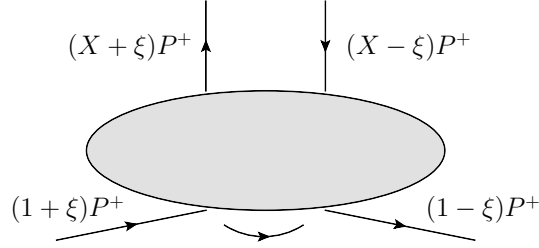


Figure 2.3: Parametrisation of the plus component of the hadronic and partonic momenta used in this work.

These generalised objects do not uphold a probabilistic interpretation like PDFs may do, but are well-defined in quantum field theory as matrix elements of bilocal quark and gluon operators at a light-like separation. In the light-cone gauge at leading twist, the quark GPD is

$$\begin{aligned} F^q(X, \xi, t) &= \frac{1}{2} \int \frac{dz^-}{2\pi} e^{iX P^+ z^-} \langle p' | \bar{\psi}^q \left( -\frac{z}{2} \right) \gamma^+ \psi^q \left( \frac{z}{2} \right) | p \rangle |_{z^+ = z_\perp = 0} \\ &= \frac{1}{2P^+} \left[ H^q(X, \xi, t) \bar{u}(p') \gamma^+ u(p) + E^q(X, \xi, t) \bar{u}(p') \frac{i\sigma^{+\mu} \Delta_\mu}{2m_N} u(p) \right] \end{aligned} \quad (2.21)$$

and the gluon GPD,

$$\begin{aligned} F^g(X, \xi, t) &= \frac{1}{P^+} \int \frac{dz^-}{2\pi} e^{iX P^+ z^-} \langle p' | F^{+\mu} \left( -\frac{z}{2} \right) F_\mu^+ \left( \frac{z}{2} \right) | p \rangle |_{z^+ = z_\perp = 0} \\ &= \frac{1}{2P^+} \left[ H^g(X, \xi, t) \bar{u}(p') \gamma^+ u(p) + E^g(X, \xi, t) \bar{u}(p') \frac{i\sigma^{+\mu} \Delta_\mu}{2m_N} u(p) \right], \end{aligned} \quad (2.22)$$

where  $z = (z^+, z_\perp, z^-)$  are the light-cone coordinates,  $u$  and  $\bar{u}$  are nucleon spinors and  $m_N$  is the mass of the nucleon. Here,  $F^q$  and  $F^g$  are both expressed as a Fourier transform of a matrix element of a chiral even operator formed from either quark fields  $\psi^q$  or the

gluon field strength tensor  $F^{\mu\nu}$ . The result is a decomposition into twist-2 parton helicity conserving GPDs  $H$  and  $E$ . The manifest gauge-invariance of eqns. (2.21) and (2.22) is restored through insertion of a Wilson line  $U$  between the two fields at position  $-z/2$  and  $z/2$ . In a general gauge, we have in addition the factor

$$U\left(-\frac{z}{2}, \frac{z}{2}\right) = \mathcal{P} \left\{ \exp \left( -ig \int_{-z/2}^{z/2} d\zeta n \cdot A \right) \right\}, \quad (2.23)$$

where  $\mathcal{P}$  is an explicit path-ordering and  $n \sim (1, 0, 0, -1)$  is a light-like vector. It follows that, as  $n \cdot A = A^+ = 0$  in the light-cone gauge,  $U = 1$  identically.

We do not consider spin dependent GPDs here, which occur at higher twist and are probed in measurements in which the spin or polarisation state is fully defined. If the spin states are averaged over, as in the description of an unpolarised measurement, then there is no way to have a direct dependence on, or be sensitive to, what these objects represent. Moreover, there are also parton helicity-flip GPDs (chiral odd) considered in the literature [60] in which the initial and final state hadrons have different polarisations, but these are again not considered as they are not needed here.

The GPD naturally encodes more information on nucleon structure than the conventional collinear PDF does and allows one to build up a more complete three-dimensional tomographic picture of hadrons, in which one is also able to account for nucleon pressure and shear forces [61, 62]. It is part of a hierarchical network of distributions in which the Parton Correlation ‘mother’ function resides at the top and the GPD and PDF stem from transformations of other functions. One can obtain PDFs from (equal initial and final state helicity) GPDs by setting  $\xi, t \rightarrow 0$ , for example [63].

Deeply-Virtual-Compton-Scattering (DVCS) [55, 56, 57, 58], a hard exclusive reaction in which an electron and proton scatter off each other via a high virtuality photon and produce a real photon, has for a long time provided the cleanest experimental probe of GPDs. There is currently DVCS Beam Spin Asymmetry data on a fixed target proton from e.g. HERMES, as well as at the Hall-A and CLAS experiments at Jefferson Lab, before and after the upgrade of its beam energy to 12 GeV [64, 65]. In addition to fixed target data also provided by the COMPASS experiment at CERN, the kinematic range of available data was extended further with first measurements of the DVCS cross section, absolute and differential in  $t$ , at the HERA collider [66, 67]. The upcoming Electron-Ion-Collider (EIC) will support these measurements with beam energies of  $\sqrt{s} = 45$  and 140



GeV in the rapidity interval  $0.01 < Y < 0.95$  [68].

The study of GPDs is a fast-evolving and dynamic field. While the extraction of GPDs within analogous global analyses as performed for PDFs is not, as of yet, mainstream phenomenology, there has been significant progress on this frontier through the understanding of Compton-Form-Factors (CFFs). These parametrise the DVCS amplitude and depend on the GPDs in convolution with known hard scattering subprocesses. See [69] for a recent phenomenological analysis and [70] for a review. In the former, an extraction of the CFFs via a LO global fit within the PARTONS framework [71] was made using available DVCS data from Hall-A, CLAS, HERMES and COMPASS. More recently, the same experimental observable provided a means to separate different quark flavour GPDs in the valence kinematic regime using neural networks, see [72]. The development of GPDs is therefore akin to that of PDFs, in which the study of elastic-form-factors via DIS ultimately paved the way to the PDFs used today.

The exclusive heavy vector meson production that we consider in this work is also susceptible to a description via the GPDs. Here, the difference in the kinematic set-up, as compared to DVCS, amounts to the replacement of the resolved final state photon with a mesonic bound state. This complicates the underlying perturbative description of the process, as additional structure is needed to describe the transition from open quarks to bound hadron. This introduces a model uncertainty with possible unconstrained mass corrections that interfere with an otherwise clean extraction of GPDs. Experimentally, however, the DVCS process requires a careful background subtraction of the interfering Bethe-Heitler process [73]. Exclusive vector meson production avoids such difficulty, while retaining sensitivity to GPDs.

### 2.3.2 Symmetries and evolution

In this section, we collect some of the properties of GPDs that are useful and employed in this work.

In the forward limit,  $p' = p$  (or  $\xi \rightarrow 0$ , see eqn. (2.20)), the defining equations for the quark and gluon GPDs, eqn. (2.21, 2.22), reduce to the forward quark,  $q(x)$ , and gluon,

$xg(x)$ , parton distribution functions,<sup>6</sup>

$$\begin{aligned} H^q(x, 0, 0) &= q(x), \text{ for } x > 0, \\ H^q(x, 0, 0) &= -\bar{q}(x), \text{ for } x < 0, \\ H^g(x, 0, 0) &= xg(x). \end{aligned} \tag{2.24}$$

Discrete time reversal invariance amounts to interchanging initial and final hadronic momenta ( $p \leftrightarrow p'$ ) so that  $\xi \rightarrow -\xi$ . This means,

$$H^q(x, \xi, t) = H^q(x, -\xi, t) \quad \text{and} \quad H^g(x, \xi, t) = H^g(x, -\xi, t). \tag{2.25}$$

As gluons are their own antiparticles, it follows further that

$$H^g(x, \xi, t) = H^g(-x, \xi, t). \tag{2.26}$$

No such symmetry exists in general for the quark distributions. The charge conjugation odd ( $C = -$ ) and charge conjugation even ( $C = +$ ) unpolarised quark GPDs, however, do uphold this symmetry and are defined by

$$\begin{aligned} (C = -) : \quad H^{q(-)} &= H^q(x, \xi, t) + H^q(-x, \xi, t), \\ (C = +) : \quad H^{q(+)} &= H^q(x, \xi, t) - H^q(-x, \xi, t). \end{aligned} \tag{2.27}$$

Lastly, the Hermitean conjugate of eqn. (2.21, 2.22) leads to

$$[H(x, \xi, t)]^* = H(x, -\xi, t), \tag{2.28}$$

which, together with eqn. (2.25), implies the GPDs considered in this work are real valued quantities. In this thesis, the imaginary part of an amplitude (which is a convolution of a coefficient function and a PDF or GPD) therefore completely arises from the imaginary part of the coefficient function.

Like forward PDFs, the GPDs also depend on a factorisation scale  $\mu_F$  and evolve according to a generalised DGLAP evolution in which the perturbatively calculable forward splitting kernels, introduced in Section 2.1, are replaced by off-forward analogues. As-

---

<sup>6</sup>No such relation holds for  $E^q$  and  $E^g$  as they decouple from the defining GPD equations in the limit  $t \rightarrow 0$  due to the explicit  $\Delta^\mu$  factor in eqns. (2.21) and (2.22). We will make use of this observation in Chapter 5.

suming an evolution in the perturbative region, the non-singlet GPDs for example evolve according to

$$\mu_F^2 \frac{d}{d\mu_F^2} F^{\text{NS}}(x, \xi, t, \mu_F^2) = \int_{-1}^1 \frac{dy}{|\xi|} V^{\text{NS}}\left(\frac{x}{\xi}, \frac{y}{\xi}\right) F^{\text{NS}}(y, \xi, t, \mu_F^2), \quad (2.29)$$

where we have kept explicit the dependence on  $\mu_F$ . Here,  $V^{\text{NS}}$  are the non-singlet off-forward splitting kernels and, for quarks  $i \in \{u, d, s\}$ ,

$$\begin{aligned} F_{i(-)}^{\text{NS}}(x, \xi, \mu_F^2) &= F^{i(-)}(x, \xi, \mu_F^2) + F^{i(-)}(-x, \xi, \mu_F^2), \\ F_{ij(+)}^{\text{NS}}(x, \xi, \mu_F^2) &= F^{i(+)}(x, \xi, \mu_F^2) - F^{j(+)}(x, \xi, \mu_F^2), \quad (i \neq j), \end{aligned} \quad (2.30)$$

are, respectively, the quark charge conjugation odd flavour diagonal ( $i = j$ ) and quark charge conjugation even flavour off-diagonal ( $i \neq j$ ) combinations derived from

$$\begin{aligned} (C = -) : \quad F^{q(-)} &= F^q(x, \xi, \mu_F^2) + F^q(-x, \xi, \mu_F^2), \\ (C = +) : \quad F^{q(+)} &= F^q(x, \xi, \mu_F^2) - F^q(-x, \xi, \mu_F^2). \end{aligned} \quad (2.31)$$

As in the forward case, the evolution of the singlet GPDs are coupled. The singlet GPDs are the gluon GPD,  $F^g(x, \xi, \mu_F^2)$ , and the quark charge conjugation even flavour diagonal singlet combination,

$$F^S(x, \xi, \mu_F^2) = \sum_i F^{i(+)}(x, \xi, \mu_F^2). \quad (2.32)$$

As we will see, only the evolution of the singlet sector GPDs are relevant in this work. See Appendix C for the explicit formulae of the corresponding singlet evolution kernels along with their, in general, mixed evolution equation.

### 2.3.3 The Shuvaev Transform

Though exclusive  $J/\psi$  production is described by GPDs, at very low values of  $x$  and small momentum transfer  $t$ , the GPD can be related to the conventional integrated PDF, via the Shuvaev transform, with accuracy  $\mathcal{O}(x)$  [74, 75]. The key observation is that the Gegenbauer (conformal) moments,  $G^N$ , of the GPDs evolve in the same manner as the Mellin moments,  $M^N$ , of the PDFs, that is the evolution is described by the same anomalous dimensions [76, 77] - a consequence of conformal invariance of the evolution

equations.<sup>7</sup> Explicitly, at LO both  $M^N$  and  $G^N$  are multiplicatively renormalised and follow the relations

$$M_i^N(Q^2) = M_i^N(Q_0^2) \left( \frac{Q^2}{Q_0^2} \right)^{\gamma_{N,i}}, \quad G_i^N(Q^2) = G_i^N(Q_0^2) \left( \frac{Q^2}{Q_0^2} \right)^{\gamma_{N,i}}, \quad (2.33)$$

where  $\gamma_{N,i}$  are the anomalous dimensions of the forward PDFs, defined as the Mellin transform of the splitting functions introduced in Section 2.1.

Gegenbauer moments of the GPDs are the analogue of Mellin moments which diagonalise the  $Q^2$  evolution of PDFs. The corresponding operator diagonalises the  $Q^2$  evolution of the GPDs [76]. As  $\xi \rightarrow 0$ , the Gegenbauer moments become equal to the Mellin moments. These facts allow one to restore the full GPD function (at a given fixed scale) through knowledge of its Gegenbauer moments. Explicitly, the relation between these moments and the coordinate space GPDs is given by [76]

$$G_i^N(\xi) = \int_{-1}^1 dX R_{N,i}(x, x') H_i(X, \xi), \quad (2.34)$$

where  $x = X + \xi$  and  $x' = X - \xi$ , and the kernels  $R_{N,i}$  are polynomials of degree  $N$  given by

$$R_{N,i}(x, x') = \sum_{k=0}^N \binom{N}{k} \binom{N+2p}{k+p} x^k x'^{N-k}, \quad (2.35)$$

with  $p = 1$  for the quark GPD and  $p = 2$  for the gluon GPD.

Owing to the polynomial condition, see e.g. [59], even for  $\xi \neq 0$  the Gegenbauer moments can be obtained from the Mellin moments of the diagonal (non-skewed) PDFs to  $\mathcal{O}(\xi)$  accuracy at NLO. This condition manifestly respects the time reversal invariance symmetry, admitting an expansion in even powers of  $\xi$ ,

$$G_i^N = \sum_{k=0}^{\lfloor (N+1)/2 \rfloor} c_{k,i}^N \xi^{2k} = c_{0,i}^N + c_{1,i}^N \xi^2 + c_{2,i}^N \xi^4 + \dots, \quad (2.36)$$

where  $c_{0,i}^N \equiv M_i^N$ , the Mellin moments of the PDFs. Here,  $\lfloor \cdot \rfloor$  denotes the floor function, giving the greatest integer less than or equal to its argument.

---

<sup>7</sup>Strictly speaking, this is true only at LO with corrections of  $\mathcal{O}(\xi^2)$ . At NLO, the evolution is susceptible to off-diagonal elements in the anomalous dimension matrix, where the conformal invariance is violated due to the running of  $\alpha_s$  which generates an  $\mathcal{O}(\alpha_s \xi)$  correction in the evolution kernel [78, 79, 80, 81]. This is an additional suppression factor at  $\mathcal{O}(\alpha_s)$  by  $\xi$ .

We emphasise that despite the values of the Mellin (and the Gegenbauer) moments maintaining sensitivity to the  $x$  behaviour throughout the whole  $x$  interval (including large  $x \sim 1$ ), the polynomiality provides the accuracy of  $G^N = M^N$ , which depends on the value of  $\xi$  only. Thus it is possible to obtain the full GPD function at small  $\xi$  from its known moments. Based on this, we can obtain an expression that transforms the low  $x$  PDF to the corresponding GPD, as shown below and first given by Shuvaev in [75].

$$\begin{aligned} H_q(X, \xi) &= \int_{-1}^1 dx' \left[ \frac{2}{\pi} \text{Im} \int_0^1 \frac{ds}{y(s) \sqrt{1 - y(s)x'}} \right] \frac{d}{dx'} \left( \frac{q(x')}{|x'|} \right), \\ H_g(X, \xi) &= \int_{-1}^1 dx' \left[ \frac{2}{\pi} \text{Im} \int_0^1 \frac{ds (X + \xi(1 - 2s))}{y(s) \sqrt{1 - y(s)x'}} \right] \frac{d}{dx'} \left( \frac{g(x')}{|x'|} \right), \end{aligned} \quad (2.37)$$

where the transform kernel,

$$y(s) = \frac{4s(1 - s)}{(X + \xi(1 - 2s))}. \quad (2.38)$$

Strictly speaking, by using such a transform we assume the absence of additional singularities in the right half,  $j > 1$ , of the complex angular momentum  $j$  plane (or  $\text{Re}N > 1$  in the Mellin  $N$  plane). This is because in the inversion of eqn. (2.34) to extract  $x$ -space GPDs, one must perform an integral transform in which the Gegenbauer moments are analytically continued into the complex- $N$  plane. Any additional singularity in the right half of this plane would introduce a non-negligible correction of  $\mathcal{O}(\xi/X)$  and impair the practicality of the Shuvaev transform, particularly for  $X \sim \xi$ . As there is no formal proof in the literature where these singularities are dismissed, the procedure has been cast into doubt [82]. As discussed in [83], however, no such additional singularity may arise from the anomalous dimensions describing the  $Q^2$  evolution of the Gegenbauer moments (i.e. the  $Q^2$  evolution of the GPD), but may come from the input PDF distribution itself. This, however, cannot happen in the right half of the  $N$ -plane in the space-like region according to the arguments presented in [83], in which a low  $x$  input distribution is described within the Regge theory<sup>8</sup> of high-energy interactions at low scales.

These arguments are in addition well motivated phenomenologically, and it was shown that the GPD results obtained from the Shuvaev transform procedure [83] agree with those

---

<sup>8</sup>Regge theory [84, 85] is the pre-QCD description of scattering amplitudes based on the analyticity and unitarity of the  $S$ -matrix. Here,  $t$ -channel exchanges are governed by Regge trajectories  $\alpha(t) = \alpha(0) + \alpha' t$ . The Pomeron, relevant in this work, corresponds to the Regge trajectory with  $\alpha(0) \approx 1$ , carrying quantum numbers of the vacuum and predating QCD for the description of the two-gluon exchange.

obtained in independent NLO and NNLO analyses of the available HERA DVCS data [86].

The use of the transform is that it allows one to relate the GPD to the conventional collinear PDF at small  $x, \xi \ll 1$  outside the timelike, or ERL, region  $X \in [-\xi, \xi]$  with  $\mathcal{O}(x)$  accuracy at NLO. In the literature [87], analytic and numerical approximations to this poorly converging, computationally expensive transform in the so-called maximal skew regime,  $X \sim \xi$ , are derived and discussed. In Chapter 3, we employ the full transform while in Chapter 4 we make use of such approximations, justified in due course. The GPD grids are constructed from a three-dimensional parameter space in  $X, \xi/X$  and scale  $Q^2$  [83] with forward PDF grids in  $X$  and  $Q^2$  taken from the LHAPDF6 [88] interface and suitably interpolated before being cast into the Shuvaev transform. The GPD grid is optimised such that an area that results in a flat interpolation is not overly populated - having more points around  $\xi/X \sim 1$ , the border between the DGLAP ( $|X| > \xi$ ) and ERL ( $|X| < \xi$ ) region, mitigates edge effects [83] while the interpolation in  $Q^2$  is relatively smooth and requires fewer points. Below, we demonstrate the simplifications that arise when one restricts the interpolation to the regime of small  $x, x \ll 1$ .

The Shuvaev transform, eqn. (2.37), for the gluon GPD may be written as

$$H_g(X, \xi) = \frac{2}{\pi} \int_{-1}^1 dx' I_s(X, \xi, x') \frac{d}{dx'} \left( \frac{g(x')}{x'} \right), \quad (2.39)$$

with

$$I_s(X, \xi, x') = \text{Im} \int_0^1 ds \frac{X + \xi(1 - 2s)}{y(s) \sqrt{1 - y(s)x'}}, \quad (2.40)$$

and  $y(s)$  given above in eqn. (2.38). Let us consider the gluon GPD in the region  $X = \xi \ll 1$  only, following the derivation of [87]. This corresponds to the point  $x = X + \xi = 2\xi$  so that  $\xi = x/2$ . By performing the integral over  $s$  in what follows, we can derive a one dimensional integral expression for the point  $H_g(x/2, x/2)$  in terms of an arbitrary input forward gluon PDF distribution. Further specification of this input distribution as the Regge-picture inspired pure power law for the gluon at low  $x$  then allows for a closed form solution to be obtained, giving rise to the so-called skewing factor  $R_g$ .

The integral,

$$I_s(x, x, x') = x^2 \text{Im} \int_0^1 ds \frac{(1 - s)}{s \sqrt{1 - 2sx'/x}}, \quad (2.41)$$

is non-vanishing for  $x/(2x') < s < 1$ . With  $a = 2x'/x = z/s$ , it follows that

$$I_s(x, x, x') = \theta(a - 1) \tilde{I}_s(x, x, x') = \theta(a - 1) x^2 \left[ -2 \arctan \sqrt{a - 1} + 2 \frac{\sqrt{a - 1}}{a} \right], \quad (2.42)$$

where the Heaviside step function restricts the outer integration over  $x'$  to be from  $x/2$  to 1. We then have

$$H_g(x, x) = \frac{2x^2}{\pi} \int_{x/2}^1 dx' \tilde{I}_s(x, x, x') \frac{d}{dx'} \left( \frac{g(x')}{x'} \right). \quad (2.43)$$

As  $\tilde{I}_s(x, x, x/2) = 0$  and  $g(1) = 0$ , an application of integration by parts will produce a vanishing surface term. The latter condition is satisfied for all physically motivated PDFs (the input distributions discussed in Section 2.2 incorporate this condition via the explicit  $(1 - x)$  factor). Together with

$$\frac{d}{dx'} \tilde{I}_s(x, x, x') = -\frac{x}{x'^2} \sqrt{\frac{2x'}{x} - 1}, \quad (2.44)$$

and the substitution  $y = x/(2x')$ , we obtain

$$H_g(x/2, x/2) = \frac{4x}{\pi} \int_{x/4}^1 dy y^{1/2} (1 - y)^{1/2} g\left(\frac{x}{4y}\right), \quad (2.45)$$

after relabelling  $x \rightarrow x/2$ .

So, for a given input gluon PDF  $xg(x, \mu^2)$ , eqn. (2.45) gives the corresponding gluon GPD,  $H_g(X, \xi, \mu^2)$ , at the phase space point  $X = \xi$  via a much simpler one dimensional integration. A similar relation holds for the quark GPD. The author of [87] further studied the accuracy of eqn. (2.45) away from the point  $X = \xi$  and found that for  $X$  deviating from  $\xi$  by  $\approx 20\%$  (or equivalently  $x \gtrsim 0.1x'$ ), there was already a  $\sim 10\%$  difference compared to the use of the full Shuvaev transform. We will make use of these results and observations in Chapters 3 and 4 since, as we will see, the point  $X \sim \xi$  is particularly important for exclusive HVM production.

If one assumes a pure power behaviour for the low  $x$  gluon PDF, as is the usual assumption in the global PDF parametrisation forms, eqn. (2.45) may be evaluated analytically. Let

$$xg(x) = Nx^{-\lambda}, \quad (2.46)$$

where  $N$  and  $\lambda$  are the normalisation and gluon slope, respectively.

Insert this into eqn. (2.45) and note that the lower limit of integration is approximately zero for  $x \ll 1$ , while for ‘realistic’ phenomenologically fitted powers<sup>9</sup> the integrand is strongly dominated by the upper boundary  $y \sim 1$  as  $\lambda + 3/2 > 0$ . The integral readily evaluates to an Euler Beta function and may be expressed as

$$R_g = \frac{H_g(x/2, x/2)}{H_g(x, 0)} \approx \frac{2^{2\lambda+3}}{\sqrt{\pi}} \frac{\Gamma(\lambda + 5/2)}{\Gamma(\lambda + 4)}, \quad (2.47)$$

where  $H_g(x, 0) = xg(x)$ . This is an analytic approximation to the Shuvaev transform and encodes skewing effects via a simple multiplicative factor which we stress is valid only at  $X = \xi$  and for an assumed pure power gluon PDF.

## 2.4 Loop calculation toolbox

The evaluation of dimensionally regularised Feynman integrals is the cornerstone of any perturbative loop calculation in quantum field theory. To avoid the explicit calculation of thousands of such integrals that can appear, in principle, in some computation, one proceeds through a programme of integral reduction. This allows for a decomposition of all integrals appearing in the loop calculation to be expressed in terms of a minimal set, the so-called master integrals, which are a finite basis set of simpler loop integrals. It is then these integrals which are dealt with numerically or, in some cases depending on the loop order and ease of extraction, analytically.

This decomposition can be achieved through the solution of a system of linear equations, obtained by exploiting the manifest Lorentz invariance of the theory, giving rise to Integration-By-Parts identities (IBPs) [90, 91] and Lorentz Invariance (LI) identities [92]. These equations form an under-determined system, with the integrals being the unknown quantities while their coefficients are explicit rational functions of the external kinematics and space-time dimension. The resolved system is one where each integral is expressed as a linear combination of master integrals, whose values are not determined from the system.

A propagator  $D_i$  is defined by  $D_i = \hat{q}_i^2 - m_i^2 + i\epsilon$ , where  $\hat{q}_i$  is some linear combination of the loop and external momenta and  $m_i$  is its mass. At one loop,  $\hat{q}_i \equiv l + q_i$ , where  $l$  is the loop momentum and  $q_i$  contains only external momenta. An integral family, or auxiliary topology, is an ordered set of  $N$  propagators  $\mathcal{D}_N = \{D_1, \dots, D_N\}$ , such that any scalar

---

<sup>9</sup>See e.g. [89] for a global NLO fit that determined  $\lambda \approx 0.25$  for the gluon density in the region  $4 \times 10^{-4} < x < 10^{-2}$  at  $Q^2 = 20 \text{ GeV}^2$  using ZEUS data on the proton structure function,  $F_2^p$ , at lower  $x$ .



product of a loop momentum  $l_i$  with another loop momentum  $l_j$  or an external momentum  $p_j$ , can be uniquely expressed as a linear combination of elements of  $\mathcal{D}_N$  and kinematic invariants. With  $E$  ( $L$ ) the number of linearly independent external (loop) momenta, the auxiliary topology must contain exactly  $L(L+1)/2 + LE$  propagators.

Associated to each auxiliary topology is an infinite set of dimensionally regularised integrals of the form

$$I = \int d^d l_1 \cdots \int d^d l_j \frac{D_{j_{t+1}}^{s_1} \cdots D_{j_N}^{s_{N-t}}}{D_{j_1}^{r_1} \cdots D_{j_t}^{r_t}}, \quad (2.48)$$

where  $\{j_1, \dots, j_t\} \subset \{1, \dots, N\}$  is a selection of  $t$  propagators, defining a sector of the auxiliary topology. Here, the  $r_i \geq 1$  and  $s_i \geq 0$  are integer powers of the propagators. Along with the sector identification number,  $ID$ , the quantities  $r$  and  $s$  are defined as

$$r = \sum_{i=1}^t r_i, \quad s = \sum_{i=1}^{N-t} s_i, \quad ID = \sum_{k=1}^t 2^{j_k-1}. \quad (2.49)$$

In dimensional regularisation [93], the integral over the total derivative of a loop momentum vanishes. With  $\hat{q}^\mu$  denoting an arbitrary loop or external momentum, and  $\tilde{I}$  an integrand of the form appearing in eqn. (2.48), this observation allows for the generation of  $L(L+E)$  equations from one (seed) integral, by considering each possible choice of  $\hat{q}$  and  $l_i$  in turn. These are the IBP identities and are obtained from

$$\int d^d l_i \frac{\partial}{\partial l_i^\mu} \left( \hat{q}^\mu \tilde{I}(p_1, \dots, p_E; l_1, \dots, l_L) \right) = 0. \quad (2.50)$$

The Lorentz invariance of the integrals  $I$  in eqn. (2.48) instead gives

$$\sum_{i=1}^E \left( p_i^\nu \frac{\partial}{\partial p_i^\nu} - p_i^\mu \frac{\partial}{\partial p_i^\mu} \right) I(p_1, \dots, p_E) = 0. \quad (2.51)$$

Explicit contractions of the left hand side with all possible antisymmetric combinations of the external momenta produce  $E(E-1)/2$  equations. These are the LI identities and, while they do not provide linearly independent equations from those generated via eqn. (2.50) [94], the equations generated from a single seed integral need not correspond to those generated from the same seed integral in the IBP approach. This allows for a faster convergence of the reduction process.

Algorithmic procedures [94, 95, 96, 97, 98, 99], such as a variant of Laporta's reduction

algorithm, automatise the application of the IBP and LI identities and are implemented in software tools, such as REDUZE 2 [100], used in this work. In REDUZE 2, each appearing integral in a given auxiliary topology is converted to an ordered string of the form

$$I(F, t, ID, r, s, \{\nu_1, \dots, \nu_N\}) \quad (2.52)$$

and subject to a lexicographic ordering, as introduced by Laporta [101]. Here,  $F$  denotes a given auxiliary topology and the  $\nu_i$  are integer powers. The numerical values of  $t, r, s$  and  $ID$  are found using eqn. (2.49). Broadly, after generation of the IBP and LI identities, Laporta first quantified and then ordered the resulting equations in a hierarchy of ‘most complicated’ to ‘least complicated’, solving the system by back substitution. See [101] for more details.

## 2.5 Taming of $\overline{\text{MS}}$ exclusive $J/\psi$ production at NLO

In this section, we will make a whistle-stop tour through the current status and developments of exclusive  $J/\psi$  production in the collinear factorisation scheme at NLO. Spanning more than a decade, we will see that the calculation is, as of now, on a firm theoretical footing.

The strong sensitivity to the choice of scale in the predictions for exclusive  $J/\psi$  photoproduction within collinear factorisation at NLO in the  $\overline{\text{MS}}$  scheme was first observed in [18, 102] and recently confirmed in [103]. There are two sources for this sensitivity to the scale choice. First, there is the double logarithmic contribution which contains a large  $\ln(1/x)$  factor. For the region of interest,  $x \sim 10^{-5}$ , this means an order of magnitude enhancement. Second, there is double counting in the coefficient functions for  $Q^2 < Q_0^2$ . After a discussion of the  $\overline{\text{MS}}$  result at NLO, we explore how these problems are overcome in turn, in Sections 2.5.1 and 2.5.2.

The NLO contribution for exclusive  $J/\psi$  photoproduction in the  $\overline{\text{MS}}$  collinear factorisation scheme has been known for some time [18]. However, it exhibited poor perturbative convergence (with the NLO correction greater than LO and of opposite sign). Moreover, there existed a strong dependence on the factorisation scale,  $\mu_F$ . Both of these features are illustrated in Fig. 2.4, showing the LO and NLO predictions for  $\text{Im } A/W^2$  at scales  $m_c^2/2, m_c^2$  and  $2m_c^2$ , the typical variation of scales around the central value for the charm quark mass squared,  $m_c^2$ , in which to quantify the theory scale uncertainty. Here,  $A$  stands

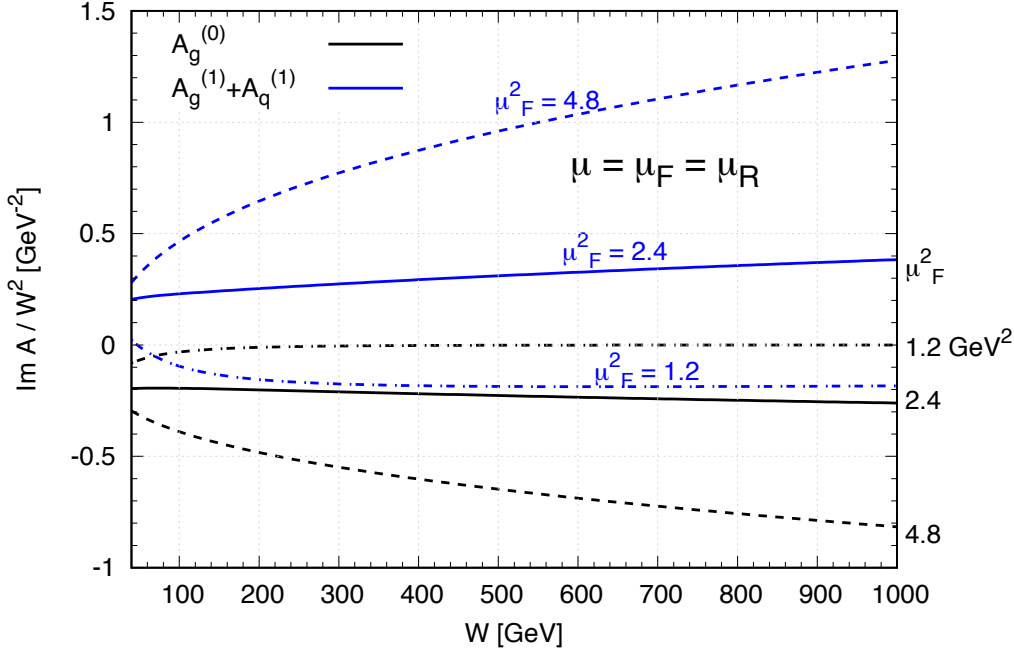


Figure 2.4:  $\overline{\text{MS}}$  scale variations of  $\text{Im } A/W^2$  at LO (black) and NLO (blue) generated using CTEQ6.6 global partons at  $\mu_F^2 = \mu_R^2 = 1.2, 2.4, 4.8 \text{ GeV}^2$ .  $\text{Im } A$  is the imaginary part of the amplitude. Plot adapted from [102].

for the amplitude for exclusive  $J/\psi$  production and  $W$  is the centre-of-mass energy for the  $\gamma p$  subprocess.

Variation of the factorisation scale at such low scales in this way (close to the PDF input scale) will drastically change the parton distributions, however. Of course, if the whole perturbative series were present, the hard matrix elements would provide the compensation and cancel this change. With a NLO truncation, the matrix element admits only *one* parton emission, while the parton distributions can emit many more. Indeed, the mean number of gluons in the interval  $\Delta \ln \mu_F^2$  is [102]

$$\langle n \rangle \simeq \frac{\alpha_s N_c}{\pi} \ln(1/x) \Delta \ln \mu_F^2 \simeq 8, \quad (2.53)$$

with the  $\mu_F$  scale variation in the interval  $\mu_F^2/2$  to  $2\mu_F^2$ . That is, at low  $x$  and at LHC energies, there is not the compensation between the contributions coming from the PDF and the coefficient function as the scale is varied.

From inspection of Fig. 2.4 and as mentioned above, the LO contribution is roughly the same size as the NLO contribution and of opposite sign. This relative difference in the contribution to the imaginary part of the amplitude for the quasi-elastic  $\gamma p \rightarrow J/\psi + p$  scattering is at odds with the interaction being modelled as an elastic forward hard scattering, where the imaginary part should not change sign [104]. The explanation is that due to the lack of data constraints at low  $x$  and low scale, the evolution of the global parton fit analyses in this part of the phase space are arbitrary and lead to too small (or arguably ‘unphysical’) parton PDFs. Once convolved with the coefficient functions, this leads to such unwanted behaviour, indicative of the lack of perturbative stability at this order. At high scales, where the PDFs are driven by evolution effects and not by the structure of the input distribution, these effects are all washed out and the NLO prediction becomes sensible.

Note that such issues are prevalent in the description of high-energy physics phenomena, particularly for low scale observables. The theoretical description of the hadroproduction of one of the simplest quarkonia, the  $\eta_c$  meson, for example, has for a long time suffered from a negative cross section yield at high energies, attributed to, perhaps, the choice of scale and/or behaviour of the PDFs [105], like above. Work is, however, ongoing to resolve this problem for this particular observable.

### 2.5.1 Treatment of double logarithmic contributions

It was shown in [102] that it is possible to find a scale (namely  $Q \equiv \mu_F = M_\psi/2$ ) which effectively ‘resums’ all the double logarithmic corrections enhanced by large values of  $\ln(1/\xi)$  into the gluon and quark PDFs, where  $\xi$  is the skewedness parameter of the Generalised Parton Distributions (GPDs) introduced earlier. That is, it is possible to take the  $(\alpha_S \ln(1/\xi) \ln(\mu_F^2))$  term from the NLO gluon (and quark) coefficient functions and move it into the LO GPDs. This allows a resummation of all the double logarithmic, i.e.  $(\alpha_S \ln(1/\xi) \ln(\mu_F^2))^n$ , terms into the LO contribution  $C_g^{(0)} \otimes F_g(\mu_F)$  by choosing the factorisation scale to be  $\mu_F = M_\psi/2$ . The details are given in [102], see also [106]. The different types of resummation are summarised in Appendix B.

The result is that the  $\gamma p \rightarrow J/\psi p$  amplitudes, taken at factorisation scale  $\mu_f$ , are schematically of the form

$$A(\mu_f) = C_g^{(0)} \otimes F_g(\mu_F) + \sum_{i=q,g} C_{i,\text{rem}}^{(1)}(\mu_F) \otimes F_i(\mu_f), \quad (2.54)$$

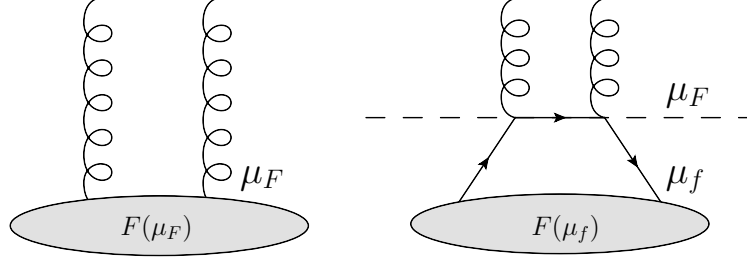


Figure 2.5: Lower part of Feynman diagrams for exclusive  $J/\psi$  production. Left panel: LO contribution evaluated at  $\mu_F$ . Right panel: Division of cells at factorisation scale  $\mu_F$  allows for a shifting of terms with virtualities  $\mu < \mu_F$  between LO and NLO.

to NLO. With the choice  $\mu_F = M_\psi/2$ , the remaining NLO coefficient function,  $C_{\text{rem}}^{(1)}(\mu_F)$ , does not contain terms enhanced by  $\ln(1/x) \simeq \ln(1/\xi)$ . Note that  $\mu_F \neq \mu_f$ , see the discussion below. The remaining  $\mu_f$  scale dependence in eqn. (2.54) is small. This equation may in principle be extended to NNLO and iterated to higher orders.

The effect of this scale change is driven by the LO DGLAP evolution. In the left panel of Fig. 2.5, we evaluate the LO amplitude at some scale  $\mu_F$  by treating the explicit pair of  $qg \rightarrow q$  corrections  $\propto \alpha_s$ , depicted in the right panel, to be part of the LO contribution. In this way, through variation of the factorisation scale, we move the contribution of this naive NLO correction into the LO result. We can therefore write

$$A^{(0)}(\mu_F) = \left( C^{(0)} + \frac{\alpha_s}{2\pi} \ln \left( \frac{\mu_F^2}{\mu_f^2} \right) C^{(0)} \otimes V \right) \otimes F(\mu_f), \quad (2.55)$$

where  $V$  denotes the skewed splitting kernels (the quark line may be replaced by gluons and, indeed at small  $x$ , gluon ladder diagrams dominate because their splitting kernels  $\sim 1/x$ ). The logarithm of  $\mu_F^2/\mu_f^2$  is generated assuming the DGLAP strong scale ordering condition,  $\mu_f^2 \ll \mu_F^2$ , giving the  $C_{i,\text{rem}}^{(1)}$  its  $\mu_F^2$  dependence. The idea is then to use this scale-shifting procedure to find the ‘optimal’ scale  $\mu_0$  that removes the largest contribution from the NLO correction. At small  $x, \xi$ , this is the double logarithmic contribution  $\sim \ln(1/\xi) \ln \mu_F^2$  which arises in the high-energy limit, or strong  $x$  ordering regime,  $1 \gg x \gg \xi$ . An explicit computation, the result of which is shown in Chapter 3, shows that these terms can be resummed with the scale setting  $\mu_F = m_c$ . Of course, we can not eliminate all possible large dependencies because the NLO coefficient function is a function of the ratio  $x/\xi$  and

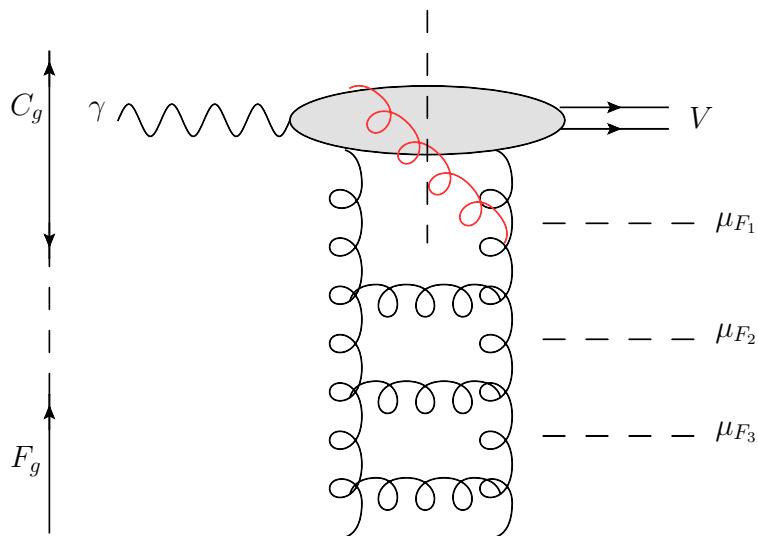


Figure 2.6: Different choices of the factorisation scale  $\mu_{F_i}$  allow for different division of cells between the parton evolution and the hard matrix element. The uppermost gluon (labelled red) may not be absorbed into the parton evolution in this scale-shifting approach, described in the text.

so is, too, energy dependent while the scale choice  $\mu_F = m_c$  is a single numerical value. However, gluon ladders strongly ordered in longitudinal momentum fraction and virtuality generate the largest enhancement, the double logarithmic contribution, and are resummed through this choice of scale. Other NLO corrections, e.g. the upper gluon correction in Fig. 2.6, amount to those not of this type (that is, they can not be affected by this scale-shifting) and contain intermediate states of mass  $\sim m_c$  that are accounted for in the hard matrix element.

Thus, to summarise, eqn. (2.54) allows one to consider different factorisation scales  $\mu_f$  with the scale in the first term on the right-hand-side, however, fixed to be  $\mu_F = m_c$  independent of the value of  $\mu_f$ . Since the contribution from the second term is small, we predominantly probe the gluon distribution at scale  $\mu_F = M_\psi/2$ . The upshot is a shifting of terms from the NLO coefficient function, now evaluated at a fixed scale  $\mu_F = m_c$ , to the LO GPD and a residual smaller scale dependence,  $\mu_f$ , residing in the NLO GPD. With this choice, large contributions arising from the specific scale and momentum fraction hierarchy, as discussed above, are absorbed into the parametrisation of the input GPD.

Moreover, it is found that after the scale  $\mu_F$  in eqn. (2.54) is fixed to  $\mu_F = M_\psi/2$ , the result (shown in the upper panel in Fig. 2.8, see later) <sup>10</sup> becomes more stable with respect to variations of the factorisation scale  $\mu_f$  in comparison to the huge variations seen in [18] and Fig. 2.4. That is, the deviation between the curves with  $\mu_f^2 = 2.4 \text{ GeV}^2$  and  $\mu_f^2 = 4.8 \text{ GeV}^2$  in the upper panel of Fig. 2.8 has decreased by roughly a factor of two as compared to that in Fig. 2.4. However, in spite of this, the NLO correction is still comparable to the LO term and opposite in sign. As we discuss and explain in Section 2.5.2, this is due to one other crucial effect - double counting between the NLO coefficient function and the contribution coming from DGLAP evolution. Once this double counting is avoided, the perturbative treatment will be seen to be finally brought under control, as well as allowing for a further reduction of the scale sensitivity.

### 2.5.2 Treatment of double counting power corrections

In this subsection, we consider a power correction which may further reduce the NLO contribution and, moreover, may reduce the sensitivity to the choice of scale. The correction is  $\mathcal{O}(Q_0^2/\mu_F^2)$  where  $Q_0$  denotes the input scale in the parton evolution and, while formally suppressed, may be numerically significant and relatively important for low scale processes where  $Q_0$  is comparable to the typical process factorisation scale,  $\mu_F$ . This power correction originates from a so-called ‘ $Q_0$ ’ subtraction that can be made within the hard matrix element at NLO (and beyond) of a pQCD calculation. For an outline of the general formulation and the procedure applied to the NLO coefficient functions of inclusive DIS and Drell-Yan production of low-mass lepton pairs, see [109]. Here, we will restrict our consideration to the effect of the ‘ $Q_0$ ’ subtraction for exclusive  $J/\psi$  production which, as the form of the correction indicates, will be important for factorisation scales around the size of the relatively light charm quark mass,  $m_c \simeq M_\psi/2 \simeq Q_0$ .

Note that despite its form, such a correction is not one of ‘higher twist’. The subtraction of the low  $l_T < Q_0$  region amounts to a power correction to the *same* leading twist operator of conventional collinear factorisation. Higher twist corrections here instead correspond to the exchange of a pair of gluon ladders in the  $t$ -channel or polarisation of the two gluon exchange. But, these contributions are outwith the scope of the leading twist PDFs

---

<sup>10</sup>In Figs. 2.4 and 2.8 we choose to use the old CTEQ6.6 partons to demonstrate the problem with the scale uncertainties simply to relate to the original papers [18, 107, 108] which long ago observed and discussed these uncertainties. The small scale variation obtained within our present approach using the modern CT14 NLO PDF is shown later in Chapter 3, see Fig. 3.2.

extracted from the global analyses in collinear factorisation and are not considered here. See Section 4.3.4 for further discussion about these higher twist corrections.

Let us explain the origin of this ‘ $Q_0$  subtraction’ following [107]. Denote the gluon virtuality by  $l$ , as shown in Fig. 2.7. We begin with the collinear factorisation approach at LO. Here, we never consider parton distributions at low virtualities, that is for  $Q^2 < Q_0^2$ . We start the PDF evolution from some phenomenological PDF input at  $Q^2 = Q_0^2$ . In other words, the contribution from  $|l^2| < Q_0^2$  of the diagrams in Fig. 2.7, (which can be considered as the LO diagram, left panel of Fig. 2.5, supplemented by one step of the DGLAP evolution from quark to gluon,  $P_{qq}$ ) is already included in the input gluon GPD at  $Q_0$ . That is, to avoid double counting, we must exclude from the NLO diagram the contribution coming from virtualities less than  $Q_0^2$ . We thereby subtract from the evolution the contribution of  $t$ -channel loop momentum  $|l|^2 < Q_0^2$ , in order to avoid a double counting. In this way, through an explicit insertion of the theta function  $\theta(|l^2| - Q_0^2)$ , we restrict the virtuality of the four momentum circulating in the gluon ladder diagrams to be above  $Q_0$ . Note that this has never been a ubiquitous feature of an  $\overline{\text{MS}}$  calculation but is important as the subtraction amounts to a power correction of  $\mathcal{O}(Q_0^2/\mu_F^2)$ , which is sizeable here because the process sits at a low scale, of the order of  $m_c$ . Regardless of this, without its inclusion, one cannot obtain an accuracy better than  $\mathcal{O}(\alpha_s^n Q_0^2/\mu_F^2)$  at each order  $n$  in the systematic expansion of the strong coupling [109]. At large scales,  $Q^2 \gg Q_0^2$ , this double-counting correction will give small power suppressed terms of  $\mathcal{O}(Q_0^2/Q^2)$ , since there is then no infrared divergence in the corresponding integrals as a result of the explicit subtraction. Practically, it is only the ladder-type diagrams that are susceptible to a double counting, see Fig. 2.7. The imaginary part of these diagrams is then obtained through application of Cutkosky’s rules, where cut propagators are replaced by on-shell momenta constraining delta distributions. The resulting expressions are then subtracted from the imaginary part of the known  $\overline{\text{MS}}$  coefficient functions. Here, with  $Q_0 \sim 1$  GeV and  $\mu_F = m_c$  ( $\sim M_\psi/2$ ), a correction of  $\mathcal{O}(Q_0^2/m_c^2)$  will typically be  $\mathcal{O}(1)$  and turns out to be crucial.

By using the NLO correction,  $C_{\text{rem}}^{(1)}$ , for  $J/\psi$  photoproduction and excluding the contribution coming from the low virtuality domain<sup>11</sup> ( $< Q_0^2$ ) it is observed that this procedure substantially reduces the resulting NLO contribution and reduces the scale dependence of

<sup>11</sup>Note that the value of  $Q_0$  may differ from the value  $q_0$  at which the initial PDFs were parametrised. For example, in the MMHT analysis [40]  $q_0$  is set equal to 1 GeV, but only data with  $Q^2 > 2$  GeV<sup>2</sup> are included in the fit. This means that actually the input was fitted at  $Q^2 = 2$  GeV<sup>2</sup> and all the partons below 2 GeV<sup>2</sup> are obtained by the extrapolation via the backward pure DGLAP evolution.



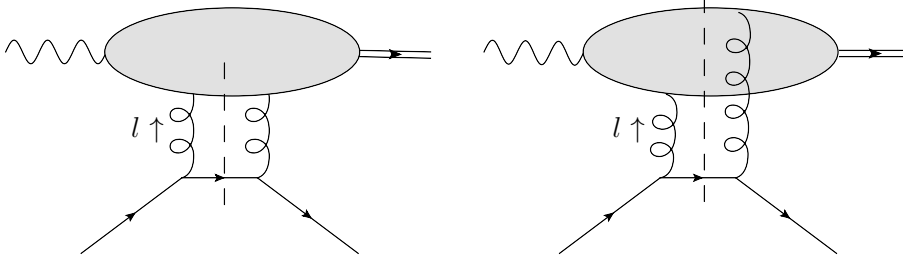


Figure 2.7: Two cut diagrams contributing to the imaginary part of the NLO quark coefficient function. The corresponding cut diagrams for the NLO gluon coefficient function can be obtained by replacing the light quark line by gluons. All permutations of the gluons to the heavy quarks are implicit.

the predictions. It indicates the stability of the perturbative series.

Indeed, as shown in the upper panel of Fig. 2.8, before the  $Q_0$  subtraction the NLO corrections may exceed the value of the LO contribution and, depending on the scale, even the sign of the amplitude can change. However, after the subtraction and choosing the optimal scale  $\mu_F = M_\psi/2$  in the leading order part of the amplitude (first term of eqn. (2.54)), a rather good scale stability is observed as shown in the lower panel of Fig. 2.8.

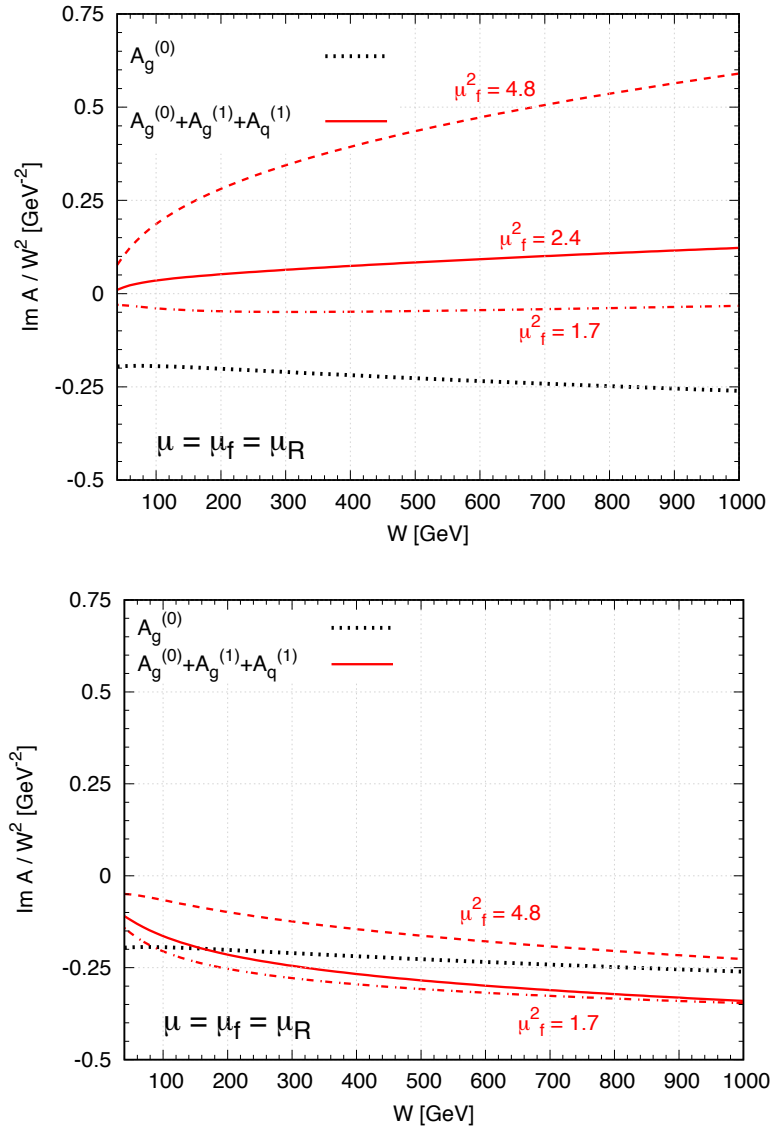


Figure 2.8: LO and LO+NLO contributions to the imaginary part of the  $\gamma p \rightarrow V + p$  amplitude as a function of the  $\gamma p$  centre-of-mass energy,  $W$ , with  $\mu_F = m_c$  before (upper panel) and after (lower panel) the double counting correction has been implemented, as explained in the text. The dashed, continuous and dot-dashed (red) curves correspond to three choices of the factorisation scale  $\mu_f$ : namely  $\mu_f^2 = 2m_c^2$ ,  $m_c^2$ ,  $Q_0^2$ , respectively, where  $m_c^2 = M_\psi^2/4 = 2.4$  GeV<sup>2</sup>. Here  $Q_0 = 1.3$  GeV is the starting scale of the input NLO PDFs from CTEQ6.6 [41] which were used. The dotted black curve is the LO contribution. Plots adapted from [107].

## Chapter 3

# How to include exclusive $J/\psi$ production data in global PDF analyses

We compare the cross section for exclusive  $J/\psi$  photoproduction calculated at NLO in the collinear factorisation approach with HERA and LHCb data. Using the optimum scale formalism together with the subtraction of the low  $k_t$  contribution (below the input scale  $Q_0$ ) from the NLO coefficient function to avoid double counting, we show that the existing global parton distribution functions (PDFs) are consistent with the data within their uncertainties. This is the first time that  $J/\psi$  production data at HERA are shown to be successfully described within the NLO collinear factorisation framework using the PDFs of the global parton analyses. At lower  $x$ , surpassing the range accessible at HERA energies, the uncertainties of the present global PDFs are large while the accuracy of the LHCb data are rather good. Therefore, these data provide the possibility to directly measure the gluon PDF over the very large interval of  $x$ ,  $10^{-6} < x < 10^{-2}$ , at a fixed low scale.

### 3.1 Introduction

The parton distributions of the proton at NLO are relatively well constrained at moderate to large  $x$  but plagued with large uncertainties at low  $x$ .<sup>1</sup> Nowadays, global analyses performed at NNLO are regarded as the state of the art, yet the small  $x$  region remains largely unconstrained. In this section, we demonstrate how to bring the small  $x$  region under control at NLO. Our approach may be generalised and extended to NNLO as well.

We note that the present uncertainties on PDFs at very small  $x$  and also as  $x$  tends to one have a completely different nature. As  $x$  approaches unity we have data and describe them using a reasonably justified ansatz for the input PDFs. On the contrary, at very low  $x$ , we have few data and the small  $x$  predictions of the current global fits are simply an extrapolation of these input distributions from larger  $x$ .

To be more specific, for  $10^{-3} \lesssim x \lesssim 10^{-1}$ , the NLO (and similarly the NNLO) results of the different groups [38, 40, 42] agree with each other quite well, see Figs. 2.1, 2.2 in Section 2. However, the uncertainty in the parton distributions strongly increases as we go to lower values of  $x$ , especially at low scales. This simply reflects the fact that no experimental data are used to directly probe this region. Besides its intrinsic value, there are at least two further reasons to be interested in the behaviour of the gluon PDF at very small  $x$  and low scales  $\mu \sim 1.5$  GeV. First, recall that the distribution of gluons as  $x \rightarrow 0$  governs the high-energy asymptotics of the scattering amplitude. In particular, the gluon distribution at some relatively low scale can be used as the boundary condition for the BFKL equation. This boundary condition for BFKL is needed to account for the effects of confinement. As was shown in [111, 112, 113], such a boundary condition replaces the BFKL cut (in the complex momentum  $j$ -plane) by a series of Regge poles. At very low  $x$ , the boundary condition should indicate the presence of saturation effects that are needed to stop the power growth of the original BFKL amplitude. Second, a reliable gluon PDF at small  $x$  may be used to evaluate the production cross section of a possible new light particle, with mass of the order of a few GeV, at the LHC (if such a new particle exists) or to put a limit on the corresponding coupling. In this thesis, we consider the distributions at a rather low scale ( $\sim M_{\psi}^2/4$ ) where the parton densities are driven mainly by some

---

<sup>1</sup>Global PDFs have also large uncertainties in the region  $x > 0.1$ , especially as  $x \rightarrow 1$ , caused, among other issues, by mass and higher-twist effects. However, this region is beyond our present interest since it gives a negligible contribution for exclusive  $J/\psi$  production at very high energies. There is, however, a fixed target collision programme underway at the LHCb detector using the upgraded SMOG2 system [110]. The data for a possible exclusive  $J/\psi$  detected in this kinematic configuration would lie at larger  $x$ .

phenomenological input ( $\text{PDF}(x, Q_0^2)$ ) and cannot be calculated within perturbative QCD. Here,  $Q_0$  is the PDF input scale. In particular at such low scales one may need to consider the effects of parton density saturation. They should reveal themselves as gluon behaviour with  $xg$  constant as  $x \rightarrow 0$ .

The LHCb detector detects particles in the forward rapidity interval,  $2 < Y < 5$ . In particular, the collaboration have measured the differential cross sections for open charm [114, 115, 116] (and bottom [117, 118]) quark pairs, and also for exclusive  $J/\psi$  (and  $\Upsilon$ ) vector mesons [47, 48], which, in principle, allow the determination of the low  $x$  gluon PDF for  $x \sim 10^{-5}$  or less at factorisation scales  $\mu_F = \sqrt{m_q^2 + p_{T,q}^2}$  and  $\mu_F = m_q$ , where  $q = c, b$  and  $p_T$  is the transverse momentum of the quark.

The differential cross sections for open  $c\bar{c}$ ,  $b\bar{b}$  production are determined by LHCb by observing  $D$  and  $B$  meson decays. These data are then studied to extract information about the gluon PDF at low  $x$  [119, 120, 121, 122, 123, 124]. Here, we may say the experimental measurement is not simple while the theory is more straightforward. In fact careful analyses, for example, [123, 124] indicate that there are serious tensions and inconsistencies in the  $D$  and  $B$  data, and that no conclusion about the very low  $x$  behaviour of the gluon PDF is possible. In a sense, for exclusive  $J/\psi$ , the opposite is true. The LHCb data are somewhat more effortless to collect and the accuracy of the exclusive  $J/\psi$  differential cross sections is much better [47, 48]. However, here the theory is more involved. In short, there are two theoretical problems to address. First, the corresponding cross section is not described by the usual PDFs but by the more complicated Generalised Parton Distributions (GPDs), see Section 2.3 and [60] for a review. Next, the NLO corrections are large and the results strongly depend on the choice of scale.

In Chapter 2, we showed how these two problems can be solved within the conventional collinear approach by using the Shuvaev transform [74, 75], which at small  $x$  allows for the calculation of the GPDs from the conventional integrated PDFs. The strong scale dependence was shown to be reduced by choosing a factorisation scale which effectively resums the double logarithmic  $\alpha_s \ln(\mu^2) \ln(1/x)$  terms (which are enhanced by the large values of  $\ln(1/x)$  at small  $x$ ) and transfers them into the incoming PDFs. Finally, and most importantly, to avoid double counting, we had to subtract the low transverse momentum,  $l_t = k_t$ , contributions below the input scale  $Q_0$  from the NLO coefficient functions, as these contributions are already included in the input PDFs. The subtraction is of the form of a power correction which, as expected, is large.

Previously, the LHCb data for forward ultraperipheral  $J/\psi$  production were successfully

described in [125] using the  $k_t$  factorisation framework. However, the  $k_t$  factorisation approach does not include the complete set of NLO corrections. Thus this approach does not allow these  $J/\psi$  data to be included in the NLO global analyses based on the collinear factorisation theorems. Our formalism is based on the conventional collinear framework and includes all NLO corrections. In Section 3.4 we show that three existing sets of PDFs (NNPDF3.0 [38], MMHT2014 [40] and CT14 [42]) taken at the optimal scale mentioned above, and convoluted with the NLO coefficient functions from which the low  $k_t < Q_0$  contribution has been subtracted, give a satisfactory description of the diffractive  $J/\psi$  HERA data [126, 127, 128, 129], but vastly different predictions in the region of the LHCb  $J/\psi$  data [47, 48].

The outlook of this chapter is as follows. In Section 3.2 we give our notation. In Section 3.3 we explain how our approach can be used to probe the PDFs. In Section 3.4 we show that the PDFs given by the existing global analyses agree with the  $J/\psi$  exclusive photoproduction data measured at HERA and that they can be constrained at even smaller  $x \sim 10^{-6}$  using LHCb ultraperipheral  $J/\psi$  data. We discuss our results in Section 3.5 and present our conclusions in Section 3.6.

## 3.2 Notation and collinear factorisation

The exclusive  $J/\psi$  photoproduction amplitude may be written, using collinear factorisation, in the form [18]

$$A = \frac{4\pi\sqrt{4\pi\alpha}e_q(\epsilon_V^* \cdot \epsilon_\gamma)}{N_c} \left( \frac{\langle O_1 \rangle_V}{m_c^3} \right)^{1/2} \int_{-1}^1 \frac{dX}{X} [C_g(X, \xi) F_g(X, \xi) + C_q(X, \xi) F_q(X, \xi)], \quad (3.1)$$

where we have suppressed the dependence on the renormalisation and factorisation scales,  $\mu_R, \mu_F$ , and on the invariant transferred momentum squared,  $t$ . Here, the non-relativistic QCD (NRQCD) matrix element  $\langle O_1 \rangle_V$  describes the formation of the  $J/\psi$  meson, with  $m_c$  the charm quark mass. We present a broader discussion of the application of NRQCD to the description of the exclusive  $J/\psi$  process below, see Section 3.2.1. The quark singlet and gluon GPDs are denoted  $F_q$  and  $F_g$ , respectively. The singlet comprises the sum over the light quark flavours  $u, d, s$ . The quark and gluon coefficient functions  $C_q$  and  $C_g$  are

known at NLO [18] and are given at tree level by

$$C_g^{(0)}(X, \xi) = \alpha_s \frac{X}{(X - \xi + i\delta)(X + \xi - i\delta)}, \quad (3.2)$$

$$C_q^{(0)}(X, \xi) = 0. \quad (3.3)$$

The kinematics of the process are displayed in Fig. 3.1. The partons carry momentum fractions  $(X + \xi)$  and  $(X - \xi)$  of the plus-component of the mean of the incoming and outgoing proton momenta  $P = (p + p')/2$ . The photon-proton centre of mass energy squared is given by  $W^2 = (q + p)^2$ , where  $q$  is the photon momentum. The asymmetry between the momentum fractions carried by the partons is parametrised by the skewness parameter,

$$\xi = \frac{p^+ - p'^+}{p^+ + p'^+} = \frac{M_\psi^2}{2W^2 - M_\psi^2}. \quad (3.4)$$

Due to the vanishing of the quark coefficient function at LO, the process is predominantly sensitive to the gluon GPD. At LO, the gluon coefficient function is strongly peaked for  $|X| \sim \xi$  and so the gluon GPD is probed close to  $F_g(\xi, \xi)$ . In fact, for the imaginary part of the amplitude, the LO gluon coefficient function acts as a Dirac delta function and the GPD is probed at exactly  $|X| = \xi$ . This follows from the form of  $C_g^{(0)}$  given above.

### 3.2.1 Non-Relativistic QCD (NRQCD)

We use NRQCD to describe the formation of the  $J/\psi$  wave function,  $\Psi$ . Ever since the discovery of the  $J/\psi$  as the first heavy quarkonium bound state at SLAC and BNL in 1974, there has been widespread interest in understanding the decay rates and production mechanisms of quarkonia. The development of NRQCD [130], an effective field theory for bound heavy quark mass systems in which one performs a well-defined Taylor expansion in the relative velocity  $v$  of the constituent heavy quark anti-quark  $q\bar{q}$  pair, allows one to consistently factorise the hard process dynamics from the non-relativistic formation of the bound state. Consideration of successively higher powers of the parameter  $v^\mu = q_1^\mu - q_2^\mu$  amount to a systematic expansion in the relativistic corrections to the production of the bound state, where  $q_1^\mu$  and  $q_2^\mu$  are the velocity of the heavy quark and anti-quark respectively. The transition amplitude,  $A(V)$ , from an open  $q\bar{q}$  pair to a bound state meson

$V$  can be expanded in powers of  $v$ ,

$$A(V) \sim (A_\rho + B_{\rho\sigma}v^\sigma + C_{\rho\sigma\tau}v^\sigma v^\tau + \dots) \epsilon_V^{\rho*}, \quad (3.5)$$

where  $\epsilon_V^{\rho*}$  is the polarisation vector for the outgoing vector meson. Here, we will work at LO in NRQCD, assuming the zeroth order term in the above relativistic velocity expansion. We will therefore set the relative velocity of the quark and anti-quark pair to be identically zero,  $q_1^\mu = q_2^\mu$  and work with the colour-singlet Fock state  $|q\bar{q}\rangle$ . That is, in the notation introduced in Section 3.3,  $M_\psi^2 = M_{q\bar{q}}^2$ . We will assume that the heavy quarks carry the same longitudinal momentum fraction  $z = 1/2$  with no relative transverse momentum,  $\kappa_\perp = 0$ . The non-relativistic form for the  $J/\psi$  wave function is then of the form

$$\Psi(z, \kappa_\perp) \sim \delta\left(z - \frac{1}{2}\right) \delta^{(2)}(\kappa_\perp). \quad (3.6)$$

At this order in  $v$ , only the NRQCD operator  $\langle O_1 \rangle_V$  contributes so that

$$A(V) = \left( \frac{\langle O_1 \rangle_V}{2N_c m} \right)^{1/2} A_\rho \epsilon_V^{\rho*}. \quad (3.7)$$

In this section, we take  $V = J/\psi$ . The  $S$ -wave spin triplet operator  $\langle O_1 \rangle_{J/\psi} \equiv \langle O_1(^3S_1) \rangle_{J/\psi}$  can be extracted from the experimentally determined leptonic decay width of the  $J/\psi$  meson [130],

$$\Gamma(J/\psi \rightarrow l^+ l^-) = \frac{2e_q^2 \pi \alpha^2}{3} \left( \frac{\langle O_1 \rangle_{J/\psi}}{m_c^2} \right) \left( 1 - \frac{8\alpha_s}{3\pi} \right)^2. \quad (3.8)$$

In this equation,  $\alpha$  ( $\alpha_s$ ) is the fine-structure constant (strong coupling) and  $m_c$  and  $e_q$  are the pole mass and electric charge of the charm quark. The factor  $(1 - 8\alpha_s/(3\pi))$  accounts for the one-loop NLO pQCD correction. So, in our LO analyses, we omit this factor from the defining relation between  $\langle O_1 \rangle_{J/\psi}$  and  $\Gamma(J/\psi \rightarrow l^+ l^-)$  for consistency.

The issue of ascertaining to what extent relativistic corrections would have an effect on the  $J/\psi$  wave function and, therefore, on cross section predictions for exclusive  $J/\psi$  production was a controversial one [131, 132, 133, 134, 135, 136]. Earlier work [134, 135] found a  $J/\psi$  wave function correction factor, with all relativistic effects ignored except accounting for non-zero Fermi motion  $\kappa_\perp \neq 0$ , which deviated far from unity and gave a significant suppression. In [131], however, the authors pointed out a possible overestimation of this factor related to the treatment of the ratio  $M_\psi/(2m_c)$  and argued that



restricting the longitudinal momentum fraction  $z$  of the heavy quarks to be equal was a valid approximation up to  $\mathcal{O}(v^4)$ .

It was realised later that, for consistency, by including relativistic corrections one must also simultaneously account for the higher,  $c\bar{c}+g$ , Fock component of the  $J/\psi$  wave function to maintain gauge invariance. As was shown in [136], with these careful considerations regarding the power counting in  $\alpha_s$  and  $v$  taken into account, the two corrections largely cancel each other, leading to a final correction of the order of a few percent provided that the NRQCD matrix element is normalised to the leptonic decay width,  $J/\psi \rightarrow l^+l^-$ , and the charm quark mass is chosen to be  $m_c = M_\psi/2$ , as is kept in our study. The gauge invariant cross section correction factor was found to be

$$\left(1 + \frac{8}{9} \frac{\nabla^2 \Psi}{M_\psi^2 \Psi}\right), \quad (3.9)$$

where  $\nabla^2 \Psi$  is the derivative of the non-relativistic  $J/\psi$  wave function. With  $\nabla^2 \Psi / (M_\psi^2 \Psi) \approx -0.07$ , the correction factor due to Fermi motion was estimated to be  $\approx 6\%$ . This correction affects the normalisation of the  $J/\psi$  cross section but does not affect the  $x$  (or  $W$ ) behaviour of it.

To summarise, in our approach, we project the open heavy  $c\bar{c}$  quark pair onto the colour singlet configuration with the corresponding transition matrix element  $\langle O_1 \rangle_V$ , which is fixed by the experimentally measured leptonic decay width of the  $J/\psi$ . The exclusive final state requires a colourless high energy scattering (modelled by the two-gluon exchange) and therefore does not allow for a colour-octet contribution, as this would populate the rapidity gap and destroy the exclusivity of the final state. Higher order corrections within NRQCD are not included here, but have been discussed in [136]. For the total cross section, they occur at  $\mathcal{O}(v^2)$  and have to be considered together with higher Fock states  $\sim \alpha_s^2$ . The resulting correction is of the order of a few percent and beyond the accuracy we require.

### 3.3 Connecting exclusive production to the PDFs

Let us recall the advantage of using the exclusive  $J/\psi$  LHCb data in global parton analyses in the collinear factorisation scheme. It offers the possibility to probe PDFs (mainly the gluon PDF) at extremely low  $x$  in a so far unexplored kinematic regime. In particular, for

forward ultraperipheral production,  $pp \rightarrow p + J/\psi + p$ , the LHCb experiment can reach<sup>2</sup>

$$x \sim (M_\psi/\sqrt{s}) e^{-Y} \sim 3 \times 10^{-6} \quad (3.10)$$

for  $\sqrt{s} = 13$  TeV and rapidity  $Y = 4.5$ . Moreover, the cross section is proportional to the square of the parton density, so the uncertainty on the PDF is reduced.

However, as mentioned in Section 3.1, there appear to be two disadvantages. First, the description of the exclusive  $J/\psi$  process depends on the GPDs, and, second, there is a strong dependence on the choice of scale, indicating a large theoretical uncertainty. In Sections 2.5.1 and 2.5.2, we discussed how these problems were resolved through a systematic taming of the naive  $\overline{\text{MS}}$  result, amounting to resumming logarithmically enhanced small- $x$  terms and implementation of a small- $Q$  power correction.

The high energy limit of the NLO correction, that is the asymptotic limit  $W^2 \gg M_\psi^2$ , takes the form [18]

$$\begin{aligned} A^{(1)}(\xi, \mu_F) \sim & -i\pi C_g^{(0)} \left[ \frac{\alpha_s(\mu_R^2) N_c}{\pi} \ln \left( \frac{m_c^2}{\mu_F^2} \right) \int_\xi^1 \frac{dX}{X} F_g(X, \xi, \mu_F^2) \right. \\ & \left. + \frac{\alpha_s(\mu_R^2) C_F}{\pi} \ln \left( \frac{m_c^2}{\mu_F^2} \right) \int_\xi^1 dX (F_q(X, \xi, \mu_F^2) - \{X \rightarrow -X\}) \right], \end{aligned} \quad (3.11)$$

where we used the symmetry properties of the quark and gluon GPDs in the regions  $X > \xi$  and  $X < -\xi$ , see Section 2.3.2. The contribution from this logarithmically large integration interval is enhanced by a  $\ln(1/\xi)$ , that is, the leading contribution to this high energy correction comes from the strongly ordered region,  $\xi \ll X \ll 1$ . Together with the explicit logarithm factors outside of the integrals shown in eqn. (5.7), this generates the NLO contribution to DLLA accuracy. The structure of this equation then warrants the choice  $\mu_F^2 = m_c^2$  argued in Section 2.5.1, allowing for a resummation of the complete NLO correction in the high energy limit into the input distributions. There is therefore no longer a logarithmically increasing large contribution at  $X \gg \xi$ .

The GPD function (denoted by  $F_a(X, \xi)$  with  $a = g, q$  in Fig. 3.1) accounts for the fact that the momenta of the ‘left’ and ‘right’ partons in the diagrams of Fig. 3.1 are different. In particular, they carry proton momentum fractions  $X + \xi$  and  $X - \xi$  respectively. The Shuvaev transform relates the GPD  $F_a(X, \xi)$  to the PDF  $f_a(X + \xi)$ . It turns out (see

---

<sup>2</sup>Note that this value corresponds to the lower limit of the  $x$  interval felt by the process. In practice the main contribution to the amplitude comes from a slightly larger value of  $x$ , as discussed in Section 3.5.

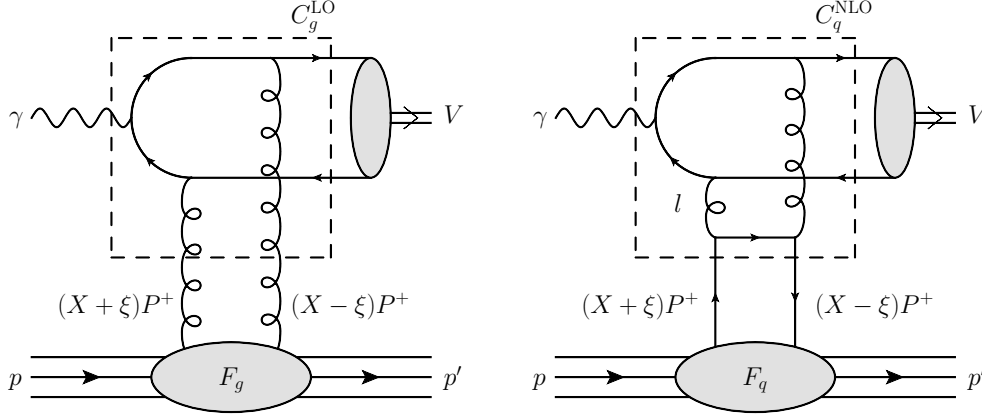


Figure 3.1: (a) LO contribution to  $\gamma p \rightarrow V + p$ . (b) NLO quark contribution. For these graphs all permutations of the parton lines and couplings of the gluon lines to the heavy-quark pair are to be understood. Here the momentum  $P \equiv (p + p')/2$  and  $l$  is the loop momentum. Note that the momentum fractions of the left and right input partons are  $x = X + \xi$  and  $x' = X - \xi$  respectively; for the gluons coupled directly to the on-shell heavy-quark pair, we have  $x' \ll x$  and so  $x \simeq 2\xi$ .

later) that the values of  $X$  that are most relevant in the convolution of the GPD with the coefficient function are of the order of  $\xi$  and so  $x' \ll x$ . Thus, in this way we probe the gluon PDF at values of  $x$  close to  $2\xi$ .

The momentum fractions carried by the  $t$ -channel gluons are

$$x = \frac{M_{q\bar{q}}^2}{W^2} \quad \text{and} \quad x' = \frac{M_{q\bar{q}}^2 - M_\psi^2}{W^2}, \quad (3.12)$$

where  $M_{q\bar{q}}^2$  is the mass of the intermediate  $q\bar{q}$  pair. This deviates from the mass squared of the  $J/\psi$  meson through corrections of  $\mathcal{O}(\varepsilon)$ , where  $\varepsilon$  is its binding energy. It therefore follows that

$$\frac{x'}{x} = 1 - \frac{M_\psi^2}{M_{q\bar{q}}^2} \sim \frac{\mathcal{O}(\varepsilon)}{M_{q\bar{q}}^2}, \quad (3.13)$$

and so the value of  $x'$  is driven by the difference of the mass of the vector meson and the energy of its on-shell constituent quarks. As will be discussed in Section 3.2.1, we set  $M_\psi^2 = M_{q\bar{q}}^2$ . This means that for the upper gluons in the last cell of evolution in Fig. 3.1(b) (or for the gluon pair in Fig. 3.1(a)) the hierarchy  $x' \ll x$  holds. In the computation of the imaginary part of the amplitude, we have checked that the on-shell constraint for the heavy

quarks necessitates  $X = \xi$ , so that at LO the momentum fractions carried by the gluons are  $x = 2\xi$  and  $x' = 0$  exactly. After one (or more steps) of evolution, i.e. at NLO and beyond, we instead deal with the many parton system, where the  $x$  and  $x'$  values carried by the gluons are both driven mainly by the momentum fraction of the lowest parton. In Fig. 3.1, this corresponds to the quark.

The results of this chapter have been obtained by incorporating the double logarithmic resummation and the ‘ $Q_0$ ’ cut procedure into the  $\overline{\text{MS}}$  result, discussed above and in Sections 2.5.1 and 2.5.2.<sup>3</sup> As  $m_c$  is a relatively low scale, there naively seems to be a need to additionally resum the single  $\alpha_s \ln(1/x)$  BFKL terms in the coefficient functions. In particular, in [137], instead of fixing  $\mu_F = \mu_0$ , it was proposed to resum the BFKL corrections, like  $\alpha_s \ln(1/x)$ , already in the coefficient function. It was stated that this would allow good scale stability to be obtained.

However, we do not resum the BFKL corrections for the following reasons. First, we note that we cannot use the standard LO BFKL summation. We would have to account for the effects of the  $Q_0$  subtraction. The LO BFKL gives the behaviour  $xg \sim x^{-\omega_0}$  where

$$\omega_0 = (3\alpha_s/\pi) 4 \ln 2 \simeq 0.6 \quad (3.14)$$

which is too large and inconsistent with the LHCb data. Next, a detailed study [111, 112, 113] found that at low  $Q^2$ , the higher-twist effects (that is, gluon reggeization [138] and absorptive corrections) strongly modify the low  $x$  behaviour of the BFKL amplitude. Absorptive effects are those that come into play at very small  $x$ , where the probability of interactions between partons, as their number density increases, becomes so sizeable that they start to recombine with each other. The consequence of these higher-twist effects is why the effective Pomeron intercept, measured for example, via the vector meson diffractive electroproduction (photoproduction) falls from  $\alpha(0)_P \simeq 1 + 0.3$  (at large  $Q^2$ ) down to  $1 + 0.1$  (at low  $Q^2$ ). Without the BFKL resummation, all these effects are absorbed in the behaviour of the ‘input’ phenomenological gluons.

In addition to the problems above, if the coefficient functions were to absorb the BFKL effects, then the convolution of the GPD with the coefficient function

$$\text{Im}A(\xi) \sim \sum_{a=q,g} \int_{-1}^1 \frac{dX}{X} C_a(X, \xi) F_a(X, \xi), \quad (3.15)$$

---

<sup>3</sup>We emphasise that the full NLO contribution was considered in the analysis that follows. The high energy limit was shown only to argue our choice of scale,  $\mu_F = m_c$ .

is such that the coefficient function,  $C_a(X, \xi)$ , occupies almost the whole available  $\ln(1/X)$  interval; that is the dominant contribution comes from  $X \sim \mathcal{O}(1)$  and not  $X \sim \xi$ . Thus, we would lose the main advantage of probing the unexplored very small  $x$  regime. Beyond NLO, single logarithmic terms,  $\ln(1/x)$ , may again be present in the amplitude and not resummed with the choice  $\mu_F = m_c$ . This was shown schematically in [137] where the  $\overline{\text{MS}}$  amplitude was shown to take the form

$$A \sim 1 + z \ln \left( \frac{m_c^2}{\mu_F^2} \right) + z^2 \left( \frac{\pi^2}{6} + \frac{1}{2} \ln^2 \left( \frac{m_c^2}{\mu_F^2} \right) \right) + \dots, \quad (3.16)$$

with  $z^n \sim \alpha_s^n \ln^n(1/\xi)$ . At NNLO, that is at order  $z^2$ , we have a BFKL-type logarithm contribution remaining with our scale choice  $\mu_F = m_c$ . The LO BFKL evolution equation can formally resum terms  $\sim \alpha_s \ln(1/x)$ , however we anticipate that by including the  $Q_0$  subtraction in the LO BFKL kernel their impact will anyway be much smaller. This is because in BFKL evolution, we have no strong  $k_t$  ordering and the exact scale dependence (the  $\tilde{c}_n(Q^2)$  of Appendix B) consists of contributions  $k_t < Q$  and  $k_t > Q$ . With our choice  $Q = Q_0 = m_c$ , one may expect that after the ‘ $Q_0$ ’ subtraction, that is after the removal of the low  $k_t < Q$  contribution, the BFKL contributions will be suppressed. The argument is multi-faceted in that we also remove the enhanced  $\alpha_s(k_t^2)$  contribution in the low  $k_t < Q$  region.

Fig. 3.2 shows the individual quark and gluon contributions to the imaginary part of the amplitude to NLO *after* the  $Q_0$  subtraction. We show the results for  $\text{Im}A_a$  with  $a = g, q$  for the choice  $\mu_F = M_\psi/2 = m_c$  and two values of the factorisation scale,  $\mu_f^2 = m_c^2, 2m_c^2$ , using eqn. (3.15). We take  $\mu_R = \mu_f$ .<sup>4</sup> Here,  $A_{a=g,q}$  are the gluon and quark contributions to the  $\gamma p \rightarrow J/\psi + p$  amplitude in the collinear factorisation scheme at NLO. The plot shows the stability of the amplitude with respect to variations of  $\mu_f$ , and also that the  $Q_0$  subtraction practically fully absorbs the quark contribution. We find that the alleviation of the factorisation scale dependence upon imposition of the low scale  $Q_0$  cut off has paid dividends in leading to the dominance of the gluon contribution over

<sup>4</sup>This corresponds to the Brodsky-Lepage-Mackenzie (BLM) scale prescription [139]. Such a choice eliminates the contribution proportional to  $\beta_0$  (i.e. the term  $\beta_0 \ln(\mu_R^2/\mu_f^2)$  from the NLO terms in eq. (3.95) of [18]). Furthermore, following the discussion in [140] for the analogous QED case, we note that the new quark loop insertion into the gluon propagator appears twice in the calculation. The part with scales  $\mu < \mu_f$  is generated by the virtual component ( $\propto \delta(1-z)$ ) of the LO splitting during DGLAP evolution, while the part with scales  $\mu > \mu_R$  accounts for the running  $\alpha_s$  behaviour obtained after the regularisation of the ultraviolet divergence. In order not to miss some contribution and/or to avoid double counting we take the renormalisation scale equal to the factorisation scale,  $\mu_R = \mu_f$ .

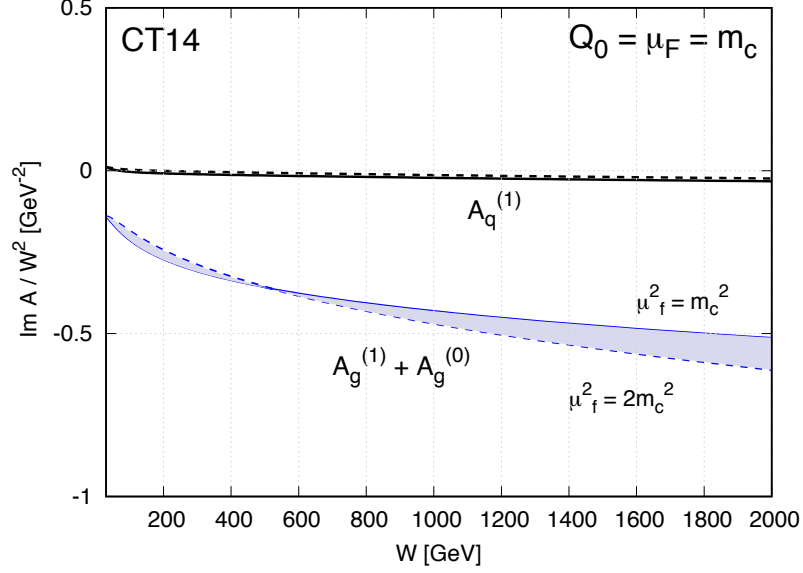


Figure 3.2: The gluon LO+NLO and quark NLO contributions to the imaginary part of the  $\gamma p \rightarrow J/\psi + p$  amplitude for two different choices of the factorisation scale  $\mu_f^2 = \mu_R^2 = m_c^2, 2m_c^2$  shown by the continuous and dashed curves respectively. CT14 NLO global PDFs [42] are used and the ‘optimal’ scale  $\mu_F = m_c$  is chosen.

the quark contribution. With this set-up, we can therefore say that low  $x$  exclusive  $J/\psi$  photoproduction probes predominantly only the gluon distribution.

This is emphasised in Fig. 3.3, where we show both the full amplitude plotted to NLO and the contribution coming from the gluon sector alone, using three global parton sets with  $Q_0 = \mu_F = \mu_R = \mu_f = m_c$ . CT14 shows the most prominent enhancement of the amplitude due to the quark inclusion. At the largest  $W$ , the CT14 NLO quark contribution provides  $\sim 6\%$  enhancement while for NNPDF3.0, the enhancement is below a percent. Actually, the relative contribution of the quarks changes sign for some  $W \gtrsim 1200 \text{ GeV}$  in the case of MMHT14. We have checked that these features are due to the small  $x$  and small scale quark behaviour of the global parton sets, also poorly constrained for  $x \lesssim 10^{-4}$ .

Note that within the DGLAP approach (with the strong  $k_t$  ordering), the  $k_t$  of the light quarks are much smaller than  $\mu_F$  (since the quark contribution is separated from the outgoing  $J/\psi$  meson by at least one step of DGLAP evolution - only the gluons may enter the hard scattering). This means that practically the whole quark contribution comes from the region  $k_t < Q_0$  and therefore, after the  $Q_0$  subtraction, is completely absorbed into

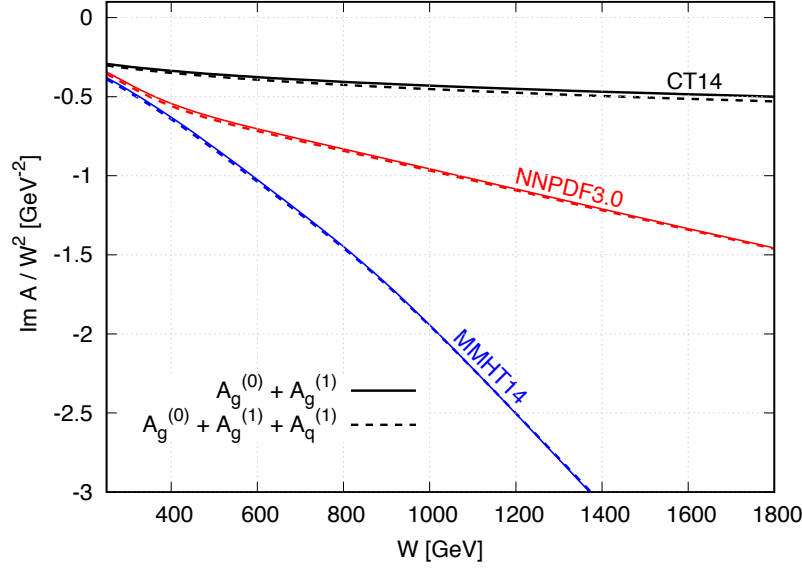


Figure 3.3: The gluon LO + NLO amplitude,  $A_g^{(0)} + A_g^{(1)}$  (solid lines) and the full amplitude,  $A_g^{(0)} + A_g^{(1)} + A_q^{(1)}$  (dashed lines) for three global parton sets with all scales set at the ‘optimal’ value,  $\mu_0 = m_c$ . The inclusion of the quark NLO contribution is negligible for the large range of  $W$  we consider.

the input PDF. Our results are therefore in line with the conceptual underpinnings of the DGLAP collinear factorisation framework.

### 3.4 Description of exclusive $J/\psi$ photoproduction data

In this section, we describe additional ingredients that are incorporated into our theoretical description of the exclusive  $J/\psi$  production process, before presenting the first comparison to data of our predictions.

#### 3.4.1 Real part correction

All of the calculations presented so far are performed for the imaginary part of the production amplitude. Indeed, from Regge theory based arguments and the optical theorem, this is expected to be the dominant contribution to the scattering amplitude, especially at high energies. This is because with the interaction modelled as a quasi-forward ( $t = 0$ )

elastic hard scattering, the imaginary part of the amplitude receives a positivity constraint from the optical theorem, with no such similar constraint for the real part. It is therefore consistently sub-dominant to the imaginary part, more so at higher energies. The real part is obtained via a dispersion relation on general grounds of analyticity, which in the high energy limit (for the even signature amplitude in which two reggeized gluons are exchanged) can be written in the simplified form [131]

$$\rho = \frac{\text{Re}A}{\text{Im}A} = \tan\left(\frac{\pi}{2} \frac{\partial(\ln \text{Im}A/W^2)}{\partial(\ln W^2)}\right) \sim \frac{\pi}{2} \lambda_{\text{eff}}. \quad (3.17)$$

This provides a correction factor of  $(1 + \rho^2)$  to the cross section and is implemented numerically by sampling points densely enough so that local gradients evaluated between neighbouring points allow for a meaningful estimate of this quantity bin by bin in  $W$ . Note that after the  $Q_0$  subtraction,  $\text{Im} A$  does not change sign over the range of  $W$  we consider and so eqn. (3.17) is well-defined. The overall phase of other model dependent factors, e.g. that of the  $J/\psi$  wavefunction, are irrelevant in this regard. For CT14, the imaginary part of the amplitude grows only moderately with energy, see Figs. 3.2 and 3.3, so that the effective lambda,  $\lambda_{\text{eff}}$ , is small, leading to a relatively small real part enhancement via the derivative in eqn. (3.17). This is demonstrated in Fig. 3.4, in comparison with the effective lambda obtained in each  $W$  bin using MMHT14 and NNPDF3.0 partons. For  $W < 100$  GeV ( $x \gtrsim 10^{-3}$ ), where the behaviour of the global gluon PDFs are similar, see Fig. 2.1, the contribution coming from the real part is at most a 10% effect for all three groups. For  $W > 100$  GeV, however, the growth of the MMHT14 and NNPDF3.0 global gluons are a lot faster than that of CT14, leading to a much larger real part enhancement. Note that this modest growth of the CT14 global gluon at lower  $x$  leads to a real part contribution that is decreasing with increasing  $W$ . As we will demonstrate in Fig. 3.5, all cross section predictions based on the three parton sets agree well with the HERA data in the region  $W < 100$  GeV, while the fast growth of the global gluons at lower  $x$  displayed by MMHT14 and NNPDF3.0 is not compatible with the LHCb data at larger  $W$ . Their growth must be much slower, which would again lead to a relatively small real part enhancement at large  $W$ , too, in line with the predictions of Regge theory.



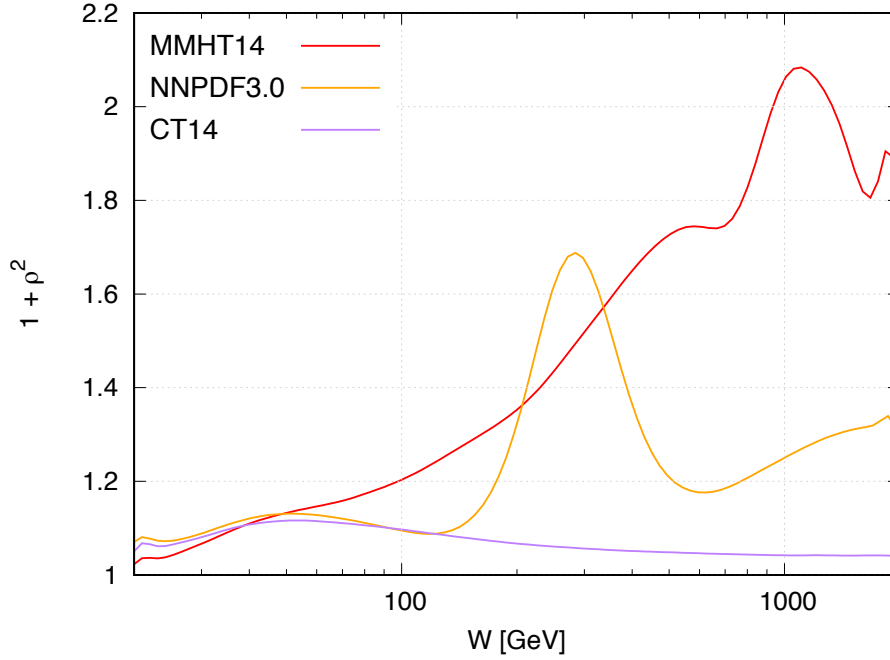


Figure 3.4: The enhancement  $(1 + \rho^2)$  at the cross section level due to the real part correction,  $\rho$ , given over the range of  $W$  considered.

### 3.4.2 Restoring the $t$ dependence

The unpolarised cross section for exclusive  $J/\psi$  production to NLO is given by the modulus square of the sum of eqn. (3.1) at LO and NLO, which represents the helicity summed amplitude with the explicit contractions of the polarisation vectors included. In the quasi-forward limit,  $t = 0$ , the differential cross section is

$$\frac{d\sigma}{dt}(\gamma p \rightarrow J/\psi p)|_{t=0} = \frac{|A|^2}{16\pi W^4}, \quad (3.18)$$

where  $1/(16\pi W^4)$  is the explicit flux factor. So far, we have tacitly assumed the kinematical limit  $t = 0$  in the description of the forward ‘elastic’ scattering. See Chapter 5 for this realised naturally in the language of the Bjorken limit at leading-twist when we construct the kinematics for HVM electroproduction. Here, we calculate the value of  $\text{Im}A$  at  $t = 0$  and then restore the total  $\gamma p \rightarrow J/\psi + p$  cross section assuming an exponential  $t$  behaviour

with the experimentally determined slope [126],

$$B = 4.9 + 4\alpha'_P \ln(W/W_0) \text{ GeV}^{-2}$$

with  $W_0 = 90 \text{ GeV}$  and  $\alpha'_P = 0.06 \text{ GeV}^{-2}$ . This parametrisation grows more slowly with  $W$  than the formula used by H1 [129], but is still compatible with the HERA data. We have chosen the slope parameter  $\alpha'_P$  to be compatible with Model 4 of [141] which fits a wider variety of data. That is, we suppose  $\sigma \sim \exp(-Bt)$  so that

$$\sigma(\gamma p \rightarrow J/\psi p) = \frac{1}{B} \frac{|A|^2}{16\pi W^4}, \quad (3.19)$$

integrated over  $t$ . In earlier analyses, see e.g. [142], the  $B$  slope is assumed to be

$$B = 4.5 \text{ GeV}^2 = \text{const}, \quad (3.20)$$

as the data only probed a limited range of  $W$  at the time and negligence of its mild energy dependence produced an offset in the predictions that was comparable to the error between the H1 and ZEUS experimental data points.

Note that the calculation of  $|A|^2 = |A^{(0)} + A^{(1)}|^2$  is truncated at  $\mathcal{O}(\alpha_s^3)$  so that, strictly speaking, we do not include a subset of corrections that we deem to be part of the NNLO contribution.

### 3.4.3 HERA data

Fig. 3.5 shows the  $J/\psi$  photoproduction data obtained at HERA [126, 127, 128, 129] are described reasonably well by all three sets of global partons [38, 40, 42] within our collinear approach. These data sample  $x$  values in the interval<sup>5</sup>

$$x = M_\psi^2/W^2 \sim 10^{-3} - 10^{-4}. \quad (3.21)$$

In our approach, we are free to choose the subtraction scale  $Q_0$  and the  $\mu_F$  scale in the NLO correction. For a given  $\mu_F$ , in principle one would like to achieve cross section stability in the small window  $q_0 \leq Q_0 \leq \mu_F$ , where  $q_0$  is the PDF input scale. We have performed some exploratory studies to ensure this is the case. In particular, as shown in Fig. 3.6,

---

<sup>5</sup>We see that when  $x \lesssim \text{few} \times 10^{-4}$  the central global partons fail to describe the HERA data.

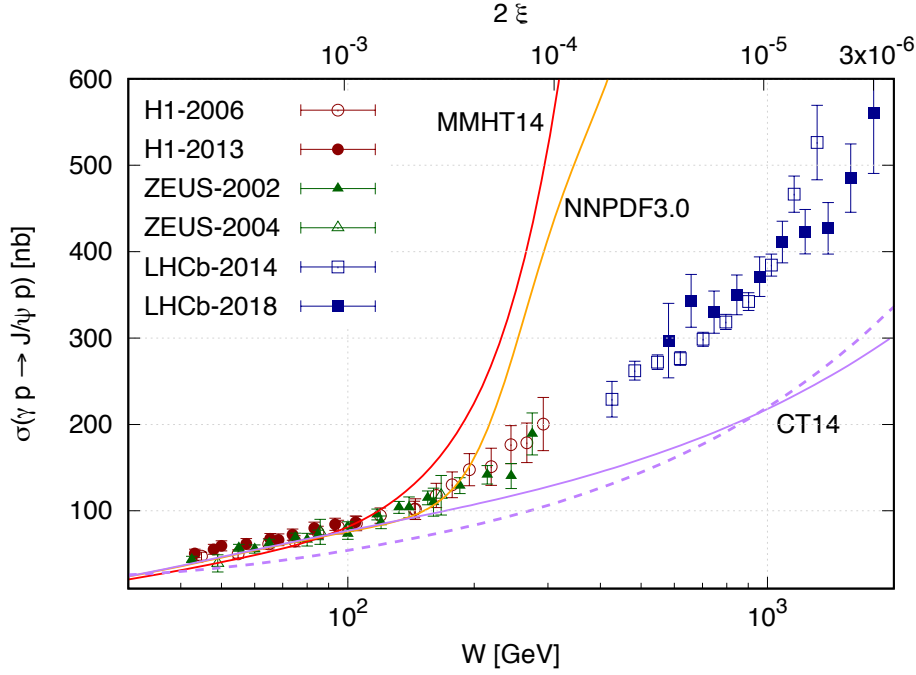


Figure 3.5: The  $\gamma p \rightarrow J/\psi + p$  data obtained at HERA [126, 127, 128, 129] and LHCb [47, 48] compared with the predictions obtained using the NLO PDFs taken from three different sets of global partons [38, 40, 42] with  $\mu_f = m_c$  (solid lines). The dashed line for the CT14 prediction, corresponding to  $\mu_f^2 = 2m_c^2$ , is added to demonstrate the scale stability of our NLO predictions; but note that our optimal choice  $\mu_f^2 = m_c^2$  agrees better with the HERA data.

for  $Q_0^2 = \mu_F^2 = 1.2 m_c^2$  fixed (a variation from our optimal value by 20%), together with  $\mu_f^2 = \mu_R^2 \in \{1.2, 2.4, 3.6\} \cdot m_c^2$  and  $q_0 = 1.3$  GeV (CTEQ6.6 input PDF scale), we find a good scale stability of our cross section predictions.

We work at LO in NRQCD and the description used for the results shown in Fig. 3.5 corresponds to the choices

$$Q_0 = \mu_F = m_c = M_\psi/2. \quad (3.22)$$

The running of  $\alpha_s$  is determined via the package `CRunDec` [143, 144], with  $\alpha_s(M_Z^2) = 0.118$ , and a two-loop evolution is used to incorporate NLO effects. Recall that the choice  $\mu_F = m_c$  provides the complete summation of the double log terms [102]. Besides giving a good description of the HERA data, the above choice of  $Q_0$  and  $\mu_F$  give a stable theoretical

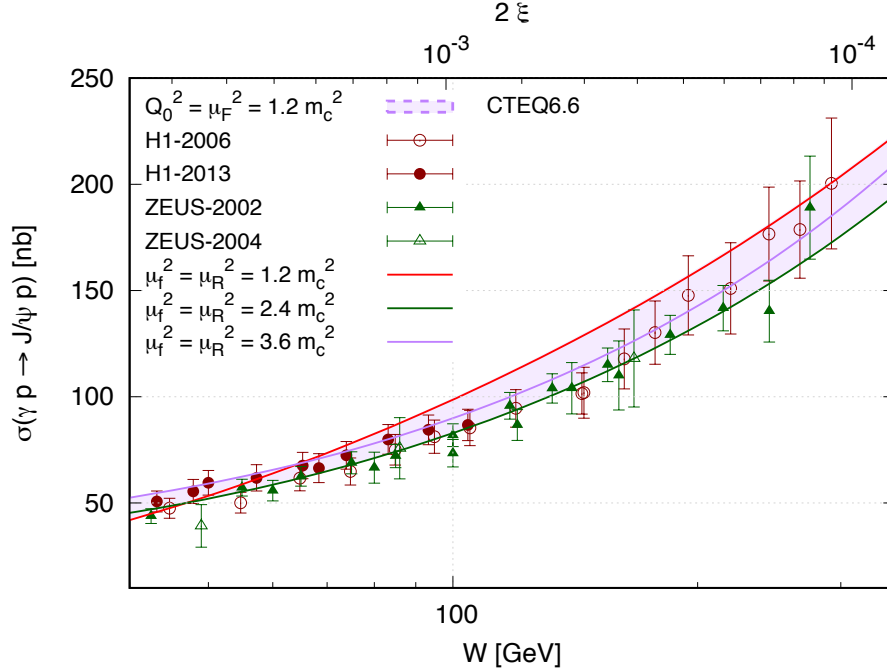


Figure 3.6: Cross section predictions evaluated with  $Q_0^2 = \mu_F^2 = 1.2 m_c^2$  fixed and variations  $\mu_f^2 = \mu_R^2 \in \{1.2, 2.4, 3.6\} \cdot m_c^2$  using CTEQ6.6 partons [41]. A good scale stability is observed over the entire HERA energy range considered.

prediction also when the scales  $\mu_f$  and  $\mu_R$  are varied, see Figs. 3.2 and 3.5. In addition, the fact that at  $x \gtrsim 0.001$  the data are well described by the existing global gluons is an argument in favour of the correct normalisation, that is, in favour of small relativistic corrections to our approach. We have added an upper axis to these figures which show the value of  $2\xi$  probed at a given  $W$ . This corresponds to the momentum transfer in the longitudinal direction and is close to the value of  $x$  carried by the incoming gluon.<sup>6</sup>

The HERA data considered for exclusive  $J/\psi$  photoproduction are summarised in Table 3.1. The ZEUS and H1 collaborations at the HERA collider have also reported events outside the  $\langle Q^2 \rangle \sim 0$  photon virtuality bin, but these do not concern us here. Moreover, we exclude photoproduction data from ZEUS-1995, 1997 and H1-1996, 2000 as these have been superseded by the data sources presented in the Table.

We would like to remark that in an earlier version of Fig. 3.5, published in our [145], the

<sup>6</sup>To be more precise,  $x = 2\xi/(1 + \xi) = 2\xi - \mathcal{O}(\xi^2)$  for small  $\xi$ . Therefore, actually  $2\xi \gtrsim x$ .

Data Source & Year	Data Period	No. of Data Points	Points Considered
ZEUS-2002 [126]	1996/7, 1999/2000	22	19*
ZEUS-2004 [127]	1998-2000	3	3
H1-2006 [128]	1999/2000	17	17
H1-2013 [129]	2006/7	11	10*

\*Data Points with  $x \gtrsim 5 \times 10^{-3}$  neglected

Table 3.1: HERA data selection for exclusive  $J/\psi$  photoproduction. 49 data points are considered with  $x \gtrsim 5 \times 10^{-3}$ .

MMHT14 NLO PDF set with  $\alpha_s(M_Z^2) = 0.120$  had been used which caused a mismatch between the MMHT14 central cross section prediction and the relatively good NNPDF3.0 and CT14 ones in the HERA domain  $10^{-3} < x < 10^{-2}$ . Down to a few units of  $10^{-4}$ , the NNPDF3.0 and CT14 predictions (which use  $\alpha_s(M_Z^2) = 0.118$ ) were essentially coincident while the MMHT14 prediction was consistently below. Despite the MMHT14 parton set including additional NMC structure function data at  $x = 10^{-2}$  that is missed by the other sets due to their low scale cut<sup>7</sup>, from plots generated in APFEL [146, 147], it was found that the MMHT14 NLO parton set with  $\alpha_s(M_Z^2) = 0.120$  gave a gluon that is around 30% lower than that of the CT14 NLO set (with  $\alpha_s(M_Z^2) = 0.118$ ) at  $x = 10^{-3}$ . This may be contrasted with the MMHT14 NLO set with  $\alpha_s(M_Z^2) = 0.118$ , shown here, in which the difference is reduced to  $\sim 10\%$ . At low scales, this difference in the coupling has therefore a sizeable effect and leads to different gluon evolutions. The difference in shape washes out at higher scales, as one might expect. The implications of this observation emphasises the utility of the exclusive data already in the HERA regime. It is non-trivial and assuring that our predictions, with our preferred scale choice, agree with the HERA data and between the global PDFs.

### 3.4.4 LHCb data

The LHCb experiment, by design, does not directly measure cross section events for  $J/\psi$  *photoproduction* but instead that for exclusive  $pp \rightarrow p + J/\psi + p$  [47, 48]. This is an ultraperipheral initiated reaction between the two colliding protons, where the impact parameter is greater than the sum of the two proton radii. As a result, an electromagnetic interaction is favoured over a strong interaction and the two protons interact via a flux of high energy

<sup>7</sup>I would like to thank Robert Thorne for this information in a private communication.

photons. In the Equivalent Photon Approximation (EPA) or Weizsacker-Williams (WW) approximation [148, 149, 150], the electromagnetic field generated by the relativistic proton is replaced by an on-shell photon. The experiment is unable to tag forward protons accompanying the  $J/\psi$  so instead only the rapidity of the  $J/\psi$  is measured. Events are selected by ensuring a large rapidity gap on both sides of the  $J/\psi$  - measurements where the transverse momentum of the  $J/\psi$  are small and assumed to correspond to *exclusive* reactions. The lack of forward proton tagging means it is also not possible to determine which of the two protons emitted the photon. The ultraperipheral amplitude for a given

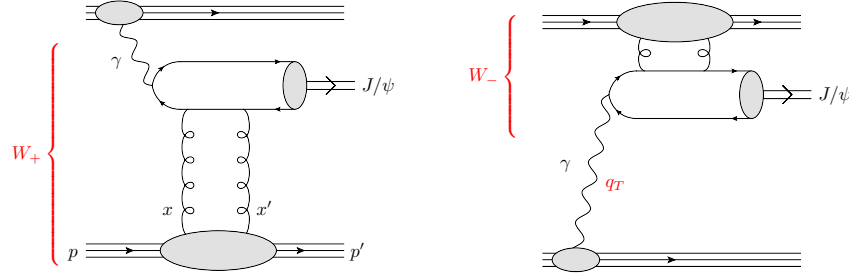


Figure 3.7: The two diagrams describing exclusive  $J/\psi$  production at the LHC. The left diagram, the  $W_+$  component, is the major contribution to the  $pp \rightarrow p + J/\psi + p$  cross section for a  $J/\psi$  produced at large rapidity  $Y$ . Thus such data allow a probe of very low  $x$  values,  $x \sim M_\psi \exp(-Y)/\sqrt{s}$ ; recall that for two-gluon exchange we have  $x \gg x'$ . The  $q_T$  of the photon is very small and so the photon can be considered as a real on-mass-shell particle.

$J/\psi$  rapidity is then generally the sum of two photoproduction amplitudes with different  $W^2$  depending on which proton emitted the photon and which was the target, see Fig. 3.7. The interference contribution is suppressed as the photon's transverse momentum,  $q_T$ , is much smaller than that of the proton exchanging the gluons. This interference term is proportional to the angle  $\phi_{pp}$  between the two outgoing protons. As the  $J/\psi$  meson is produced at small transverse momentum,  $\phi_{pp}$  is small and this azimuthal-angle correlation may be neglected. In fact, in the absence of absorptive corrections (additional strongly interacting factorisation breaking corrections such as those accounted for in the survival factor mentioned below), this correlation vanishes identically [151]. The contribution corresponding to the right graph, with a smaller photon-proton energy  $W_-$ , comes from relatively large  $x \sim 10^{-2}$ , and can be subtracted using the existing description of HERA data. The power law fit to existing HERA data proposed by the H1 collaboration [129],  $\sigma_{\gamma p \rightarrow J/\psi p}(W) = 81(W/90)^{0.67} \text{ nb}$ , provides an alternative means to extract the  $W = W_-$

component. The cross section for  $J/\psi$  photoproduction at the large energy,  $W_+$ , may therefore be extracted from the LHCb measurements.

$Y$	7 TeV		13 TeV	
	$S^2(W_+)$	$S^2(W_-)$	$S^2(W_+)$	$S^2(W_-)$
2.125	0.766	0.882	0.786	0.885
2.375	0.752	0.885	0.744	0.888
2.625	0.736	0.888	0.762	0.891
2.875	0.718	0.891	0.748	0.893
3.125	0.698	0.894	0.732	0.896
3.375	0.676	0.897	0.715	0.899
3.625	0.650	0.899	0.695	0.901
3.875	0.621	0.902	0.672	0.903
4.125	0.587	0.904	0.647	0.905
4.375	0.550	0.906	0.618	0.907

Table 3.2: Rapidity gap survival factors  $S^2$  for exclusive  $J/\psi$  production,  $pp \rightarrow p + J/\psi + p$ , in each  $J/\psi$  rapidity  $Y$  bin, as measured by the LHCb. For each  $pp$  centre of mass energy, 7 TeV and 13 TeV, we give the survival probability for each of the two independent  $\gamma p \rightarrow J/\psi p$  subprocesses at  $\gamma p$  centre of mass energies  $W_{\pm}$ .

Additionally, at the LHC, there is a non-negligible probability of additional soft interactions between the two colliding protons that can result in secondary particles polluting the rapidity gaps used to select the exclusive events. This will suppress the number of events deemed exclusive and therefore one must account for the gap survival probability,  $S^2 < 1$ , to have no such additional interaction. See Fig. 3.8 for the classes of spurious emissions considered here. The value of  $S^2$  depends on the  $pp$  collider energy and the partonic energy  $W$ . The survival factors are estimated from general rescattering principles, accounting for factorisation breaking corrections and describe the probability that the rapidity gap will not become populated with additional emissions. In this work, the values of  $S^2(W)$  as a function of  $W$  were calculated using the Khoze-Martin-Ryskin (KMR) eikonal model [152] which well describes the data for the differential  $d\sigma(pp)/dt$  cross section and low-mass diffractive dissociation. In particular, as compared to [141, 153], we use an updated model for the gap survival probabilities tuned to the precise TOTEM data [154] for  $pp$  scattering at 7 TeV. The values of the survival factors used for  $pp$  centre-of-mass energies 7 TeV and 13 TeV for the relevant range of the  $J/\psi$  rapidity  $Y$  is given in Table 3.2.

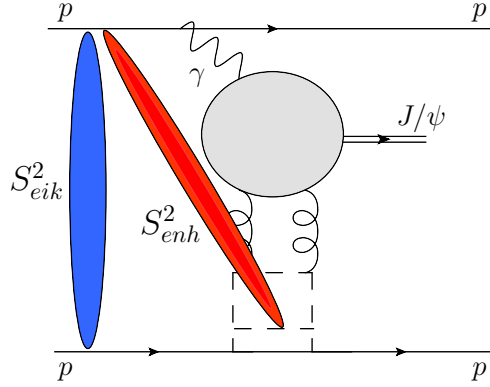


Figure 3.8: The ultraperipheral exclusive  $J/\psi$  production process with rescattering corrections. The blue shaded segment represents interactions between so-called spectator partons in the protons, contributing to the eikonal survival factor,  $S_{eik}^2$ . The red shaded segment represents interactions between spectator partons in one proton and the partons (gluon or quark) in the hard process evolution ladder, contributing to the enhanced survival factor,  $S_{enh}^2$ . The enhanced rescattering effects are highly suppressed in comparison with those entering the eikonal contribution.

As the proton is an extended object with an extended charge distribution, the photon flux  $dN/dk$  of quasi-real photons will not be that due to a point particle but instead have an explicit dependence on the proton form factors. To describe the photon flux, we will follow [155], using a precise expression and keeping all corrections of  $\mathcal{O}(x)$ .<sup>8</sup> The photon flux double-differential in the photon energy,  $k$ , and its virtuality  $Q^2$  can be written as

$$\frac{dN}{dkdQ^2} = \frac{\alpha}{\pi} \frac{1}{kQ^2} \left( \left(1 - \frac{k}{E_P}\right) \left(1 - \frac{Q_{\min}^2}{Q^2}\right) F_E + \frac{k^2}{2E_P^2} F_M \right), \quad (3.23)$$

where  $Q_{\min}^2$  is the minimum photon virtuality permitted by the kinematics and  $E_P = \sqrt{s}/2$  is the energy of the incoming proton, of mass  $m_P$ . Here,  $F_E$  ( $F_M$ ) is the electric (magnetic) proton form factor. In the dipole approximation [155],

$$F_M = G_M^2, \quad F_E = (4m_P^2 G_E^2 + Q^2 G_M^2)/(4m_P^2 + Q^2), \quad G_E^2 = G_M^2/\mu_P^2 = \left(1 + \frac{Q^2}{Q_0^2}\right)^{-4}, \quad (3.24)$$

<sup>8</sup>The numerical analysis was performed using the simpler form in [156], which yields essentially the same photon flux result of [155].



where the magnetic moment of the proton is  $\mu_P^2 = 7.78$  [157] and the fitted scale  $Q_0^2 = 0.71 \text{ GeV}^2$  [155]. Due to the steep decrease in the form factors with increasing  $Q^2$ , the photon flux is dominated by a density of on-shell photons. This thereby warrants the application of the WW approximation. Integration of eqn. (3.23) over  $Q^2$  from  $Q_{\min}^2 = m_P^2 k^2 / (E_P(E_P - k))$  to a sufficiently large value  $Q_{\max}^2 \approx 2 - 4 \text{ GeV}^2$  gives

$$\frac{dN}{dk} = \frac{\alpha}{\pi} \frac{1}{k} \left(1 - \frac{k}{E_P}\right) \left( \phi\left(\frac{Q_{\max}^2}{Q_0^2}\right) - \phi\left(\frac{Q_{\min}^2}{Q_0^2}\right) \right), \quad (3.25)$$

where

$$\begin{aligned} \phi(x) = (1 + ay) & \left( -\ln(1 + 1/x) + \sum_{k=1}^3 \frac{1}{k(1+x)^k} \right) + \frac{(1-b)y}{4x(1+x)^3} \\ & + c(1 + y/4) \left( \ln\left(\frac{1+x-b}{1+x}\right) + \sum_{k=1}^3 \frac{b^k}{k(1+x)^k} \right), \end{aligned} \quad (3.26)$$

with

$$y = \frac{k^2}{E_P(E_P - k)}, \quad (3.27)$$

$$a = \frac{1 + \mu_P^2}{4} + \frac{4m_P^2}{Q_0^2} \approx 7.16, \quad (3.28)$$

$$b = 1 - \frac{4m_P^2}{Q_0^2} \approx -3.96, \quad (3.29)$$

$$c = \frac{\mu_P^2 - 1}{b^4} \approx 0.028. \quad (3.30)$$

The LHCb collaboration present values of  $d\sigma(pp)/dY$  in 10 rapidity bins, each at 7 TeV [47] and at 13 TeV [48]. In the EPA, we write  $\sigma(pp)$  as the convolution of the above WW photon flux and the on-shell photon initiated subprocess  $\sigma(\gamma p)$ ,

$$\sigma(pp) = \int \frac{dN}{dk} \sigma(\gamma p) dk. \quad (3.31)$$

Using the chain rule, we can express

$$\frac{d\sigma(pp)}{dY} = \frac{d\sigma(pp)}{dk} \frac{dk}{dY} = k \frac{dN}{dk} \sigma(\gamma p), \quad (3.32)$$

where  $k = M_\psi/2 e^Y$ .

The details of the procedure to extract  $\sigma(\gamma p \rightarrow J/\psi + p)$  at large  $W_+$  energies is described in [125]. Using measurements of the cross section for  $pp \rightarrow p + J/\psi + p$ , differential in bins of rapidity  $Y \sim 2.0 - 4.5$ , the LHCb collaboration extract the cross section for  $\gamma p \rightarrow J/\psi p$  upon rearrangement of

$$\frac{d\sigma(pp)}{dY} = S^2(W_+)k_+ \frac{dN}{dk_+} \sigma_+(\gamma p) + S^2(W_-)k_- \frac{dN}{dk_-} \sigma_-(\gamma p), \quad (3.33)$$

with  $S^2(W_\pm)$  and  $k_\pm dN/dk_\pm$  the rapidity gap survival factors and photon fluxes, respectively, for  $\gamma p$  centre of mass energies  $W_\pm^2 = M_{J/\psi} \sqrt{s} e^{\pm|Y|}$ . For each value of  $Y$ , we evaluate  $k_\pm$  and  $dN/dk_\pm$ , using eqn. (3.25). Together with the corresponding values of the survival factors  $S^2(W_+)$  and  $S^2(W_-)$  at each  $Y$ , as given in Table 3.2, we can determine the corresponding prediction for  $\sigma_+(\gamma p)$ .

In Figs. 3.5 and 3.9 we plot the low  $x$  LHCb ‘data’ points obtained in this way by the LHCb collaboration [47, 48]. In eqn. (3.33), the interference term is manifestly set to zero. In [151], it is shown to vanish identically neglecting the dependence on  $S^2$ . Restoring this dependence then yields a non-zero interference, albeit strongly suppressed. For consistency, as the survival factors depend implicitly on the photon flux, we must determine them using the same expression as we do for the photon flux factor appearing explicitly in eqn. (3.33).

Note that the two-fold ambiguity present in eqn. (3.33) is ubiquitous in the description of ultraperipheral collisions, in the absence of  $p$ -tagging in the experimental set-up. It is resolved when one of the colliding objects is instead a heavy ion because then the emitted photon flux is enhanced by the atomic number  $Z$ .

### 3.5 Towards the bigger picture

The theoretical predictions, obtained using the approach described above, are presented in Fig. 3.5. There we compare our predictions for the cross section for  $J/\psi$  photoproduction obtained using three different sets of global partons [38, 40, 42] with the HERA and LHCb data. The curves correspond to using the central values of the global PDFs. At the lower energy of the HERA data, where the global gluon PDF uncertainty is not too large, the predictions agree with the experimental values reasonably well. In the kinematic region covered by the LHCb experiment the present global PDF analyses do not sample any data, and hence they have almost no predictive power in this low  $x$  regime. This is well illustrated

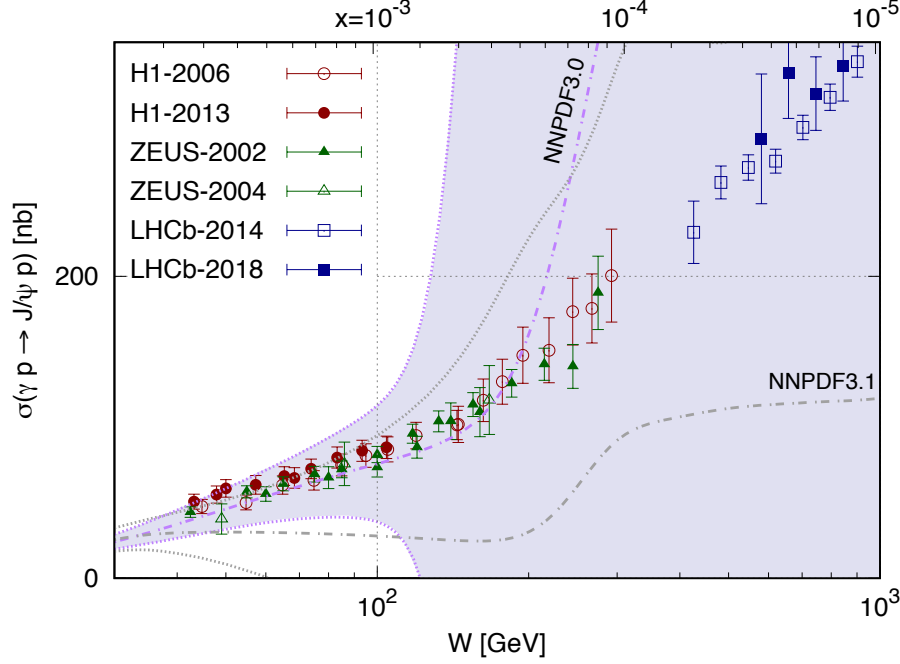


Figure 3.9: The central scale prediction  $\sigma$  for a given global input set of NLO partons, here NNPDF3.0 [38], together with its  $1\sigma$  (shaded) error band show that the current PDF uncertainties are much greater than the experimental uncertainty and the scale variations of the theoretical result. For comparison we also show the NNPDF3.1 [39] predictions, indicated by the dotted lines but with the error band unshaded; in this case the  $\sigma + \delta\sigma$  upper limit follows the HERA data for  $x > 10^{-3}$  while for smaller  $x$  it widens to encompass the data. The exclusive  $J/\psi$  data are therefore in a position to improve the global PDF analyses at low  $x$ .

in Fig. 3.9 which shows the prediction of, for example, the NNPDF3.0 [38] parton set together with its  $1\sigma$  error band. A similar plot has been produced for MMHT14 and CT14, however the qualitative features of the display are as presented in Fig. 3.9. Consequently, we do not show them here, as they do not illuminate the argument further but see our [158] for the band obtained using MMHT14 partons. We also show, for completeness, the corresponding prediction based on NNPDF3.1. We have checked, via **APFEL** [146, 147], that the behaviour of the NNPDF3.1 central cross section prediction is wholly reflective of the shape of the NNPDF3.1 NLO gluon at low scale. Its plateau-like behaviour for larger  $W$  (smaller  $x$ ) is washed out at NNLO.

A comparison of the uncertainties on the data and the predictions in Fig. 3.9 show

that by exploiting the LHCb data for exclusive  $J/\psi$  production we have the possibility to greatly improve our knowledge of the gluon PDF down to  $x \sim 3 \times 10^{-6}$ . The GPD  $F_g(X, \xi)$ , obtained via the Shuvaev transform, is driven dominantly by the value of  $x = X + \xi \simeq 2\xi$ , while  $x' = X - \xi \ll x$  is small. Recall that in the LO contribution (given by the first term of eqn. (2.54)) we sample the gluon PDF at  $x = X + \xi = 2\xi$  exactly, while in the NLO contribution (the second term) the momentum fraction carried by the gluon may be larger. As a check we have calculated the median value,  $\text{med}(X)$ , of the corresponding  $X$ , defined in such a way that  $X > \text{med}(X)$  gives 0.5 of the NLO contribution. By interval halving, in the convolution of the coefficient function with the GPD (see eqn. (3.15)), we find that the  $X$  distribution is sharply peaked at  $X \simeq \xi$  for the gluon contribution, while for the quark NLO contribution the value of  $\text{med}(X) \simeq 1.2\xi$ , approximately 20% larger than  $\xi$ . This procedure is equivalent to finding some constant  $M_0 \in [\xi, 1]$  such that the one dimensional integration at a given  $\xi = \xi_0$ , with a monotonic and suitably normalised integrand,

$$f(M_0) = 2 \int_{\xi_0}^{M_0} \frac{dX}{X} |C_a(X, \xi_0) F_a(X, \xi_0)| = 2 \int_{M_0}^1 \frac{dX}{X} |C_a(X, \xi_0) F_a(X, \xi_0)| = \frac{1}{2}, \quad (3.34)$$

for  $a = q, g$ . Note that the factor of two reflects the symmetry of the integrand in the other half of the DGLAP region,  $X \in [-1, -\xi]$ , see Section 2.3.2. In other words, we perform the ‘Newton-Raphson’ method to find, by iteration, the value  $M = M_0$  satisfying

$$f(M_0) - \frac{1}{2} = 0. \quad (3.35)$$

However, as it is seen from Fig. 3.2 and 3.3, the quark term is practically negligible. Thus we can say that the exclusive  $J/\psi$  production indeed probes the gluons at  $x = X + \xi \simeq 2\xi$ .

### 3.6 Summary

We have shown that the  $J/\psi$  meson photoproduction process and ultraperipheral exclusive  $J/\psi$  production,  $pp \rightarrow p + J/\psi + p$ , at the LHC, can be consistently described in the collinear factorisation framework at NLO. The choice of the optimal scale  $\mu_F = \mu_0 = M_\psi/2$  effectively resums the large double logarithmic terms, i.e.  $(\alpha_s \ln \mu_F^2 \ln(1/\xi))^n$ , which, together with the  $Q_0$  subtraction (needed to avoid double counting between the NLO

coefficient function and the DGLAP input PDFs), leads to a largely improved scale stability of the theoretical prediction. In other words, this framework overcomes the extremely large scale uncertainties found in the existing NLO predictions [18, 102, 103] of diffractive  $J/\psi$  photoproduction in the collinear factorisation approach. It is not surprising that at these low scales the power correction arising from the  $Q_0$  subtraction is crucial. Another power correction coming from absorptive effects should reveal itself as the saturation of the gluon density. At the moment this is not noticeable; for small  $x$  the data appear to be compatible with the gluon PDF parametrisation  $xg \propto x^{-\lambda}$ .

Huge uncertainties in the low  $x$  gluon PDF found in the existing global PDF analyses reflect the fact that no corresponding low  $x$  data were included in the fitting procedure. The current cross section errors shown within an individual PDF set (Fig. 3.9) together with the discrepancy of the predictions between the sets (Fig. 3.5), contrasted with the data quality and the relative stability of our theoretical predictions, provides support for our claim that the exclusive  $J/\psi$  data are in a unique position to provide constraints down to unprecedented values of  $x$  in a fully-fledged global fit analysis. Using the proposed approach, the good accuracy of the exclusive  $J/\psi$  cross section presented by LHCb will allow the determination of the NLO gluon PDF down to  $x \sim 3 \times 10^{-6}$ , and the HERA data will improve the determination of the gluon for  $10^{-4} \lesssim x \lesssim 10^{-3}$ .

## Chapter 4

# A low $x$ determination of the gluon PDF via exclusive $J/\psi$ production

The low  $x$  behaviour of the gluon density  $xg(x, \mu^2)$  at scale  $\mu^2 = 2.4 \text{ GeV}^2$  is determined using exclusive  $J/\psi$  production data from HERA and LHCb within the framework of collinear factorisation at NLO. It is shown that in the interval  $3 \times 10^{-6} < x < 10^{-3}$  the gluon distribution function grows as  $xg(x, \mu^2) \propto x^{-\lambda}$  with  $\lambda = 0.135 \pm 0.006$ . The impact this experimental data will have for the global PDF analyses in this low  $x$  domain is quantified. No indication in favour of parton density saturation is observed.

### 4.1 Introduction

In the previous chapter, we showed that the stability of the perturbative predictions at the amplitude level allowed one to sensibly obtain results at the cross section level, producing a sound description of the HERA data on diffractive  $J/\psi$  photoproduction [126, 127, 128, 129] with energies corresponding to  $x > 10^{-3}$  and affirming cross section stability in this regime and indeed for the large range of  $W$  considered. Despite the central NLO global gluon for all three parton sets decreasing with smaller  $x$  in the interval  $10^{-3} < x < 10^{-2}$ , see Fig. 2.1, once convolved with the  $Q_0$ -subtracted and double-log resummed NLO coefficient function, produced a  $W$  dependence that collectively gave rise to a monotonically increasing cross section that well described the exclusive data in this regime (see Fig. 3.5). The individual global gluon errors propagated through to the  $J/\psi$  cross section for  $x < 10^{-3}$  were shown to be comparable to the spread in the current low  $x$  central cross section predictions based

on the global gluons from the three sets, but much greater than the uncertainties on the experimental data points and the scale dependence of the theoretical result. In turn, this quality and accuracy of the data sets at small  $x$  as well as the reliability and dependability of the collinear factorisation prediction, allows one to seriously consider the implications of their inclusion into the global analyses that constrain the PDFs. In this chapter, having demonstrated the efficiency of our method, we will extract the behaviour of the NLO gluon in the low  $x$  region ( $x < 10^{-3}$ ) from the exclusive  $J/\psi$  LHCb data [47, 48] (as well as HERA photoproduction data that lie in this region).

As was shown in Figs. 3.2 and 3.3, after the  $k_t < Q_0$  subtraction, the quark contribution to the exclusive  $J/\psi$  production is negligibly small in this  $x$  region. Thus we determine just the gluon PDF and use the quark PDF from the existing global fits. The evolution of the gluon PDF and the singlet quark PDF is intertwined, so to treat them differently is, strictly speaking, not fully consistent but permissible at this level.

Of course, at the moment, global PDF analyses are performed to NNLO accuracy. However, as a first step, we start fitting the  $J/\psi$  data at NLO. In the future this approach can be extended to NNLO.<sup>1</sup>

This chapter is organised as follows. In Section 4.2 we describe the ansatz that we will use to parametrise the NLO gluon PDF in the collinear factorisation scheme in the low  $x$  domain,  $x < 0.001$ . In Section 4.3, after a brief comparison of the LO and NLO approaches, we describe how we determine the low  $x$  gluon directly from the data. In Section 4.4, we compare the results we find for the low  $x$  gluon with those obtained by reweighting the NNPDF gluon using the  $D$ -meson LHCb data. Finally, in Section 4.5, we provide a reweighting of the NNPDF3.0 gluon via the exclusive  $J/\psi$  data and compare and contrast this with the gluon obtained from the above alternative approaches. Our conclusions are briefly summarised in Section 4.6.

## 4.2 Ansatz for the low $x$ gluon

It was demonstrated in Chapter 3 that the diffractive  $J/\psi$  cross section is driven by the Generalised Parton Distribution,  $\text{GPD}(X + \xi, X - \xi)$ , of the gluon with  $X \simeq \xi$ , see Fig. 3.1. That is, to describe the LHCb data, we effectively need the gluon in the region of low  $x \simeq X + \xi$  only. So, it is sufficient to parametrise the gluon in the region  $x < 10^{-3}$ . On

---

<sup>1</sup>This would require knowledge of the 2-loop hard scattering coefficient function and extension of NRQCD to NNLO.

the other hand, the Shuvaev transform, that relates the GPD to the conventional collinear gluon PDF, includes an integral over the whole  $x < 1$  interval. Moreover, the transform was derived assuming that the gluon had a smooth analytical behaviour with the property that  $g(x) \rightarrow 0$  as  $x \rightarrow 1$ . In order to satisfy these requirements we choose the following ansatz for the conventional gluon PDF,

$$xg(x, \mu_0^2) = C xg^{\text{global}}(x, \mu_0^2) + (1 - C) xg^{\text{new}}(x, \mu_0^2) \quad (4.1)$$

$$\text{with } C = \frac{x^2}{x^2 + x_0^2}, \quad (4.2)$$

where  $xg^{\text{global}}$  is the value of the gluon PDF obtained in a global PDF analysis. The simplest low  $x$  form for the gluon would be the power ansatz

$$xg^{\text{new}}(x, \mu_0^2) = nN_0 (1 - x) x^{-\lambda}, \quad (4.3)$$

where the normalisation factor  $N_0$  is chosen so that for  $n = 1$  the gluon PDF has the matching at  $x = x_0$ ,

$$x_0 g^{\text{new}}(x_0, \mu_0^2) = x_0 g^{\text{global}}(x_0, \mu_0^2). \quad (4.4)$$

The parameters to be fitted are denoted  $n$  and  $\lambda$ . Here,  $n$  is a normalisation and the power growth of the gluon PDF is governed by  $\lambda$ . The factor  $n$  in (4.3) is close to 1. It allows the possibility of matching to a global gluon whose normalisation differs from  $N_0$  but still lies within the global gluon error band at  $x = x_0$ . The factor  $(1 - x)$  in (4.3) provides the vanishing  $xg \rightarrow 0$  as  $x \rightarrow 1$ . This factor was added to satisfy the formal conditions for the validity of the Shuvaev transform, allowing for the elimination of a crucial surface term, see Section 2.3.3. Practically, the results do not depend on the behaviour of the gluon at relatively large  $x$ . The corresponding effects are not visible in our Figs. 4.2, 4.3, 4.5, see later. Note that due to the smooth form of  $C$  in (4.2) the complete distribution (4.1) does not violate analyticity even for  $n \neq 1$ .

Alternatively, in order to compare our present collinear determination of  $xg^{\text{new}}$  with an earlier determination of the low  $x$  gluon obtained in the  $k_t$  factorisation approach [125], we also use the DLA-inspired ansatz

$$xg^{\text{new}}(x, \mu_0^2) = nN_0 (1 - x) x^{-a} \left( \frac{\mu_0^2}{q_0^2} \right)^{-0.2} \exp \left[ \sqrt{16(N_c/\beta_0) \ln(1/x) \ln G} \right] \quad (4.5)$$



$$\text{with } G = \frac{\ln(\mu_0^2/\Lambda_{\text{QCD}}^2)}{\ln(q_0^2/\Lambda_{\text{QCD}}^2)}, \quad (4.6)$$

where the parameter  $a$  now plays the role of  $\lambda$ . Here, with three light quarks ( $N_f = 3$ ) and  $N_c = 3$  we have  $\beta_0 = 9$ . We take  $\Lambda_{\text{QCD}} = 200 \text{ MeV}$  and  $q_0^2 = 1 \text{ GeV}^2$ , as in [125], with  $\mu_0^2 = 2.4 \text{ GeV}^2$  fixed. The exponent in eqn. (4.5) resums, to all orders in  $m$ , the double logarithmic terms  $(\alpha_s \ln(1/x) \ln \mu^2)^m$  and hence we find that, to good accuracy, we reproduce the NLO DGLAP low  $x$  evolution in the interval of  $Q^2$  from 2 to about 30  $\text{GeV}^2$ . Therefore this parametrisation can be used to describe  $\Upsilon$  photoproduction data as well. In this way, the construction of eqn. (4.5) provides a reasonable deviation from the pure power behaviour of eqn. (4.3) and allows us to study if the low  $x$  data prefer an input distribution that deviates from a pure power exponent.

In what follows, by virtue of the heavily peaked diffractive  $J/\psi$  cross section at  $X = \xi$ , we construct the input GPDs via the result in eqn. (2.45) derived at the end of Section 2.3.3. When it comes to using these ansatze in a fitting procedure, the employment of these simpler one dimensional integrations will make the procedure less time-consuming and less computationally straining, while introducing a negligible error [87].

### 4.3 Determination of the low $x$ gluon from $J/\psi$ data

Here, we show the results of our fits to  $J/\psi$  photoproduction data for  $x < 10^{-3}$ , using an ansatz for the gluon PDF as described in eqns. (4.1)–(4.4). In the following, we refer to this as a ‘power fit’ to the data. The matching is made at  $x_0 = 10^{-3}$  using the gluon PDF from three NLO parton global analyses, NNPDF3.0 [38], MMHT14 [40] and CT14 [42]. Due to the small contribution of the quark sector at NLO to the  $J/\psi$  cross section, we do not attempt to fit the quark PDFs but only the gluon PDF around its input scale. The quark PDFs obtained in the global NLO analyses are therefore used for all  $x$ .

#### 4.3.1 Description of the $J/\psi$ data

To set the scene, we first use eqns. (3.1, 3.19, 3.33) at LO and NLO to generate and compare cross section predictions using the existing LO and NLO partons from [38, 40, 42], respectively, for the  $x$ -range where we have used exclusive  $J/\psi$  data from H1, ZEUS and LHCb. In this way, we are able to quantify the scale dependence of the theoretical prediction as well as the size of the NLO result relative to the LO one. In Fig. 4.1, we show such

a comparison using CT14 partons [42]. Our choice of scales is explained in Section 2.5.2. The NLO scale variation is smaller than that at LO and a better description of the HERA data is obtained with the NLO result. The plot emphasises that the LO prediction is not sufficient and that in the region where the current PDFs are well constrained, it is still crucial to use the NLO description. We see that our NLO prediction at the ‘optimum’ scale choice agrees most favourably with the HERA data - this is non-trivial and need not have been the case but provides reassurance for our procedure.

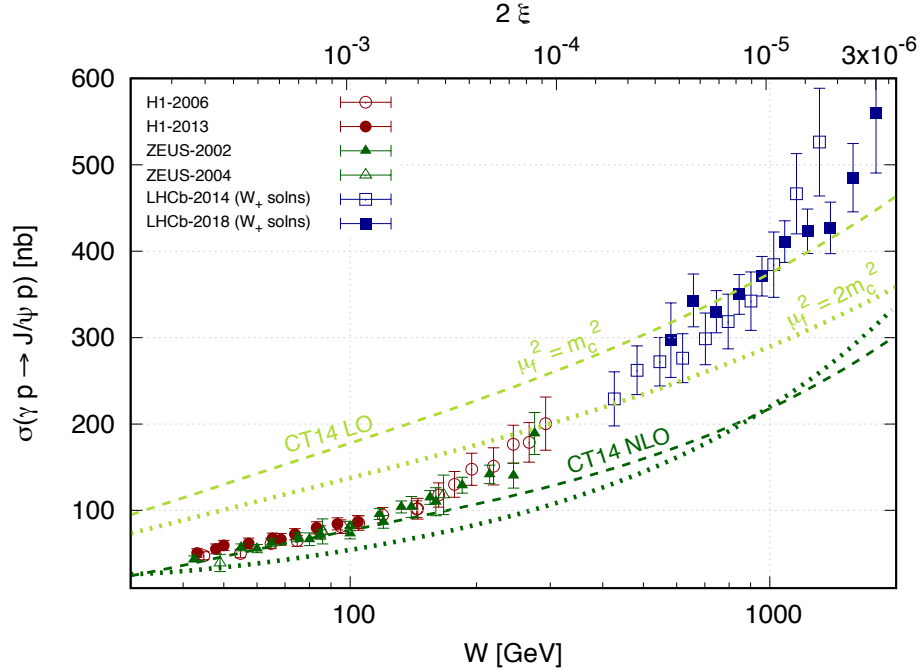


Figure 4.1: LO and NLO cross section predictions obtained using the central values of the existing global partons from [42]. Dashed (dotted) lines correspond to the scale choices  $\mu_f^2 = \mu_R^2 = m_c^2$  ( $\mu_f^2 = \mu_R^2 = 2m_c^2$ ) with  $\mu_F = Q_0 = m_c$  fixed.

We now determine the low- $x$  gluon by performing a two-parameter ( $\lambda$  and  $n$ , as defined in eq. (4.3)) fit of all the  $\sigma(\gamma p \rightarrow J/\psi + p)$  LHCb and HERA data with  $x < 0.001$  using, as input, NLO parton PDFs from [38, 40, 42]. The results are shown in Table 4.1 and Fig. 4.2.

	$\lambda$	$n$	$\chi^2_{\min}$	$\chi^2_{\min}/\text{d.o.f}$
NNPDF3.0	$0.136 \pm 0.006$	$0.966 \pm 0.024$	44.51	1.04
MMHT14	$0.136 \pm 0.006$	$1.082 \pm 0.027$	47.00	1.09
CT14	$0.132 \pm 0.006$	$0.946 \pm 0.024$	48.25	1.12

Table 4.1: The values of  $\lambda$  and  $n$  obtained from fits to the  $J/\psi$  data using three sets of global partons. The respective values of the total  $\chi^2_{\min}$  (and  $\chi^2_{\min}/\text{d.o.f}$ ) for 45 data points are also shown.

The construction of our  $\chi^2$  figure of merit is as follows,

$$\chi^2(\lambda, n) = \sum_{i,j=1}^{N_{\text{dat}}} (\sigma_i(\lambda, n) - m_i)(\text{cov}_{t_0}^{-1})_{ij}(\sigma_j(\lambda, n) - m_j), \quad (4.7)$$

where  $N_{\text{dat}}$  is the number of experimental data points,  $\sigma_i(\lambda, n)$  is the theoretical cross section prediction in energy bin  $i$  for a given  $\lambda$  and  $n$ , and  $m_i$  are the experimental measurements. Our definition of the input ‘ $t_0$ ’ prescribed covariance matrix, which gives the covariance between the measurements in energy bins  $i$  and  $j$ , is

$$(\text{cov}_{t_0})_{ij} = \left( \sum_{k=1}^{N_{\text{corr}}} \Delta\sigma_{i,k} \Delta\sigma_{j,k} + \delta_{ij} \Delta\sigma_{i,\text{uncorr}}^2 \right) m_i m_j + \left( \sum_{l=1}^{N_{\text{mult.}}} \Delta\sigma_{i,l} \Delta\sigma_{j,l} \right) \sigma_i^{(0)} \sigma_j^{(0)}, \quad (4.8)$$

where  $\Delta\sigma_{i,k}$  are the relative  $N_{\text{corr}}$  correlated sources of uncertainty,  $\Delta\sigma_{i,\text{uncorr}}$  are the uncorrelated sources of uncertainty (and therefore proportional to  $\delta_{ij}$ , the Kronecker delta) and  $\Delta\sigma_{i,l}$  are the relative  $N_{\text{mult.}}$  multiplicative (normalisation) sources of uncertainty. These last set of errors are organised in this way in order to avoid the d’Agostini bias [159, 160], which becomes important when systematic errors are multiplicative rather than additive. The  $\sigma_i^{(0)}$  are iteratively-refined quantities that are updated at each step in the fit procedure - at the zeroth iteration or initialisation step, they may, for example, presume the values of the experimental measurements. In this treatment of the normalisation uncertainties, we do not have to introduce additional shift parameters to counteract such a bias, as is commonly done instead in other approaches.

For the ZEUS 2002 and 2004 data sets [126, 127] we allow for a fully correlated 6.5% normalisation error. For the H1 2006 data set [128] we include a fully correlated 5% normalisation error while for the H1 2013 data set [129] we use the full covariance matrix

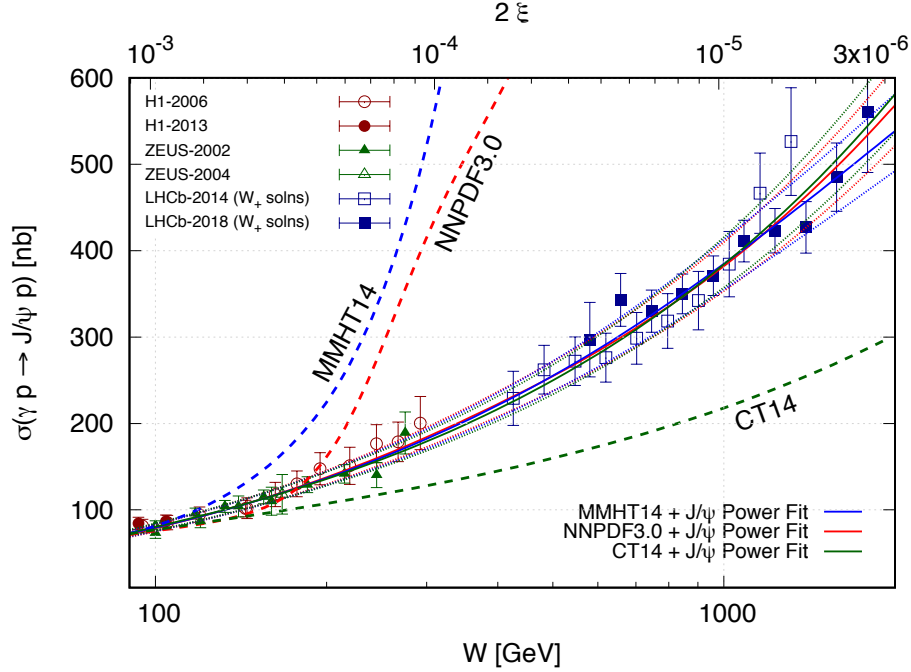


Figure 4.2: The description of the  $J/\psi$  photoproduction HERA [126, 127, 128, 129] and LHCb [47, 48] data based on using the central value of the global gluon PDF from the three global parton analyses [38, 40, 42] for  $x > 0.001$ . The solid red, blue and green lines show the central power fit predictions while the dotted lines show the  $\pm 1\sigma$  boundaries, using the errors of the parameters in Table 4.1. We also show by dashed lines the cross section predictions obtained using the current central values of the global gluons for all  $x$ .

as provided by H1. For the LHCb 2014 data [47] we allow for a fully correlated  $\sim 7\%$  normalisation error. Finally, for the LHCb 2018 data [48], we use the covariance matrices supplied by the collaboration as well as a fully correlated normalisation error of  $\sim 4\%$ . This error accounts for the uncertainties in the luminosity and branching fraction to dimuon determinations, correlated between bins.

The respective values of the  $\chi^2_{\min}$  statistic, the minimum value of our  $\chi^2$  function in the space of  $\lambda$  and  $n$ , were calculated accounting for the bin-to-bin correlated errors within each individual experimental data set as well as uncorrelated errors.<sup>2</sup> The covariance

<sup>2</sup>An earlier exploratory analysis was performed in which only the *diagonal* covariance matrix was used. Here, the resulting  $\chi^2_{\min}/\text{d.o.f} \sim 0.3 < 1$ , an artificially small  $\chi^2_{\min}$  and underestimation of this statistic as a result of the negligence of the correlations between the experimental data points.

matrix was constructed, and iterated, according to the ‘ $t_0$  prescription’ as outlined above, see [161] for more details. We use all HERA data points [126, 127, 128, 129] with  $W > 100$  GeV ( $x \lesssim 10^{-3}$ ) and all LHCb [47, 48] data points.

Below, in Table 4.2, we show a more detailed breakdown of contributions to our  $\chi^2$  statistic. Let LHCb-14 (LHCb-18) denote the LHCb data taken at  $\sqrt{s} = 7$  TeV ( $\sqrt{s} = 13$  TeV) and published in 2014 (2018) [47, 48]. For each global parton set, we find that  $\chi^2_{\min, \text{HERA}}/\text{d.o.f} < 1$  and  $\chi^2_{\min, \text{LHCb-14}}/\text{d.o.f} > 1$ , while  $\chi^2_{\min, \text{LHCb-18}}/\text{d.o.f} \sim 1$ . We have checked that the relatively larger value of the contribution to the chi-square due to the LHCb data taken at  $\sqrt{s} = 7$  TeV is the result of its last two data points at the highest  $W$ . These points favour a larger gluon slope, as is clear from Fig. 4.2. Removing their contribution from the chi-square construction gives then  $\chi^2_{\min, \text{LHCb-14}}/\text{d.o.f} \sim 1$ . However, we emphasise these points are nonetheless kept in our numerical analysis and are not treated as statistical outliers. The consistently small value of  $\chi^2_{\min, \text{HERA}}$  across all three global sets is attributed to an overestimation of the underlying statistical and systematic uncertainties in [126, 127, 128, 129]. The structure of our fit ansatz and interrelation of

	$\chi^2_{\min}$	$\chi^2_{\min, \text{HERA}}$	$\chi^2_{\min, \text{LHCb-14}}$	$\chi^2_{\min, \text{LHCb-18}}$
NNPDF3.0	44.51	8.10	26.18	10.23
MMHT14	47.00	8.12	30.63	8.26
CT14	48.25	8.42	27.20	12.63

Table 4.2: Individual  $\chi^2_{\min}$  contributions due to HERA ( $N_{\text{dat}} = 25$ ), LHCb-14 ( $N_{\text{dat}} = 10$ ) and LHCb-18 ( $N_{\text{dat}} = 10$ ) data for the three global parton sets.

the parameters, together with the monotonically increasing data, explain why the fitting procedure was readily able to find a global minimum. The locus of  $\{n, \lambda, \chi^2\}$  points maps out a tunnel-like surface in this space.

The description of the exclusive  $J/\psi$  cross section is shown in Fig. 4.2, while the gluons extracted from the  $J/\psi$  data at  $\mu^2 = 2.4$  GeV<sup>2</sup> and  $x < 0.001$  are shown in Fig. 4.3. The error bands are obtained by sampling over the two parameters within their individual  $1\sigma$  standard deviations, accounting for their correlation. The hatched green band in Fig. 4.3 in addition accounts for the uncertainty due to the choice of the global (NNPDF3.0, MMHT2014 or CT14) partons. The shaded blue band is the NNPDF3.0 global gluon PDF. The gluon at very small  $x$  shows no hint of the onset of saturation; the data are consistent with a rising power and a  $\chi^2_{\min}$  of the order of unity. Starting from

three different sets of global partons, we obtain practically the same low  $x$  gluons with the same quality ( $\chi^2_{\min}$ ) of the description. The typical errors are  $\pm 2.5\%$  for the normalisation and  $\pm 4\%$  for  $\lambda$ . The covariance matrix in the space of  $\lambda$  and  $n$  gives the variances and covariances of our fitted parameters due to the experimental error. Specifically, it is given by

$$C^{\text{cov}} = \frac{1}{2} \begin{pmatrix} \partial^2 \chi^2 / \partial \lambda^2 & \partial^2 \chi^2 / \partial \lambda \partial n \\ \partial^2 \chi^2 / \partial n \partial \lambda & \partial^2 \chi^2 / \partial n^2 \end{pmatrix}, \quad (4.9)$$

evaluated at the best fit values for  $\lambda$  and  $n$ . In the NNPDF3.0 fit, for example, we obtain the  $2 \times 2$  covariance matrix,

$$C^{\text{cov}}_{\text{NNPDF3.0}} = \begin{pmatrix} 3.29 \times 10^{-5} & -1.11 \times 10^{-4} \\ -1.11 \times 10^{-4} & 5.95 \times 10^{-4} \end{pmatrix}. \quad (4.10)$$

Here, the diagonal elements give the variances  $\sigma_{\lambda\lambda}^2$  and  $\sigma_{nn}^2$  of the fitted parameters and the off-diagonal elements are a measure of the correlation between them and give the covariance,  $\sigma_{\lambda n}$ , of  $\lambda$  and  $n$ . The negative sign is indicative of an anti-correlation. The square root of the matrix element  $C^{\text{cov}}_{11}$  ( $C^{\text{cov}}_{22}$ ) gives the  $1\sigma$  standard deviation error for  $\lambda$  ( $n$ ), given in Table 4.1.

We see from Fig. 4.2 that the simple two-parameter form of the gluon density provides an excellent description of the  $J/\psi$  data in the fitted  $x < 10^{-3}$  region, irrespective of which global parton set is used. In fact, the three descriptions only visibly differ for  $x < 10^{-5}$ . Note that the observed hierarchy of central cross section predictions at  $x \sim 3 \times 10^{-6}$  differs from that expected given the power behaviours in Table 4.1. That is to say, the value of the central cross section prediction at  $2\xi = 3 \times 10^{-6}$  using CT14 partons is largest yet the best fit value of its gluon slope is smallest. We have checked that this is due to the small  $x$  and small scale quark behaviour of the global sets.

Figure 4.2 also shows the cross section predictions obtained using the central values of the gluon from the global parton sets extrapolated into the low  $x$  region. Clearly here the global analyses have no predictive power and in each case they have huge uncertainty bands (shown in Fig. 4.3 for NNPDF3.0 only) which cover the (unfitted)  $J/\psi$  data. The value of including the  $J/\psi$  data is apparent.

In the left hand side of Fig. 4.4 we compare the uncertainties of the gluon densities given at  $x = 0.001$  and  $\mu^2 = 2.4 \text{ GeV}^2$  by the global analyses, while in the right hand side we show the values that are obtained after fitting the  $J/\psi$  data. The  $J/\psi$  data are seen to

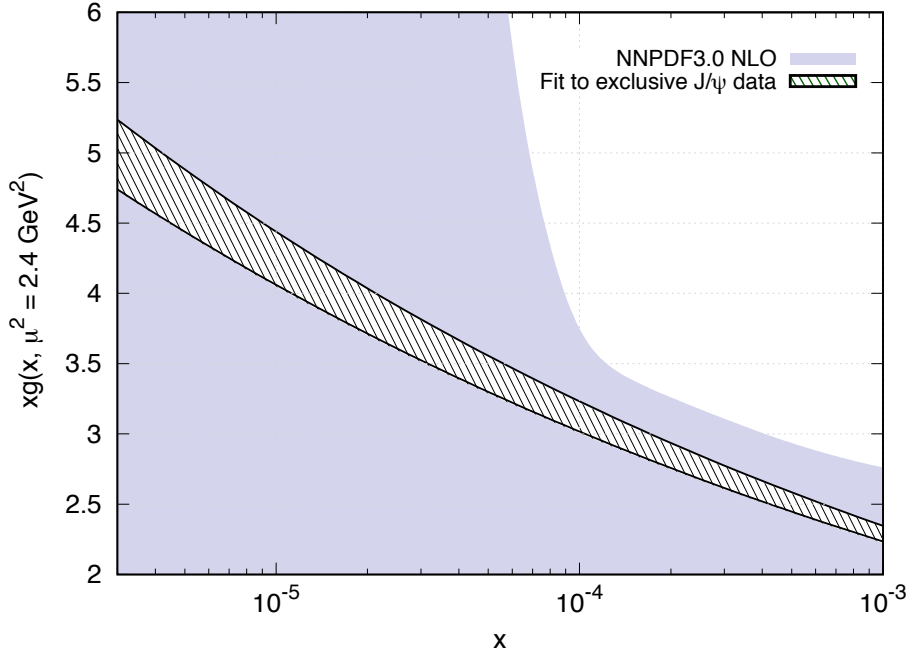


Figure 4.3: The cross-hatched region shows the range of behaviour of the low  $x$  NLO gluon determined by fitting to exclusive  $J/\psi$  data using ansatz eqn. (4.3) with  $xg^{\text{global}}$  taken from NNPDF3.0 [38], MMHT14 [40] or CT14 [42] parton sets. The shaded blue area is the NNPDF3.0 global gluon PDF error band.

greatly improve the knowledge of the gluon in the low  $x$  interval  $3 \times 10^{-6} < x < 10^{-3}$ . In particular, we find at  $x_0 = 0.001$  that, by averaging the results from the three sets,

$$x_0 g(x_0, \mu^2 = 2.4 \text{ GeV}^2) = 2.28 \pm 0.06, \quad (4.11)$$

where the central value is determined from eqns. (4.1)-(4.3) and the  $1\sigma$  standard deviation from

$$\Delta xg(x) = N_0 (1-x) x^{-\lambda} \sqrt{\sigma_{nn}^2 + n^2 \ln^2 \left( \frac{x_0}{x} \right) \sigma_{\lambda\lambda}^2 + 2n \ln \left( \frac{x_0}{x} \right) \sigma_{\lambda n}} \quad (4.12)$$

evaluated at  $x = x_0 = 10^{-3}$ . This follows from the sum in quadrature of correlated

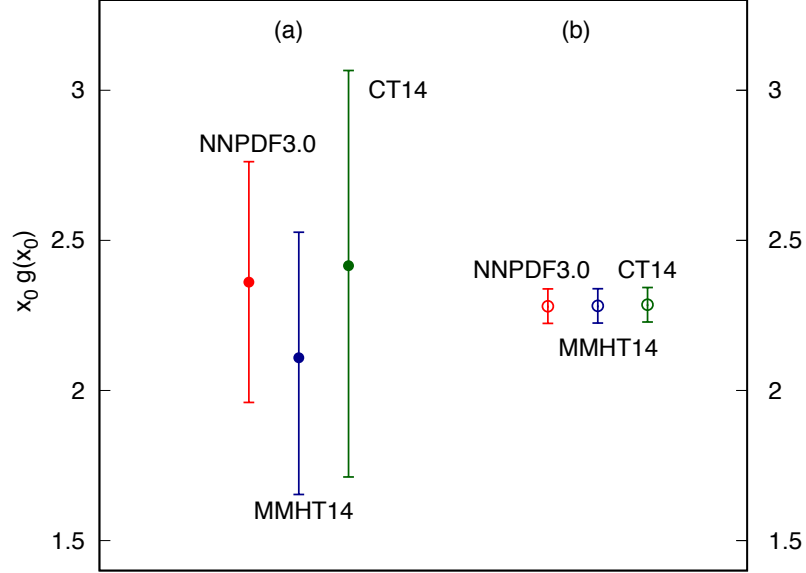


Figure 4.4: (a) The global gluon PDF,  $xg(x, \mu^2)$ , at the matching point  $x = 0.001$  and  $\mu^2 = 2.4 \text{ GeV}^2$ , (b) the global gluon PDF,  $xg(x, \mu^2)$ , at the matching point  $x = 0.001$  and  $\mu^2 = 2.4 \text{ GeV}^2$  after fitting to HERA+LHCb exclusive  $J/\psi$  data. Note that the errors shown on the right hand side are those obtained by propagating the  $1\sigma$  experimental data errors to our result, but do not account for theoretical uncertainties.

variables,

$$\delta xg(x) = \sqrt{\sum_{ij} \frac{\partial xg}{\partial a_i} C_{ij}^{\text{cov}} \frac{\partial xg}{\partial a_j}}, \quad (4.13)$$

with  $\{a_i\} = \{\lambda, n\}$ .

### 4.3.2 The alternative double-log parametrisation

While the simple two parameter ansatz in eqn. (4.3) leads to a very good description of the  $J/\psi$  data, it is still informative to repeat the procedure using the double-log ansatz in eqn. (4.5). Recall that a similar form was used in [125]. In the low  $x$  region, the expected  $x$  dependence of the gluon density follows a pure power law but evolution in the scale quickly modifies this behaviour, with a larger effective  $\lambda$  at larger  $\mu^2$ . For sufficiently low  $x$  and large  $\mu^2$ , the gluon density is well approximated by an asymptotic form  $xg \sim \sqrt{\alpha_s \ln(1/x) \ln(\mu^2)}$ . This double-log enhancement is contained (and resummed) in



eqn. (4.5). The fit result obtained using the NNPDF3.0 NLO parton set is

$$a = -0.046 \pm 0.006, \quad n = 0.979 \pm 0.025, \quad \chi^2_{\min}/\text{d.o.f} = 1.05.$$

The description and the behaviour of the low  $x$  gluon are very similar to that obtained using eqn. (4.3). We find that the fit using the double log parametrisation gives the central value  $x_0 g(x_0, \mu^2 = 2.4 \text{ GeV}^2) = 2.31$  in agreement with eqn. (4.11).

Note that the double-log parametrisation gives a result close to that obtained in the  $k_t$ -factorisation approach [125]. However now, accounting for the complete set of NLO corrections, we find that the gluon growth with energy ( $1/x$ ) is less steep than that obtained in [125]. Instead of  $a = -0.10$  we now have  $a \sim -0.05$ . The data used in [125] have been replaced by the data in [48] that is used here, but this is not accountable for the difference in  $a$ . This points towards genuine differences between the two factorisation schemes.

### 4.3.3 Is there evidence of saturation from exclusive $J/\psi$ data?

High energy exclusive  $J/\psi$  production was recently described in [162] based on a BFKL approach. The authors claim that ‘there are strong hints for the presence of the saturation effects in exclusive photo-production of  $J/\psi$  at small  $x$ ’. We have to emphasise that actually the authors of [162] refer to *absorptive corrections* rather than *saturation*. Indeed, saturation means that the gluon density tends to a constant value,  $xg(x, \mu^2) \rightarrow \text{const}$  as  $x \rightarrow 0$  and at a fixed scale  $\mu$  [163]. That is, the power  $\lambda$  in (4.3) behaves as  $\lambda \rightarrow 0$ . A first hint of saturation would be to observe that the power  $\lambda$  (measured in some small- $x$  interval) starts to decrease with decreasing  $x$ . The data, as shown in Fig. 3, do not indicate such behaviour.

What is actually shown in [162] is that the LO BFKL intercept,  $\alpha_{\text{BFKL}} = 1 + \omega_0 = 1 + \lambda$  is too large to describe the high energy  $J/\psi$  data and that absorptive corrections (which are included into the non-linear BK [164, 165] equation) are needed to tame the growth of the gluon density (4.3), that is to decrease the value of  $\lambda$ .

It is well known that the LO BFKL intercept is too large [166, 167, 168]. It becomes smaller in the next-to-leading-log- $1/x$  (NLL $_x$ A) approximation. Indeed, it is seen from [162] (the short dashed green curve of their Fig. 1) that the HSS gluons [169, 170], based on the NLO BFKL *linear* equation, are in agreement with the exclusive  $J/\psi$  data. Moreover, the approach of [162] does not use a stable NLO prediction (which we have within the framework of collinear factorisation via the important  $Q_0$  subtraction) and contains some-

what arbitrary  $K$  factors. From our viewpoint, this makes it impossible to make conclusive statements about the non-linear corrections. The authors of [171] concur with our analysis that we presented in [172] and affirmed that the exclusive data are not indicative of gluon saturation at current centre-of-mass energies.

Therefore, the growth of the gluon density with a smaller but non-zero  $\lambda$  is not evidence for ‘saturation’. At the moment, no hint of saturation is observed in exclusive  $J/\psi$  data at the scale  $\mu^2 = 2.4 \text{ GeV}^2$  and  $x$  down to  $10^{-5}$ .

#### 4.3.4 Note on higher-twist contributions

Absorptive corrections, which provide the saturation at some low value of  $x$ , are described by higher-twist operators. Formally, within the collinear factorisation approach, we do not know the value of these higher-twist terms. They have their own evolution and input conditions/functions that must be fitted from experiment. In other words, only experiment can give us the values of the higher-twist operator contributions. Nevertheless, let us estimate the possible role of the higher-twist absorptive effects in the  $J/\psi$  photoproduction amplitude.

The relative size of the contribution of the next twist absorptive correction (in our  $\mu^2$  region of interest) is driven by the parameter (see [163])

$$c = \alpha_s \frac{xg(x)}{R^2 \mu_0^2}, \quad (4.14)$$

where  $R$  can be as large as the proton radius ( $R \sim 0.84 \text{ fm} = 4.2 \text{ GeV}^{-1}$ ). Eqn. (4.14) gives an estimate of the relative percentage effect of absorptive corrections and is the factor appearing in the Gribov-Levin-Ryskin (GLR) equation [163]. This equation provides non-linear negative terms through the computation of so-called ‘fan’ diagrams in pQCD that tame the BFKL evolution. This was later improved upon in the BK equation [164, 165]. It may be assumed that the low  $x$  partons group together in so-called ‘hot-spots’, with a radius smaller than that of the proton. If we consider the value of  $R$  as the ‘hot spot’ radius, then we have to take a smaller gluon density,  $xg$ , corresponding to only one hot spot. With  $\alpha_s = 1/3$  and  $\mu_0 = M_\psi/2$  we obtain  $c = 0.008 xg \sim 0.04$  for our gluon density  $xg \leq 5$ . A relatively large value of  $xg = 5$  includes/accounts for the power growth of gluon densities at low  $x$ . However, actually this result is overestimated. Indeed, the cross section of an additional high energy (gluon) interaction is proportional to the  $c$ -quark

separation  $\langle r^2 \rangle$ . This means that we have to replace in eqn. (4.14) the factor  $1/(R^2\mu_0^2)$  by the ratio  $\langle r^2 \rangle/R^2$ . At the beginning of the photoproduction process, the photon produces a *point-like*  $c\bar{c}$  pair. The lifetime of this pair is about  $2E_\gamma/M_\psi^2$ , where  $E_\gamma$  is the energy of the photon. Accounting in addition for the Lorentz factor of the  $J/\psi$ , the quarks have their ‘own’ time  $\tau \sim 2/M_\psi = 1/\mu_0$  to separate from each other. However, the  $J/\psi$  meson is a non-relativistic system and the heavy quark velocity  $\langle v^2 \rangle \propto \alpha_s$  is small. That is we expect the higher-twist contribution to be suppressed by an additional power of  $\alpha_s$  and, correspondingly, actually  $c < 0.015$ .<sup>3</sup> Accounting for the velocity  $\langle v^2 \rangle \propto \alpha_s$  can be considered as a NNLO contribution.

Therefore, this semi-quantitative order of magnitude estimate anticipates, in the region relevant to our fit ( $\mu^2 = 2.4 \text{ GeV}^2$  and  $x = 3 \times 10^{-6} - 10^{-3}$ ) a percent level enhancement due to higher-twist absorptive terms. In our approach, all physics below  $Q_0$  (i.e. at scales  $\mu^2 < 2.4 \text{ GeV}^2$ ) is considered as a phenomenological input distribution formed mainly by non-perturbative interactions inside the proton. We never go below  $Q_0$ , subtracting all the contributions with  $k_t < Q_0$ . One therefore cannot use our higher-twist estimate (of perturbative origin) at lower scales. In principle, there may be other sources of higher-twist contributions which are not known and that must be extracted from experiment (e.g. in DIS there is the so-called Vector Meson Dominance (VMD) contribution [173]). However, there are no reasons for these other contributions to be large or to grow as  $x \rightarrow 0$ .

## 4.4 Comparison with low $x$ gluons from $D$ -meson data

As mentioned in the introduction of Chapter 3, it is also possible to determine the low  $x$  gluon density from the data for various modes of inclusive open charm production of  $D$ -mesons and their excited states. In this section, we provide a comparison of the results obtained from the data for inclusive  $D$ -meson production, already appearing in the literature, and that for exclusive  $J/\psi$  production, considered in this work.

Inclusive  $D$ -meson production data via  $pp$  collisions at the LHC are available at centre of mass energies 5, 7 and 13 TeV [114, 115, 116]. The kinematics of the different modes

---

<sup>3</sup>This correction factor is susceptible to modification by an overall numerical factor which could inflate our estimate of the relative size of the higher-twist contribution. If one takes into consideration the colour factor calculated assuming that the low  $x$  gluon is emitted by the valence quark in the proton, then there is an additional factor of  $81/16$  which enhances our estimate to  $\sim 6.5\%$ . However, we stress that our intention here was solely to show that the higher-twist contribution may be relatively small and that, together with the additional factor of  $\alpha_s$ , all the parametric dependence is included in eqn. (4.14).

of production of the  $D$ -mesons allow for a coverage down to  $x \sim \text{few} \times 10^{-6}$ . In [122] the authors studied the impact these data for  $\{D^0, D^+, D_s^+\}$  final states would have on the small  $x$  NLO gluon within the NNPDF3.0 global analysis through a Bayesian reweighting. While the corresponding NLO calculation for  $D$ -meson production suffers from large theory uncertainties attributed to the dependence on the factorisation scale and large higher order corrections, construction of ratios of the double-differential cross section in rapidity and transverse momentum bins provides a means to combat this residual scale dependence (through cancellation of uncertainties between the numerator and denominator of the ratio) and thereby quantitatively assess the impact the data would have in the PDF fit. Of course, the overall normalisation is forfeited but the sensitivity to the  $x$  dependence of the gluon is maintained in this approach. In Fig. 4.5 we show the NNPDF3.0 global gluon reweighted using the ratios of inclusive  $D$ -meson cross section data at  $\sqrt{s} = 5, 7, 13$  TeV and evolved down to the  $J/\psi$  scale  $\mu^2 = 2.4 \text{ GeV}^2$  (the lower grey band). Note that this band is entirely contained within the blue band for the NNPDF3.0 global gluon. As shown and explained in [122], the data favour a decreasing gluon at the lowest value of  $x$  which the  $D$ -meson data may probe.

This is to be contrasted with the same analysis performed for NNPDF3.1 supplemented with the inclusive  $D$ -meson data but now together with small  $x$  resummation [174].<sup>4</sup> In this case, the reweighting favours a much higher gluon, as shown by the upper grey band in Fig. 4.5. It is known that including the BFKL (small  $x$ ) resummation (*without a  $k_t < Q_0$  subtraction*) the low scale gluons extrapolated into the low  $x < 0.001$  region are too large and grow too fast (see e.g. [175]). That is, as shown in Fig. 4.6, the cross section prediction using NNPDF3.1 together with the resummation strongly overshoots the exclusive  $J/\psi$  data while the prediction using NNPDF3.0 is too low.

The comparison of these two (based on NNPDF3.0 and on NNPDF3.1) bands, together with the inconsistencies of  $D$ -meson data mentioned in [123, 124], demonstrates that the quality and accuracy of  $D$ -meson data are not sufficient to get an unambiguous result and to obtain accurate low  $x$  gluons.

---

<sup>4</sup>I would like to thank Valerio Bertone for private communications and for providing us with these constraints in LHAPDF6 format.

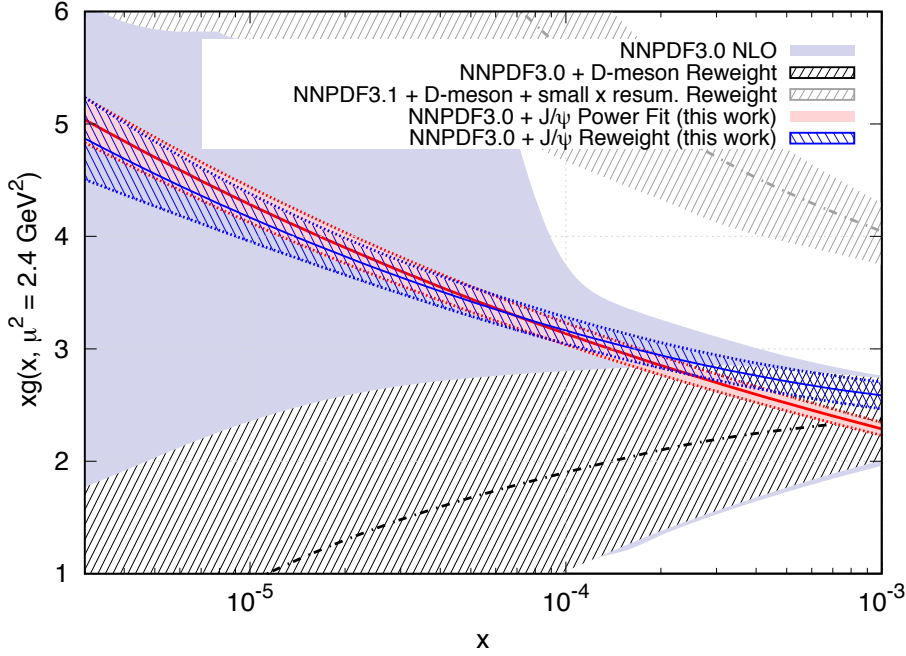


Figure 4.5: Comparison of the low  $x$  behaviour of the NLO gluon density  $xg(x, \mu^2)$  at  $\mu^2 = 2.4 \text{ GeV}^2$  obtained from exclusive  $J/\psi$  data and from inclusive  $D$ -meson data, see text for details.

#### 4.5 Reweighting of NNP3.0 gluon via exclusive $J/\psi$ data

In this work, we too have performed a Bayesian reweighting of the NNP3.0 gluon but this time constrained by the exclusive  $J/\psi$  cross section. As discussed above, these data are in a position to be readily included in a collinear NLO global analysis due to alleviation of the large scale dependence through implementation of a  $Q_0$  cut and resummation of a class of large logarithms.

The Bayesian reweighting approach [176] takes PDF probability distributions as input and applies weights  $w_k$  to these distributions, in accordance with their description of the new data set. A refined, updated probability distribution is then outputted in this procedure. Here, the PDF probability distributions correspond to finite ensembles of  $N_{\text{rep}}$  parton distribution Monte-Carlo replicas,  $f_k$ . Observables  $O$  dependent on these PDF

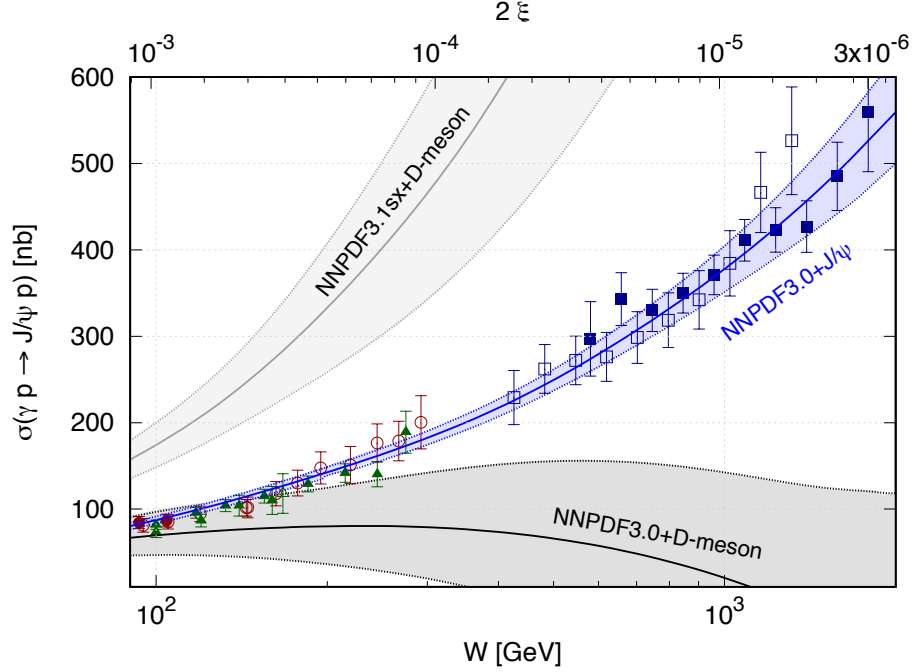


Figure 4.6: The lower and upper bands are, respectively, the cross section predictions obtained using NNPDF3.0 and NNPDF3.1 global partons constrained by the  $D$ -meson LHCb data [122, 174]. The latter includes low  $x$  resummation effects. The shaded blue band is the cross section prediction obtained based on our reweighting of the NNPDF3.0 NLO global gluon via the exclusive  $J/\psi$  data. The experimental data points are presented as in Fig. 4.2.

distributions are obtained via the expectation values,

$$\langle O \rangle = \frac{1}{N_{\text{rep}}} \sum_{k=1}^{N_{\text{rep}}} O(f_k), \quad (4.15)$$

which are updated to

$$\langle O^{\text{new}} \rangle = \frac{1}{N_{\text{rep}}} \sum_{k=1}^{N_{\text{rep}}} w_k O(f_k), \quad (4.16)$$

in the reweighting prescription. In the literature, two different functional forms have appeared for the  $w_k$ , the so-called  $w_k^{\text{GK}}$  weights proposed by the authors in [176] and those advocated by the NNPDF collaboration,  $w_k^{\text{NNPDF}}$ , see [177]. The latter have been shown to work consistently with the NNPDF fit methodology and are used in this work. The utility

of this procedure is the ability to assess quantitatively the impact a new data constraint has on a PDF set, without having to redo a new fit. Another procedure via a Hessian matrix profiling has also been discussed in the literature, see [178]. Both techniques are fully implemented in the **xFitter** framework [179]. An update of the quark and gluon PDFs from early LHCb electroweak data based on the Hessian method is given in e.g. [180].

We perform the reweighting using the  $J/\psi$  data in the region  $x < 0.01$  for the NNPDF3.0 NLO set with  $N_{\text{rep}} = 1000$  replicas. Since the central NNPDF3.0 low  $x$  gluons are too large to describe the  $J/\psi$  data (see Fig. 4.2), the Shannon entropy (or effective number of contributing replicas)<sup>5</sup>,

$$N_{\text{eff}} = \exp \left( \frac{1}{N_{\text{rep}}} \sum_{k=1}^{N_{\text{rep}}} w_k \ln(N_{\text{rep}}/w_k) \right) \approx 40 \ll N_{\text{rep}}. \quad (4.17)$$

Therefore, the reweighting approach is not fully adequate. Still, the gluon obtained as a result of the reweighting procedure, the hatched blue band in Fig. 4.5, is rather close to that obtained within the fit using ansatz (4.3) (the red band). Since the NNPDF input distribution is mainly driven by other data at larger  $x \sim 0.01$  (where the effective value of  $\lambda$  is noticeably smaller), the reweighted NNPDF3.0 gluon has a slightly less steep growth at  $x < 0.001$  in comparison with that coming from the power fit (4.3). Correspondingly, the  $J/\psi$  reweighted gluon density overshoots our (power fit) result at  $x = x_0 = 0.001$  while undershooting it at the smallest  $x = 3 \times 10^{-6}$ .<sup>6</sup> On the other hand, our  $J/\psi$  reweighting result demonstrates that the additional  $J/\psi$  data add important or new information, which is to be expected as there were no data in the previous PDF analyses in this domain. The small value of the Shannon entropy means it would be desirable for the reweighting procedure to be backed up by a full new global fit. This quantifies the statements in the last chapter about the utility of the  $J/\psi$  data. The closeness of our reweighted gluon with the

<sup>5</sup>The same analysis was also performed with  $N_{\text{rep}} = 100$ , but here  $N_{\text{eff}} = \mathcal{O}(1)$  and the low- $x$  region was not sampled densely enough. This resulted in the inability to quantify the error in this region in a statistically meaningful manner.

<sup>6</sup>The slightly larger normalisation, at  $x = 10^{-3}$ , of the prediction based on the reweighting procedure is due to the greater number of data points that are fitted in this region in the global analysis. For smaller  $x$ , where the only constraining power comes from the exclusive  $J/\psi$  data in both the reweighting and power fit approaches, the predictions are in better agreement. The power fit gluon in Fig. 4.3, however, exhibits a steeper slope than our reweighted gluon at  $x = 10^{-3}$ , evident in the comparison plot of Fig. 4.5. The effective lambda of the former,  $\lambda_{\text{eff}} > 0$ , is therefore more enhanced by the Shuvaev transform than the latter, with  $\lambda_{\text{eff}} \approx 0$ . This provides for overlapping bands in the cross section predictions at  $x \approx 10^{-3}$  based on both power and reweighted gluons.

fitted gluons, using particular ansatze, that we have obtained, provides further support for this claim. Considering all data points with  $W > 100$  GeV, the effective  $\chi^2_{\min}/N_{\text{dat}} \sim 1.07$  for the reweighted central cross section prediction. This compares well with the same statistic computed for the NNPDF3.0 power fit, where  $\chi^2_{\min}/N_{\text{dat}} = 0.99$ . The deviation of 8% is attributed to the differing behaviours of the two predictions around  $x = 10^{-3}$ , explained above. In principle, one could repeat the analysis using MMHT14 and CT14 parton sets. This would allow us to probe the relevance of the different input distributions of the three sets. As the MMHT and CT collaborations provide their error sets in Hessian eigenvector format by default, the first step in the reweighting procedure when using these sets would be to convert the eigenvector error representation to a Monte-Carlo replica probability distribution. See also [181] for an alternate approach.

As a main result of this work, exploiting the  $J/\psi$  exclusive data we reach a much better accuracy. Now, down to  $x = 3 \times 10^{-6}$ , the low scale gluons (near the input  $Q_0$  value) are known to better than 5-7% uncertainty.

An interesting observation is that in the low  $x < 0.001$  region, the low scale fitted gluons start to grow (with  $1/x$ ) even faster (as  $xg(x) \propto x^{-\lambda}$  with  $\lambda \simeq 0.14$ ) than the low scale global gluons do in the interval  $0.001 < x < 0.01$ . We are able to fit a low  $x$  gluon power ansatz for the large range  $x < 0.001$  with a *single* slope but find that we cannot extend this same description to  $0.001 < x < 0.01$ . Attempting to do so results in a worsened fit and a much smaller  $\lambda$ . Indeed, this reflects the differing behaviour of the NLO global gluons in the intervals  $0.001 < x < 0.01$  and  $x < 0.001$ , see Fig. 2.1. The fact that the effective power  $\lambda$  *increases* with  $1/x$  (within the  $10^{-2} - 10^{-5}$  interval) is in contradiction with the assumption of saturation for which one would expect a decreasing  $\lambda \rightarrow 0$  as  $x \rightarrow 0$ . The data with  $x < 0.01$ , therefore, cannot be described by a single power behaviour, indicative of non-trivial non-perturbative effects in the input proton wave function.

On the other hand note that the power  $\lambda \simeq 0.14$  (that we obtained in the description of the  $J/\psi$  data with  $x < 0.001$ ) is close to that predicted by the NLL BFKL re-summed with the optimal (BLM [139]) scale renormalisation [182]. Moreover, contrary to the common expectation, even at  $x \sim 10^{-5}$  and  $\mu^2 = 2.4 \text{ GeV}^2$  in our approach we see no hint for the beginning of parton density saturation.



## 4.6 Summary

High energy HERA and LHCb data on exclusive  $J/\psi$  production were described using a consistent collinear factorisation approach at NLO. We fix the ‘optimal’ factorisation scale  $\mu_F = M_\psi/2$ , which allows for the resummation of the double-logarithmic  $(\alpha_s \ln(1/x) \ln \mu_F)^m$  corrections into the incoming PDF, and subtract the low  $k_t < Q_0$  contribution from the coefficient function to avoid double counting between the NLO coefficient function and the contribution hidden in the input PDF (or GPD) at  $Q = Q_0$ . This provides good stability of the results with respect to variations of  $\mu_f$ . The generalised GPD distribution was related to the conventional (non-skewed) PDF via the Shuvaev transform. The renormalisation scale is  $\mu_R = \mu_f$ .

With this, we find collinear NLO gluons at  $\mu^2 = 2.4 \text{ GeV}^2$  which give an excellent description of all available accurate  $J/\psi$  data throughout the very low  $x$  interval,  $3 \times 10^{-6} < x < 10^{-3}$ , to about  $\pm 5\text{--}7\%$  accuracy at the lowest  $x$ . The gluon PDF  $xg(x, \mu^2) \propto x^{-\lambda}$  increases with  $1/x$  with  $\lambda = 0.135 \pm 0.006$  without any hint in favour of parton density saturation at  $\mu^2 = 2.4 \text{ GeV}^2$  and  $x$  down to  $10^{-5}$ . We emphasise that this does not infer that the power growth of  $xg \propto x^{-\lambda}$  will continue indefinitely. Clearly, it must stop at some very small  $x$ . The question was, whether we can see if this growth is directly tamed by using very low  $x$  exclusive  $J/\psi$  production data. The present data do not indicate such a behaviour. This does not mean that the data cannot be described by a more complicated expression which ultimately, at very small  $x$ , will provide saturation. However, within the presently available  $x$  interval, a simple power dependence is consistent with the data and provides a good description without including the higher-twist terms.

A Bayesian reweighting approach leads to a similar behaviour of the small  $x$  gluon that was determined from our power fits, emphasising the utility and constraining power of the exclusive  $J/\psi$  data. This work therefore clearly demonstrates the gains which will be achieved once these data are included in the global PDF fits.

## Chapter 5

# Exclusive HVM electroproduction in collinear factorisation at NLO

We compute the exclusive electroproduction,  $\gamma^*p \rightarrow Vp$ , of heavy quarkonia  $V$  to NLO in the collinear factorisation scheme, which has been formally proven for this process. The inclusion of an off-shell virtuality  $Q^2$  carried by the photon extends the photoproduction phase space of the exclusive heavy quarkonia observable to electroproduction kinematics. This process is relevant for diffractive scattering at HERA and the upcoming EIC, as well as at the proposed LHeC and FCC.

### 5.1 Introduction

As emphasised in Chapter 1, the exclusive production of vector mesons has long been an interesting and attractive observable to study. First measured in the fixed target mode and then in diffractive deep-inelastic scattering (DIS) events at the  $ep$  linear HERA collider more than 25 years ago, they constitute  $\sim 10\%$  of the total inclusive DIS cross-section and are characterised by the presence of a large rapidity gap. They provide a means to investigate the phenomenology of quarkonium production and function as more sensitive probes of the low- $x$  and low scale input gluon parton distribution than any other known high-energy physics phenomenon.

In 1993, around the same time as the first measurements of such diffractive activity in a collider environment, the exclusive *electro*production of a *heavy* vector meson (HVM),  $V = J/\psi, \Upsilon, \psi(2S), \dots$  via  $\gamma^*p \rightarrow Vp$ , was showcased to be proportional to the square

of the gluon PDF [16] in the leading-logarithmic-approximation (LLA) of perturbative QCD (pQCD), within the framework of  $k_T$ -factorisation [183, 184, 185, 186]. This is a high-energy factorisation scheme where observables are expressed as a convolution of a universal parton distribution function with an *off*-shell matrix element, retaining the transverse momentum dependence in the hard scattering coefficient function. The use of this scheme at LLA is coincident with the leading-order (LO) term in the systematic expansion of the strong coupling,  $\alpha_s$ , within the alternate collinear factorisation scheme, where matrix elements are explicitly *on*-shell. This process is on solid ground in terms of the applicability of factorisation theorems and viability of a pQCD treatment due to the large virtuality  $Q^2$  ( $\sim$  few  $\text{GeV}^2$ ) provided by the incoming photon,  $\gamma^*$ . See [187, 134] for the proof of the factorisation theorem for this observable.

On the experimental side, the HERMES collaboration [188] reported leptonproduction measurements for the lightest vector mesons in the range  $1 \text{ GeV}^2 < Q^2 < 7 \text{ GeV}^2$  in fixed-target kinematics. Exclusive electroproduction data for the  $J/\psi$  HVM via dimuon and dielectron decays has been measured in the collider mode at HERA in a narrow range of photon virtualities at both ZEUS and H1 experiments, extending up to the largest bin of  $\langle Q^2 \rangle = 22.4 \text{ GeV}^2$  [127, 128]. As in photoproduction, the cross section exhibits a steep rise with increasing centre of mass energies of the  $\gamma^*p \rightarrow J/\psi p$  subprocess. Today, in the LHC era of collider physics, central exclusive *photoproduction* of vector mesons  $V$  have been measured in the forward rapidity interval  $2.0 < Y < 4.5$  by the LHCb collaboration via ultraperipheral  $pp \rightarrow p + V + p$  collisions instead [47, 189, 48]. These are driven by the hard scattering subprocesses  $\gamma p \rightarrow V p$ , measured directly at HERA. Here, the photoproduction reaction ( $Q^2 = 0$ ) is initiated by a real on-shell photon,  $\gamma$ . Despite the vanishing of this scale, the factorisation theorems are still assumed to hold for photoproduction since the masses of the produced final state heavy mesons are above the perturbative scale threshold.

Various theoretical models within pQCD exist in the literature that provide a description of the exclusive heavy vector meson photo and electroproduction processes, see [190] for a review. In the colour dipole approach, the exclusive HVM formation is dominated by scatterings in which the photon fluctuates into a  $q\bar{q}$  pair with a transverse separation  $r \approx 0$ , carrying fractions  $z \approx 1/2$  and  $1 - z \approx 1/2$  of the incoming photon momentum. The dipole model formulation is also able to describe light meson production and photon hadron scattering and is equivalent to the  $k_T$ -factorisation formalism in the leading- $\ln(1/x)$ -approximation. Following earlier work, in [125], the explicit  $k_T$  integral had been performed in the last cell of evolution, in effect leading to a description beyond the LLA,

to mimic a subset of the full next-to-leading order (NLO) contribution. This accounts for those terms in the conventional DGLAP evolution that are enhanced at small  $x$  and that in an axial gauge correspond strictly to gluon-ladder-rung Feynman diagrams. However, we emphasise this does not encompass the complete NLO contribution that one would obtain in the conventional systematic evaluation of Feynman diagrams within the  $\overline{\text{MS}}$  collinear factorisation framework.

In this chapter, we remain entirely within the collinear factorisation set-up at NLO to extract the electroproduction renormalised transverse and longitudinal coefficient functions to NLO in the  $\overline{\text{MS}}$  scheme. Previously in the literature [18, 191], next-to-leading order  $\overline{\text{MS}}$  coefficient functions were calculated in the case of photoproduction of HVMs. The authors of [18] constructed the imaginary part of Feynman diagrams via Cutkosky-cuts in the  $s$ -channel and then restored their real parts using the corresponding  $u$ -channel contributions, via a dispersion relation. For the quark initiated subprocess, which only occurs at NLO, they find that such a dispersion integral is readily convergent and are able to directly restore the real part. However, for the gluon contribution at NLO, they find it necessary to construct a once-subtracted dispersion integral. The gluon contribution at the subtracted point is computed by arguing the extension of the low energy theorem for radiation of a soft photon, a result from QED and due to Low [192], to the non-abelian case of QCD. In our approach for electroproduction, we directly compute the real and imaginary parts of the amplitude using a semi-automated integral reduction procedure. As will be discussed and explained, the zero photon virtuality limit of our electroproduction coefficient functions coincide with these photoproduction results. Note that a subset of the authors in [18] also computed the electroproduction of *light* neutral vector mesons  $\tilde{V} = \rho^0, \omega$  and  $\phi$  [193]. In our computation, both the virtuality of the photon *and* the mass of the heavy quark are included and constitute massive scales, which adds complexity.

In [102, 107], and as discussed in Section 2.5.1 and 2.5.2, the exclusive  $J/\psi$  photoproduction result within collinear factorisation at NLO was shown to no longer have a huge theory scale uncertainty as a result of the implementation of a crucial low- $Q$  power correction and resummation of logarithmically enhanced low- $x$  terms. This treatment, that avoids a critical double counting, was a necessary supplement in combating the residual scale dependence of the  $\overline{\text{MS}}$  result, as the exclusive  $J/\psi$  photoproduction sits at a low  $x \sim 10^{-5}$  and low  $Q^2 \sim 2.4 \text{ GeV}^2$ . Upsilon photoproduction [194],  $\gamma p \rightarrow \Upsilon p$ , on the other hand, suffers less from such perturbative instability due to its higher mass, but this comes hand in hand with suppressed cross-section rates and lack of statistics. The exclusive  $J/\psi$

production has therefore been, as of late, the more forthcoming phenomenological mode of study, particularly in searches of gluon saturation and/or recombination effects. We anticipate that the effects of this  $Q_0$ -subtraction [109], where  $Q_0$  is the input scale of DGLAP evolution, are also less important for our electroproduction calculation as the typical process factorisation scale is much greater and the subtraction generates a power correction  $\sim \mathcal{O}(Q_0^2/Q^2)$  which is formally suppressed in this case.

The chapter is organised as follows. In Section 5.2.1, we give our set-up and model assumptions within collinear factorisation at NLO. In Section 5.3, we outline the workflow of our calculation. In Section 5.4 and Section 5.5, we give analytic expressions for the LO and NLO coefficient functions for the quark and gluon initiated subprocesses. We finish, in Section 5.6, by checking the explicit cancellation of initial state mass divergences to NLO within a consistent UV and IR subtraction scheme, before making a comparison with literature and presenting the chapter summary in Sections 5.8 and 5.9 respectively.

## 5.2 Notation and collinear factorisation

### 5.2.1 Kinematics and set-up

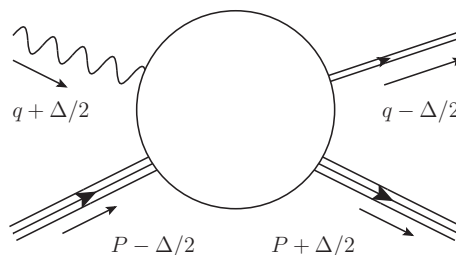


Figure 5.1: Schematic representation of HVM electroproduction.

We describe the matrix element for exclusive HVM electroproduction as the fluctuation of a hard incoming photon with momentum  $q^\mu + \Delta^\mu/2$  into a heavy  $Q\bar{Q}$  pair, which then interacts with the proton (or nuclei) carrying momentum  $P^\mu - \Delta^\mu/2$  via a two-parton colour singlet exchange mechanism, as shown in Fig. 5.1. The proton recoils slightly with momentum  $P^\mu + \Delta^\mu/2$ . The modelling of the open quark-antiquark recombination into the observed exclusive final state HVM with momentum  $q^\mu - \Delta^\mu/2$  is made, as in [18, 191], via LO Non-Relativistic-QCD (NRQCD). In this approach, the amplitude for the

production of two on-shell heavy quarks is calculated and projected onto the outgoing HVM quarkonium state. The amplitude can be expanded in powers of  $\alpha_s$  and the heavy quark relative velocity. Here, we compute the  $\alpha_s$  corrections. The relativistic corrections have been studied elsewhere, see [136]. To LO in the NRQCD relative velocity expansion, the momenta of the quark and anti-quark are equal such that their sum equals the momentum of the HVM.

Following the set-up in [195], the three independent momenta defined above may be decomposed in terms of high energy light-like Sudakov basis vectors  $\{p, n, \Delta_\perp\}$ , satisfying  $p \cdot p = n \cdot n = 0$  and  $p \cdot n = 1$ . See Appendix A.0.1 for their explicit definition. The mean of the incoming and outgoing proton momenta,  $P^\mu$ , defines the collinear direction.

In this basis, the momenta decompose as

$$P^\mu = p^\mu + \frac{M_N^2 - t/4}{2} n^\mu, \quad (5.1)$$

$$q^\mu = -\zeta p^\mu + \frac{\tilde{Q}^2}{2\zeta} n^\mu, \quad (5.2)$$

$$\Delta^\mu = -2\xi p^\mu + \xi(M_N^2 - t/4)n^\mu + \Delta_\perp^\mu, \quad (5.3)$$

where  $M_N$  is the initial and final state proton mass and  $q^2 = -\tilde{Q}^2$  and  $\zeta$  are auxiliary parameters. Here,  $t = \Delta^2$  and  $\xi$  is the skewedness parameter. The analogue of the Bjorken scaling variable is defined as

$$x_B = \frac{\tilde{Q}^2}{2P \cdot q}, \quad (5.4)$$

which allows us to write

$$\zeta = \frac{\tilde{Q}^2}{2x_B(M_N^2 - t/4)} \left( -1 + \sqrt{1 + \frac{4x_B^2(M_N^2 - t/4)}{\tilde{Q}^2}} \right). \quad (5.5)$$

To leading-twist accuracy, we may take the Bjorken limit,  $\tilde{Q}^2 \rightarrow \infty$  with  $x_B$  fixed. Then

$$\lim_{\tilde{Q}^2 \rightarrow \infty, x_B \text{ fixed}} \zeta = x_B \quad (5.6)$$

with

$$\lim_{\tilde{Q}^2 \rightarrow \infty, x_B \text{ fixed}} P^\mu = p^\mu, \quad (5.7)$$

$$\lim_{\tilde{Q}^2 \rightarrow \infty, x_B \text{ fixed}} q^\mu = -x_B p^\mu + \frac{\tilde{Q}^2}{2x_B} n^\mu, \quad (5.8)$$

$$\lim_{\tilde{Q}^2 \rightarrow \infty, x_B \text{ fixed}} \Delta^\mu = -2\xi p^\mu. \quad (5.9)$$

Let us now impose that the incoming photon (outgoing HVM) is off-shell (on-shell). This means

$$(q^\mu + \Delta^\mu/2)^2 = -\tilde{Q}^2 \left(1 + \frac{\xi}{x_B}\right) = Q^2, \quad (5.10)$$

$$(q^\mu - \Delta^\mu/2)^2 = -\tilde{Q}^2 \left(1 - \frac{\xi}{x_B}\right) = M^2, \quad (5.11)$$

and therefore,

$$\tilde{Q}^2 = -\frac{Q^2 + M^2}{2} \quad \text{and} \quad \frac{\xi}{x_B} = \frac{Q^2 - M^2}{Q^2 + M^2}, \quad (5.12)$$

where  $Q^2$  is the virtuality of the photon and  $M^2$  is the mass squared of the HVM.

In the Bjorken limit to leading-twist accuracy, i.e. neglecting the masses of the protons, the kinematics of the process have simplified and can be entirely expressed in terms of  $Q^2$ ,  $M^2$  and  $\xi$ . It is in this sense we call  $\tilde{Q}^2$  and  $\zeta$  ‘auxiliary’ variables. Here,  $P^\mu \approx p^\mu$  and  $\Delta^\mu \approx -2\xi p^\mu$ , where  $2\xi$  is the ‘kick’ which the active quark or gluon receives along the *collinear* direction so that the  $t$ -channel momentum exchange,  $t = \Delta^2 = 0$ . The probed partons (gluons or quarks) carry momenta  $p_1 = (X + \xi) p$  and  $p_2 = -(X - \xi) p$ , the momentum fraction  $X$  is integrated over in the convolution with the GPDs.

Note that, as can be seen from eqn. (5.12), the off-shellness,  $Q^2$ , of the incoming photon permits the use of the leading-twist term only. The higher inverse powers of  $\tilde{Q}^2$  in the systematic twist-expansion are formally sub-dominant. As the photon tends to on-shell kinematics,  $Q^2 \rightarrow 0$ , the scale  $\tilde{Q}^2$  is kept sufficiently large only due to the mass of the *heavy* quark.

We further perform the mappings

$$p^\mu \rightarrow \hat{p}^\mu = X p^\mu, \quad n^\mu \rightarrow \hat{n}^\mu = n^\mu / X, \quad \xi \rightarrow \hat{\xi} = \xi / X, \quad (5.13)$$

which reduces the number of dimensionless variables appearing in our description by one. Note that these transformed basis vectors still respect  $\hat{p} \cdot \hat{p} = \hat{n} \cdot \hat{n} = 0$  and  $\hat{p} \cdot \hat{n} = 1$  and so all possible scalars formed from our momenta are unaffected by this change.

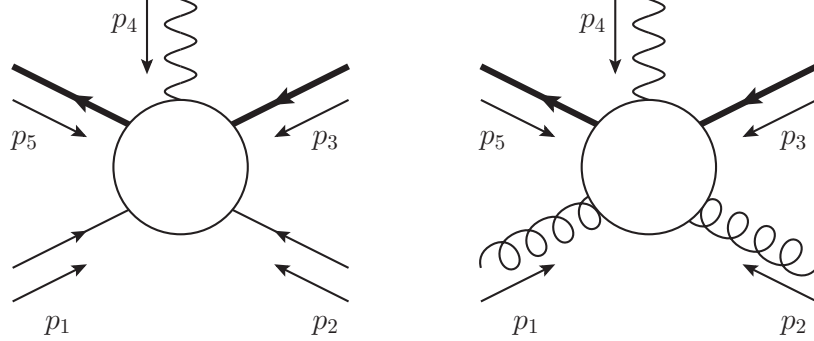


Figure 5.2: The kinematics of quark and gluon initiated processes. Massive quark lines are indicated in bold.

Therefore, to leading order in the relative heavy quark velocity and in the Bjorken limit, the Sudakov decomposed momenta of Figure 5.2 are<sup>1</sup>

$$p_1^\mu = (1 + r_1/r_3)p^\mu, \quad p_2^\mu = -(1 - r_1/r_3)p^\mu, \quad (5.14)$$

$$p_3^\mu = p_5^\mu = \frac{(r_2 - r_1)}{2r_3}p^\mu + \frac{r_3}{2}n^\mu, \quad p_4^\mu = -\frac{(r_1 + r_2)}{r_3}p^\mu - r_3n^\mu, \quad (5.15)$$

where

$$r_{1,2} = \frac{Q^2 \mp 4m^2}{4} \quad \text{and} \quad r_3 = \frac{Q^2 - 4m^2}{4\hat{\xi}}.$$

Our convention is that all momenta are incoming. Moreover, in accordance with the leading term in the NRQCD expansion, we make the approximation that the on-shell pole mass of the heavy quarks is  $m = M/2$ .

At leading order only the gluon induced process,

$$\gamma^*(p_4) + g(p_1) \rightarrow Q(-p_5) + \bar{Q}(-p_3) + g(-p_2), \quad (5.16)$$

contributes. At NLO the  $Q\bar{Q}$  pair may scatter from a light quark via a gluon exchange

---

<sup>1</sup>Henceforth, for notational simplicity, we will suppress the hat notation from the transformed Sudakov vectors  $p$  and  $n$ .



and so a new partonic channel opens. We compute in addition the quark induced process:

$$\gamma^*(p_4) + q(p_1) \rightarrow Q(-p_5) + \bar{Q}(-p_3) + q(-p_2), \quad q = u, \bar{u}, d, \bar{d}, s, \bar{s}. \quad (5.17)$$

### 5.2.2 HVM and GPD spin projections

The S-wave, spin-triplet projection may be written to leading order in the heavy quark relative velocity as [196, 197, 198]

$$v_\alpha^i(-p_3)\bar{u}_\beta^j(-p_5) \rightarrow \frac{-\delta^{ij}}{4N_c} \frac{1}{4m^2} \left( \frac{\langle O_1 \rangle_V}{m} \right)^{\frac{1}{2}} \left[ (-\not{p}_3 - m)\not{\epsilon}_S^*(-\not{K} + M)(-\not{p}_5 + m) \right]_{\alpha\beta}, \quad (5.18)$$

where, in the non-relativistic limit, we take the vector meson momenta  $K = 2p_3 = 2p_5$  and mass  $M = 2m$ . Here,  $\bar{u}_\beta^j$  ( $v_\alpha^i$ ) is the outgoing heavy quark (anti-quark) spinor. The indices  $i$  and  $j$  label their colour while  $\alpha$  and  $\beta$  label their spin.  $\langle O_1 \rangle_V$  represents the non-perturbative NRQCD matrix element. The vector  $\epsilon_S$  describes the polarisation of the HVM; it satisfies  $\epsilon_S \cdot \epsilon_S^* = -1$  and  $K \cdot \epsilon_S^* = 0$ . In eqn. (5.18), relative to [198], we have an overall minus sign. It multiplies the overall amplitude and so has no effect on the cross section. Note that the form of eqn. (5.18) differs from that used in [18]. There, they use

$$v_\alpha^i(-p_3)\bar{u}_\beta^j(-p_5) \rightarrow \frac{\delta^{ij}}{4N_c} \frac{1}{4m^2} \left( \frac{\langle O_1 \rangle_V}{m} \right)^{\frac{1}{2}} [\not{\epsilon}_S^*(-\not{K} + M)]_{\alpha\beta} \quad (5.19)$$

for the HVM spin projection. Our projector has therefore an additional term  $\sim K^\nu$  which will in any case vanish due to  $K \cdot \epsilon_S^* = 0$ . In essence, this allows for gauge dependent terms to cancel at the diagram level thereby avoiding the introduction of extraneous terms that would conspire to cancel. The utility of this modification to the projector will become clear in the next subsection.

*Quark:* On a pragmatic level, in our calculation the quark GPD contraction is implemented as a spin projection of the on-shell quark scattering matrix. We replace the spinors of the quark and anti-quark connecting to the quark GPD,  $F^q(X, \xi)$ , by

$$u_\alpha^i(p_1)\bar{u}_\beta^j(-p_2) \rightarrow \frac{\delta^{ij}}{N_c} \frac{1}{2} F^q(X, \xi) \not{p}_{\alpha\beta}. \quad (5.20)$$

The factor  $\not{p}_{\alpha\beta}$  will result in a trace over the spin line of the quarks connecting to the GPD at the amplitude level. This can be understood by considering the numerator of a quark

diagram. Representing the product of quark propagator numerators as  $[A]$  and applying the spin projection we obtain

$$\bar{u}_\beta(-p_2) [A]_{\beta\alpha} u_\alpha(p_1) \rightarrow [A]_{\beta\alpha} \not{p}_{\alpha\beta} = \text{Tr} [A \not{p}]. \quad (5.21)$$

*Gluon:* Similarly, for the gluon induced partonic channel the contraction with the gluon GPD,  $F^g(X, \xi)$ , is implemented as a projection of the on-shell gluon scattering matrix. Throughout this chapter we will use dimensional regularisation in  $d = 4 - 2\epsilon$  space-time dimensions and make the replacement

$$\epsilon_1^\mu \epsilon_2^{*\nu} \rightarrow -\frac{\delta_{ab}}{(N_c^2 - 1)} \frac{1}{2} \frac{1}{(d-2)} \frac{F^g(X, \xi)}{x_+ x_-} g_\perp^{\mu\nu}, \quad (5.22)$$

where  $\epsilon_1^\mu$  and  $\epsilon_2^{*\nu}$  are the polarisations of the incoming and outgoing gluons respectively. Here,  $x_+ = X + \xi - i\delta$  and  $x_- = X - \xi + i\delta$ . The correct  $i\delta$  prescription for the poles has been discussed extensively in the literature, see for example [199]. The prescription given here is valid for both DVCS and HVM production [200, 18]. Here the indices  $a, b$  are gluon colour indices in the adjoint representation. The factor  $1/(N_c^2 - 1)$  averages over the gluon colours. The factor  $1/(d-2)$  is the reciprocal of the number of transverse polarisations of a gluon in  $d$  dimensions. It appears due to the average over the gluon polarisations. The factor of  $1/2$  is required to prevent double counting when both  $s$  and  $u$  channel gluon diagrams are computed (as done here) and the momentum fraction  $X$  is integrated over from  $-1$  to  $1$  (see later). The object  $g_\perp^{\mu\nu}$  carrying the gluons' Lorentz indices is the perpendicular metric tensor, see Appendix A.0.1.

### 5.2.3 Lorentz-invariant tensor decomposition

We consider only the vector part of the amplitude at leading twist and at  $t = 0$ . Higher-twist terms are formally suppressed and axial-vector contributions are neglected, as they are not needed here with an unpolarised nucleon in the initial state. As shown in Section 5.2.1, in the Bjorken limit at leading twist, all of our external kinematics can be expressed in the Sudakov basis  $\{p, n\}$  with  $\Delta_\perp = 0$ . We decompose the part of the amplitude insensitive to the helicities of the incoming partons in the nucleon target in terms of the available Lorentz structure in this basis. Explicitly, we factor off the polarisation vectors for the

incoming photon and outgoing HVM and work with the amputated amplitude  $\mathcal{T}^{(\mu\nu)}$ .<sup>2</sup> It follows that

$$\mathcal{T}^{(\mu\nu)} = Ag^{\mu\nu} + Bp^\mu n^\nu + Cn^\mu p^\nu + Dp^\mu p^\nu + En^\mu n^\nu, \quad (5.23)$$

where  $A, B, C, D$  and  $E$  are the arbitrary coefficients of the decomposition. Imposing local current conservation at the photon vertex,  $p_{4,\mu}\mathcal{T}^{(\mu\nu)} = 0$ , together with the identity  $K_\nu\mathcal{T}^{(\mu\nu)} = 0$ , constrains the coefficients. The former is the familiar Ward-identity while the latter is, strictly speaking, not as it holds at the Feynman diagram level and is true due to our choice of HVM spin projection, eqn. (5.18), as discussed in Section 5.2.2. The equations  $p_{4,\mu}\mathcal{T}^{(\mu\nu)} = 0$  and  $K_\nu\mathcal{T}^{(\mu\nu)} \equiv 2p_{3,\nu}\mathcal{T}^{(\mu\nu)} = 0$  give

$$Ap_4^\nu + B(p \cdot p_4)n^\nu + C(n \cdot p_4)p^\nu + D(p \cdot p_4)p^\nu + E(n \cdot p_4)n^\nu = 0, \quad (5.24)$$

$$Ap_3^\mu + B(n \cdot p_3)p^\mu + C(p \cdot p_3)n^\mu + D(p \cdot p_3)p^\mu + E(n \cdot p_3)n^\mu = 0. \quad (5.25)$$

Insertion of the momenta,  $p_{3,4}^\mu = \alpha_{p_{3,4}}p^\mu + \beta_{p_{3,4}}n^\mu$ , and using the linear independence of  $p^\mu, p^\nu, n^\mu$  and  $n^\nu$ , the system admits the resulting matrix form:

$$\begin{pmatrix} \alpha_{p_4} & 0 & \alpha_{p_4} & \beta_{p_4} & 0 \\ \beta_{p_4} & \beta_{p_4} & 0 & 0 & \alpha_{p_4} \\ \alpha_{p_3} & \alpha_{p_3} & 0 & \beta_{p_3} & 0 \\ \beta_{p_3} & 0 & \beta_{p_3} & 0 & \alpha_{p_3} \end{pmatrix} \begin{pmatrix} A \\ B \\ C \\ D \\ E \end{pmatrix} = \mathbf{0}. \quad (5.26)$$

This matrix has rank 3 so there are at most only two linearly independent coefficients in the system. If we parametrise freely,  $A = -T_\perp$  and  $D = \tilde{T}_L/4$ , then

$$\mathcal{T}^{(\mu\nu)} = -g_\perp^{\mu\nu}T_\perp + \left( \frac{p_4 \cdot p}{p_4 \cdot n} n^\mu - p^\mu \right) \left( \frac{p_3 \cdot p}{p_3 \cdot n} n^\nu - p^\nu \right) \frac{\tilde{T}_L}{4} \quad (5.27)$$

$$= -g_\perp^{\mu\nu}T_\perp + \ell^{\mu\nu}T_L, \quad (5.28)$$

where

$$\ell^{\mu\nu} = \frac{\mathcal{N}}{4} (\alpha n^\mu - p^\mu) (\beta n^\nu - p^\nu) \quad \text{and} \quad T_L = \tilde{T}_L/\mathcal{N}, \quad (5.29)$$

---

<sup>2</sup>The round brackets  $(\mu\nu)$  denote the vector part of the amplitude,  $\mathcal{T}$ , which is all that is needed in the description of an unpolarised measurement.

with

$$\alpha \equiv \frac{p_4 \cdot p}{p_4 \cdot n} \quad \text{and} \quad \beta \equiv \frac{p_3 \cdot p}{p_3 \cdot n}. \quad (5.30)$$

An explicit exposition of the available Lorentz structure has therefore produced a manifest decoupling of the system into two overarching degrees of freedom, parametrised by  $T_\perp$  and  $T_L$ . Contractions of eqn. (5.28) with explicit realisations of the physical transverse and longitudinal polarisation vectors of the photon  $\varepsilon_\mu^\gamma$  and HVM  $\varepsilon_\nu^{V*}$  pick out one of the two scalar coefficients in each case. This may be seen as follows. The transverse polarisation vectors have only a transverse component in their Sudakov-basis decomposition so, by construction, their contraction with  $p^\mu, p^\nu, n^\mu, n^\nu$  in  $\ell^{\mu\nu}$  vanishes and the only contribution is due to  $g_\perp^{\mu\nu}$ :

$$\varepsilon_{\pm,\mu}^\gamma \varepsilon_{\pm,\nu}^{V*} \mathcal{T}^{(\mu\nu)} = -\varepsilon_{\pm,\mu}^\gamma \varepsilon_{\pm,\nu}^{V*} g_\perp^{\mu\nu} T_\perp = -\varepsilon_\pm^\gamma \cdot \varepsilon_\pm^{V*} T_\perp = T_\perp, \quad (5.31)$$

where  $\varepsilon_{\pm,\mu}^\gamma$  and  $\varepsilon_{\pm,\nu}^{V*}$  are the transverse polarisation vectors for the photon and HVM in the helicity basis, respectively. The corresponding longitudinal polarisation vectors are

$$\varepsilon_L^{\gamma,\mu} = \frac{2Q\hat{\xi}}{M^2 - Q^2} p^\mu + \frac{(Q^2 - M^2)}{4Q\hat{\xi}} n^\mu, \quad (5.32)$$

$$\varepsilon_L^{V,\nu*} = \frac{2M\hat{\xi}}{M^2 - Q^2} p^\nu + \frac{(Q^2 - M^2)}{4M\hat{\xi}} n^\nu, \quad (5.33)$$

satisfying  $\varepsilon_L^\gamma \cdot \varepsilon_L^\gamma = -1$  and  $p_4 \cdot \varepsilon_L^\gamma = 0$ , with similar relations for the HVM. Then,

$$\varepsilon_{L,\mu}^\gamma \varepsilon_{L,\nu}^{V*} \mathcal{T}^{(\mu\nu)} = \varepsilon_{L,\mu}^\gamma \varepsilon_{L,\nu}^{V*} \ell^{\mu\nu} T_L, \quad (5.34)$$

where there is now no contribution from  $g_\perp^{\mu\nu}$ . This may be understood from the general expression for a longitudinal polarisation vector,  $\varepsilon_L^\mu(q)$ , of a boson of mass  $M$  carrying momentum  $q$ ,

$$\varepsilon_L^\mu(q) = \frac{1}{M} \frac{(l \cdot q) q^\mu - M^2 l^\mu}{\sqrt{(l \cdot q)^2 - M^2}}. \quad (5.35)$$

Indeed, the contraction of this object and the perpendicular metric tensor gives

$$-\varepsilon_{L,\mu}(q) g_\perp^{\mu\nu} \sim ((l \cdot q) q_\mu - M^2 l_\mu) (-g^{\mu\nu} + p^\mu n^\nu + p^\nu n^\mu) = 0, \quad (5.36)$$

where, for example,  $l = (1, 0, 0, 0)$  satisfies  $l^2 = 1$ .

The decompositions in eqns. (5.27,5.28) are therefore readily identifiable as a separation into transverse and longitudinal components, with  $T_\perp$  and  $T_L$  having the physical interpretation now as the process's transverse and longitudinal form factors, respectively.

We choose  $\mathcal{N}$  in  $\ell^{\mu\nu}$  such that

$$\varepsilon_{L,\mu}^\gamma \varepsilon_{L,\nu}^{V*} \ell^{\mu\nu} = 1. \quad (5.37)$$

With this choice<sup>3</sup>, the transverse and longitudinal helicity amplitudes,  $A^{\pm\pm} = \varepsilon_{\pm,\mu}^\gamma \varepsilon_{\pm,\nu}^{V*} \mathcal{T}^{(\mu\nu)}$  and  $A^{00} = \varepsilon_{L,\mu}^\gamma \varepsilon_{L,\nu}^{V*} \mathcal{T}^{(\mu\nu)}$ , are equal to  $T_\perp$  and  $T_L$ , respectively. Note also that the introduction of the  $\mathcal{N}$  factor into  $\ell^{\mu\nu}$  in eqn. (5.29) allows for both tensors in multiplication with the scalar coefficients  $T_\perp$  and  $T_L$  to have mass dimension zero. In this way, one may extract these coefficients in turn through suitable projections onto the  $\mathcal{T}^{(\mu\nu)}$  structure.

We remark that eqn. (5.27) coincides with the leading-twist tensor decomposition found in Generalised-Deeply-Virtual-Compton-Scattering (GDVCS), see e.g. [201], upon neglecting the axial-vector and helicity flip contributions. This is to be expected as the only distinction in the kinematical set-up is the final state production of a heavy photon instead of a heavy vector meson that we have here, however this remains indifferent in the construction of the underlying tensorial structure and the applicability of our Ward and Ward-like identities.

The vector part of the amplitude may be written, using collinear factorisation, as

$$\begin{aligned} \mathcal{T}^{(\mu\nu)} = & -g_\perp^{\mu\nu} \int_{-1}^1 \frac{dX}{X} \left[ \sum_q F^q(X, \xi) C_{\perp,q} \left( \frac{\xi}{X}, Q^2 \right) + C_{\perp,g} \left( \frac{\xi}{X}, Q^2 \right) \frac{F^g(X, \xi)}{X} \right] \\ & + \ell^{\mu\nu} \int_{-1}^1 \frac{dX}{X} \left[ \sum_q F^q(X, \xi) C_{L,q} \left( \frac{\xi}{X}, Q^2 \right) + C_{L,g} \left( \frac{\xi}{X}, Q^2 \right) \frac{F^g(X, \xi)}{X} \right] \quad (5.38) \\ & + \dots \end{aligned}$$

where the ellipses represent contributions that appear beyond the leading term in the twist expansion and outwith the chiral-even theory with  $t = 0$ , but which would appear in e.g. polarised scattering or if the nucleon mass would not be neglected. The renormalised quark and gluon GPDs are denoted  $F^q$  and  $F^g$  respectively.  $C_{\perp,q}$  and  $C_{\perp,g}$  are the renormalised quark and gluon vector transverse coefficient functions, while  $C_{L,q}$  and  $C_{L,g}$  are the renor-

---

<sup>3</sup>This degree of freedom is evident in eqn. (5.29), where the introduction of  $\mathcal{N}$  allows for a shuffling of terms between  $\ell^{\mu\nu}$  and  $T_L$ .

malised quark and gluon vector longitudinal coefficient functions. The dependence of the GPDs  $F^q$  and  $F^g$  on the factorisation scale  $\mu_F$  and on  $t$  has been suppressed. The dependence of the renormalised coefficient functions  $C_{\perp,q}$ ,  $C_{\perp,g}$ ,  $C_{L,q}$  and  $C_{L,g}$  on  $m^2$ ,  $\mu_F$  and the renormalisation scale  $\mu_R$  has been suppressed, too. We recall that the Lorentz indices  $\mu$  and  $\nu$  are those of the incoming photon and outgoing HVM respectively. Measurements of HVM production from unpolarised targets probe only the charge conjugation even quark GPD and so we may replace  $\sum_q F^q$  with the singlet quark GPD  $F^S/2$ . There is also an additional photon helicity flip term which is not considered here due to our kinematical set-up.

### 5.3 Overview of calculation

We generate all LO and NLO Feynman diagrams using **QGRAF** [202] and select those diagrams that are compatible with our external colour and kinematical constraints. Each selected diagram is converted into an expression through insertion of Feynman rules, derived in an arbitrary linear covariant gauge. The appropriate GPD quark or gluon projector is applied to each diagram, together with the HVM spin projection, and the resulting Dirac traces are computed and handled in **FORM4.2** [203] in  $d = 4 - 2\epsilon$  space-time dimensions.

Due to the external colour and kinematical constraints, the integral structures obtained contain in general linearly *dependent* propagators. They therefore cannot be reduced in the typical fashion using standard integral reduction tools. We express them first as structures containing only linearly *independent* propagators by applying a partial fractioning routine in line with the Leinartas' algorithm [204]. In this way, we eliminate the linear dependence amongst the propagators and proceed with the integral reduction via **REDUZE 2** [100] which encodes Laporta's integration by parts algorithm [101].

We obtain bare electroproduction transverse and longitudinal NLO coefficient functions expressed in a basis of logarithms and dilogarithms arising from the Feynman integration. Finally, the singular terms in  $\epsilon$  are removed via a consistent ultraviolet (UV) and infrared (IR) subtraction scheme to render finite renormalised coefficient functions that may be suitably convoluted with GPDs to produce observable predictions.

All results presented below are given in the ERBL region,  $|\hat{\xi}| > 1$  (i.e.  $|X| < \xi$ ), where we expect an absence of imaginary parts. The results in the physical region,  $|\hat{\xi}| < 1$  (i.e.  $|X| > \xi$ ), may be obtained by restoring the correct analytic continuation. Explicitly, this

is

$$\hat{\xi} \rightarrow \hat{\xi} - \text{sgn}(\hat{\xi}) \text{i}\delta \quad \text{with} \quad \delta \rightarrow 0^+. \quad (5.39)$$

The coefficient functions are expanded in the bare strong coupling  $\hat{a}_s = \hat{\alpha}_s/(4\pi)$  as,

$$\hat{C}_{i,j} = \hat{a}_s \hat{C}_{i,j}^{(0)} + \hat{a}_s^2 \hat{C}_{i,j}^{(1)} + \mathcal{O}(\hat{a}_s^3), \quad (5.40)$$

with  $i = \perp, L$  and  $j = q, g$ .

## 5.4 LO results

At leading-order (LO) in  $\alpha_s$ , there is only a gluon initiated subprocess. There is no contribution from an initial state light quark as it may only couple to the outgoing heavy quark system via a loop-induced gluon insertion at next-to-leading-order (NLO).

There are 8 tree level diagrams at LO generated by **QGRAF**, two of which contain a single gluon exchange. A single gluon exchange is  $\propto f^{abc}$ , which vanishes due to our GPD spin projection  $\propto \delta^{ab}$  and antisymmetry of the SU(3) structure constants. The tree level contribution is therefore dominated by a gluon-gluon (pomeron-like) exchange,

$$\gamma^*(p_4) + g(p_1) \rightarrow Q(-p_5) + \bar{Q}(-p_3) + g(-p_2). \quad (5.41)$$

The six tree level gluon initiated subprocess diagrams are shown in Fig. 5.3. The bare (denoted by hat script) transverse and longitudinal coefficient functions at LO are

$$\hat{C}_{\perp,q}^{(0)} = \hat{C}_{L,q}^{(0)} = 0, \quad (5.42)$$

while

$$\hat{C}_{\perp,g}^{(0)} = \frac{2(w^2 - 1)}{w^2} \frac{T_F}{N_c} B_0, \quad (5.43)$$

and

$$\hat{C}_{L,g}^{(0)} = -\frac{2\sqrt{w^2 - 1}}{w^2} \frac{T_F}{N_c} B_0. \quad (5.44)$$

Here,

$$B_0 = (4\pi)^2 g_e e_q \left( \frac{\langle O_1 \rangle_V}{m^3} \right)^{\frac{1}{2}} \frac{X^2}{(X - \xi + \text{i}\delta)(X + \xi - \text{i}\delta)}, \quad (5.45)$$

where  $g_e$  ( $g_s$ ) is the electromagnetic (strong) coupling,  $e_q$  is the photon-quark charge and

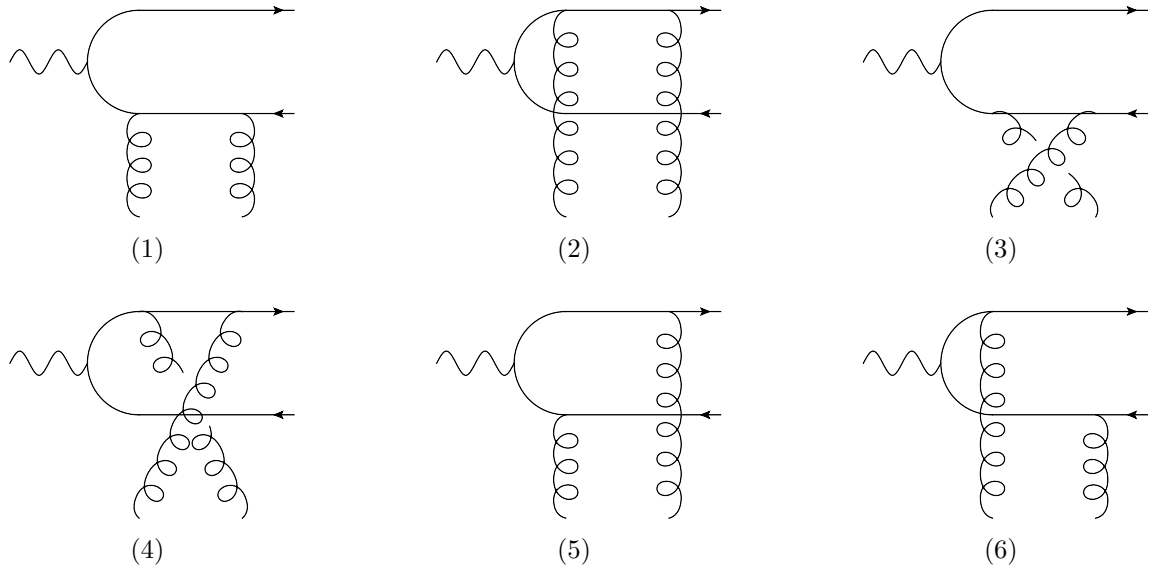


Figure 5.3: The six gluon LO diagrams.

$\langle O_1 \rangle_V$  is the NRQCD matrix element. The colour factor  $T_F = 1/2$ , and

$$w = \sqrt{1 - \frac{4m^2}{Q^2}}. \quad (5.46)$$

Eqns. (5.42-5.44) are true up to and including  $\mathcal{O}(\epsilon)$ . There is a cancellation of  $\epsilon$  terms between those appearing in the  $1/(d-2)$  factor of eqn. (5.22) and those in the numerators of the Feynman diagrams. This observation is important as the tree level results enter into the renormalisation of the NLO result. We will therefore not generate finite surplus contributions of the form  $\epsilon/\epsilon$  in the computation of the NLO counterterms, see Section 5.6.

The  $Q^2 \rightarrow 0$  (i.e.  $w \rightarrow \infty$ ) limit of these results coincide with the photoproduction result, [18], where only the amplitude to produce a transversely polarised HVM is non-vanishing.<sup>4</sup> Note that the limiting point  $w \rightarrow 0$  is not kinematically attainable. The production of a time-like vector meson (with invariant mass squared,  $M^2 = 4m^2 > 0$ ) initiated by a space-like photon,  $Q^2 < 0$ , does not, as expected within the analytic structure of the  $S$ -matrix, produce a pole at LO.

<sup>4</sup>Away from  $t = 0$ , the quantum numbers of the photon and the HVM need not be the same so there is an (albeit suppressed) amplitude to produce a longitudinally polarised HVM from a transversely polarised photon.



## 5.5 NLO results

At NLO, there are quark and gluon initiated subprocesses. We compute

$$\gamma^*(p_4) + g(p_1) \rightarrow Q(-p_5) + \bar{Q}(-p_3) + g(-p_2), \quad (5.47)$$

$$\gamma^*(p_4) + q(p_1) \rightarrow Q(-p_5) + \bar{Q}(-p_3) + q(-p_2), \quad q = u, \bar{u}, d, \bar{d}, s, \bar{s}, \quad (5.48)$$

and express our bare quark and gluon NLO coefficient functions in terms of sets of coefficients  $c_i$  and a universal basis set  $\{f_i, i = 1, \dots, 12\}$  of logarithms and dilogarithms that arise from the Feynman loop integration. They are

$$\begin{aligned} f_1 &= 1, \quad f_2 = \ln\left(\frac{w-1}{w+1}\right), \quad f_3 = f_2^2, \quad f_4 = \ln\left(\frac{2w^2}{w^2-1}\right), \\ f_5 &= f_4^2, \quad f_6 = \ln\left(\frac{2vw^2}{vw^2-1}\right), \quad f_7 = 2f_4f_6 - f_6^2 \\ f_8 &= \text{Li}_2\left(\frac{1-v}{v(w^2-1)}\right), \quad f_9 = \text{Li}_2\left(\frac{1+w^2}{1-w^2}\right), \\ f_{10} &= \text{Li}_2\left(-\frac{1}{vw^2}\right) + \text{Li}_2\left(\frac{1+v}{1-vw}\right) + \text{Li}_2\left(\frac{1+v}{1+vw}\right) + \text{Li}_2\left(\frac{v-1}{v^2w^2-1}\right), \\ f_{11} &= \sqrt{-1 + \frac{2(1+v)}{1+vw^2}} \ln\left(\frac{1+vw^2}{v(w^2-1)} \left(\frac{1+v}{1+vw^2} + \sqrt{-1 + \frac{2(1+v)}{1+vw^2}}\right)\right), \\ f_{12} &= f_{11}^2. \end{aligned} \quad (5.49)$$

See Appendix A.0.2 for the definition of the dilogarithm,  $\text{Li}_2$ . Here,  $v = \hat{\xi}/w^2$  and so, with this choice of variables, the analytic continuation to the DGLAP regime, as specified in eqn. (5.39), is restored via

$$v \rightarrow v - \text{sgn}(v)i\delta \quad \text{with } \delta \rightarrow 0^+ \quad \text{and where } \text{sgn}(v) = \text{sgn}(\hat{\xi}). \quad (5.50)$$

### 5.5.1 Linear Reduction

Within the framework of collinear factorisation in the Bjorken limit, the initial state quark and gluons connected to the non-perturbative GPDs are *collinear* partons. Moreover, at leading-order in the NRQCD expansion, the relative velocity of the outgoing heavy quark and anti-quark is zero. Together with overall energy-momentum conservation, this amounts to non-trivial linear dependences in the external kinematic scales due to the inputs of our

model construction. Explicitly, from eqns. (5.14-5.15), these are

- $\sum_{i=1}^5 p_i = 0$ ,
- $p_1 \propto p_2$ ,
- $p_3 = p_5$ .

This leads to linearly dependent propagators in our loop integrals. We exploit the possible linear relationships amongst the propagators, obtainable via the `SolveAlways` routines in `MATHEMATICA`, and use them in the first step to cure the problem of linear dependence in our five-leg NLO matrix element computation.

### Algorithm

The permissible (cubic) interaction vertices for the quark and the gluon within the QCD Lagrangian allow for at most a pentagon integral to appear in our NLO one-loop matrix element. In order to proceed with a programme of integral reduction using standard tools such as e.g. `REDUZE 2` [100], the problem of linear dependence amongst the external kinematic scales must be eliminated. With this in mind, we utilise a generalised partial fractioning routine in line with the Leonartas' algorithm [204], in which linear relations amongst the propagators are used to iteratively remove this linear dependence. Valid only at one-loop, this allows for the systematic decomposition of the pentagon integral (containing five propagators) to box integrals (containing four propagators) and then finally to triangle integrals (containing three propagators). This is sufficient as the constraints above imply that one can form at most *three* linearly independent momenta from the set  $\{l, p_i\}$ , where  $l$  is the loop momentum. This coincides with the combinatorial number  $N = L(L + 1)/2 + LE$  of scalar products or linearly independent propagators one can form between  $L$  loop momenta and  $E$  linearly independent external scales. Here,  $L = 1$  and  $E = 2$  as we compute a *one*-loop correction with all external momenta decomposed in terms of *two* basis vectors,  $p$  and  $n$ .

In a generic multi-loop and multi-scale computation, one deals with tensor integrals comprising products of the various loop momenta,  $l_1^\mu, l_2^\nu, \dots$  in the numerator and products of propagators in the denominator, containing the external scales  $p_j$ . The aim is to write such integrals as a sum of scalar integrals, which are then subsequently reduced to a basis of master integrals using reduction procedures implemented in various tools, such as

REDUZE 2 used here. At one-loop, the tensor integrals are of the form

$$I^{\mu\dots\nu}(\nu_1, \dots, \nu_N) = \int [dl] \frac{l^\mu \dots l^\nu}{D_1^{\nu_1} \dots D_N^{\nu_N}}, \quad (5.51)$$

where  $D_i = (l + q_i)^2 - m_i^2 + i\epsilon$ , with  $m_i$  the mass of the  $i$ th propagator and  $\nu_i$  are integer powers. Here, the notation  $[dl]$  denotes the integration measure for the loop integration and contains the overall normalisation factors of our loop integrals, given later in eqn. (5.73). The  $q_i$  are linear combinations of the external momenta. As our amplitude is written with two free Lorentz indices,  $\mu$  and  $\nu$ , for the incoming photon and outgoing HVM, we need at most a basis decomposition for the rank-two tensor  $l^\mu l^\nu$ . The rank-one tensor decomposition in our chosen Sudakov basis is simply

$$l^\mu = (l \cdot n)p^\mu + (l \cdot p)n^\mu, \quad (5.52)$$

while

$$l^\mu l^\nu = g^{\mu\nu}T_{00} + p^\mu p^\nu T_{11} + p^\mu n^\nu T_{12} + n^\mu p^\nu T_{21} + n^\mu n^\nu T_{22}, \quad (5.53)$$

where the tensor coefficients are found to be

$$T_{00} = \frac{l^\rho l^\sigma}{(d-2)}(g_{\rho\sigma} - p_\rho n_\sigma - n_\rho p_\sigma), \quad (5.54)$$

$$T_{11} = l^\rho l^\sigma n_\rho n_\sigma, \quad (5.55)$$

$$T_{12} = \frac{l^\rho l^\sigma}{(d-2)}(-g_{\rho\sigma} + p_\rho n_\sigma + (d-1)n_\rho p_\sigma), \quad (5.56)$$

$$T_{21} = \frac{l^\rho l^\sigma}{(d-2)}(-g_{\rho\sigma} + (d-1)p_\rho n_\sigma + n_\rho p_\sigma), \quad (5.57)$$

$$T_{22} = l^\rho l^\sigma p_\rho p_\sigma. \quad (5.58)$$

After performing this tensor reduction in the Sudakov basis<sup>5</sup> the resulting scalar integrals resume the form

$$I(\tilde{\nu}_1, \dots, \tilde{\nu}_N) = \int [dl] \frac{\mathcal{N}(l \cdot l, p_i \cdot l)}{D_1^{\tilde{\nu}_1} \dots D_N^{\tilde{\nu}_N}} \quad (5.59)$$

multiplied by tensor structures depending only on the external momenta (those structures

---

<sup>5</sup>Expansion of the rank-one and -two tensors in the basis of external momenta  $\{p_j, j = 1, \dots, 5\}$  instead leads to a vanishing Gram determinant in the solution of the coefficients  $T_{ij}$  via linear algebra matrix inversion. This is a reflection of the linear dependence amongst the external momenta. Note also in four dimensions, there can be at most four linearly independent external momenta.

appearing in eqn. 5.53). In general,  $\tilde{\nu}_i \neq \nu_i$ .

The massive version of the Passarino-Veltmann reduction formulae [205] are employed to cast each appearing scalar product as a linear combination of the  $D_i$ . These are

$$l \cdot l = D_1 + m_1^2, \quad (5.60)$$

$$l \cdot p_i = \frac{1}{2} [(l + q_i)^2 + m_i^2 - (l + q_{i-1})^2 - m_{i-1}^2 - q_i^2 + q_{i-1}^2], \quad (5.61)$$

$$= \frac{1}{2} [D_i - D_{i-1} + m_i^2 - m_{i-1}^2 - q_i^2 + q_{i-1}^2]. \quad (5.62)$$

For higher powers of scalar products, these formulae may be used iteratively. The naive finalised set of scalar integrals are then

$$I(\hat{\nu}_1, \dots, \hat{\nu}_N) = \int [dl] \frac{1}{D_1^{\hat{\nu}_1} \dots D_N^{\hat{\nu}_N}}, \quad (5.63)$$

where again, in general,  $\hat{\nu}_i \neq \tilde{\nu}_i$ . At this point, typically all such integrals obtained are converted to an ordered string and read by the software that is used to perform the reduction to a basis of master integrals. However, as noted above, due to the linear dependence in our external scales giving rise to linearly dependent propagators, this step is premature and would otherwise lead to an incomplete reduction (where the basis of master integrals is not minimal). We now discuss the manner in which we alleviate this linear dependence.

For each integral structure of the form  $C \cdot D_1^{\hat{\nu}_1} \dots D_n^{\hat{\nu}_n}$ , where  $C$  is a function of the external scales only, establish whether there exists a linear dependence amongst the denominators. If not, then the integral need not be considered further here and may be passed to the integral reduction stage. If there is such a dependence, then there exists a relation of the form

$$\sum_i A_i D_i + B = 0, \quad (5.64)$$

where again the  $A_i$  and  $B$  are functions of the external scales only. Suppose  $B \neq 0$ . Then we can multiply the integral structure by the identity

$$1 = -\frac{1}{B} \sum_i A_i D_i. \quad (5.65)$$

If, however, there is a dependence but  $B = 0$ , then choose some  $D_k$  and multiply the

integral structure instead by

$$1 = -\frac{1}{A_k D_k} \sum_{i \neq k} A_i D_i. \quad (5.66)$$

In this way, through a careful resolution of unity, we have systematically expressed an integral structure containing  $n$  denominators as a sum of structures containing  $n - 1$  denominators. The procedure should be repeated until the linear dependence has been removed. In one (two) iteration(s) of the algorithm, this allows, for example, the box (pentagon) integral to be linearly decomposed into a sum of triangle integrals.

Other solutions also exist in the literature to cure such linear dependences. In [206], for example, a method was devised to generate supplementary IBP identities accounting for linearly dependent momenta. This, however, requires a manual override of the IBP identities generated within the integral reduction tools and, moreover, leads to the introduction of many additional redundant equations in the system. A different procedure from this, but again based on a generalised partial fractioning routine, was implemented in the **\$Apart** package. In its first guise [207], this allowed for the decomposition of a product of propagators from the integral topology  $\{D_1, \dots, D_n\}$ , containing linearly dependent momenta, to be expressed as a sum of terms containing propagators  $\{\widetilde{D}_1, \dots, \widetilde{D}_n\}$  with linearly independent momenta. Here, in general,  $\widetilde{D}_i \neq D_i$ . The momentum shifts that the package performs therefore may produce a decomposition into structures containing different propagators from those in the original topology, which can be non-optimal for some applications. Recently, this was circumvented through an updated **\$FCApart** routine in **FeynCalc** for one-loop integrals and **\$ApartFF** for multi-loop ones. We have checked that the package then produces results in the same vein as that of the Leonartas' algorithm.

### 5.5.2 Integral Reduction

We map each Feynman diagram topology appearing in the quark and gluon subprocesses to a so-called *naive* auxiliary topology (NAT), defined as an auxiliary topology, see Section 2.4, generated neglecting the linear dependence of the external momenta (except that due to overall energy-momentum conservation). This mapping is surjective and we find that we can associate every diagram topology to at least one NAT in a collective set of fourteen. The explicit composition of each NAT is given in Appendix D.

As mentioned above, the rank-one and -two tensor user-specified decompositions above allow each diagram to be expressed as a linear combination of integral structures built

out of the linearly dependent propagators within its associated NAT and powers of scalar products between  $p, n$  and the loop momentum,  $l$ . After the use of the Passarino-Veltmann reduction formulae, the resulting integral structures are then linearly decomposed according to the Leinartas' algorithm [204], see above, before the finalised set of scalar integrals are expressed in terms of a basis of master integrals according to the output of REDUZE 2 [100]. This linear reduction algorithm maps integrals in a given NAT to integrals belonging to a sub-topology of the given NAT. The sub-topologies are chosen such that their propagators contain only linearly *independent* momenta. Importantly, the algorithm will not produce a linear decomposition of an integral appearing in NAT  $A$  into integrals belonging to a different NAT  $B$  - it therefore maintains the original mapping of the diagrams to a single NAT. The utility of this observation is that it allows us to construct a REDUZE 2 database with at most  $s = 4$  and  $r = 7$  for each NAT and readily express each diagram as a sum of master integrals. Note that without the implementation of such a procedure, a priori, the resulting scalar to master integral reduction via common reduction algorithms, such as REDUZE 2 used here, would be incomplete, as they assume the input external momenta are linearly independent. We find that all appearing integrals across all NAT's can be reduced to a basis set of master integrals comprising one tadpole, six bubbles and fourteen triangles. For the quark-subprocess, the results may be expressed in terms of the tadpole, three bubble and two triangle master integrals. All master integrals appearing in the quark subprocess also appear in the calculation of the gluon subprocess.

The integral reduction procedure generates decompositions containing  $d$  dependent coefficients that multiply the master integrals. These coefficients can give rise to spurious poles in  $\epsilon$ . We find that, in all decompositions across all NATs, a *single* spurious pole is only introduced in multiplication with a tadpole or bubble master integral. When an integral is multiplied by a spurious pole, we expand the integral to  $\mathcal{O}(\epsilon)$  inclusive. This produces terms of the form  $\epsilon/\epsilon$  which therefore contribute to the finite part of our coefficient functions. The spurious pole overlaps with the manifest poles in the  $\epsilon$  expansion of the tadpole and the bubble integral and gives rise to double poles in  $\epsilon$ . We find, however, that all double pole contributions vanish at the amplitude level. This is to be expected within the framework of collinear factorisation.

All one-loop master integrals obtained may be expressed analytically using existing literature, see [208] and [209]. We have derived expressions for all our master integrals in the ERL region,  $|\hat{\xi}| > 1$ , and checked them numerically to order  $\epsilon$  inclusive, where required, via QCDLoop [210] and pySecDec [211]. An initial attempt to extract an analytical expres-

sion for a particular triangle master integral appearing in both the quark and gluon subprocesses via **PackageX** [212] led to a bug being uncovered in the software’s analytic continuation prescription. This resulted in the generation of an incorrect non-vanishing imaginary part for this particular integral. Explicitly, the analytic expression that is produced for the two-mass propagator triangle `ScalarC0[Qsq, (4msq + Qsq(-1+xi))/(4 xi), (-4msq + Qsq(1+xi))/(4 xi), m, m, 0]` gives incorrect numerical results for a subset of the ERBL phase space, namely  $Q^2 < 4m^2/(1 - \hat{\xi}^2)$ , for a given  $m > 0$  and  $|\hat{\xi}| > 1$ . The fault was reported to the current author of the package and is to be corrected in its next patch version.<sup>6</sup>

### 5.5.3 Quark subprocess

At NLO, there are 62 quark initiated subprocess diagrams generated by **QGRAF**. All but 12 of these diagrams are not compatible with our colour and external kinematical constraints, so are rejected. A further 6 collectively vanish, as explained below. The quark  $q$  subprocess amplitude,  $A_q$ , to NLO therefore consists of the 6 Feynman diagram contributions,  $A_{a,q}$ , of Fig. 5.4 with

$$A_q = \sum_{a=1}^6 A_{a,q} \quad \text{and where} \quad A_{a,q} \sim \int \frac{d^d l}{(2\pi)^d} \text{Tr} \left( \chi_1 \Gamma_a^{(1)} \right) \text{Tr} \left( \chi_2 \Gamma_a^{(2)} \right). \quad (5.67)$$

Here,  $\chi_{1,2}$  are the HVM and GPD projectors and  $\Gamma_a^{(1,2)}$  encode the Dirac structure for each spin line in diagram  $a$ . The appearance of a trace at amplitude level is particularly noteworthy and is a reflection of our external colour and kinematical constraints.

Each of the four quark diagrams where the external photon couples to the open heavy quark or antiquark lines ((1),(2),(3) and (4) of Fig. 5.4) may be decomposed into a tadpole and two bubble master integrals that emerge from the Laporta algorithm. When the photon instead attaches to the heavy quark propagator ((5) and (6) of Fig. 5.4), there is in addition two triangle master integrals in the diagram decomposition. In this latter case, we have decomposed a pentagon integral, containing linearly dependent propagators, into a sum of triangles, bubbles and the tadpole integral which, by construction, contain only linearly independent propagators.

There are an additional six diagrams, analogous to those of Fig. 5.4, where the photon

---

<sup>6</sup>I would like to thank Hiren Patel for this private communication.

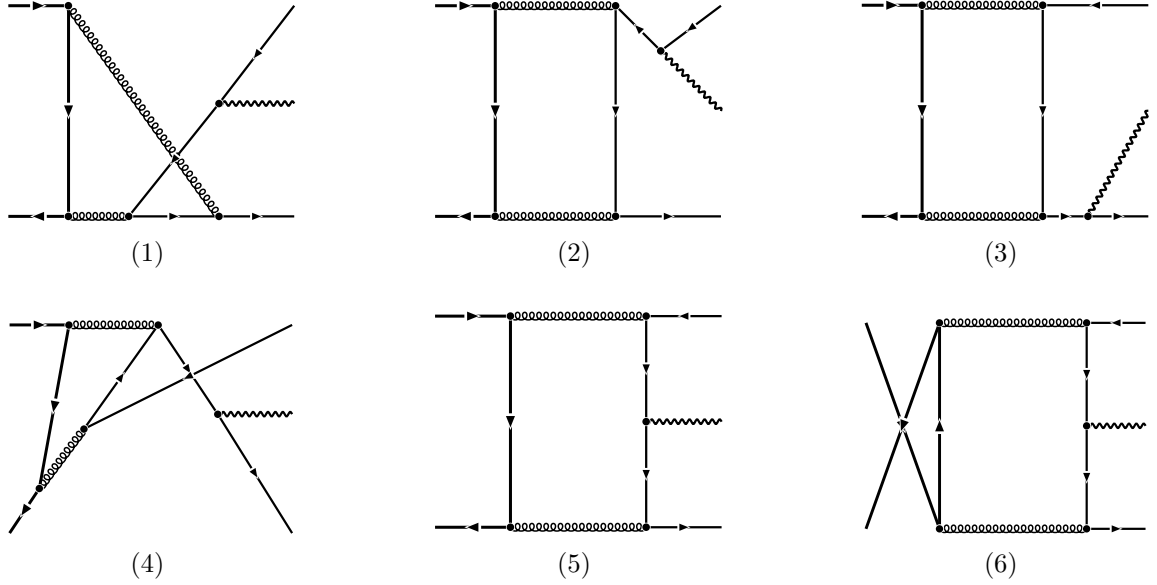


Figure 5.4: The six NLO quark subprocess diagrams.

instead attaches to the light quark line. We have checked that the sum of these diagrams equals zero. In fact, they cancel pairwise and this can be understood as a relative sign appearing between a diagram and its crossed counterpart. It arises as follows. Consider, without loss of generality, the two diagrams where the photon attaches to the light quark propagator on the lower spin line. The trace over the upper heavy quark spin line is the same for the diagram and its crossed version. The trace over the lower light quark spin line for the diagram is

$$\text{Tr}(\gamma^\sigma(\not{l} + q_1)\gamma^\mu(\not{l} + q_2)\gamma^\rho\not{p}), \quad (5.68)$$

while that for the crossed diagram is,

$$\text{Tr}(\gamma^\rho(-(\not{l} - q_1))\gamma^\mu(-(\not{l} - q_2))\gamma^\sigma\not{p}) \quad (5.69)$$

$$= \text{Tr}(\gamma^\rho(\not{l} + q_1)\gamma^\mu(\not{l} + q_2)\gamma^\sigma\not{p}) \quad (5.70)$$

$$= -\text{Tr}(\gamma^\sigma(\not{l} + q_1)\gamma^\mu(\not{l} + q_2)\gamma^\rho\not{p}). \quad (5.71)$$

Here,  $q_i$  are combinations of external momenta and, in the first equality, we used the reparametrisation invariance of the loop momentum  $l \rightarrow -l$  under the integral. In the second equality, we used the anticommutivity of the gamma matrices to reorder terms,



generating a minus relative to eqn. (5.68). Their sum therefore vanishes; a similar argument holds for the diagrams where the photon instead attaches to an external light quark line.

We normalise our quark NLO coefficient function with the factor

$$A_1 = (4\pi)^4 g_e e_q \left( \frac{\langle O_1 \rangle_V}{m^3} \right)^{1/2} C_\epsilon \left( \frac{\mu_0^2}{m^2} \right)^\epsilon, \quad (5.72)$$

where

$$C_\epsilon = \frac{\pi^{d/2}}{(2\pi)^d} \frac{\Gamma^2(d/2 - 1) \Gamma(3 - d/2)}{\Gamma(d - 3)} = \frac{1}{16\pi^2} \left( 1 - \epsilon(\gamma_E - \ln(4\pi)) \right) + \mathcal{O}(\epsilon^2), \quad (5.73)$$

arises from our loop integrals and the scale  $\mu_0$  is a mass parameter introduced in dimensional regularisation to maintain a dimensionless bare coupling. We recall that  $\gamma_E$  is the Euler-Mascheroni constant. The bare transverse quark NLO coefficient function can be written in the form

$$\hat{C}_{\perp,q}^{(1)} = \frac{T_F^2}{N_c^2} A_1 \left( \sum_{i=1}^{12} c_{\perp,i} f_i + \{v \rightarrow -v\} \right), \quad (5.74)$$

where the  $f_i$  are given in eqn. (5.49) and the  $c_{\perp,i}$  are

$$\begin{aligned} c_{\perp,1} &= \pi^2 \left( \frac{-8v^2 + 16v - 8}{-1 + vw^2} + \frac{8v^2 + 16v + 8}{1 + vw^2} + \frac{16}{w^4} - \frac{32}{w^2} \right), \\ c_{\perp,2} &= \frac{32}{w^3} - \frac{32}{w}, \quad c_{\perp,3} = \frac{-12v^2 + 24v - 12}{-1 + vw^2} + \frac{12v^2 + 24v + 12}{1 + vw^2} + \frac{24}{w^4} - \frac{48}{w^2}, \\ c_{\perp,4} &= -\frac{32}{(v+1)(w^2+1)} + \frac{16}{(v+1)w^2} + \frac{32}{(v-1)(w^2+1)} - \frac{16}{(v-1)w^2} + \frac{32}{w^2} - 32, \\ c_{\perp,5} &= 0, \quad c_{\perp,6} = \frac{1}{\epsilon} \left( \frac{64}{vw^4} + \frac{64v + 64}{1 + vw^2} - \frac{64}{vw^2} - \frac{64}{w^2} \right) + \frac{-32v - 64}{1 + vw^2} - \frac{64}{(v-1)(1 + vw^2)} \\ &\quad + \frac{32}{(v-1)w^2} + 32, \quad c_{\perp,7} = -\frac{64}{vw^4} + \frac{-64v - 64}{1 + vw^2} + \frac{64}{vw^2} + \frac{64}{w^2}, \quad c_{\perp,8} = -c_{\perp,7}, \\ c_{\perp,9} &= \frac{-24v^2 + 16v + 8}{-1 + vw^2} + \frac{24v^2 + 16v - 8}{1 + vw^2} + \frac{48}{w^4} - \frac{32}{w^2}, \\ c_{\perp,10} &= \frac{-48v^2 + 96v - 48}{-1 + vw^2} + \frac{-48v^2 - 96v - 48}{1 + vw^2} - \frac{64}{vw^4} + \frac{64v}{w^2} + \frac{64}{vw^2} + 32v, \\ c_{\perp,11} &= 0, \quad c_{\perp,12} = 0. \end{aligned} \quad (5.75)$$

Similarly, the bare longitudinal quark NLO coefficient function can be expressed as

$$\hat{C}_{L,q}^{(1)} = \frac{T_F^2}{N_c^2} A_1 \sqrt{w^2 - 1} \left( \sum_{i=1}^{12} c_{L,i} f_i + \{v \rightarrow -v\} \right), \quad (5.76)$$

where the  $f_i$  are given in eqn. (5.49) and the  $c_{L,i}$  are

$$\begin{aligned} c_{L,1} &= 0, \quad c_{L,2} = \frac{32}{w} - \frac{64}{w^3}, \quad c_{L,3} = 0, \\ c_{L,4} &= \frac{16}{(v+1)w^2} - \frac{16}{(v-1)w^2} - \frac{16}{v+1} + \frac{16}{v-1} - \frac{64}{w^2} + 32, \\ c_{L,5} &= 0, \quad c_{L,6} = \frac{1}{\epsilon} \left( \frac{64}{vw^4} + \frac{64v}{1+vw^2} - \frac{64}{w^2} \right) + \frac{64v}{1+vw^2} + \frac{32}{(v-1)w^2} - \frac{32}{v-1} - 32, \\ c_{L,7} &= -\frac{64}{vw^4} - \frac{64v}{1+vw^2} + \frac{64}{w^2}, \quad c_{L,8} = -c_{L,7}, \quad c_{L,9} = -\frac{32v}{-1+vw^2} - \frac{32v}{1+vw^2} + \frac{64}{w^2}, \\ c_{L,10} &= -\frac{64}{vw^4} + \frac{64v}{w^2} - 32v, \quad c_{L,11} = 0, \quad c_{L,12} = 0. \end{aligned} \quad (5.77)$$

The expressions for both the bare quark transverse and longitudinal coefficient functions are written in a manifestly symmetrised form, where  $v \rightarrow -v$  corresponds to the physical  $\hat{\xi} \rightarrow -\hat{\xi}$  symmetry. The expressions have been expanded in  $\epsilon$ , retaining the singular term in  $1/\epsilon$  and the finite term, while neglecting  $\mathcal{O}(\epsilon)$  terms which are not required at this order.

#### 5.5.4 Gluon subprocess

There are 160 gluon initiated subprocess diagrams at NLO, again generated in **QGRAF**, of which 63 are zero due to the GPD and NRQCD kinematical constraints. A further 16 vanish because they consist of an internal light quark or heavy quark fermion loop with two gluon attachments and one photon attachment. The vacuum expectation value of a time ordered product of an odd number of vector current insertions is zero so, as the time ordering encapsulates the two possible orientations of the fermion loop flow at the Feynman diagram level, we have a pairwise cancellation of diagrams in the gluon sector too, consisting of a closed polygon with three vector boson attachments. This is an analogous cancellation to that demonstrated in eqns. (5.68)-(5.71), following the same argument and is the perturbative realisation of Furry's theorem [213]. There are therefore 81 non-vanishing diagrams for the gluon subprocess at NLO, shown in Fig. 5.5.

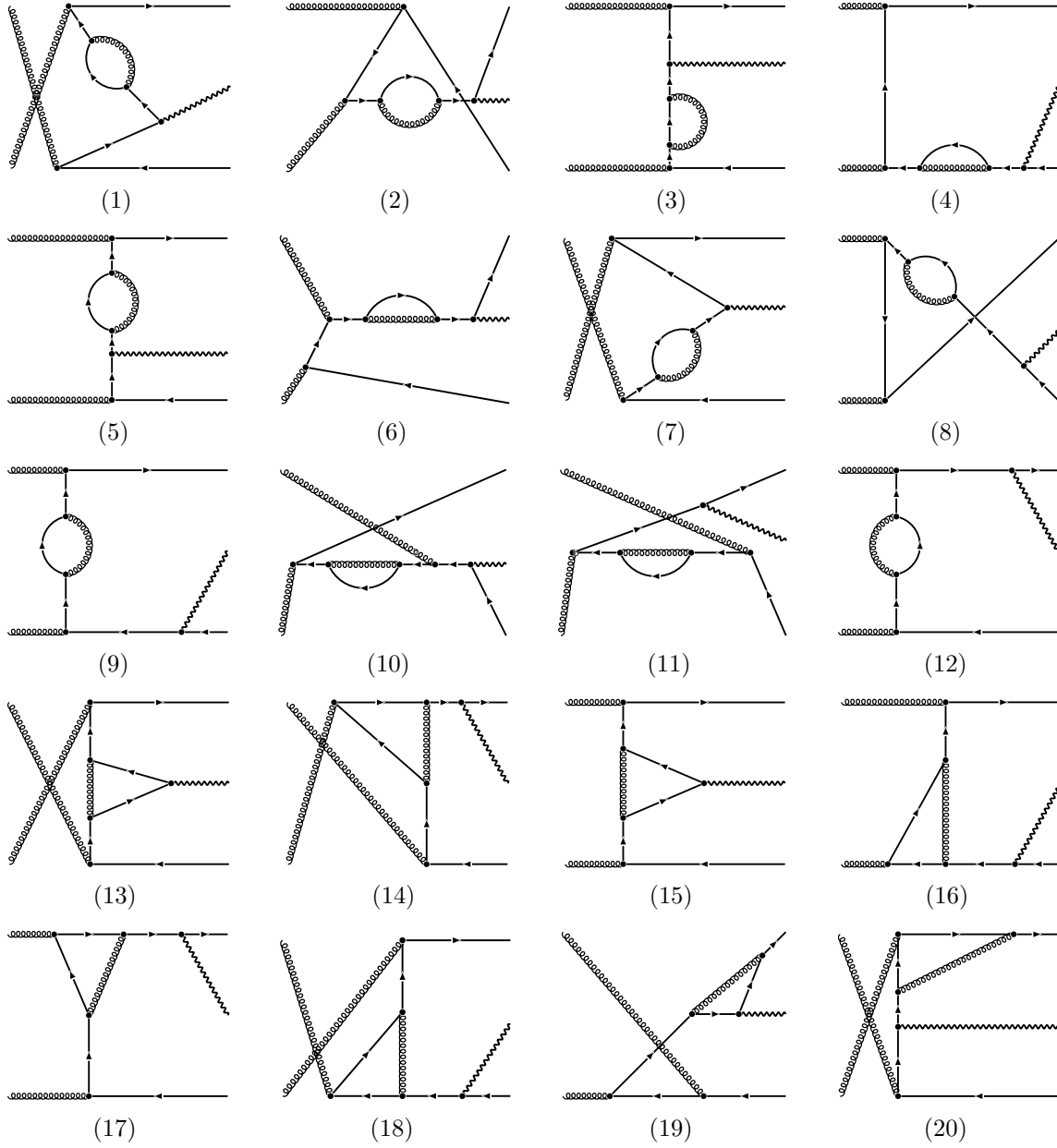


Figure 5.5: The NLO gluon subprocess diagrams, continued.

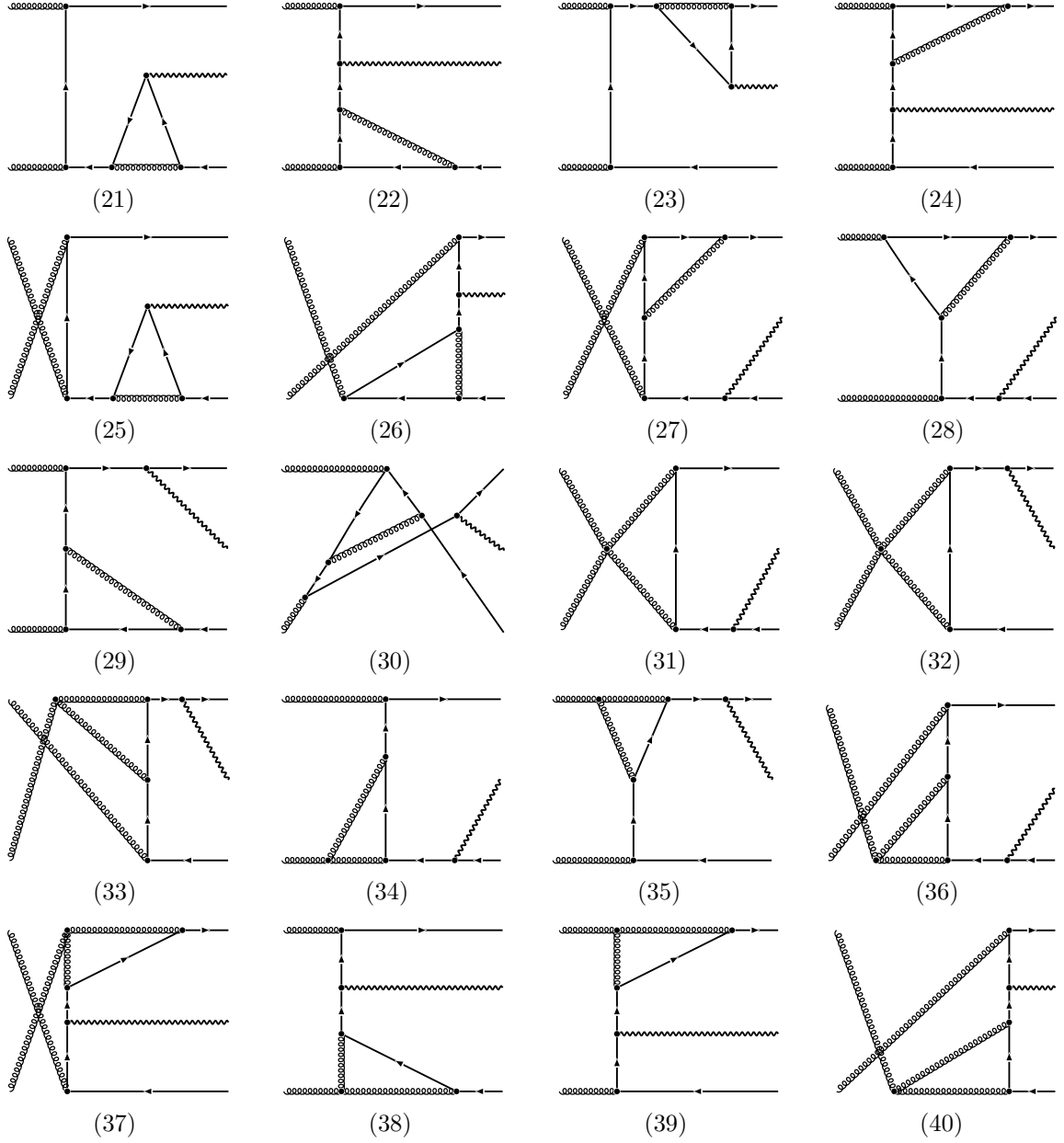


Figure 5.5: The NLO gluon subprocess diagrams, continued.

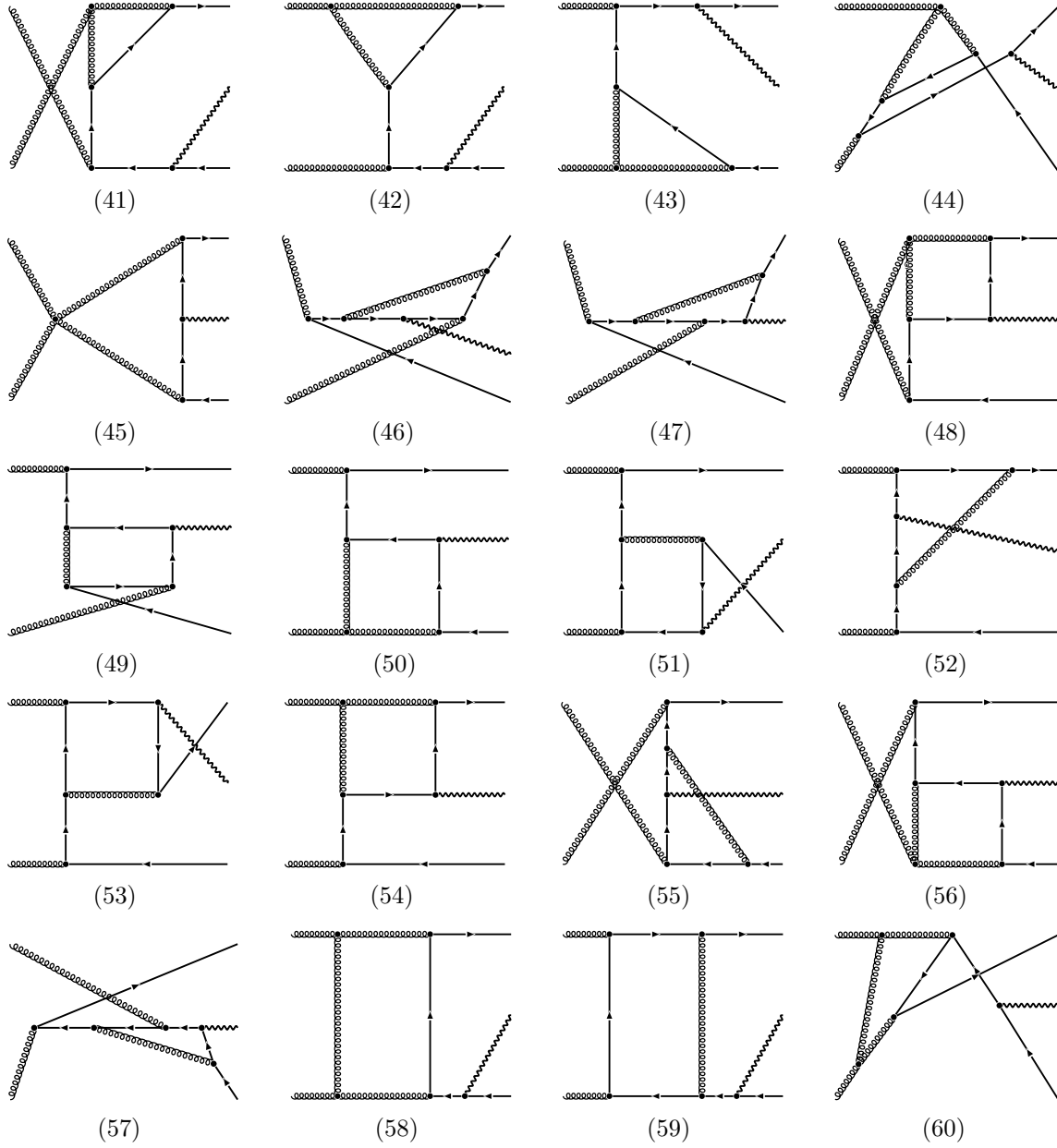


Figure 5.5: The NLO gluon subprocess diagrams, continued.

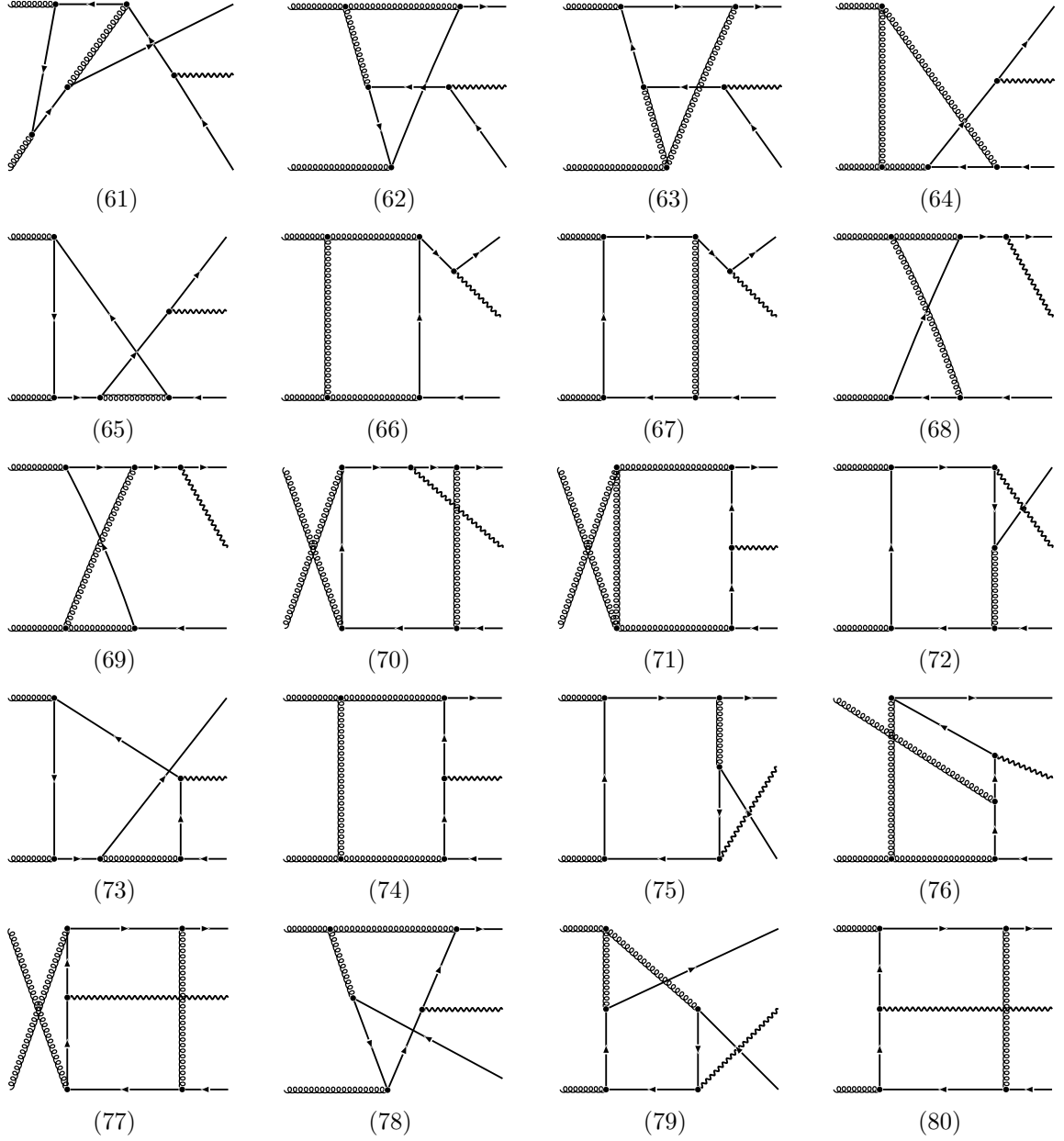


Figure 5.5: The NLO gluon subprocess diagrams, continued.

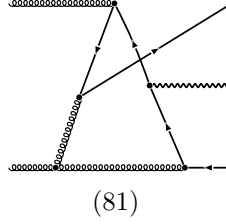


Figure 5.5: The NLO gluon subprocess diagrams.

We normalise our gluon NLO coefficient function with the factor

$$B_1 = (4\pi)^4 g_e e_q \left( \frac{\langle O_1 \rangle_V}{m^3} \right)^{1/2} \frac{X^2}{(X - \xi + i\delta)(X + \xi - i\delta)} C_\epsilon \left( \frac{\mu_0^2}{m^2} \right)^\epsilon, \quad (5.78)$$

where  $C_\epsilon$  is defined in eqn. (5.73).

The bare transverse gluon NLO coefficient function can be written in the form

$$\hat{C}_{\perp,g}^{(1)} = \frac{B_1}{N_c(N_c^2 - 1)} \left( \sum_{i=1}^{12} c_{\perp,i} f_i + \{v \rightarrow -v\} \right), \quad (5.79)$$

where the  $f_i$  are given in eqn. (5.49) and the  $c_{\perp,i}$  are

$$\begin{aligned} c_{\perp,1} = & \frac{C_F}{\epsilon} \left( -6 - \frac{12}{w^4} + \frac{6}{w^2} + \frac{-6+6v}{-1+vw^2} + \frac{6+6v}{1+vw^2} \right) + C_F \left( -32 + \frac{2}{1+v} - \frac{2}{-1+v} \right. \\ & + \pi^2 \left( -16 + \frac{16}{3w^4} - \frac{22-80v^2}{3w^2} \right) - \frac{16}{w^4} + \frac{40}{w^2} - \frac{2}{(1+v)w^2} + \frac{2}{(-1+v)w^2} + \frac{8}{1+w^2} \\ & + \frac{\pi^2 \left( -\frac{22}{3} + \frac{85v}{3} - \frac{104v^2}{3} + \frac{41v^3}{3} \right)}{(-1+vw^2)^2} - \frac{2-2v}{-1+vw^2} + \frac{\pi^2 \left( -\frac{49}{3} + 32v - \frac{7v^2}{3} - \frac{40v^3}{3} \right)}{-1+vw^2} \\ & + \frac{\pi^2 \left( -\frac{22}{3} - \frac{85v}{3} - \frac{104v^2}{3} - \frac{41v^3}{3} \right)}{(1+vw^2)^2} + \frac{2+2v}{1+vw^2} + \frac{\pi^2 \left( \frac{49}{3} + 32v + \frac{7v^2}{3} - \frac{40v^3}{3} \right)}{1+vw^2} \Big) \\ & + C_A \left( \pi^2 \left( \frac{22}{3} - \frac{4}{w^4} + \frac{8(1-v^2)}{w^2} \right) + \frac{\pi^2 \left( \frac{10}{3} - \frac{37v}{3} + \frac{44v^2}{3} - \frac{17v^3}{3} \right)}{(-1+vw^2)^2} \right. \\ & + \frac{\pi^2 \left( 9 - \frac{58v}{3} + \frac{19v^2}{3} + 4v^3 \right)}{-1+vw^2} + \frac{\pi^2 \left( \frac{10}{3} + \frac{37v}{3} + \frac{44v^2}{3} + \frac{17v^3}{3} \right)}{(1+vw^2)^2} \\ & \left. + \frac{\pi^2 \left( -9 - \frac{58v}{3} - \frac{19v^2}{3} + 4v^3 \right)}{1+vw^2} \right), \end{aligned}$$

$$\begin{aligned}
c_{\perp,2} &= C_F \left( 8v^2w^3 - 24v^2w + \frac{128v^2}{w} + \frac{-56v^3w + 52v^2w - 4vw}{-1 + vw^2} + \frac{-56v^3w - 52v^2w - 4vw}{1 + vw^2} \right. \\
&\quad \left. + \frac{40}{w^3} - \frac{40}{w} \right) + C_A \left( -\frac{64v^2}{w} + \frac{32v^3w - 52v^2w + 20vw}{-1 + vw^2} + \frac{32v^3w + 52v^2w + 20vw}{1 + vw^2} \right. \\
&\quad \left. - \frac{8}{w^3} + \frac{8}{w} \right), \\
c_{\perp,3} &= C_F \left( \frac{32v^2}{w^2} + \frac{-16v^3 + 32v^2 - 24v + 8}{-1 + vw^2} + \frac{-16v^3 - 32v^2 - 24v - 8}{1 + vw^2} + \frac{-3v^3 + 8v^2 - 7v + 2}{(-1 + vw^2)^2} \right. \\
&\quad \left. + \frac{3v^3 + 8v^2 + 7v + 2}{(1 + vw^2)^2} + \frac{10}{w^4} - \frac{12}{w^2} + 14 \right) + C_A \left( -\frac{8v^2}{w^2} + \frac{4v^3 - 6v^2 + 2}{-1 + vw^2} + \frac{4v^3 + 6v^2 - 2}{1 + vw^2} \right. \\
&\quad \left. + \frac{3v^3 - 8v^2 + 7v - 2}{(-1 + vw^2)^2} + \frac{-3v^3 - 8v^2 - 7v - 2}{(1 + vw^2)^2} - \frac{6}{w^4} + \frac{12}{w^2} + 2 \right), \\
c_{\perp,4} &= C_F \left( 8v^2w^4 - 24v^2w^2 + \frac{72v^2 - 44v - 16}{-1 + vw^2} + \frac{8v^2 - 52v - 56}{1 + vw^2} + 16v^2 - 4vw^4 + 20vw^2 \right. \\
&\quad \left. + \frac{4w^2 + \frac{4}{w^2} - 8}{(v+1)^2} + \frac{8}{(v+1)(w^2+1)} - \frac{8}{(v+1)(vw^2-1)} + \frac{8}{(w^2+1)(vw^2+1)} - \frac{64v}{w^2} \right. \\
&\quad \left. + \frac{-4w^4 - 8w^2 - \frac{8}{w^2} + 12}{v+1} - 32v + 4w^4 + 4w^2 - \frac{72}{w^2+1} + \frac{16}{(w^2+1)^2} + \frac{56}{w^2} \right) \\
&\quad + C_A \left( \frac{-8v^2 + 20v - 12}{-1 + vw^2} + \frac{8v^2 + 4v - 4}{1 + vw^2} + \frac{8 - \frac{8}{w^2}}{v+1} + \frac{16}{w^2+1} - \frac{8}{w^2} - 8 \right), \\
c_{\perp,5} &= C_A \left( \frac{16}{vw^4} + \frac{16 - 16v}{-1 + vw^2} + \frac{16v + 16}{1 + vw^2} - \frac{16}{vw^2} \right), \\
c_{\perp,6} &= \frac{C_A}{\epsilon} \left( -\frac{16}{vw^4} - \frac{32v + 32}{vw^2 + 1} + \frac{16}{vw^2} + \frac{16}{w^2} + 16 \right) \\
&\quad + C_F \left( -8v^2w^4 + 24v^2w^2 + \frac{-88v^2 + 136v - 48}{-1 + vw^2} + \frac{168v^2 + 128v - 16}{1 + vw^2} - 16v^2 - 4vw^4 \right. \\
&\quad \left. + 20vw^2 + \frac{-4w^2 - \frac{4}{w^2} + 8}{(v-1)^2} + \frac{16}{(v-1)(vw^2+1)} - \frac{64v}{w^2} + \frac{-4w^4 - 8w^2 - \frac{8}{w^2} + 12}{v-1} - 32v \right. \\
&\quad \left. - 4w^4 - 4w^2 - 16 \right) + C_A \left( \frac{-40v^2 - 80v - 40}{1 + vw^2} + \frac{40v^2 - 64v + 24}{-1 + vw^2} + \frac{8 - \frac{8}{w^2}}{v-1} + 64 \right), \\
c_{\perp,7} &= C_A \left( \frac{16}{vw^4} + \frac{32(v+1)}{vw^2+1} - \frac{16}{vw^2} - \frac{16}{w^2} - 16 \right), \\
c_{\perp,8} &= C_F \left( -\frac{64v^2}{w^2} + \frac{-12v^3 - 56v^2 + 100v - 32}{-1 + vw^2} + \frac{76v^3 + 24v^2 - 84v - 32}{1 + vw^2} \right. \\
&\quad \left. + \frac{76v^3 - 192v^2 + 156v - 40}{(-1 + vw^2)^2} + \frac{12v^3 + 32v^2 + 28v + 8}{(1 + vw^2)^2} + \frac{32v}{w^2} + \frac{8}{w^2} + 24 \right) \\
&\quad + C_A \left( \frac{32v^2}{w^2} + \frac{4v^3 + 16v^2 - 28v + 8}{-1 + vw^2} + \frac{-36v^3 - 16v^2 + 20v}{1 + vw^2} + \frac{-28v^3 + 72v^2 - 60v + 16}{(-1 + vw^2)^2} \right)
\end{aligned}$$



$$\begin{aligned}
& + \frac{-12v^3 - 32v^2 - 28v - 8}{(1 + vw^2)^2} - \frac{16}{vw^4} + \frac{16}{vw^2} + \frac{16}{w^2} - 16 \Big), \\
c_{\perp,9} = & C_F \left( \frac{96v^2}{w^2} + \frac{-48v^3 + 42v^2 + 16v - 10}{-1 + vw^2} + \frac{-48v^3 - 42v^2 + 16v + 10}{1 + vw^2} + \frac{28}{w^4} - \frac{36}{w^2} - 12 \right) \\
& + C_A \left( -\frac{32v^2}{w^2} + \frac{16v^3 - 6v^2 - 12v + 2}{-1 + vw^2} + \frac{16v^3 + 6v^2 - 12v - 2}{1 + vw^2} - \frac{12}{w^4} + \frac{8}{w^2} + 8 \right), \\
c_{\perp,10} = & C_F \left( -8v^3w^4 + 24v^3w^2 - 16v^3 + \frac{-20v^3 + 60v^2 - 52v + 12}{-1 + vw^2} + \frac{20v^3 + 60v^2 + 52v + 12}{1 + vw^2} \right. \\
& + \frac{-12v^3 + 32v^2 - 28v + 8}{(-1 + vw^2)^2} + \frac{-12v^3 - 32v^2 - 28v - 8}{(1 + vw^2)^2} + 8vw^2 - 64v \Big) \\
& + C_A \left( \frac{-4v^3 + 4v^2 - 4v + 4}{-1 + vw^2} + \frac{4v^3 + 4v^2 + 4v + 4}{1 + vw^2} + \frac{12v^3 - 32v^2 + 28v - 8}{(-1 + vw^2)^2} \right. \\
& + \frac{12v^3 + 32v^2 + 28v + 8}{(1 + vw^2)^2} + \frac{16}{vw^4} - \frac{32v}{w^2} - \frac{16}{vw^2} + 8v \Big), \\
c_{\perp,11} = & C_F \left( \frac{-88v^2 + 64v + 8}{-1 + vw^2} + \frac{88v^2 + 136v + 48}{1 + vw^2} + \frac{16(v + 1)}{vw^2 - 2v - 1} - 24 \right) \\
& + C_A \left( \frac{40v^2 - 64v + 24}{-1 + vw^2} - \frac{40v^2 + 64v + 24}{1 + vw^2} - \frac{8(v + 1)}{vw^2 - 2v - 1} + 40 \right), \\
c_{\perp,12} = & C_F \left( -\frac{22v^2 + 34v + 12}{1 + vw^2} + \frac{22v^2 - 34v - 10w^2 + 22}{-1 + vw^2} - \frac{-4v - 10w^2 + 6}{vw^2 - 2v - 1} + 28 \right) \\
& + C_A \left( \frac{10v^2 + 16v + 6}{1 + vw^2} - \frac{10v^2 - 14v + 2(w^2 + 1)}{-1 + vw^2} + \frac{6v + 2w^2 + 4}{vw^2 - 2v - 1} - 4 \right).
\end{aligned}$$

We have checked that the  $Q^2 \rightarrow 0$  ( $w \rightarrow \infty$ ) limit of the above maps onto the expression given in [18] for the photoproduction set-up. We remind that

$$v = \frac{\hat{\xi}}{w^2} \quad \text{with} \quad w = \sqrt{1 - \frac{4m^2}{Q^2}}. \quad (5.80)$$

The bare longitudinal gluon NLO coefficient function can be written in the form

$$\hat{C}_{L,g}^{(1)} = \frac{B_1}{N_c(N_c^2 - 1)} \sqrt{w^2 - 1} \left( \sum_{i=1}^{12} c_{L,i} f_i + \{v \rightarrow -v\} \right), \quad (5.81)$$

where the  $f_i$  are given in eqn. (5.49) and the  $c_{L,i}$  are

$$c_{L,1} = -\frac{C_F}{\epsilon} \frac{12}{w^4} + C_F \left( \frac{272v - 256v^3}{-1 + vw^2} + \frac{256v^3 - 272v}{1 + vw^2} + \pi^2 \left( -\frac{64v^2}{3w^2} - \frac{20}{3w^4} + \frac{28}{3w^2} \right) \right)$$

$$\begin{aligned}
 & + \frac{\pi^2 \left( \frac{32v^3}{3} + 14v^2 - \frac{74v}{3} \right)}{-1 + vw^2} + \frac{\pi^2 \left( \frac{32v^3}{3} - 14v^2 - \frac{74v}{3} \right)}{1 + vw^2} + \frac{\pi^2 \left( -\frac{64v^3}{3} + \frac{128v^2}{3} - \frac{64v}{3} \right)}{(-1 + vw^2)^2} \\
 & + \frac{256v^3 - 512v^2 + 256v}{(-1 + vw^2)^2} + \frac{\pi^2 \left( \frac{64v^3}{3} + \frac{128v^2}{3} + \frac{64v}{3} \right)}{(1 + vw^2)^2} + \frac{256v^3 + 512v^2 + 256v}{(1 + vw^2)^2} \\
 & - \frac{2w^2}{v-1} + \frac{2w^2}{v+1} + \frac{2}{(v-1)w^2} - \frac{2}{(v+1)w^2} - \frac{16}{w^4} - 4w^2 + \frac{32}{w^2} \Big) \\
 & + C_A \left( \frac{64v^3 - 64v}{-1 + vw^2} + \frac{64v - 64v^3}{1 + vw^2} + \frac{8\pi^2 v^2}{w^2} + \frac{\pi^2 \left( -4v^3 - \frac{8v^2}{3} + \frac{20v}{3} \right)}{-1 + vw^2} \right. \\
 & + \frac{\pi^2 \left( -4v^3 + \frac{8v^2}{3} + \frac{20v}{3} \right)}{1 + vw^2} + \frac{-64v^3 + 128v^2 - 64v}{(-1 + vw^2)^2} + \frac{\pi^2 \left( \frac{16v^3}{3} - \frac{32v^2}{3} + \frac{16v}{3} \right)}{(-1 + vw^2)^2} \\
 & \left. + \frac{-64v^3 - 128v^2 - 64v}{(1 + vw^2)^2} + \frac{\pi^2 \left( -\frac{16v^3}{3} - \frac{32v^2}{3} - \frac{16v}{3} \right)}{(1 + vw^2)^2} \right), \\
 c_{L,2} = & C_F \left( -8v^2 w^3 + 32v^2 w - \frac{160v^2}{w} + \frac{64v^3 w - 72v^2 w}{-1 + vw^2} + \frac{64v^3 w + 72v^2 w}{1 + vw^2} - \frac{32}{w^3} + \frac{32}{w} \right) \\
 & + C_A \left( \frac{32v^2}{w} + \frac{16v^2 w - 16v^3 w}{-1 + vw^2} + \frac{-16v^3 w - 16v^2 w}{1 + vw^2} + \frac{16}{w^3} - \frac{8}{w} \right), \\
 c_{L,3} = & C_F \left( -\frac{40v^2}{w^2} + \frac{20v^3 - 26v^2 + 2v}{-1 + vw^2} + \frac{20v^3 + 26v^2 + 2v}{1 + vw^2} - \frac{8}{w^4} + \frac{12}{w^2} \right) \\
 & + C_A \left( \frac{16v^2}{w^2} + \frac{-8v^3 + 16v^2 - 8v}{-1 + vw^2} + \frac{-8v^3 - 16v^2 - 8v}{1 + vw^2} \right), \\
 c_{L,4} = & C_F \left( -8v^2 w^4 + 32v^2 w^2 + \frac{-48v^2 + 48v - 16}{-1 + vw^2} + \frac{80v^2 + 80v}{1 + vw^2} - 32v^2 + 4vw^4 - 24vw^2 \right. \\
 & - \frac{16}{(v+1)(w^2+1)} + \frac{16}{(v+1)(-1+vw^2)} - \frac{16}{(w^2+1)(1+vw^2)} - \frac{64v+16}{w^2} - \frac{8}{(v+1)w^2} \\
 & + \frac{4}{(v+1)^2 w^2} + \frac{-4w^4 - 16w^2 + 44}{v+1} - \frac{-4w^4 + 4w^2 + 4}{(v+1)^2} + 48v + 20w^2 + \frac{48}{w^2+1} - 40 \Big) \\
 & + C_A \left( \frac{-16v^2 - 48v}{1 + vw^2} + \frac{16v^2 + 16v}{-1 + vw^2} - \frac{8}{(v+1)w^2} + \frac{8}{v+1} + \frac{16}{w^2} - 8 \right), \\
 c_{L,5} = & C_A \left( \frac{16}{vw^4} - \frac{16v}{-1 + vw^2} + \frac{16v}{1 + vw^2} \right), \\
 c_{L,6} = & \frac{C_A}{\epsilon} \left( -\frac{16}{vw^4} - \frac{32v}{1 + vw^2} + \frac{16}{w^2} \right) + C_F \left( 8v^2 w^4 - 32v^2 w^2 + \frac{128v^2 - 128v}{-1 + vw^2} + \frac{-96v^2 - 96v - 32}{1 + vw^2} \right. \\
 & + 32v^2 + 4vw^4 - 24vw^2 - \frac{32}{(v-1)(1+vw^2)} - \frac{64v}{w^2} + \frac{-4w^4 - 16w^2 - \frac{8}{w^2} + 44}{v-1} \\
 & \left. + \frac{-4w^4 + 4w^2 - \frac{4}{w^2} + 4}{(v-1)^2} + 48v - 20w^2 + 40 \right) + C_A \left( \frac{32v - 32v^2}{-1 + vw^2} + \frac{32v^2 - 32v}{1 + vw^2} \right)
 \end{aligned}$$

$$\begin{aligned}
& + \frac{8 - \frac{8}{w^2}}{v - 1} + 8 \Big), \\
c_{L,7} &= C_A \left( \frac{16}{vw^4} + \frac{32v}{1 + vw^2} - \frac{16}{w^2} \right), \\
c_{L,8} &= C_F \left( -\frac{64v^2}{w^2} + \frac{96v^3 - 16v^2 - 80v}{-1 + vw^2} + \frac{-32v^3 - 16v^2 + 16v}{1 + vw^2} + \frac{-128v^3 + 256v^2 - 128v}{(-1 + vw^2)^2} \right. \\
& \quad \left. + \frac{32v}{w^2} + \frac{8}{w^2} \right) + C_A \left( \frac{32v - 32v^3}{-1 + vw^2} + \frac{32v^2}{w^2} + \frac{32v^3 - 64v^2 + 32v}{(-1 + vw^2)^2} - \frac{16}{vw^4} - \frac{32v}{1 + vw^2} + \frac{16}{w^2} \right), \\
c_{L,9} &= C_F \left( -\frac{48v^2}{w^2} + \frac{24v^3 - 24v^2}{-1 + vw^2} + \frac{24v^3 + 24v^2}{1 + vw^2} - \frac{8}{w^4} + \frac{8}{w^2} \right) \\
& \quad + C_A \left( \frac{16v^2}{w^2} + \frac{-8v^3 + 16v^2 + 8v}{-1 + vw^2} + \frac{-8v^3 - 16v^2 + 8v}{1 + vw^2} - \frac{16}{w^2} \right), \\
c_{L,10} &= C_F \left( 8v^3w^4 - 32v^3w^2 + 32v^3 + \frac{16v^3 - 32v^2 + 16v}{-1 + vw^2} + \frac{-16v^3 - 32v^2 - 16v}{1 + vw^2} + 16v \right) \\
& \quad + C_A \left( \frac{-16v^3 + 32v^2 - 16v}{-1 + vw^2} + \frac{16v^3 + 32v^2 + 16v}{1 + vw^2} + \frac{16}{vw^4} - \frac{32v}{w^2} - 8v \right), \\
c_{L,11} &= C_F \left( \frac{-128v^2 - 128v}{1 + vw^2} + \frac{128v^2 - 144v}{-1 + vw^2} \right) + C_A \left( \frac{32v - 32v^2}{-1 + vw^2} + \frac{32v^2 + 32v}{1 + vw^2} \right), \\
c_{L,12} &= C_F \left( \frac{-32v^2 + 36v + 4}{-1 + vw^2} + \frac{32v^2 + 32v}{1 + vw^2} - \frac{4v + 4}{vw^2 - 2v - 1} \right) \\
& \quad + C_A \left( \frac{8v^2 - 16v + 8}{-1 + vw^2} - \frac{8v^2 + 8v}{1 + vw^2} - \frac{8(v + 1)}{vw^2 - 2v - 1} \right).
\end{aligned}$$

Here,  $C_F$  and  $C_A$  are the fundamental and adjoint Casimirs of  $SU(N_c)$ . With  $N_c = 3$ ,  $C_F = 4/3$  and  $C_A = 3$ . The result is expressed using the recent **MultivariateApart** package [214] which performs a partial fractioning routine of rational functions via polynomial reductions, resulting in coefficients that contain terms with modest numerator and denominator degrees. Diagram group theory factors recur in three combinations:  $C_F, C_A$  and  $C_F - C_A/2$ , see Appendix A.0.3. The  $C_F$  factor arises from the one loop bubble insertions in Figs. 5.5.1-5.5.12, while a gluon attachment to the gluon or quark line therein gives a factor  $C_A$  or  $C_F - C_A/2$ , respectively, which are all diagrams in the NLO computation. The physical symmetry  $\hat{\xi} \rightarrow -\hat{\xi}$  is again made apparent in our presentation of the NLO gluon coefficient functions, eqns. (5.79) and (5.81).

We remark that the length of the expressions is due to the appearance of two independent massive scales,  $Q^2$  and  $m^2$ , in our kinematic set-up which, nonetheless, possess a physical symmetry and well-defined  $Q^2 \rightarrow 0$  limit. The  $m^2 \rightarrow 0$  limit, however, is not well-defined and therefore does not map onto the coefficient functions for the electroproduction

of a light vector meson. The  $\hat{\xi} \rightarrow 0$  limit corresponds to the high energy limit and will be considered in Section 5.7.

We have observed that a subset of the diagrams of Fig. 5.5 contribute at  $\mathcal{O}(\epsilon)$  or  $\mathcal{O}(\epsilon^2)$  to the gluon transverse NLO coefficient function and therefore vanish in the limit  $\epsilon \rightarrow 0$ . In particular, diagrams in Figs. 5.5.20, 5.5.22, 5.5.24, 5.5.26, 5.5.37, 5.5.38, 5.5.39 and 5.5.40 contribute at  $\mathcal{O}(\epsilon)$  and diagrams in Figs. 5.5.13 and 5.5.15 contribute at  $\mathcal{O}(\epsilon^2)$ . The latter correspond to a gluon correction of the photon, heavy-quark, heavy-antiquark vertex and correspond to one-loop corrections of the tree level diagrams in Figs. 5.3.5 and 5.3.6 which contribute at  $\mathcal{O}(\epsilon)$  to the gluon transverse LO coefficient function. Of those diagrams mentioned above that contribute at  $\mathcal{O}(\epsilon)$  to the gluon transverse NLO coefficient function, we find that their contribution to the gluon longitudinal NLO coefficient function vanishes. These correspond to an equivalence class of one-particle reducible diagrams where a triangle loop insertion is on one side of the diagram after snipping a heavy-quark propagator. Another analogous set of diagrams in Figs. 5.5.1, 5.5.3, 5.5.5 and 5.5.7, where there is instead a bubble loop insertion on one side, again have a vanishing contribution to the gluon longitudinal NLO coefficient function but contribute at  $\mathcal{O}(\epsilon^0)$  to the transverse degree of freedom.

## 5.6 UV renormalisation and mass factorisation

We renormalise the gluon, heavy quark field and heavy quark mass in the on-shell (OS) scheme. The strong coupling constant is renormalised with light flavours treated in the  $\overline{\text{MS}}$  scheme and with the heavy quark loop of the gluon self-energy subtracted at zero momentum. The UV renormalised amplitude  $\mathcal{A}_{\text{UV}}$  may be written in terms of the bare amplitude  $\mathcal{A}$  using the relation<sup>7</sup>,

$$\begin{aligned} \mathcal{A}^{\text{UV}} &= Z_A^{n_g/2} Z_2^{n_q/2} \mathcal{A}(\hat{a}_s \rightarrow a_s S_\epsilon^{-1} (\mu_R^2/\mu_0^2)^\epsilon Z_\alpha, \hat{m} \rightarrow m Z_m) \\ &= a_s S_\epsilon^{-1} \left( \frac{\mu_R^2}{\mu_0^2} \right)^\epsilon \left( \mathcal{A}^{(0)} + a_s \left( \frac{n_g}{2} \delta Z_A + \frac{n_q}{2} \delta Z_2 + \delta Z_\alpha \right) \mathcal{A}^{(0)} \right. \\ &\quad \left. + a_s \delta Z_m \mathcal{A}^{\text{mct},(0)} + a_s S_\epsilon^{-1} \left( \frac{\mu_R^2}{\mu_0^2} \right)^\epsilon \mathcal{A}^{(1)} + \mathcal{O}(a_s^2) \right). \end{aligned} \quad (5.82)$$

---

<sup>7</sup>Here we omit the renormalisation of the light-quark wave function, which is not relevant at this order as the quark amplitudes enter only at  $a_s^2$ .

Here,  $\hat{a}_s = \hat{\alpha}_s/(4\pi)$  and  $a_s = \alpha_s(\mu_R^2)/(4\pi)$  are the bare and renormalised strong couplings, respectively. We have introduced  $S_\epsilon = (4\pi)^\epsilon e^{-\gamma_E \epsilon}$ , which accounts for the modification of eqn. (2.6) in the  $\overline{\text{MS}}$  scheme. The heavy quark bare mass parameter is denoted  $\hat{m}$  and the renormalised quark mass is denoted  $m$ . The gluon and heavy quark renormalisation constants are denoted  $Z_A$  and  $Z_2$  and the number of external gluons and heavy quarks are denoted  $n_g$  and  $n_q$ , respectively. In the second line the bare amplitude and renormalisation constants are expanded using

$$\begin{aligned}\mathcal{A} &= \hat{a}_s \mathcal{A}^{(0)} + \hat{a}_s^2 \mathcal{A}^{(1)} + \mathcal{O}(\hat{a}_s^3), \\ Z_i &= 1 + a_s \delta Z_i + \mathcal{O}(a_s^2) \quad (i = A, 2, \alpha, m).\end{aligned}\tag{5.83}$$

We have also introduced the mass counterterm amplitude  $\mathcal{A}^{\text{mct}}$  which is found, as part of the typical quantum field theory UV renormalisation procedure, by inserting mass counterterm vertices into the tree level gluon diagrams of Fig. 5.3 and cross-checked by computing the derivative of the bare amplitude with respect to  $\hat{m}$ . Explicitly,

$$A(\hat{m}) \rightarrow A(Z_m m) = A(m) + a_s \delta Z_m \left. \frac{dA(\hat{m})}{d\hat{m}} \right|_{\hat{m}=m} + \dots\tag{5.84}$$

We emphasise that this is a derivative with respect to the *bare* mass. We therefore made a distinction, in the computation of this derivative, between the bare heavy quark mass  $\hat{m}$  appearing in the QCD Lagrangian (and which therefore appears in the propagators  $D_i$  of our loop integrals) and the mass parameter  $M$  in the HVM spin projector (which is set numerically equal to twice the *renormalised* heavy quark mass at LO in NRQCD). One must be mindful of this distinction too in a similar computation performed for the UV mass renormalisation at a higher-order so as to allow for a consistent and correct treatment of the UV physics.

The explicit expressions for the renormalisation constants at one-loop are

$$\delta Z_\alpha = -\frac{1}{\epsilon} \beta_0 + \delta Z_\alpha^{\text{hq}}, \quad \beta_0 = \frac{11}{3} C_A - \frac{4}{3} T_F N_f,\tag{5.85}$$

$$\delta Z_A = -\delta Z_\alpha^{\text{hq}} = \left( \frac{\mu_R^2}{m^2} \right)^\epsilon \left( -\frac{4}{3\epsilon} T_F \right),\tag{5.86}$$

$$\delta Z_2 = \delta Z_m = \left( \frac{\mu_R^2}{m^2} \right)^\epsilon C_F \left( -\frac{3}{\epsilon} - 4 \right).\tag{5.87}$$

The last relation follows as  $Z_2 = Z_m$  at one-loop [215], where  $Z_m$  is the renormalisation constant for  $\hat{m}$ .

Although the above renormalisation procedure is stated for the bare amplitudes, it can equally be applied to each of the bare coefficient functions  $\hat{C}_{i=\perp,L,j=g,q}$ . The UV renormalised coefficient functions are thus given by

$$\hat{C}_{i,j}^{(0),\text{UV}} = S_\epsilon^{-1} \left( \frac{\mu_R^2}{\mu_0^2} \right)^\epsilon \hat{C}_{i,j}^{(0)}, \quad (5.88)$$

$$\begin{aligned} \hat{C}_{i,j}^{(1),\text{UV}} = & S_\epsilon^{-2} \left( \frac{\mu_R^2}{\mu_0^2} \right)^{2\epsilon} \hat{C}_{i,j}^{(1)} + \left( \frac{n_g}{2} \delta Z_A + \frac{n_q}{2} \delta Z_2 + \delta Z_\alpha \right) \hat{C}_{i,j}^{(0),\text{UV}} \\ & + S_\epsilon^{-1} \left( \frac{\mu_R^2}{\mu_0^2} \right)^\epsilon \delta Z_m \hat{C}_{i,j}^{\text{mct},(0)}. \end{aligned} \quad (5.89)$$

The relevant mass counterterm coefficient functions are

$$\hat{C}_{\perp,g}^{\text{mct},(0)} = \frac{4B_0}{N_c(N_c^2 - 1)} \left( \frac{v-1}{vw^2-1} (1-\epsilon) + \frac{v+1}{vw^2+1} (1-\epsilon) - \frac{2}{w^4} + \frac{3}{w^2} - 3 + 2\epsilon \right), \quad (5.90)$$

$$\hat{C}_{L,g}^{\text{mct},(0)} = \frac{8B_0}{N_c(N_c^2 - 1)} \frac{(w^2 - 1)^{3/2}}{w^4}. \quad (5.91)$$

Note that the  $v$  and  $w$  dependence in  $\hat{C}_{i,g}^{\text{mct},(0)}$  differ from that in the corresponding bare tree level coefficient functions because of the derivative in  $A^{\text{mct},(0)}$ . Since the quark amplitudes enter only at  $a_s^2$  they are trivially modified by the above procedure.

After renormalisation in the UV, poles in  $\epsilon$  still remain in both the quark and gluon one-loop coefficient functions and must be absorbed into the definition of the GPDs via mass factorisation, as outlined in Section 2.1. This procedure generates additional counterterms which finally render the coefficient functions finite at the amplitude level. Concretely, we replace the bare quark singlet ( $\hat{F}^S$ ) and gluon ( $F^g$ ) GPDs with the mass factorised, factorisation scale ( $\mu_F$ ) dependent, GPDs,

$$\begin{aligned} \hat{F}^S(X, \xi) = & F^S(X, \xi, \mu_F^2) + \frac{a_s}{\epsilon} \left( \frac{\mu_R^2}{\mu_F^2} \right)^\epsilon \\ & \times \int_{-1}^1 \frac{dz}{|\xi|} \left[ V_{qq}^{(1)} \left( \frac{X}{\xi}, \frac{z}{\xi} \right) F^S(z, \xi, \mu_F^2) + \xi^{-1} V_{qg}^{(1)} \left( \frac{X}{\xi}, \frac{z}{\xi} \right) F^g(z, \xi, \mu_F^2) \right], \end{aligned} \quad (5.92)$$

$$\begin{aligned} \hat{F}^g(X, \xi) &= F^g(X, \xi, \mu_F^2) + \frac{a_s}{\epsilon} \left( \frac{\mu_R^2}{\mu_F^2} \right)^\epsilon \\ &\times \int_{-1}^1 \frac{dz}{|\xi|} \left[ \xi V_{gq}^{(1)} \left( \frac{X}{\xi}, \frac{z}{\xi} \right) F^S(z, \xi, \mu_F^2) + V_{gg}^{(1)} \left( \frac{X}{\xi}, \frac{z}{\xi} \right) F^g(z, \xi, \mu_F^2) \right]. \end{aligned} \quad (5.93)$$

Here  $V^{(1)}$  is the coefficient of  $\alpha_s/(4\pi)$  in the generalised splitting function  $V$ . See Appendix C for their explicit expressions. Inserting these relations into the bare version of the factorisation formula eqn. (5.38) and absorbing the divergent terms into the coefficient functions we obtain

$$C_{i,j}^{(1)} = \hat{C}_{i,j}^{(1),\text{UV}} + \hat{C}_{i,j}^{\text{mf},(1)}, \quad (5.94)$$

where  $\hat{C}_{i,j}^{\text{mf},(1)}$  are the mass factorisation counterterms. Explicitly, expanding the transverse part of eqn. (5.38) in terms of bare coefficient functions and GPDs, and to  $\mathcal{O}(\hat{a}_s^2)$ , gives

$$\begin{aligned} \mathcal{T}^{(\mu\nu)} &= -g_\perp^{\mu\nu} \int_{-1}^1 \frac{dX}{X} \left[ \hat{a}_s \hat{C}_{\perp,q}^{(0)} \left( \frac{\xi}{X}, Q^2 \right) \frac{\hat{F}^S(X, \xi)}{2} + \hat{a}_s \hat{C}_{\perp,g}^{(0)} \left( \frac{\xi}{X}, Q^2 \right) \frac{\hat{F}^g(X, \xi)}{X} \right. \\ &\quad \left. + \hat{a}_s^2 \hat{C}_{\perp,q}^{(1)} \left( \frac{\xi}{X}, Q^2 \right) \frac{\hat{F}^S(X, \xi)}{2} + \hat{a}_s^2 \hat{C}_{\perp,g}^{(1)} \left( \frac{\xi}{X}, Q^2 \right) \frac{\hat{F}^g(X, \xi)}{X} \right] + \dots, \end{aligned} \quad (5.95)$$

where the ellipses denote contributions that are higher twist or higher order in  $\hat{a}_s$ . As  $\hat{C}_{\perp,q}^{(0)} = 0$ , the mass factorisation counterterms generated in the convolution of the GPDs with the bare quark coefficient functions start at  $\mathcal{O}(\hat{a}_s^3)$  and are therefore not needed here. The mass factorisation counterterms generated by the convolutions of the GPDs with the bare gluon coefficient functions start at  $\mathcal{O}(\hat{a}_s^2)$  and so do contribute to the renormalisation of the amplitude at NLO. Extraction of the term proportional to  $\hat{C}_{\perp,g}^{(0)}$  in eqn. (5.95), replacing the bare GPDs in terms of the renormalised ones as given in eqns. (5.92) and (5.93), relabelling  $z \leftrightarrow X$  and identifying the outer  $z$  integral, gives the  $\mathcal{O}(a_s^2)$  transverse mass factorisation counterterms in the quark and gluon sector,

$$\hat{C}_{\perp,q}^{\text{mf},(1)} = \frac{1}{\epsilon} \left( \frac{\mu_R^2}{\mu_F^2} \right)^\epsilon \frac{\xi}{|\xi|} \int_{-1}^1 \frac{dz}{z^2} \hat{C}_{\perp,g}^{(0),\text{UV}} \left( \frac{\xi}{z}, Q^2 \right) 2V_{gq}^{(1)} \left( \frac{z}{\xi}, \frac{X}{\xi} \right), \quad (5.96)$$

$$\hat{C}_{\perp,g}^{\text{mf},(1)} = \frac{1}{\epsilon} \left( \frac{\mu_R^2}{\mu_F^2} \right)^\epsilon \frac{1}{|\xi|} \int_{-1}^1 \frac{dz}{z^2} \hat{C}_{\perp,g}^{(0),\text{UV}} \left( \frac{\xi}{z}, Q^2 \right) V_{gg}^{(1)} \left( \frac{z}{\xi}, \frac{X}{\xi} \right). \quad (5.97)$$

The corresponding equations for the  $\mathcal{O}(a_s^2)$  longitudinal mass factorisation counterterms can be obtained with the replacement  $\hat{C}_{\perp,g}^{(0),\text{UV}} \rightarrow \hat{C}_{L,g}^{(0),\text{UV}}$ ,

$$\hat{C}_{L,q}^{\text{mf},(1)} = \frac{1}{\epsilon} \left( \frac{\mu_R^2}{\mu_F^2} \right)^\epsilon \frac{\xi}{|\xi|} \int_{-1}^1 \frac{dz}{z^2} \hat{C}_{L,g}^{(0),\text{UV}} \left( \frac{\xi}{z}, Q^2 \right) 2V_{gq}^{(1)} \left( \frac{z}{\xi}, \frac{X}{\xi} \right), \quad (5.98)$$

$$\hat{C}_{L,g}^{\text{mf},(1)} = \frac{1}{\epsilon} \left( \frac{\mu_R^2}{\mu_F^2} \right)^\epsilon \frac{1}{|\xi|} \int_{-1}^1 \frac{dz}{z^2} \hat{C}_{L,g}^{(0),\text{UV}} \left( \frac{\xi}{z}, Q^2 \right) V_{gg}^{(1)} \left( \frac{z}{\xi}, \frac{X}{\xi} \right). \quad (5.99)$$

The only  $z$ -dependence in the tree level gluon coefficient functions is that due to the  $z^2/((z-\xi)(z+\xi))$  factor. The kernels  $V_{gq}^{(1)}$  and  $V_{gg}^{(1)}$  resume the form

$$\begin{aligned} V_{gq}^{(1)} &= \rho(x, y) \hat{V}_{+,gq} + \rho(-x, -y) \hat{V}_{-,gq}, \\ V_{gg}^{(1)} &= \rho(x, y) \hat{V}_{+,gg} + \rho(-x, -y) \hat{V}_{-,gg} + A\delta(x - y), \end{aligned} \quad (5.100)$$

where  $\hat{V}_+$  and  $\hat{V}_-$  are the coefficients of the support functions  $\rho(x, y)$  and  $\rho(-x, -y)$  in each case, respectively, see eqn. (C.9) in Appendix C. The factor  $A$  does not depend on  $x$  or  $y$ . The part of the integration over  $z$  that is dependent on  $\rho$  may be simplified using the representation of  $\rho$  in terms of explicit theta functions given in Appendix C. In the quark subprocess, for example, upon imposition of the physical restriction  $0 < \xi < 1$ , we encounter integrals of the form,

$$\begin{aligned} \hat{C}_{i,q}^{\text{mf},(1)} &\sim \int_{-1}^1 \frac{dz}{z^2} \hat{C}_{i,g}^{(0),\text{UV}} \left( \frac{\xi}{z}, Q^2 \right) V_{gq}^{(1)} \left( \frac{z}{\xi}, \frac{X}{\xi} \right) \\ &= \int_{-1}^1 \frac{dz}{z^2} \hat{C}_{i,g}^{(0),\text{UV}} \left( \rho \left( \frac{z}{\xi}, \frac{X}{\xi} \right) \hat{V}_{+,gq} + \rho \left( -\frac{z}{\xi}, -\frac{X}{\xi} \right) \hat{V}_{-,gq} \right) \\ &= \left( \theta(X + \xi) \int_{-\xi}^X \frac{dz}{z^2} \hat{C}_{i,g}^{(0),\text{UV}} \hat{V}_{+,gq} - \theta(-\xi - X) \int_X^{-\xi} \frac{dz}{z^2} \hat{C}_{i,g}^{(0),\text{UV}} \hat{V}_{+,gq} \right) \\ &\quad - \left( \theta(\xi - X) \int_X^\xi \frac{dz}{z^2} \hat{C}_{i,g}^{(0),\text{UV}} \hat{V}_{-,gq} - \theta(X - \xi) \int_\xi^X \frac{dz}{z^2} \hat{C}_{i,g}^{(0),\text{UV}} \hat{V}_{-,gq} \right) \\ &= \int_{-\xi}^X \frac{dz}{z^2} \hat{C}_{i,g}^{(0),\text{UV}} \hat{V}_{+,gq} - \int_X^\xi \frac{dz}{z^2} \hat{C}_{i,g}^{(0),\text{UV}} \hat{V}_{-,gq}, \end{aligned} \quad (5.101)$$

where  $\hat{C}_{i,g}^{(0),\text{UV}} \equiv \hat{C}_{i,g}^{(0),\text{UV}}(\xi/z, Q^2)$ .



We find

$$\hat{C}_{\perp,g}^{\text{mf},(1)} = \frac{1}{\epsilon} \left( \frac{\mu_R^2}{\mu_F^2} \right)^\epsilon S_\epsilon^{-1} \left( \frac{\mu_R^2}{\mu_0^2} \right)^\epsilon \frac{4T_F}{N_c} B_0 \left( C_A \left( \frac{1}{vw^4} + \frac{2v+2}{vw^2+1} - \frac{1}{vw^2} - \frac{1}{w^2} - 1 \right) f_6 + \frac{\beta_0}{4} \frac{w^2-1}{w^2} + \{v \rightarrow -v\} \right), \quad (5.102)$$

$$\hat{C}_{L,g}^{\text{mf},(1)} = -\frac{\hat{C}_{\perp,g}^{\text{mf},(1)}}{\sqrt{w^2-1}}, \quad (5.103)$$

$$\hat{C}_{\perp,q}^{\text{mf},(1)} = \frac{1}{\epsilon} \left( \frac{\mu_R^2}{\mu_F^2} \right)^\epsilon S_\epsilon^{-1} \left( \frac{\mu_R^2}{\mu_0^2} \right)^\epsilon \frac{64T_F^2}{N_c^2} B_0 \frac{x_+x_-}{x^2} \left( \frac{1}{vw^2} + \frac{1}{w^2} - \frac{1}{vw^4} - \frac{v+1}{vw^2+1} \right) f_6 + \{v \rightarrow -v\}, \quad (5.104)$$

$$\hat{C}_{L,q}^{\text{mf},(1)} = -\frac{\hat{C}_{\perp,q}^{\text{mf},(1)}}{\sqrt{w^2-1}}. \quad (5.105)$$

Using these expressions in eqn. (5.94) gives finally our renormalised, finite coefficient functions that can be numerically convoluted with renormalised, finite GPDs to produce a renormalised amplitude and predictions for physical observables. These renormalised coefficient functions constitute the main results of this chapter and are provided in an ancillary `MATHEMATICA` file alongside the arXiv submission of our [216].

## 5.7 High-energy limit

One can make an expansion in the parameter  $\hat{\xi}$  to extract the high-energy asymptotic behaviour of the exclusive electroproduction amplitude. In the integration over  $X \in [-1, 1]$  in our NLO collinear factorisation set-up, the high-energy result receives contributions from the broad sub-integration interval  $\xi \ll |X| \ll 1$ . As is shown explicitly below, this corresponds to the part of the DGLAP region which is (double)-logarithmically enhanced.

As our results above are expressed entirely within the ERBL region, we first perform acutely the analytic continuation into the physical regime and then proceed with the Laurent expansion in  $\xi$  around zero of the resulting expression. Care was taken to ensure the logarithms and dilogarithms in our result were evaluated on the correct side of their

respective branch-cuts. See Appendix A.0.2 for their correct analytic continuations.

The only  $X$ -dependence in the LO gluon coefficient function comes from that within the GPD projection, residing in  $B_0$  in the LO coefficient function, eqns. (5.43, 5.44), so here we can proceed analytically. Let  $A_{\text{LO}}^{\pm\pm}$  and  $A_{\text{LO, HE}}^{\pm\pm}$  denote the LO transverse amplitudes and their high-energy limits respectively.  $A_{\text{LO}}^{00}$  and  $A_{\text{LO, HE}}^{00}$  represent the analogous quantities for the longitudinal component. Then, from eqn. (5.38),

$$-\sqrt{w^2 - 1}A_{\text{LO}}^{00} = A_{\text{LO}}^{\pm\pm} \sim \lim_{\delta \rightarrow 0^+} \int_{-1}^1 \frac{dX}{X^2} \frac{X^2}{(X + \xi - i\delta)(X - \xi + i\delta)} F^g(X, \xi) \quad (5.106)$$

$$= \lim_{\delta \rightarrow 0^+} 2 \int_{-1}^0 \frac{dX}{X^2} \frac{X^2}{(X + \xi - i\delta)(X - \xi + i\delta)} F^g(X, \xi), \quad (5.107)$$

where we used the fact that the integrand is an even function of  $X$ , see Section 2.3.2. With  $0 < \xi < 1$  and  $X < 0$  in the above, it follows that  $X - \xi \neq 0$  and so we may drop the  $+i\delta$  from one of the denominator terms. Then,

$$= \lim_{\delta \rightarrow 0^+} 2 \int_{-1}^0 \frac{dX}{(X - \xi)(X + \xi - i\delta)} F^g(X, \xi) = \lim_{\delta \rightarrow 0^+} 2 \int_{-1}^0 \frac{dX}{(X - \xi)} \frac{X + \xi + i\delta}{((X + \xi)^2 + \delta^2)} F^g(X, \xi) \quad (5.108)$$

$$= \lim_{\delta \rightarrow 0^+} \left[ 2 \int_{-1}^0 \frac{dX}{(X - \xi)} \frac{X + \xi}{((X + \xi)^2 + \delta^2)} F^g(X, \xi) + 2i \int_{-1}^0 \frac{\pi dX}{(X - \xi)} \eta_\delta(X + \xi) F^g(X, \xi) \right] \quad (5.109)$$

$$= 2\mathcal{P} \int_{-1}^0 \frac{dX}{(X - \xi)(X + \xi)} F^g(X, \xi) + 2i \int_{-1}^0 \frac{\pi dX}{(X - \xi)} \delta(X + \xi) F^g(X, \xi) \quad (5.110)$$

$$= 2\mathcal{P} \int_{-1}^0 \frac{dX}{(X - \xi)(X + \xi)} F^g(X, \xi) - \frac{i\pi}{\xi} F^g(-\xi, \xi), \quad (5.111)$$

where, in the last few lines, we used the fact that

$$\pi \eta_\delta(\alpha) = \frac{\delta}{\alpha^2 + \delta^2} \quad \text{and} \quad \lim_{\delta \rightarrow 0^+} \eta_\delta(\alpha) = \delta(\alpha), \quad (5.112)$$

with  $\mathcal{P}$  the principal value integral. Here,  $\eta_\delta(\alpha)$  is a nascent Dirac delta distribution. As mentioned in Chapter 4, for very small  $x$ , one expects the gluon density to tend to a constant  $F^g(X, \xi) \sim \text{const}$ , with the singlet quarks growing as a power law,  $F^q(X, \xi) \sim$

$1/X$ . Then,

$$A_{\text{LO, HE}}^{\pm\pm} \sim -\frac{i\pi}{\xi} F^g(\xi, \xi), \quad (5.113)$$

where we took the most singular term in  $\xi$ , giving the leading behaviour in the high-energy limit. In the NLO coefficient functions, there is an additional  $X$ -dependence in both the  $f_i$  and  $c_i$ . The complete high-energy result to NLO, showing only the dominant term in  $\xi$ , is

$$\begin{aligned} A_{\text{HE}}^{\pm\pm} = & -\frac{2m}{\sqrt{-Q^2}} A_{\text{HE}}^{00} \sim -\frac{4i\pi^2 e_q 4m^2}{N_c \xi (4m^2 - Q^2)} \left( \frac{\langle O_1 \rangle_V}{m^3} \right)^{1/2} \times \\ & \times \left[ \alpha_s F^g(\xi, \xi) + \frac{\alpha_s^2 N_c}{\pi} \ln \left( \frac{4m^2 - Q^2}{4\mu_F^2} \right) \int_\xi^1 \frac{dX}{X} F^g(X, \xi) \right. \\ & \left. + \frac{\alpha_s^2 C_F}{\pi} \ln \left( \frac{4m^2 - Q^2}{4\mu_F^2} \right) \int_\xi^1 dX (F^q(X, \xi) - F^q(-X, \xi)) \right]. \end{aligned} \quad (5.114)$$

The overall  $i$  implies the high-energy result is dominated by the imaginary part of the amplitude, a general feature of amplitudes in the asymptotic energy regime based on Regge theory considerations. The photoproduction limit of eqn. (5.114) coincides with the high-energy result in [18]. With  $F^g(X, \xi) \sim \text{const}$  and  $F^q(X, \xi) \sim 1/X$  at high-energy, where  $\xi \ll 1$ , the lower boundary of the integration generates another logarithmic enhancement  $\sim \ln(1/\xi)$  which, together with the explicit large logarithm already appearing in eqn. (5.114), gives the electroproduction amplitude to double-logarithmic-accuracy.

The structure of the high-energy limit is therefore highly suggestive of the factorisation scale choice,

$$\mu_F^2 = \frac{4m^2 - Q^2}{4}, \quad (5.115)$$

which provides for a resummation of this double logarithmic enhancement in the NLO contribution at high-energies. The  $Q^2 \rightarrow 0$  limit of this equation reproduces  $\mu_F^2 = m^2$ , as used in the photoproduction phenomenological analyses of Chapters 3 and 4.

## 5.8 Comparison with literature

The authors of [103] have also computed the transverse and longitudinal renormalised amplitudes at NLO for the exclusive electroproduction of heavy quarkonia, within the

same calculational framework of collinear factorisation and LO NRQCD. Their paper was published while our calculation was still on-going, so our work serves as an independent, simultaneous analysis of the process and, in addition, a check on the results they have presented. We have obtained agreement numerically with both their quark and gluon transverse and longitudinal renormalised amplitudes after publication of their erratum, in which they corrected typographical errors and resolved an inconsistency in their high energy limit that we had pointed out.<sup>8</sup>

From our point of view, some notable aspects of the manner in which we have presented the results, in comparison with those of [103], include the following. First and foremost, our results are expressed in terms of a basis set comprising of a smaller number of appearing logarithms and dilogarithms. Besides this being aesthetically desirable, the set we have selected is such that all basis functions appearing are manifestly real *if* the coefficient function is real. This is not the case for the set presented in [103]. Throughout the entire ERL phase space, all of our basis functions evaluate to a real number. In addition, hand in hand with our basis constituting a more minimal set with a smaller cardinality, we have also only one non-rationalised square root argument appearing therein. The substitution  $z^2 = (1 + 2v - vw^2)/(1 + vw^2)$  would allow all arguments to become rationalised, however this would upset our explicit  $v \rightarrow -v$  symmetry which we deem to be a more important feature to maintain. We have also decided to keep track of all the group theory factors that arise and refrain from inserting their numerical evaluations in the presentation of our analytical results. Amongst other reasons, this allows one to generalise the expressions for  $N_c \neq 3$  and be valid for an arbitrary  $SU(N_c)$  gauge theory instead.

## 5.9 Summary

In this chapter, we have computed renormalised coefficient functions for exclusive electroproduction of heavy vector mesons to NLO in the collinear factorisation framework. The description of the  $Q\bar{Q} \rightarrow V$  transition vertex was made within LO NRQCD and the mass of the heavy vector meson set equal to twice the on-shell mass of the heavy quark. Our results respect the physical  $\xi \rightarrow -\xi$  symmetry and coincide with the renormalised coefficient functions for exclusive production of heavy vector mesons in the  $Q^2 \rightarrow 0$  limit. In this limit, the longitudinal component vanishes and there is only a non-vanishing amplitude to

---

<sup>8</sup>I thank Zi-Qiang Chen and Cong-Feng Qiao for this private communication.

produce a transversely polarised HVM from a transversely polarised photon. Note that the  $m^2 \rightarrow 0$  limit is not smooth and cannot be taken. The tensor decomposition of the amplitude in eqn. (5.27) was verified explicitly and all partial fraction linear reductions were checked numerically. Moreover, at one-loop, gluon propagators introduce a gauge parameter dependence on the Feynman diagram level if computed in a linear covariant gauge, as done here. The cancellation of all gauge parameter dependent terms at the amplitude level provides a further check.

Our results can be used in a phenomenological analysis of the exclusive electroproduction data already measured at HERA and, in time, with the data from LHC, the upcoming EIC and the proposed LHeC and FCC. They may also help in studying the onset of saturation physics and, importantly, our predictions and these data can collectively provide further constraints on the gluon distribution in nuclei at moderate to low values of the scale  $Q^2$  and Bjorken  $x$ .

## Chapter 6

# Conclusions

In this thesis, we have cast a light on the new and improved prediction for exclusive  $J/\psi$  production at NLO in the collinear factorisation scheme, as well as on PDF determinations at small  $x$ .

In Chapter 3, after supplementing the naive  $\overline{\text{MS}}$  result with a low  $Q$  cut off procedure and low  $x$  resummation, the observable prediction was demonstrated to have sufficient stability and precision to improve on the large PDF uncertainties in the very low  $x$  domain. Indications that evolution à la BFKL and inclusion of effects beyond the standard collinear factorisation framework are not relevant in the HERA region for this observable were realised. The resummation of the large logarithms and, more importantly, the  $Q_0$  subtraction provided for a stable and reliable prediction at NLO with excellent agreement with the data at larger  $x$ . The exclusive process was shown, as a result, to be driven by the gluon parton distribution function with a vanishingly small quark PDF contribution over the entire HERA and LHC energy range considered.

With this, in Chapter 4, we performed a reweighted fitting procedure within a framework of Bayesian statistics, to extract a low  $x$  and low scale gluon PDF in the kinematic region  $\mu^2 \sim 2.4 \text{ GeV}^2$  and  $3 \times 10^{-6} < x < 10^{-3}$ . This was backed up with a fit in which the gluon PDF is ansatzed to grow as a pure power, agreeing favourably with the reweighted prediction. The chi square statistic obtained using this power law rise of the gluon PDF was found to be close to unity, with an extracted gluon slope in line with arguments from previous literature. The quantitative features of our extracted gluon PDFs were compared to that obtained in an independent similar reweighted analysis using the inclusive  $D$  meson data appearing in the literature. In this comparison, we observed some tension in the low

$x$  growth and provided explanations. A note regarding the absence of saturation effects in the given kinematic range considered was also made. The constraining power of the low  $x$  exclusive data, evident from our results, was emphasised and the repercussions for the global fit extractions made clear.

In Chapter 5, using a semi-automated state of the art computational workflow, we provided renormalised NLO coefficient functions for exclusive electroproduction of HVMS in collinear factorisation. The novel features of our calculation, amounting to linear dependencies in the external kinematics due to our specific gluon and quark GPD and HVM projections, were discussed and alleviated. A brief comparison with existing work was made.

The work presented in this thesis motivates several future exploratory studies. More immediate avenues of work surrounding the exclusive  $J/\psi$  production mechanism presented in this thesis, which would complement its study at higher orders, comprise the following.

- The effect of explicit  $\ln 1/x$  terms were surmised to be small in the BFKL equation after the  $Q_0$  subtraction, but this can be quantified by actually performing the cut to extract a modified  $Q_0$  subtracted BFKL kernel. As well as being of obvious application elsewhere, this would be expected to reinforce the statements we have made regarding our choice of resummation.
- The dependability of the Shuvaev Transform as a reliable means to relate the GPD to the PDF at low  $x, \xi$  and low scales at NNLO should perhaps not be taken for granted. As discussed in Section 2.3.3, at LO the relation is valid at  $\mathcal{O}(\xi^2)$  while at NLO it is instead  $\mathcal{O}(\xi)$ . What happens at NNLO? Is there a saturation of the accuracy or is it demoted further? In any case, we expect the higher order relation to be suppressed by the higher powers of  $\alpha_s$ , but this is an interesting question to explore and acknowledge.
- From the rather technical side, it may be useful to incorporate the low  $x$  gluon constraints we have obtained from the furnished exclusive  $J/\psi$  prediction into **xFitter**, extending the scope of this software to include exclusive observables, and provide a LHAPDF6 formatted grid computer package. This would be of practical use and benefit to the PDF fitter groups and, indeed, to the wider particle physics community.
- The tool-chain we have developed for the computation of exclusive HVM electroproduction is easily extendable to allow predictions for e.g. open exclusive quarks

and/or open jets to be made. It would be interesting to explore the interplay between the higher orders in NRQCD and that of collinear factorisation, as well as to understand the weighting the modelling of the exclusive HVM within NRQCD has on our predictions. As a next step, we can perform numerical analyses using the coefficient functions presented in Chapter 5, comparing e.g. the resulting cross section predictions with the electroproduction data.

More broadly, it is our intention to extend the framework developed for exclusive  $J/\psi$  production via  $pp$  ultraperipheral collisions at the LHC, to the nuclear sector. In particular, the potential of heavy-ion data at the LHC, together with exclusive vector meson production data at the upcoming EIC, will allow for additional constraints on e.g. the nuclear gluon PDF, which is even less constrained at low values of  $x$ . In addition, such observables are typically anticipated to present signals of saturation more forthcomingly due to the different properties of the colliding ion compared to the proton.

While there are measurements of inclusive  $C$ -even quarkonia hadroproduction from LHCb with kinematic cuts at  $p_T > 6$  GeV, see e.g. [217] for the  $\eta_c$  meson, it would be useful to probe the lower transverse momentum domain of this observable due to its sensitivity to the gluon distribution at low scales, too. This would complement the studies we have done here, except now with another measurement in the conventional inclusive mode. It would be interesting to ascertain the manner in which a gluon extracted in a phenomenological analysis of this data compares with that obtained from the inclusive  $D$  sector and our exclusive  $J/\psi$  study. The reconciliation of the tension between these latter independent analyses, as presented in this work, would provide a nice future platform of interaction between theory and experiment.

Furthermore, the measurements of  $S$ -wave charmonia at LHCb are susceptible to large uncertainties [105], alike that of the  $D$ -mesons, which cannot be mitigated via the construction of ratios due to large statistical data errors on the experimental front. While the original scale dependence of the exclusive  $J/\psi$  prediction within collinear factorisation can, in principle, instead be combated through such ratios we would argue the  $Q_0$  subtraction is more fundamental and, in any case, the data statistics for exclusive  $J/\psi$  production at low  $x$ , at the time of writing, are not sufficient to make this a practical mode of study. The upcoming High-Luminosity LHC program will help facilitate greater data statistics here. For this reason, from the theory side, it would be virtuous to probe the effect the low  $Q_0$  cut has for scale dependencies in other low scale observable predictions.



# Appendix A

## Conventions and Properties

In this Appendix, we will collect some of the conventions used in this thesis and present the definition and analytic continuation properties of the logarithms and dilogarithms. These functions appear in the photoproduction NLO coefficient functions used in Chapters 3 and 4 and in the electroproduction NLO coefficient functions presented in Chapter 5. The group theory algebra needed in Chapter 5 is also given.

### A.0.1 Sudakov Decomposition

We use the following convention for the metric tensor in four dimensions,

$$g_{\mu\nu} = g^{\mu\nu} = \text{diag}(+1, -1, -1, -1). \quad (\text{A.1})$$

The generic Sudakov decomposition of a four vector  $A^\mu = (A^0, A^1, A^2, A^3)$  is

$$A^\mu = (A \cdot n)p^\mu + (A \cdot p)n^\mu + A_\perp^\mu, \quad (\text{A.2})$$

where  $p, n$  are two Sudakov light-like basis vectors and

$$A_\perp^\mu = (0, A^1, A^2, 0) = (0, \mathbf{A}_\perp, 0). \quad (\text{A.3})$$

We define

$$p^\mu = \frac{1}{\sqrt{2}} \Lambda(1, 0, 0, 1), \quad (\text{A.4})$$

$$n^\mu = \frac{1}{\sqrt{2}} \frac{1}{\Lambda}(1, 0, 0, -1), \quad (\text{A.5})$$

from which

$$p \cdot p = n \cdot n = p \cdot A_\perp = n \cdot A_\perp = 0, \quad p \cdot n = 1, \quad A_\perp \cdot A_\perp = -\mathbf{A}_\perp^2. \quad (\text{A.6})$$

Here, the Sudakov parameter  $\Lambda$  has a mass dimension of one. The perpendicular metric tensor is defined as the projection of the metric tensor onto the plane perpendicular to  $p$  and  $n$ ,

$$g_\perp^{\mu\nu} = g^{\mu\nu} - p^\mu n^\nu - p^\nu n^\mu. \quad (\text{A.7})$$

### A.0.2 Polylogarithms

If  $s > 0$ , the analytic continuation for the logarithm is

$$\lim_{\delta \rightarrow 0^+} \ln(-s \pm i\delta) = \ln(s) \pm i\pi. \quad (\text{A.8})$$

The dilogarithm is defined as

$$\text{Li}_2(s) = - \int_0^s \frac{dz}{z} \ln(1-z) \quad (\text{A.9})$$

$$\equiv \sum_{n=1}^{\infty} \frac{s^n}{n^2}, \quad \text{for } |s| \leq 1. \quad (\text{A.10})$$

If  $s \leq 1$ , the analytic continuation for the dilogarithm is

$$\lim_{\delta \rightarrow 0^+} \text{Li}_2(s \pm i\delta) = \text{Li}_2(s) \quad (\in \mathbb{R}). \quad (\text{A.11})$$

If  $s > 1$ ,

$$\lim_{\delta \rightarrow 0^+} \text{Li}_2(s \pm i\delta) = \text{Re Li}_2(s) \pm i\pi \ln(s) \quad (\in \mathbb{C}). \quad (\text{A.12})$$

### A.0.3 Trace identities

In this section, we summarise aspects of the group theory needed in Chapter 5 of this thesis. Let  $T^a$ ,  $a = 1, 2, \dots, N_c^2 - 1$ , denote the group generators of  $\text{SU}(N_c)$  in the fundamental representation. All relevant traces can be obtained from the relation

$$T^a T^b = \frac{1}{2} \left( \frac{1}{N_c} \delta^{ab} + (d^{abc} + i f^{abc}) T^c \right), \quad (\text{A.13})$$

or a contracted product of generators,

$$(T^a)_{ij} (T^a)_{kl} = \frac{1}{2} \left( \delta_{il} \delta_{jk} - \frac{1}{N_c} \delta_{ij} \delta_{kl} \right), \quad i, j, k, l = 1, 2, \dots, N_c, \quad (\text{A.14})$$

where  $f^{abc}$  is the totally antisymmetric structure constant,

$$[T^a, T^b] = i f^{abc} T^c, \quad a, b, c = 1, 2, \dots, N_c^2 - 1, \quad (\text{A.15})$$

and  $d^{abc}$  is the totally symmetric constant satisfying,

$$\{T^a, T^b\} = \frac{1}{N_c} \delta^{ab} + d^{abc} T^c. \quad (\text{A.16})$$

It follows from eqn. (A.13) that

$$\text{Tr}(T^a T^b T^c) = \frac{1}{4} (d^{abc} + i f^{abc}) \quad (\text{A.17})$$

and from eqn. (A.14) that

$$\text{Tr}(T^c T^a T^c T^b) = -\frac{1}{4N_c} \delta^{ab} = \frac{1}{2} \left( C_F - \frac{C_A}{2} \right) \delta^{ab} \quad (\text{A.18})$$

and

$$\text{Tr}(T^a T^b T^c T^c) = \frac{1}{4} \left( N_c - \frac{1}{N_c} \right) \delta^{ab} = \frac{1}{2} C_F \delta^{ab}, \quad (\text{A.19})$$

where the fundamental and adjoint Casimirs of  $\text{SU}(N_c)$  are

$$C_F = \frac{N_c^2 - 1}{2N_c} \quad \text{and} \quad C_A = N_c, \quad (\text{A.20})$$

respectively, with the normalisation

$$\text{Tr} (T^a T^b) = T_F \delta^{ab} = \frac{1}{2} \delta^{ab}. \quad (\text{A.21})$$

Inversion of eqn. (A.15) for  $f^{abc}$  using eqn. (A.21), it follows that

$$f^{acd} f^{bcd} = N_c \delta^{ab} = C_A \delta^{ab} \quad (\text{A.22})$$

after repeated application of eqn. (A.14). Then,

$$f^{adc} \text{Tr} (T^b T^d T^c) = \frac{i}{4} f^{adc} f^{bdc} = \frac{i}{4} C_A \delta^{ab}, \quad (\text{A.23})$$

as  $f^{adc} d^{bdc} = 0$  identically.

Eqn. (A.21) shows up in the computation of the quark coefficient function while eqns. (A.18), (A.19), (A.22) and (A.23) are all relevant for the gluon coefficient function.

## Appendix B

# Resummation in the $(x, Q^2)$ plane

Every physical observable, within perturbative QCD, may be written as a systematic power expansion in the strong coupling,  $\alpha_s$ , accompanied by coefficients  $c_n(x, Q^2)$  at each order  $n$  in the series:  $\sum_n \alpha_s^n c_n(x, Q^2)$ . These coefficients include logarithms which can become enhanced (relative to the smallness of  $\alpha_s$ ) in certain parts of the  $(x, Q^2)$  plane, leading to the need for a so-called *resummation* of such terms. One obtains different evolution equations depending on the type and power of logarithms which are considered in the resummation procedure.

In the leading-log( $Q^2$ )-approximation (LL<sub>Q</sub>A), at each order in perturbation theory only the highest power in  $\ln(Q^2)$  is retained. That is, in this approximation, the above series is of the form

$$\text{LL}_Q\text{A: } \sum_n \alpha_s^n \ln^n(Q^2) \left( \ln^n \left( \frac{1}{x} \right) + \ln^{n-1} \left( \frac{1}{x} \right) + \dots \right), \quad (\text{B.1})$$

which amounts to, in a physical gauge, the strong ordering in transverse momentum

$$Q^2 \gg k_{T_1}^2 \gg k_{T_2}^2 \gg k_{T_3}^2 \gg \dots \gg k_{T_n}^2,$$

where  $k_{T_i}^2$  is the  $i^{\text{th}}$  successive transverse momentum of the parton in evolution cell  $i$  towards the hard scattering scale  $Q^2$ . This is to say in the LL<sub>Q</sub>A, the resummed coefficients are of the form

$$c_n(x, Q^2) = \tilde{c}_n(x) \ln^n(Q^2),$$

retaining the *exact*  $x$ -dependence at each order in  $n$ .

In the next-to-leading-log( $Q^2$ )-approximation (NLL<sub>Q</sub>A), sub-dominant terms of the form  $\alpha_s^n \ln^{n-1}(Q^2)$  are in addition kept. The LL<sub>Q</sub>A and NLL<sub>Q</sub>A give rise to the LO and NLO DGLAP evolution equations respectively.

In the leading-log( $1/x$ )-approximation (LL<sub>x</sub>A), it is instead the highest power of  $\ln(1/x)$  that is kept. These logarithms are clearly relevant in the limit of asymptotically small  $x$  with a relatively moderate momentum transfer  $Q^2$ . The series is then of the form

$$\text{LL}_x\text{A: } \sum_n \alpha_s^n \ln^n \left( \frac{1}{x} \right) (\ln^n(Q^2) + \ln^{n-1}(Q^2) + \dots), \quad (\text{B.2})$$

where (LL<sub>Q</sub>A)  $\leftrightarrow$  (LL<sub>x</sub>A) corresponds to  $Q^2 \leftrightarrow 1/x$ . In this case, the strong ordering is in the longitudinal momentum

$$x \ll x_1 \ll x_2 \ll x_3 \ll \dots \ll x_n \ll 1,$$

where  $x_i$  is the  $i^{\text{th}}$  successive longitudinal momentum of the parton in evolution cell  $i$  and the resummed coefficients are of the form

$$c_n(x, Q^2) = \tilde{c}_n(Q^2) \ln^n \left( \frac{1}{x} \right).$$

This leads to the LO BFKL evolution equation [166, 167, 168]. The BFKL approach is based on the so-called reggeized gluon and describes the evolution of the unintegrated gluon distribution,

$$f(x, k_T^2) = \frac{\partial x g(x, k_T^2)}{\partial \ln k_T^2} \quad (\text{B.3})$$

in  $\ln(1/x)$ . Schematically, the BFKL equation takes the form

$$\frac{\partial f}{\partial \ln(1/x)} = \kappa \otimes f, \quad (\text{B.4})$$

where  $\kappa$  is the BFKL kernel and  $\otimes$  is a convolution over the transverse momenta, in contrast to the DGLAP evolution equation where this is instead a convolution over longitudinal momenta. Resummation of the terms  $(\alpha_s \ln(1/x))^n$  in the BFKL kernel give rise to the LL<sub>x</sub>A and the LO BFKL equation. It predicts that the gluon density grows as  $x^{-\omega_0}$  at low  $x$ , with the Pomeron intercept  $\alpha_{\text{BFKL}} = 1 + \omega_0 = 1 + 4N_c \alpha_s / \pi \ln 2 \approx 1.6$ , which is, however, too large [166, 167, 168]. The NLO BFKL kernel is also known, see [218] and

corresponds to the  $\text{NLL}_x\text{A}$  and resummation of terms  $\alpha_s(\alpha_s \ln(1/x))^n$ .

When both  $\ln(Q^2)$  and  $\ln(1/x)$  are large, a *double* logarithm  $\sim \alpha_s^n \ln^n(Q^2) \ln^n(1/x)$  is enhanced relative to the single logarithms  $\sim \alpha_s^n \ln^n(Q^2)$  or  $\sim \alpha_s^n \ln^n(1/x)$  and one may then consider the double-leading-logarithmic-approximation (DLA)

$$\text{DLA: } \sum_n \alpha_s^n \ln^n(Q^2) \ln^n\left(\frac{1}{x}\right), \quad (\text{B.5})$$

where here the strong ordering is in both the transverse momentum and longitudinal momentum while the resummed coefficient is uniquely identified,

$$c_n(x, Q^2) = \ln^n(Q^2) \ln^n\left(\frac{1}{x}\right).$$

Note that the resummation of the double logarithms is included in the DGLAP evolution, see the first term of eqn (B.1). If one wants to resum *only* the double logarithmic terms, then strong ordering in  $k_n^2 = k_{T_n}^2$  and  $x$  is required, as shown structurally below in the DGLAP integrals<sup>1</sup>

$$\begin{aligned} & \left( \int_{\mu^2}^{Q^2} \frac{dk_n^2}{k_n^2} \int_{\mu^2}^{k_n^2} \frac{dk_{n-1}^2}{k_{n-1}^2} \cdots \int_{\mu^2}^{k_2^2} \frac{dk_1^2}{k_1^2} \right) \left( \int_x^1 \frac{dx_n}{x_n} \int_{x_n}^1 \frac{dx_{n-1}}{x_{n-1}} \cdots \int_{x_2}^1 \frac{dx_1}{x_1} \right) \\ & \sim \frac{1}{(n!)^2} [\alpha_s \ln(Q^2/\mu^2) \ln(1/x)]^n = \alpha_s^n C_n(x, Q^2). \end{aligned} \quad (\text{B.6})$$

Here,  $\mu^2$  ( $Q^2$ ) is the initial (final) scale of the DGLAP evolution. The summation over  $n$  of  $\alpha_s^n C_n(x, Q^2)$  is related to the modified  $I_0$  Bessel function of the first kind. Using its asymptotic expansion gives

$$\sum_{n=0}^{\infty} \alpha_s^n C_n(x, Q^2) \sim \exp \left( \sqrt{\alpha_s \ln\left(\frac{1}{x}\right) \ln\left(\frac{Q^2}{\mu^2}\right)} \right), \quad (\text{B.7})$$

providing an all order resummation to DLA accuracy.

---

<sup>1</sup>This corresponds to the DGLAP contribution that is enhanced, relative to  $\ln(Q^2)$ , by a  $\ln(1/x)$  arising from the integrands  $1/x_1, 1/x_2, \dots, 1/x_n$  corresponding to the leading terms of the LO  $P_{gg}$  splitting functions at small  $x$  in each iteration of the strongly ordered  $x$  evolution. In a physical gauge, this corresponds to only gluon ladder diagrams.

## Appendix C

# GPD Singlet Evolution Kernels

As shown in Section 2.3.2, the non-singlet quantities represent the quark contributions that decouple from the gluon density in their evolution. The evolution of the singlet GPDs, however, is coupled and the matrix evolution equation mixes the quark and gluon sectors as follows,

$$\mu_F^2 \frac{d}{d\mu_F^2} \begin{pmatrix} F^S(x, \xi, \mu_F^2) \\ F^g(x, \xi, \mu_F^2) \end{pmatrix} = \int_{-1}^1 \frac{dy}{|\xi|} \begin{pmatrix} V^{qq} \left( \frac{x}{\xi}, \frac{y}{\xi} \right) & \xi^{-1} V^{qg} \left( \frac{x}{\xi}, \frac{y}{\xi} \right) \\ \xi V^{gq} \left( \frac{x}{\xi}, \frac{y}{\xi} \right) & V^{gg} \left( \frac{x}{\xi}, \frac{y}{\xi} \right) \end{pmatrix} \begin{pmatrix} F^S(x, \xi, \mu_F^2) \\ F^g(x, \xi, \mu_F^2) \end{pmatrix}. \quad (\text{C.1})$$

The LO [219, 220, 54, 221] and NLO [222, 81, 223, 224, 225] evolution kernels,  $V$ , are known in the literature. To  $\mathcal{O}(\alpha_s)$ , the singlet evolution kernels for the GPDs considered in this work, i.e. the unpolarised GPDs, are collected below and taken from [108]. Together with

$$V^{\text{NS}}(x, y) = V^{qq}(x, y), \quad (\text{C.2})$$



identically at  $\mathcal{O}(\alpha_s)$  for all  $V^{\text{NS}}$ , we have,

$$V^{qq}(x, y) = \frac{\alpha_s}{4\pi} C_F \left[ \rho(x, y) \frac{1+x}{1+y} \left( 1 + \frac{2}{y-x} \right) + \{x \rightarrow -x, y \rightarrow -y\} \right]_+, \quad (\text{C.3})$$

$$V^{qg}(x, y) = -\frac{\alpha_s}{4\pi} 2T_F N_f \left( \rho(x, y) \frac{1+x}{(1+y)^2} (1 - 2x + y - xy) - \{x \rightarrow -x, y \rightarrow -y\} \right), \quad (\text{C.4})$$

$$V^{gq}(x, y) = \frac{\alpha_s}{4\pi} C_F \left( \rho(x, y) \left( (2-x)(1+x)^2 - \frac{(1+x)^2}{1+y} \right) - \{x \rightarrow -x, y \rightarrow -y\} \right), \quad (\text{C.5})$$

$$V^{gg}(x, y) = \frac{\alpha_s}{4\pi} C_A \left[ \rho(x, y) \frac{(1+x)^2}{(1+y)^2} \left( 2 + \frac{2}{y-x} \right) + \{x \rightarrow -x, y \rightarrow -y\} \right]_+ \quad (\text{C.6})$$

$$+ \frac{\alpha_s}{4\pi} C_A \left[ \rho(x, y) \frac{(1+x)^2}{(1+y)^2} (1 - 2x + 2y - xy) + \{x \rightarrow -x, y \rightarrow -y\} \right] \quad (\text{C.7})$$

$$+ \frac{\alpha_s}{4\pi} \left( \beta_0 - \frac{14}{3} C_A \right) \delta(x-y), \quad (\text{C.8})$$

where  $N_f$  is the number of light quark flavours and  $\rho(x, y)$  specifies the support as

$$\rho(x, y) = \theta \left( \frac{1+x}{1+y} \right) \theta \left( 1 - \frac{1+x}{1+y} \right) \text{sgn}(1+y) = \theta(y-x)\theta(x+1) - \theta(x-y)\theta(-x-1). \quad (\text{C.9})$$

Here,  $C_A = 3$ ,  $C_F = 4/3$  and  $T_F = 1/2$  and  $[\cdot]_+$  denotes the plus-prescription regulator such that,

$$\int_{-1}^1 dx f(x, y) [g(x, y)]_+ = \int_{-1}^1 dx (f(x, y) - f(y, y)) g(x, y). \quad (\text{C.10})$$

In the forward limit,  $\xi \rightarrow 0$ , the two-dimensional off-forward splitting kernels above reduce to the conventional one-dimensional forward ones, with each resulting expression manifestly a function of the single variable  $z = x/y$ .

## Appendix D

# HVM Auxiliary Topologies

In this Appendix, we present the fourteen distinct auxiliary topologies constructed and used in the computation of exclusive HVM electroproduction to NLO in collinear factorisation in Chapter 5. We also give, in Table D.1, the association of each topology with the corresponding Feynman diagrams appearing in Fig. 5.5.

**Auxiliary topology (1):**

$$\mathcal{D}_5^{(1)} = \left\{ D_1^{(1)}, D_2^{(1)}, D_3^{(1)}, D_4^{(1)}, D_5^{(1)} \right\}, \text{ where} \quad (\text{D.1})$$

$$D_1^{(1)} = l^2, \quad (\text{D.2})$$

$$D_2^{(1)} = (l + p_1)^2, \quad (\text{D.3})$$

$$D_3^{(1)} = (l + p_1 + p_3)^2 - m^2, \quad (\text{D.4})$$

$$D_4^{(1)} = (l + p_1 + p_3 + p_4)^2 - m^2, \quad (\text{D.5})$$

$$D_5^{(1)} = (l + p_1 + p_3 + p_4 + p_5)^2, \quad (\text{D.6})$$

**Auxiliary topology (2):**

$$\mathcal{D}_5^{(2)} = \left\{ D_1^{(2)}, D_2^{(2)}, D_3^{(2)}, D_4^{(2)}, D_5^{(2)} \right\}, \text{ where} \quad (\text{D.7})$$

$$D_1^{(2)} = l^2, \quad (\text{D.8})$$

$$D_2^{(2)} = (l + p_1)^2, \quad (\text{D.9})$$

$$D_3^{(2)} = (l + p_1 + p_5)^2 - m^2, \quad (\text{D.10})$$

$$D_4^{(2)} = (l + p_1 + p_5 + p_2)^2 - m^2, \quad (\text{D.11})$$

$$D_5^{(2)} = (l + p_1 + p_5 + p_2 + p_4)^2 - m^2, \quad (\text{D.12})$$

**Auxiliary topology (3):**

$$\mathcal{D}_5^{(3)} = \left\{ D_1^{(3)}, D_2^{(3)}, D_3^{(3)}, D_4^{(3)}, D_5^{(3)} \right\}, \text{ where} \quad (\text{D.13})$$

$$D_1^{(3)} = l^2, \quad (\text{D.14})$$

$$D_2^{(3)} = (l + p_1)^2, \quad (\text{D.15})$$

$$D_3^{(3)} = (l + p_1 + p_5)^2 - m^2, \quad (\text{D.16})$$

$$D_4^{(3)} = (l + p_1 + p_5 + p_4)^2 - m^2, \quad (\text{D.17})$$

$$D_5^{(3)} = (l + p_1 + p_5 + p_4 + p_2)^2 - m^2, \quad (\text{D.18})$$

**Auxiliary topology (4):**

$$\mathcal{D}_5^{(4)} = \left\{ D_1^{(4)}, D_2^{(4)}, D_3^{(4)}, D_4^{(4)}, D_5^{(4)} \right\}, \text{ where} \quad (\text{D.19})$$

$$D_1^{(4)} = l^2, \quad (\text{D.20})$$

$$D_2^{(4)} = (l + p_1)^2, \quad (\text{D.21})$$

$$D_3^{(4)} = (l + p_1 + p_2)^2, \quad (\text{D.22})$$

$$D_4^{(4)} = (l + p_1 + p_2 + p_3)^2 - m^2, \quad (\text{D.23})$$

$$D_5^{(4)} = (l + p_1 + p_2 + p_3 + p_4)^2 - m^2, \quad (\text{D.24})$$

**Auxiliary topology (5):**

$$\mathcal{D}_5^{(5)} = \{D_1^{(5)}, D_2^{(5)}, D_3^{(5)}, D_4^{(5)}, D_5^{(5)}\}, \text{ where} \quad (\text{D.25})$$

$$D_1^{(5)} = l^2, \quad (\text{D.26})$$

$$D_2^{(5)} = (l + p_1)^2, \quad (\text{D.27})$$

$$D_3^{(5)} = (l + p_1 + p_4)^2, \quad (\text{D.28})$$

$$D_4^{(5)} = (l + p_1 + p_4 + p_2)^2, \quad (\text{D.29})$$

$$D_5^{(5)} = (l + p_1 + p_4 + p_2 + p_3)^2 - m^2, \quad (\text{D.30})$$

**Auxiliary topology (6):**

$$\mathcal{D}_5^{(6)} = \{D_1^{(6)}, D_2^{(6)}, D_3^{(6)}, D_4^{(6)}, D_5^{(6)}\}, \text{ where} \quad (\text{D.31})$$

$$D_1^{(6)} = l^2, \quad (\text{D.32})$$

$$D_2^{(6)} = (l + p_1)^2, \quad (\text{D.33})$$

$$D_3^{(6)} = (l + p_1 + p_4)^2, \quad (\text{D.34})$$

$$D_4^{(6)} = (l + p_1 + p_4 + p_2)^2, \quad (\text{D.35})$$

$$D_5^{(6)} = (l + p_1 + p_4 + p_2 + p_5)^2 - m^2, \quad (\text{D.36})$$

**Auxiliary topology (7):**

$$\mathcal{D}_5^{(7)} = \{D_1^{(7)}, D_2^{(7)}, D_3^{(7)}, D_4^{(7)}, D_5^{(7)}\}, \text{ where} \quad (\text{D.37})$$

$$D_1^{(7)} = l^2 - m^2, \quad (\text{D.38})$$

$$D_2^{(7)} = (l + p_1)^2 - m^2, \quad (\text{D.39})$$

$$D_3^{(7)} = (l + p_1 + p_2)^2 - m^2, \quad (\text{D.40})$$

$$D_4^{(7)} = (l + p_1 + p_2 + p_4)^2 - m^2, \quad (\text{D.41})$$

$$D_5^{(7)} = (l + p_1 + p_2 + p_4 + p_3)^2, \quad (\text{D.42})$$

**Auxiliary topology (8):**

$$\mathcal{D}_5^{(8)} = \left\{ D_1^{(8)}, D_2^{(8)}, D_3^{(8)}, D_4^{(8)}, D_5^{(8)} \right\}, \text{ where} \quad (\text{D.43})$$

$$D_1^{(8)} = l^2 - m^2, \quad (\text{D.44})$$

$$D_2^{(8)} = (l + p_1)^2 - m^2, \quad (\text{D.45})$$

$$D_3^{(8)} = (l + p_1 + p_2)^2 - m^2, \quad (\text{D.46})$$

$$D_4^{(8)} = (l + p_1 + p_2 + p_3)^2, \quad (\text{D.47})$$

$$D_5^{(8)} = (l + p_1 + p_2 + p_3 + p_5)^2 - m^2, \quad (\text{D.48})$$

**Auxiliary topology (9):**

$$\mathcal{D}_5^{(9)} = \left\{ D_1^{(9)}, D_2^{(9)}, D_3^{(9)}, D_4^{(9)}, D_5^{(9)} \right\}, \text{ where} \quad (\text{D.49})$$

$$D_1^{(9)} = l^2 - m^2, \quad (\text{D.50})$$

$$D_2^{(9)} = (l + p_1)^2 - m^2, \quad (\text{D.51})$$

$$D_3^{(9)} = (l + p_1 + p_4)^2 - m^2, \quad (\text{D.52})$$

$$D_4^{(9)} = (l + p_1 + p_4 + p_2)^2 - m^2, \quad (\text{D.53})$$

$$D_5^{(9)} = (l + p_1 + p_4 + p_2 + p_3)^2, \quad (\text{D.54})$$

**Auxiliary topology (10):**

$$\mathcal{D}_5^{(10)} = \left\{ D_1^{(10)}, D_2^{(10)}, D_3^{(10)}, D_4^{(10)}, D_5^{(10)} \right\}, \text{ where} \quad (\text{D.55})$$

$$D_1^{(10)} = l^2 - m^2, \quad (\text{D.56})$$

$$D_2^{(10)} = (l + p_1)^2 - m^2, \quad (\text{D.57})$$

$$D_3^{(10)} = (l + p_1 + p_4)^2 - m^2, \quad (\text{D.58})$$

$$D_4^{(10)} = (l + p_1 + p_4 + p_3)^2, \quad (\text{D.59})$$

$$D_5^{(10)} = (l + p_1 + p_4 + p_3 + p_5)^2 - m^2, \quad (\text{D.60})$$

**Auxiliary topology (11):**

$$\mathcal{D}_5^{(11)} = \left\{ D_1^{(11)}, D_2^{(11)}, D_3^{(11)}, D_4^{(11)}, D_5^{(11)} \right\}, \text{ where} \quad (\text{D.61})$$

$$D_1^{(11)} = l^2 - m^2, \quad (\text{D.62})$$

$$D_2^{(11)} = (l + p_1)^2 - m^2, \quad (\text{D.63})$$

$$D_3^{(11)} = (l + p_1 + p_4)^2 - m^2, \quad (\text{D.64})$$

$$D_4^{(11)} = (l + p_1 + p_4 + p_5)^2, \quad (\text{D.65})$$

$$D_5^{(11)} = (l + p_1 + p_4 + p_5 + p_2)^2, \quad (\text{D.66})$$

**Auxiliary topology (12):**

$$\mathcal{D}_5^{(12)} = \left\{ D_1^{(12)}, D_2^{(12)}, D_3^{(12)}, D_4^{(12)}, D_5^{(12)} \right\}, \text{ where} \quad (\text{D.67})$$

$$D_1^{(12)} = l^2 - m^2, \quad (\text{D.68})$$

$$D_2^{(12)} = (l + p_1)^2 - m^2, \quad (\text{D.69})$$

$$D_3^{(12)} = (l + p_1 + p_3)^2, \quad (\text{D.70})$$

$$D_4^{(12)} = (l + p_1 + p_3 + p_5)^2 - m^2, \quad (\text{D.71})$$

$$D_5^{(12)} = (l + p_1 + p_3 + p_5 + p_2)^2 - m^2, \quad (\text{D.72})$$

**Auxiliary topology (13):**

$$\mathcal{D}_5^{(13)} = \left\{ D_1^{(13)}, D_2^{(13)}, D_3^{(13)}, D_4^{(13)}, D_5^{(13)} \right\}, \text{ where} \quad (\text{D.73})$$

$$D_1^{(13)} = l^2 - m^2, \quad (\text{D.74})$$

$$D_2^{(13)} = (l + p_1)^2 - m^2, \quad (\text{D.75})$$

$$D_3^{(13)} = (l + p_1 + p_3)^2, \quad (\text{D.76})$$

$$D_4^{(13)} = (l + p_1 + p_3 + p_5)^2 - m^2, \quad (\text{D.77})$$

$$D_5^{(13)} = (l + p_1 + p_3 + p_5 + p_4)^2 - m^2, \quad (\text{D.78})$$

**Auxiliary topology (14):**

$$\mathcal{D}_5^{(14)} = \left\{ D_1^{(14)}, D_2^{(14)}, D_3^{(14)}, D_4^{(14)}, D_5^{(14)} \right\}, \text{ where} \quad (\text{D.79})$$

$$D_1^{(14)} = l^2 - m^2, \quad (\text{D.80})$$

$$D_2^{(14)} = (l + p_1)^2 - m^2, \quad (\text{D.81})$$

$$D_3^{(14)} = (l + p_1 + p_5)^2, \quad (\text{D.82})$$

$$D_4^{(14)} = (l + p_1 + p_5 + p_2)^2, \quad (\text{D.83})$$

$$D_5^{(14)} = (l + p_1 + p_5 + p_2 + p_3)^2 - m^2, \quad (\text{D.84})$$

NAT	Quark diagrams	Gluon diagrams
1	5.4.2, 5.4.3, 5.4.5	5.5.13, 5.5.33, 5.5.36, 5.5.37, 5.5.41, 5.5.44 5.5.48, 5.5.56, 5.5.60, 5.5.64, 5.5.71
2	N/A	5.5.4, 5.5.16, 5.5.51, 5.5.62, 5.5.79
3	N/A	5.5.22, 5.5.29, 5.5.40, 5.5.49, 5.5.68, 5.5.78
4	5.4.1, 5.4.4, 5.4.6	5.5.2, 5.5.19, 5.5.23, 5.5.31, 5.5.32, 5.5.35, 5.5.39 5.5.42, 5.5.45, 5.5.54, 5.5.58, 5.5.66, 5.5.74
5	LQ	N/A
6	LQ	N/A
7	N/A	5.5.24, 5.5.28, 5.5.59, 5.5.75
8	N/A	5.5.6, 5.5.17, 5.5.53, 5.5.67, 5.5.72
9	N/A	5.5.52, 5.5.80
10	N/A	5.5.1, 5.5.10, 5.5.18, 5.5.20, 5.5.27, 5.5.61, 5.5.73
11	N/A	5.5.3, 5.5.12, 5.5.26, 5.5.38, 5.5.43, 5.5.69, 5.5.76
12	N/A	5.5.46, 5.5.55, 5.5.77
13	N/A	5.5.7, 5.5.11, 5.5.14, 5.5.30, 5.5.47, 5.5.65, 5.5.70
14	N/A	5.5.5, 5.5.8, 5.5.9, 5.5.15, 5.5.21, 5.5.25 5.5.34, 5.5.50, 5.5.57, 5.5.63, 5.5.81

Table D.1: NAT assignment to each quark and gluon Feynman diagram. The ‘LQ’ quark diagrams refer to those where the photon attaches to the light quark line.

# Bibliography

- [1] H. Fritzsch, M. Gell-Mann, and H. Leutwyler, *Advantages of the Color Octet Gluon Picture*, *Phys. Lett. B* **47** (1973) 365–368.
- [2] M. Constantinou and H. W. Kendall, *Deep inelastic electron scattering*, *Ann. Rev. Nucl. Part. Sci.* **22** (1972) 203–254.
- [3] A. De Rujula, S. Glashow, H. Politzer, S. Treiman, F. Wilczek, and A. Zee, *Possible NonRegge Behavior of Electroproduction Structure Functions*, *Phys. Rev. D* **10** (1974) 1649.
- [4] P. Marage, *Hadronic structure, low  $x$  physics and diffraction*, in *1999 International Europhysics Conference on High-Energy Physics*, pp. 71–90, 7, 1999. [hep-ph/9911426](#).
- [5] **ZEUS** Collaboration, M. Derrick et al., *Observation of events with a large rapidity gap in deep inelastic scattering at HERA*, *Phys. Lett. B* **315** (1993) 481–493.
- [6] **H1** Collaboration, T. Ahmed et al., *Deep inelastic scattering events with a large rapidity gap at HERA*, *Nucl. Phys. B* **429** (1994) 477–502.
- [7] **H1** Collaboration, S. Aid et al., *A Direct determination of the gluon density in the proton at low  $x$* , *Nucl. Phys. B* **449** (1995) 3–21, [[hep-ex/9505014](#)].
- [8] R. Brandelik et al., *Evidence for Planar Events in  $e^+e^-$  Annihilation at High-Energies*, *Phys. Lett. B* **86** (1979) 243–249.
- [9] R. Devenish and A. Cooper-Sarkar, *Deep inelastic scattering*. 3, 2004.
- [10] V. Barone and E. Predazzi, *High-Energy Particle Diffraction*, vol. v.565 of *Texts and Monographs in Physics*. Springer-Verlag, Berlin Heidelberg, 2002.



- 
- [11] A. De Roeck, *Unpolarised structure functions*, *Nucl. Phys. A* **666** (2000) 129–140.
- [12] **H1** Collaboration, T. Ahmed et al., *First measurement of the deep inelastic structure of proton diffraction*, *Phys. Lett. B* **348** (1995) 681–696, [[hep-ex/9503005](#)].
- [13] **ZEUS** Collaboration, M. Derrick et al., *Measurement of the diffractive structure function in deep elastic scattering at HERA*, *Z. Phys. C* **68** (1995) 569–584, [[hep-ex/9505010](#)].
- [14] **ZEUS** Collaboration, M. Derrick et al., *Measurement of the diffractive cross-section in deep inelastic scattering*, *Z. Phys. C* **70** (1996) 391–412, [[hep-ex/9602010](#)].
- [15] J. Bjorken, *Rapidity gaps and jets as a new physics signature in very high-energy hadron hadron collisions*, *Phys. Rev. D* **47** (1993) 101–113.
- [16] M. Ryskin, *Diffractive  $J/\psi$  electroproduction in LLA QCD*, *Z. Phys. C* **57** (1993) 89–92.
- [17] J. C. Collins, D. E. Soper, and G. F. Sterman, *Factorization of Hard Processes in QCD*, vol. 5, pp. 1–91. 1989. [hep-ph/0409313](#).
- [18] D. Ivanov, A. Schafer, L. Szymanowski, and G. Krasnikov, *Exclusive photoproduction of a heavy vector meson in QCD*, *Eur. Phys. J. C* **34** (2004), no. 3 297–316, [[hep-ph/0401131](#)]. [Erratum: *Eur.Phys.J.C* 75, 75 (2015)].
- [19] D. J. Gross and F. Wilczek, *Asymptotically Free Gauge Theories - I*, *Phys. Rev. D* **8** (1973) 3633–3652.
- [20] D. J. Gross and F. Wilczek, *ASYMPTOTICALLY FREE GAUGE THEORIES. 2.*, *Phys. Rev. D* **9** (1974) 980–993.
- [21] H. D. Politzer, *Reliable Perturbative Results for Strong Interactions?*, *Phys. Rev. Lett.* **30** (1973) 1346–1349.
- [22] D. J. Gross and F. Wilczek, *Ultraviolet Behavior of Nonabelian Gauge Theories*, *Phys. Rev. Lett.* **30** (1973) 1343–1346.
- [23] W. E. Caswell, *Asymptotic Behavior of Nonabelian Gauge Theories to Two Loop Order*, *Phys. Rev. Lett.* **33** (1974) 244.

- [24] S. A. Larin and J. A. M. Vermaseren, *The Three loop QCD Beta function and anomalous dimensions*, *Phys. Lett. B* **303** (1993) 334–336, [[hep-ph/9302208](#)].
- [25] O. V. Tarasov, A. A. Vladimirov, and A. Y. Zharkov, *The Gell-Mann-Low Function of QCD in the Three Loop Approximation*, *Phys. Lett. B* **93** (1980) 429–432.
- [26] V. Gribov and L. Lipatov, *Deep inelastic ep scattering in perturbation theory*, *Sov. J. Nucl. Phys.* **15** (1972) 438–450.
- [27] G. Altarelli and G. Parisi, *Asymptotic Freedom in Parton Language*, *Nucl. Phys. B* **126** (1977) 298.
- [28] Y. Dokshitzer, *Calculation of structure functions of deep-inelastic scattering and  $e^+e^-$  annihilation by perturbation theory in quantum chromodynamics*, *Sov. Phys. JETP* **46** (1977) 641.
- [29] S. Moch, J. A. M. Vermaseren, and A. Vogt, *The Three loop splitting functions in QCD: The Nonsinglet case*, *Nucl. Phys. B* **688** (2004) 101–134, [[hep-ph/0403192](#)].
- [30] A. Vogt, S. Moch, and J. A. M. Vermaseren, *The Three-loop splitting functions in QCD: The Singlet case*, *Nucl. Phys. B* **691** (2004) 129–181, [[hep-ph/0404111](#)].
- [31] K. G. Wilson, *Nonlagrangian models of current algebra*, *Phys. Rev.* **179** (1969) 1499–1512.
- [32] R. A. Brandt and G. Preparata, *Operator product expansions near the light cone*, *Nucl. Phys. B* **27** (1971) 541–567.
- [33] Y. Frishman, *Operator products at almost light like distances*, *Annals Phys.* **66** (1971) 373–389.
- [34] J. C. Collins and D. E. Soper, *Parton Distribution and Decay Functions*, *Nucl. Phys. B* **194** (1982) 445–492.
- [35] M. Constantinou et al., *Parton distributions and lattice QCD calculations: toward 3D structure*, [arXiv:2006.08636](#).
- [36] S. Forte and G. Watt, *Progress in the Determination of the Partonic Structure of the Proton*, *Ann. Rev. Nucl. Part. Sci.* **63** (2013) 291–328, [[arXiv:1301.6754](#)].

- 
- [37] J. J. Ethier and E. R. Nocera, *Parton Distributions in Nucleons and Nuclei*, *Ann. Rev. Nucl. Part. Sci.* (2020), no. 70 1–34, [arXiv:2001.07722].
  - [38] **NNPDF** Collaboration, R. D. Ball et al., *Parton distributions for the LHC Run II*, *JHEP* **04** (2015) 040, [arXiv:1410.8849].
  - [39] **NNPDF** Collaboration, R. D. Ball et al., *Parton distributions from high-precision collider data*, *Eur. Phys. J. C* **77** (2017), no. 10 663, [arXiv:1706.00428].
  - [40] L. Harland-Lang, A. Martin, P. Motylinski, and R. Thorne, *Parton distributions in the LHC era: MMHT 2014 PDFs*, *Eur. Phys. J. C* **75** (2015), no. 5 204, [arXiv:1412.3989].
  - [41] P. M. Nadolsky, H.-L. Lai, Q.-H. Cao, J. Huston, J. Pumplin, D. Stump, W.-K. Tung, and C.-P. Yuan, *Implications of CTEQ global analysis for collider observables*, *Phys. Rev. D* **78** (2008) 013004, [arXiv:0802.0007].
  - [42] S. Dulat, T.-J. Hou, J. Gao, M. Guzzi, J. Huston, P. Nadolsky, J. Pumplin, C. Schmidt, D. Stump, and C. Yuan, *New parton distribution functions from a global analysis of quantum chromodynamics*, *Phys. Rev. D* **93** (2016), no. 3 033006, [arXiv:1506.07443].
  - [43] R. D. Ball, V. Bertone, M. Bonvini, S. Marzani, J. Rojo, and L. Rottoli, *Parton distributions with small- $x$  resummation: evidence for BFKL dynamics in HERA data*, *Eur. Phys. J. C* **78** (2018), no. 4 321, [arXiv:1710.05935].
  - [44] M. Botje, *QCDNUM: Fast QCD Evolution and Convolution*, *Comput. Phys. Commun.* **182** (2011) 490–532, [arXiv:1005.1481].
  - [45] A. Martin, W. Stirling, R. Thorne, and G. Watt, *Parton distributions for the LHC*, *Eur. Phys. J. C* **63** (2009) 189–285, [arXiv:0901.0002].
  - [46] T.-J. Hou et al., *New CTEQ global analysis of quantum chromodynamics with high-precision data from the LHC*, arXiv:1912.10053.
  - [47] **LHCb** Collaboration, R. Aaij et al., *Updated measurements of exclusive  $J/\psi$  and  $\psi(2S)$  production cross-sections in  $pp$  collisions at  $\sqrt{s} = 7$  TeV*, *J. Phys. G* **41** (2014) 055002, [arXiv:1401.3288].

- [48] **LHCb** Collaboration, R. Aaij et al., *Central exclusive production of  $J/\psi$  and  $\psi(2S)$  mesons in  $pp$  collisions at  $\sqrt{s} = 13$  TeV*, *JHEP* **10** (2018) 167, [[arXiv:1806.04079](#)].
- [49] A. Accardi, M. Christy, C. Keppel, W. Melnitchouk, P. Monaghan, J. Morfin, and J. Owens, *New parton distributions from large- $x$  and low- $Q^2$  data*, *Phys. Rev. D* **81** (2010) 034016, [[arXiv:0911.2254](#)].
- [50] S. Kuhlmann, J. Huston, J. Morfin, F. I. Olness, J. Pumplin, J. Owens, W. Tung, and J. Whitmore, *Large  $x$  parton distributions*, *Phys. Lett. B* **476** (2000) 291–296, [[hep-ph/9912283](#)].
- [51] **PHENIX** Collaboration, S. Afanasiev et al., *Photoproduction of  $J/\psi$  and of high mass  $e^+e^-$  in ultra-peripheral Au+Au collisions at  $\sqrt{s} = 200$  GeV*, *Phys. Lett. B* **679** (2009) 321–329, [[arXiv:0903.2041](#)].
- [52] **ALICE** Collaboration, B. B. Abelev et al., *Exclusive  $J/\psi$  photoproduction off protons in ultra-peripheral  $p$ -Pb collisions at  $\sqrt{s_{NN}} = 5.02$  TeV*, *Phys. Rev. Lett.* **113** (2014), no. 23 232504, [[arXiv:1406.7819](#)].
- [53] **LHCb** Collaboration, A. Bursche, *Study of coherent  $J/\psi$  production in lead-lead collisions at  $\sqrt{s_{NN}} = 5$  TeV with the LHCb experiment*, *Nucl. Phys. A* **982** (2019) 247–250.
- [54] D. Müller, D. Robaschik, B. Geyer, F.-M. Dittes, and J. Hořejši, *Wave functions, evolution equations and evolution kernels from light ray operators of QCD*, *Fortsch. Phys.* **42** (1994) 101–141, [[hep-ph/9812448](#)].
- [55] X.-D. Ji, *Deeply virtual Compton scattering*, *Phys. Rev. D* **55** (1997) 7114–7125, [[hep-ph/9609381](#)].
- [56] X.-D. Ji, *Gauge-Invariant Decomposition of Nucleon Spin*, *Phys. Rev. Lett.* **78** (1997) 610–613, [[hep-ph/9603249](#)].
- [57] A. Radyushkin, *Scaling limit of deeply virtual Compton scattering*, *Phys. Lett. B* **380** (1996) 417–425, [[hep-ph/9604317](#)].
- [58] A. Radyushkin, *Nonforward parton distributions*, *Phys. Rev. D* **56** (1997) 5524–5557, [[hep-ph/9704207](#)].

- 
- [59] X.-D. Ji, *Off forward parton distributions*, *J. Phys. G* **24** (1998) 1181–1205, [[hep-ph/9807358](#)].
  - [60] M. Diehl, *Generalized parton distributions*. PhD thesis, 2003. [hep-ph/0307382](#).
  - [61] M. V. Polyakov and P. Schweitzer, *Forces inside hadrons: pressure, surface tension, mechanical radius, and all that*, *Int. J. Mod. Phys. A* **33** (2018), no. 26 1830025, [[arXiv:1805.06596](#)].
  - [62] C. Lorcé, H. Moutarde, and A. P. Trawiński, *Revisiting the mechanical properties of the nucleon*, *Eur. Phys. J. C* **79** (2019), no. 1 89, [[arXiv:1810.09837](#)].
  - [63] M. Diehl, *Introduction to GPDs and TMDs*, *Eur. Phys. J. A* **52** (2016), no. 6 149, [[arXiv:1512.01328](#)].
  - [64] **CLAS** Collaboration, G. Gavalian et al., *Beam spin asymmetries in deeply virtual Compton scattering (DVCS) with CLAS at 4.8 GeV*, *Phys. Rev. C* **80** (2009) 035206, [[arXiv:0812.2950](#)].
  - [65] **HERMES** Collaboration, A. Airapetian et al., *Beam-helicity and beam-charge asymmetries associated with deeply virtual Compton scattering on the unpolarised proton*, *JHEP* **07** (2012) 032, [[arXiv:1203.6287](#)].
  - [66] **ZEUS** Collaboration, S. Chekanov et al., *Measurement of deeply virtual Compton scattering at HERA*, *Phys. Lett. B* **573** (2003) 46–62, [[hep-ex/0305028](#)].
  - [67] **H1** Collaboration, F. Aaron et al., *Measurement of deeply virtual Compton scattering and its  $t$ -dependence at HERA*, *Phys. Lett. B* **659** (2008) 796–806, [[arXiv:0709.4114](#)].
  - [68] A. Accardi et al., *Electron Ion Collider: The Next QCD Frontier: Understanding the glue that binds us all*, *Eur. Phys. J. A* **52** (2016), no. 9 268, [[arXiv:1212.1701](#)].
  - [69] H. Moutarde, P. Sznajder, and J. Wagner, *Border and skewness functions from a leading order fit to DVCS data*, *Eur. Phys. J. C* **78** (2018), no. 11 890, [[arXiv:1807.07620](#)].
  - [70] K. Kumericki, S. Liuti, and H. Moutarde, *GPD phenomenology and DVCS fitting: Entering the high-precision era*, *Eur. Phys. J. A* **52** (2016), no. 6 157, [[arXiv:1602.02763](#)].

- [71] B. Berthou et al., *PARTONS: PARtonic Tomography Of Nucleon Software: A computing framework for the phenomenology of Generalized Parton Distributions*, *Eur. Phys. J. C* **78** (2018), no. 6 478, [arXiv:1512.06174].
- [72] M. Cuic, K. Kumericki, and A. Schafer, *Separation of Quark Flavors using DVCS Data*, arXiv:2007.00029.
- [73] H. Bethe and W. Heitler, *On the Stopping of fast particles and on the creation of positive electrons*, *Proc. Roy. Soc. Lond. A* **146** (1934) 83–112.
- [74] A. Shuvaev, K. J. Golec-Biernat, A. D. Martin, and M. Ryskin, *Off diagonal distributions fixed by diagonal partons at small  $x$  and  $\xi$* , *Phys. Rev. D* **60** (1999) 014015, [hep-ph/9902410].
- [75] A. Shuvaev, *Solution of the off forward leading logarithmic evolution equation based on the Gegenbauer moments inversion*, *Phys. Rev. D* **60** (1999) 116005, [hep-ph/9902318].
- [76] T. Ohrndorf, *Constraints From Conformal Covariance on the Mixing of Operators of Lowest Twist*, *Nucl. Phys. B* **198** (1982) 26–44.
- [77] A. P. Bukhvostov, G. V. Frolov, L. N. Lipatov, and E. A. Kuraev, *Evolution Equations for Quasi-Partonic Operators*, *Nucl. Phys. B* **258** (1985) 601–646.
- [78] S. J. Brodsky, P. Damgaard, Y. Frishman, and G. Lepage, *CONFORMAL SYMMETRY: EXCLUSIVE PROCESSES BEYOND LEADING ORDER*, *Phys. Rev. D* **33** (1986) 1881.
- [79] D. Mueller, *Conformal constraints and the evolution of the nonsinglet meson distribution amplitude*, *Phys. Rev. D* **49** (1994) 2525–2535.
- [80] A. V. Belitsky, D. Mueller, L. Niedermeier, and A. Schafer, *Evolution of nonforward parton distributions in next-to-leading order: Singlet sector*, *Nucl. Phys. B* **546** (1999) 279–298, [hep-ph/9810275].
- [81] A. V. Belitsky and D. Mueller, *Broken conformal invariance and spectrum of anomalous dimensions in QCD*, *Nucl. Phys. B* **537** (1999) 397–442, [hep-ph/9804379].

- 
- [82] M. Diehl and W. Kugler, *Some numerical studies of the evolution of generalized parton distributions*, *Phys. Lett. B* **660** (2008) 202–211, [[arXiv:0711.2184](#)].
  - [83] A. Martin, C. Nockles, M. Ryskin, A. Shuvaev, and T. Teubner, *Generalised parton distributions at small  $x$* , *Eur. Phys. J. C* **63** (2009) 57–67, [[arXiv:0812.3558](#)].
  - [84] T. Regge, *Introduction to complex orbital momenta*, *Nuovo Cim.* **14** (1959) 951.
  - [85] T. Regge, *Bound states, shadow states and Mandelstam representation*, *Nuovo Cim.* **18** (1960) 947–956.
  - [86] K. Kumericki and D. Mueller, *Deeply virtual Compton scattering at small  $x_B$  and the access to the GPD  $H$* , *Nucl. Phys. B* **841** (2010) 1–58, [[arXiv:0904.0458](#)].
  - [87] L. Harland-Lang, *Simple form for the low- $x$  generalized parton distributions in the skewed regime*, *Phys. Rev. D* **88** (2013), no. 3 034029, [[arXiv:1306.6661](#)].
  - [88] A. Buckley, J. Ferrando, S. Lloyd, K. Nordström, B. Page, M. Rüfenacht, M. Schönherr, and G. Watt, *LHAPDF6: parton density access in the LHC precision era*, *Eur. Phys. J. C* **75** (2015) 132, [[arXiv:1412.7420](#)].
  - [89] **ZEUS** Collaboration, M. Derrick et al., *Extraction of the gluon density of the proton at small  $x$* , *Phys. Lett. B* **345** (1995) 576–588.
  - [90] F. Tkachov, *A Theorem on Analytical Calculability of Four Loop Renormalization Group Functions*, *Phys. Lett. B* **100** (1981) 65–68.
  - [91] K. Chetyrkin and F. Tkachov, *Integration by Parts: The Algorithm to Calculate beta Functions in 4 Loops*, *Nucl. Phys. B* **192** (1981) 159–204.
  - [92] T. Gehrmann and E. Remiddi, *Differential equations for two loop four point functions*, *Nucl. Phys. B* **580** (2000) 485–518, [[hep-ph/9912329](#)].
  - [93] G. 't Hooft and M. Veltman, *Regularization and Renormalization of Gauge Fields*, *Nucl. Phys. B* **44** (1972) 189–213.
  - [94] R. Lee, *Group structure of the integration-by-part identities and its application to the reduction of multiloop integrals*, *JHEP* **07** (2008) 031, [[arXiv:0804.3008](#)].

- [95] A. Smirnov and V. A. Smirnov, *Applying Grobner bases to solve reduction problems for Feynman integrals*, *JHEP* **01** (2006) 001, [[hep-lat/0509187](#)].
- [96] A. Smirnov, *An Algorithm to construct Grobner bases for solving integration by parts relations*, *JHEP* **04** (2006) 026, [[hep-ph/0602078](#)].
- [97] J. Gluza, K. Kajda, and D. A. Kosower, *Towards a Basis for Planar Two-Loop Integrals*, *Phys. Rev. D* **83** (2011) 045012, [[arXiv:1009.0472](#)].
- [98] R. M. Schabinger, *A New Algorithm For The Generation Of Unitarity-Compatible Integration By Parts Relations*, *JHEP* **01** (2012) 077, [[arXiv:1111.4220](#)].
- [99] A. Grozin, *Integration by parts: An Introduction*, *Int. J. Mod. Phys. A* **26** (2011) 2807–2854, [[arXiv:1104.3993](#)].
- [100] A. von Manteuffel and C. Studerus, *Reduze 2 - Distributed Feynman Integral Reduction*, [arXiv:1201.4330](#).
- [101] S. Laporta, *High precision calculation of multiloop Feynman integrals by difference equations*, *Int. J. Mod. Phys. A* **15** (2000) 5087–5159, [[hep-ph/0102033](#)].
- [102] S. Jones, A. Martin, M. Ryskin, and T. Teubner, *Exclusive  $J/\psi$  and  $\Upsilon$  photoproduction and the low  $x$  gluon*, *J. Phys. G* **43** (2016), no. 3 035002, [[arXiv:1507.06942](#)].
- [103] Z.-Q. Chen and C.-F. Qiao, *NLO QCD corrections to exclusive electroproduction of quarkonium*, *Phys. Lett. B* **797** (2019) 134816, [[arXiv:1903.00171](#)]. [Erratum: *Phys.Lett. B*, 135759 (2020)].
- [104] V. N. Gribov and I. Y. Pomeranchuk, *Properties of the elastic scattering amplitude at high energies*, *Sov. Phys. JETP* **16** (1963) 220.
- [105] G. A. Schuler, *Quarkonium production and decays*. PhD thesis, Hamburg U., 1994. [hep-ph/9403387](#).
- [106] E. de Oliveira, A. Martin, and M. Ryskin, *Drell-Yan as a probe of small  $x$  partons at the LHC*, *Eur. Phys. J. C* **72** (2012) 2069, [[arXiv:1205.6108](#)].



- 
- [107] S. Jones, A. Martin, M. Ryskin, and T. Teubner, *The exclusive  $J/\psi$  process at the LHC tamed to probe the low  $x$  gluon*, *Eur. Phys. J. C* **76** (2016), no. 11 633, [[arXiv:1610.02272](#)].
  - [108] M. Diehl and W. Kugler, *Next-to-leading order corrections in exclusive meson production*, *Eur. Phys. J. C* **52** (2007) 933–966, [[arXiv:0708.1121](#)].
  - [109] A. Martin and M. Ryskin, *Comments on Global Parton Analyses*, *Acta Phys. Polon. B* **51** (2020) 1079, [[arXiv:1912.09304](#)].
  - [110] C. M. LHCb Collaboration, *LHCb SMOG Upgrade*, Tech. Rep. CERN-LHCC-2019-005. LHCb-TDR-020, CERN, Geneva, May, 2019.
  - [111] H. Kowalski, L. Lipatov, and D. Ross, *The Green Function for the BFKL Pomeron and the Transition to DGLAP Evolution*, *Eur. Phys. J. C* **74** (2014), no. 6 2919, [[arXiv:1401.6298](#)].
  - [112] H. Kowalski, L. Lipatov, and D. Ross, *The Behaviour of the Green Function for the BFKL Pomeron with Running Coupling*, *Eur. Phys. J. C* **76** (2016), no. 1 23, [[arXiv:1508.05744](#)].
  - [113] H. Kowalski, L. Lipatov, D. Ross, and O. Schulz, *Decoupling of the leading contribution in the discrete BFKL Analysis of High-Precision HERA Data*, *Eur. Phys. J. C* **77** (2017), no. 11 777, [[arXiv:1707.01460](#)].
  - [114] **LHCb** Collaboration, R. Aaij et al., *Measurements of prompt charm production cross-sections in  $pp$  collisions at  $\sqrt{s} = 5$  TeV*, *JHEP* **06** (2017) 147, [[arXiv:1610.02230](#)].
  - [115] **LHCb** Collaboration, R. Aaij et al., *Prompt charm production in  $pp$  collisions at  $\sqrt{s} = 7$  TeV*, *Nucl. Phys. B* **871** (2013) 1–20, [[arXiv:1302.2864](#)].
  - [116] **LHCb** Collaboration, R. Aaij et al., *Measurements of prompt charm production cross-sections in  $pp$  collisions at  $\sqrt{s} = 13$  TeV*, *JHEP* **03** (2016) 159, [[arXiv:1510.01707](#)]. [Erratum: *JHEP* 09, 013 (2016), Erratum: *JHEP* 05, 074 (2017)].

- [117] **LHCb** Collaboration, R. Aaij et al., *Measurement of  $B$  meson production cross-sections in proton-proton collisions at  $\sqrt{s} = 7$  TeV*, *JHEP* **08** (2013) 117, [[arXiv:1306.3663](#)].
- [118] **LHCb** Collaboration, R. Aaij et al., *Measurement of the  $b$ -quark production cross-section in 7 and 13 TeV  $pp$  collisions*, *Phys. Rev. Lett.* **118** (2017), no. 5 052002, [[arXiv:1612.05140](#)]. [Erratum: *Phys.Rev.Lett.* 119, 169901 (2017)].
- [119] **PROSA** Collaboration, O. Zenaiev et al., *Impact of heavy-flavour production cross sections measured by the LHCb experiment on parton distribution functions at low  $x$* , *Eur. Phys. J. C* **75** (2015), no. 8 396, [[arXiv:1503.04581](#)].
- [120] R. Gauld, J. Rojo, L. Rottoli, and J. Talbert, *Charm production in the forward region: constraints on the small- $x$  gluon and backgrounds for neutrino astronomy*, *JHEP* **11** (2015) 009, [[arXiv:1506.08025](#)].
- [121] M. Cacciari, M. L. Mangano, and P. Nason, *Gluon PDF constraints from the ratio of forward heavy-quark production at the LHC at  $\sqrt{s} = 7$  and 13 TeV*, *Eur. Phys. J. C* **75** (2015), no. 12 610, [[arXiv:1507.06197](#)].
- [122] R. Gauld and J. Rojo, *Precision determination of the small- $x$  gluon from charm production at LHCb*, *Phys. Rev. Lett.* **118** (2017), no. 7 072001, [[arXiv:1610.09373](#)].
- [123] R. Gauld, *Understanding forward  $B$  hadron production*, *JHEP* **05** (2017) 084, [[arXiv:1703.03636](#)].
- [124] E. De Oliveira, A. Martin, and M. Ryskin, *Open charm production and low  $x$  gluons*, *Phys. Rev. D* **97** (2018), no. 7 074021, [[arXiv:1712.06834](#)].
- [125] S. Jones, A. Martin, M. Ryskin, and T. Teubner, *Exclusive  $J/\psi$  production at the LHC in the  $k_T$  factorization approach*, *J. Phys. G* **44** (2017), no. 3 03LT01, [[arXiv:1611.03711](#)].
- [126] **ZEUS** Collaboration, S. Chekanov et al., *Exclusive photoproduction of  $J/\psi$  mesons at HERA*, *Eur. Phys. J. C* **24** (2002) 345–360, [[hep-ex/0201043](#)].
- [127] **ZEUS** Collaboration, S. Chekanov et al., *Exclusive electroproduction of  $J/\psi$  mesons at HERA*, *Nucl. Phys. B* **695** (2004) 3–37, [[hep-ex/0404008](#)].

- 
- [128] **H1** Collaboration, A. Aktas et al., *Elastic  $J/\psi$  production at HERA*, *Eur. Phys. J. C* **46** (2006) 585–603, [[hep-ex/0510016](#)].
  - [129] **H1** Collaboration, C. Alexa et al., *Elastic and Proton-Dissociative Photoproduction of  $J/\psi$  Mesons at HERA*, *Eur. Phys. J. C* **73** (2013), no. 6 2466, [[arXiv:1304.5162](#)].
  - [130] G. T. Bodwin, E. Braaten, and G. Lepage, *Rigorous QCD analysis of inclusive annihilation and production of heavy quarkonium*, *Phys. Rev. D* **51** (1995) 1125–1171, [[hep-ph/9407339](#)]. [Erratum: *Phys.Rev.D* 55, 5853 (1997)].
  - [131] M. Ryskin, R. Roberts, A. D. Martin, and E. Levin, *Diffraction  $J/\psi$  photoproduction as a probe of the gluon density*, *Z. Phys. C* **76** (1997) 231–239, [[hep-ph/9511228](#)].
  - [132] H. Jung, D. Krucker, C. Greub, and D. Wyler, *Relativistic corrections to photoproduction of  $J/\psi$* , *Z. Phys. C* **60** (1993) 721–730.
  - [133] S. J. Brodsky, L. Frankfurt, J. Gunion, A. H. Mueller, and M. Strikman, *Diffraction leptonproduction of vector mesons in QCD*, *Phys. Rev. D* **50** (1994) 3134–3144, [[hep-ph/9402283](#)].
  - [134] L. Frankfurt, W. Koepf, and M. Strikman, *Hard diffractive electroproduction of vector mesons in QCD*, *Phys. Rev. D* **54** (1996) 3194–3215, [[hep-ph/9509311](#)].
  - [135] L. Frankfurt, W. Koepf, and M. Strikman, *Diffraction heavy quarkonium photoproduction and electroproduction in QCD*, *Phys. Rev. D* **57** (1998) 512–526, [[hep-ph/9702216](#)].
  - [136] P. Hoodbhoy, *Wave function corrections and off forward gluon distributions in diffractive  $J/\psi$  electroproduction*, *Phys. Rev. D* **56** (1997) 388–393, [[hep-ph/9611207](#)].
  - [137] D. Ivanov, B. Pire, L. Szymanowski, and J. Wagner, *Probing GPDs in photoproduction processes at hadron colliders*, in *International Conference on the Structure and Interactions of the Photon and 21st International Workshop on Photon-Photon Collisions and International Workshop on High Energy Photon Linear Colliders*, 10, 2015. [arXiv:1510.06710](#).

- [138] V. S. Fadin and L. N. Lipatov, *High-Energy Production of Gluons in a QuasimultiRegge Kinematics*, *JETP Lett.* **49** (1989) 352.
- [139] S. J. Brodsky, G. Lepage, and P. B. Mackenzie, *On the Elimination of Scale Ambiguities in Perturbative Quantum Chromodynamics*, *Phys. Rev. D* **28** (1983) 228.
- [140] L. Harland-Lang, V. Khoze, and M. Ryskin, *Sudakov effects in photon-initiated processes*, *Phys. Lett. B* **761** (2016) 20–24, [[arXiv:1605.04935](#)].
- [141] V. Khoze, A. Martin, and M. Ryskin, *Diffraction at the LHC*, *Eur. Phys. J. C* **73** (2013) 2503, [[arXiv:1306.2149](#)].
- [142] A. Martin, C. Nockles, M. G. Ryskin, and T. Teubner, *Small  $x$  gluon from exclusive  $J/\psi$  production*, *Phys. Lett. B* **662** (2008) 252–258, [[arXiv:0709.4406](#)].
- [143] B. Schmidt and M. Steinhauser, *CRunDec: a C++ package for running and decoupling of the strong coupling and quark masses*, *Comput. Phys. Commun.* **183** (2012) 1845–1848, [[arXiv:1201.6149](#)].
- [144] K. G. Chetyrkin, J. H. Kuhn, and M. Steinhauser, *RunDec: A Mathematica package for running and decoupling of the strong coupling and quark masses*, *Comput. Phys. Commun.* **133** (2000) 43–65, [[hep-ph/0004189](#)].
- [145] C. Flett, S. Jones, A. Martin, M. Ryskin, and T. Teubner, *Towards a determination of the low  $x$  gluon via exclusive  $J/\psi$  production*, *PoS DIS2019* (2019) 053, [[arXiv:1907.06471](#)].
- [146] V. Bertone, S. Carrazza, and J. Rojo, *APFEL: A PDF Evolution Library with QED corrections*, *Comput. Phys. Commun.* **185** (2014) 1647–1668, [[arXiv:1310.1394](#)].
- [147] S. Carrazza, A. Ferrara, D. Palazzo, and J. Rojo, *APFEL Web: a web-based application for the graphical visualization of parton distribution functions*, *J. Phys. G* **42** (2015), no. 5 057001, [[arXiv:1410.5456](#)].
- [148] E. Fermi, *On the Theory of the impact between atoms and electrically charged particles*, *Z. Phys.* **29** (1924) 315–327.

- 
- [149] E. Williams, *Nature of the high-energy particles of penetrating radiation and status of ionization and radiation formulae*, *Phys. Rev.* **45** (1934) 729–730.
  - [150] C. von Weizsacker, *Radiation emitted in collisions of very fast electrons*, *Z. Phys.* **88** (1934) 612–625.
  - [151] W. Schafer and A. Szczurek, *Exclusive photoproduction of  $J/\psi$  in proton-proton and proton-antiproton scattering*, *Phys. Rev. D* **76** (2007) 094014, [[arXiv:0705.2887](#)].
  - [152] V. Khoze, A. Martin, and M. Ryskin, *High Energy Elastic and Diffractive Cross Sections*, *Eur. Phys. J. C* **74** (2014), no. 2 2756, [[arXiv:1312.3851](#)].
  - [153] V. Khoze, A. Martin, and M. Ryskin, *Photon exchange processes at hadron colliders as a probe of the dynamics of diffraction*, *Eur. Phys. J. C* **24** (2002) 459–468, [[hep-ph/0201301](#)].
  - [154] **TOTEM** Collaboration, G. Antchev et al., *Measurement of proton-proton elastic scattering and total cross-section at  $\sqrt{s} = 7$  TeV*, *EPL* **101** (2013), no. 2 21002.
  - [155] V. Budnev, I. Ginzburg, G. Meledin, and V. Serbo, *The Two photon particle production mechanism. Physical problems. Applications. Equivalent photon approximation*, *Phys. Rept.* **15** (1975) 181–281.
  - [156] O. Kepka, *QCD and Diffraction in the ATLAS Experiment at the LHC*. PhD thesis, Orsay Charles U., 2009.
  - [157] **Particle Data Group** Collaboration, J. Beringer et al., *Review of Particle Physics (RPP)*, *Phys. Rev. D* **86** (2012) 010001.
  - [158] C. A. Flett, S. P. Jones, A. D. Martin, M. G. Ryskin, and T. Teubner, *Exclusive production of heavy quarkonia as a probe of the low  $x$  and low scale gluon PDF*, *PoS LC2019* (2020) 040, [[arXiv:1912.09128](#)].
  - [159] G. D’Agostini, *Bayesian reasoning in data analysis: A critical introduction*. 11, 2003.
  - [160] G. D’Agostini, *On the use of the covariance matrix to fit correlated data*, *Nucl. Instrum. Meth. A* **346** (1994) 306–311.

- [161] **NNPDF** Collaboration, R. D. Ball, L. Del Debbio, S. Forte, A. Guffanti, J. I. Latorre, J. Rojo, and M. Ubiali, *Fitting Parton Distribution Data with Multiplicative Normalization Uncertainties*, *JHEP* **05** (2010) 075, [[arXiv:0912.2276](#)].
- [162] A. Arroyo Garcia, M. Hentschinski, and K. Kutak, *QCD evolution based evidence for the onset of gluon saturation in exclusive photo-production of vector mesons*, *Phys. Lett. B* **795** (2019) 569–575, [[arXiv:1904.04394](#)].
- [163] L. Gribov, E. Levin, and M. Ryskin, *Semihard Processes in QCD*, *Phys. Rept.* **100** (1983) 1–150.
- [164] I. Balitsky, *Operator expansion for high-energy scattering*, *Nucl. Phys. B* **463** (1996) 99–160, [[hep-ph/9509348](#)].
- [165] Y. V. Kovchegov, *Small  $x$   $F_2$  structure function of a nucleus including multiple pomeron exchanges*, *Phys. Rev. D* **60** (1999) 034008, [[hep-ph/9901281](#)].
- [166] V. S. Fadin, E. Kuraev, and L. Lipatov, *On the Pomernanchuk Singularity in Asymptotically Free Theories*, *Phys. Lett. B* **60** (1975) 50–52.
- [167] E. Kuraev, L. Lipatov, and V. S. Fadin, *The Pomernanchuk Singularity in Nonabelian Gauge Theories*, *Sov. Phys. JETP* **45** (1977) 199–204.
- [168] I. Balitsky and L. Lipatov, *The Pomernanchuk Singularity in Quantum Chromodynamics*, *Sov. J. Nucl. Phys.* **28** (1978) 822–829.
- [169] M. Hentschinski, A. Sabio Vera, and C. Salas, *Hard to Soft Pomeron Transition in Small- $x$  Deep Inelastic Scattering Data Using Optimal Renormalization*, *Phys. Rev. Lett.* **110** (2013), no. 4 041601, [[arXiv:1209.1353](#)].
- [170] M. Hentschinski, A. Sabio Vera, and C. Salas,  *$F_2$  and  $F_L$  at small  $x$  using a collinearly improved BFKL resummation*, *Phys. Rev. D* **87** (2013), no. 7 076005, [[arXiv:1301.5283](#)].
- [171] M. Hentschinski and E. P. Molina, *Exclusive  $J/\Psi$  and  $\Psi(2s)$  photo-production as a probe of QCD low  $x$  evolution equations*, [arXiv:2011.02640](#).

- 
- [172] C. A. Flett, A. D. Martin, M. G. Ryskin, and T. Teubner, *Very low  $x$  gluon density determined by LHCb exclusive  $J/\psi$  data*, *Phys. Rev. D* **102** (2020) 114021, [[arXiv:2006.13857](#)].
  - [173] A. D. Martin and M. Ryskin, *Higher twists in deep inelastic scattering*, *Phys. Lett. B* **431** (1998) 395–404, [[hep-ph/9802366](#)].
  - [174] V. Bertone, R. Gauld, and J. Rojo, *Neutrino Telescopes as QCD Microscopes*, *JHEP* **01** (2019) 217, [[arXiv:1808.02034](#)].
  - [175] **xFitter Developers’ Team** Collaboration, H. Abdolmaleki et al., *Impact of low- $x$  resummation on QCD analysis of HERA data*, *Eur. Phys. J. C* **78** (2018), no. 8 621, [[arXiv:1802.00064](#)].
  - [176] W. T. Giele and S. Keller, *Implications of hadron collider observables on parton distribution function uncertainties*, *Phys. Rev. D* **58** (1998) 094023, [[hep-ph/9803393](#)].
  - [177] R. D. Ball, V. Bertone, F. Cerutti, L. Del Debbio, S. Forte, A. Guffanti, N. P. Hartland, J. I. Latorre, J. Rojo, and M. Ubiali, *Reweighting and Unweighting of Parton Distributions and the LHC  $W$  lepton asymmetry data*, *Nucl. Phys. B* **855** (2012) 608–638, [[arXiv:1108.1758](#)].
  - [178] H. Paukkunen and P. Zurita, *PDF reweighting in the Hessian matrix approach*, *JHEP* **12** (2014) 100, [[arXiv:1402.6623](#)].
  - [179] S. Alekhin et al., *HERAFitter*, *Eur. Phys. J. C* **75** (2015), no. 7 304, [[arXiv:1410.4412](#)].
  - [180] F. De Lorenzi, *Parton Distribution Function sensitivity studies using electroweak processes at LHCb*, in *18th International Workshop on Deep Inelastic Scattering and Related Subjects*, 11, 2010. [arXiv:1011.4260](#).
  - [181] G. Watt and R. Thorne, *Study of Monte Carlo approach to experimental uncertainty propagation with MSTW 2008 PDFs*, *JHEP* **08** (2012) 052, [[arXiv:1205.4024](#)].
  - [182] S. J. Brodsky, V. S. Fadin, V. T. Kim, L. N. Lipatov, and G. B. Pivovarov, *The QCD pomeron with optimal renormalization*, *JETP Lett.* **70** (1999) 155–160, [[hep-ph/9901229](#)].

- [183] S. Catani, M. Ciafaloni, and F. Hautmann, *GLUON CONTRIBUTIONS TO SMALL  $x$  HEAVY FLAVOR PRODUCTION*, *Phys. Lett. B* **242** (1990) 97–102.
- [184] S. Catani, M. Ciafaloni, and F. Hautmann, *High-energy factorization and small  $x$  heavy flavor production*, *Nucl. Phys. B* **366** (1991) 135–188.
- [185] J. C. Collins and R. K. Ellis, *Heavy quark production in very high-energy hadron collisions*, *Nucl. Phys. B* **360** (1991) 3–30.
- [186] S. Catani and F. Hautmann, *High-energy factorization and small  $x$  deep inelastic scattering beyond leading order*, *Nucl. Phys. B* **427** (1994) 475–524, [[hep-ph/9405388](#)].
- [187] J. C. Collins, L. Frankfurt, and M. Strikman, *Factorization for hard exclusive electroproduction of mesons in QCD*, *Phys. Rev. D* **56** (1997) 2982–3006, [[hep-ph/9611433](#)].
- [188] **HERMES** Collaboration, W. Augustyniak, *Exclusive electroproduction of vector mesons in lepton nucleon scattering at the HERMES experiment*, *Nucl. Phys. B Proc. Suppl.* **245** (2013) 207–214.
- [189] **LHCb** Collaboration, R. Aaij et al., *Measurement of the exclusive  $\Upsilon$  production cross-section in  $pp$  collisions at  $\sqrt{s} = 7$  TeV and 8 TeV*, *JHEP* **09** (2015) 084, [[arXiv:1505.08139](#)].
- [190] I. Ivanov, N. Nikolaev, and A. Savin, *Diffractional vector meson production at HERA: From soft to hard QCD*, *Phys. Part. Nucl.* **37** (2006) 1–85, [[hep-ph/0501034](#)].
- [191] S. P. Jones, *Exclusive processes to NLO and Small  $x$  PDFs from LHC data*. PhD thesis, University of Liverpool, 2014, *Unpublished*.
- [192] F. Low, *Bremsstrahlung of very low-energy quanta in elementary particle collisions*, *Phys. Rev.* **110** (1958) 974–977.
- [193] D. Ivanov, M. Kotsky, and A. Papa, *The Impact factor for the virtual photon to light vector meson transition*, *Eur. Phys. J. C* **38** (2004) 195–213, [[hep-ph/0405297](#)].



- 
- [194] **ZEUS** Collaboration, J. Breitweg et al., *Measurement of elastic Upsilon photoproduction at HERA*, *Phys. Lett. B* **437** (1998) 432–444, [[hep-ex/9807020](#)].
  - [195] X.-D. Ji and J. Osborne, *One loop corrections and all order factorization in deeply virtual Compton scattering*, *Phys. Rev. D* **58** (1998) 094018, [[hep-ph/9801260](#)].
  - [196] A. Petrelli, M. Cacciari, M. Greco, F. Maltoni, and M. L. Mangano, *NLO production and decay of quarkonium*, *Nucl. Phys. B* **514** (1998) 245–309, [[hep-ph/9707223](#)].
  - [197] G. T. Bodwin and A. Petrelli, *Order- $v^4$  corrections to S-wave quarkonium decay*, *Phys. Rev. D* **66** (2002) 094011, [[hep-ph/0205210](#)]. [Erratum: *Phys.Rev.D* **87**, 039902 (2013)].
  - [198] E. Braaten and J. Lee, *Exclusive Double Charmonium Production from  $e^+e^-$  Annihilation into a Virtual Photon*, *Phys. Rev. D* **67** (2003) 054007, [[hep-ph/0211085](#)]. [Erratum: *Phys.Rev.D* **72**, 099901 (2005)].
  - [199] V. M. Braun, D. Ivanov, A. Schafer, and L. Szymanowski, *Towards the theory of coherent hard dijet production on hadrons and nuclei*, *Nucl. Phys. B* **638** (2002) 111–154, [[hep-ph/0204191](#)].
  - [200] B. Pire, L. Szymanowski, and J. Wagner, *NLO corrections to timelike, spacelike and double deeply virtual Compton scattering*, *Phys. Rev. D* **83** (2011) 034009, [[arXiv:1101.0555](#)].
  - [201] A. V. Belitsky, D. Müller, and Y. Ji, *Compton scattering: from deeply virtual to quasi-real*, *Nucl. Phys. B* **878** (2014) 214–268, [[arXiv:1212.6674](#)].
  - [202] P. Nogueira, *Automatic Feynman graph generation*, *J. Comput. Phys.* **105** (1993) 279–289.
  - [203] B. Ruijl, T. Ueda, and J. Vermaseren, *FORM version 4.2*, [arXiv:1707.06453](#).
  - [204] E. Leinartas, *Factorization of rational functions of several variables into partial fractions*, *Soviet Math. (Iz. VUZ)* **22** (1978) 35–38.
  - [205] G. Passarino and M. Veltman, *One Loop Corrections for  $e^+e^-$  Annihilation Into  $\mu^+\mu^-$  in the Weinberg Model*, *Nucl. Phys. B* **160** (1979) 151–207.

- [206] M. Butenschoen, *Photoproduction of the  $J/\psi$  meson at HERA at next-to-leading order within the framework of nonrelativistic QCD*, other thesis, 6, 2009.
- [207] F. Feng, *\$Apart: A Generalized Mathematica Apart Function*, *Comput. Phys. Commun.* **183** (2012) 2158–2164, [[arXiv:1204.2314](#)].
- [208] R. Ellis and G. Zanderighi, *Scalar one-loop integrals for QCD*, *JHEP* **02** (2008) 002, [[arXiv:0712.1851](#)].
- [209] J. Andersen, T. Binoth, G. Heinrich, and J. Smillie, *Loop induced interference effects in Higgs Boson plus two jet production at the LHC*, *JHEP* **02** (2008) 057, [[arXiv:0709.3513](#)].
- [210] S. Carrazza, R. K. Ellis, and G. Zanderighi, *QCDLoop: a comprehensive framework for one-loop scalar integrals*, *Comput. Phys. Commun.* **209** (2016) 134–143, [[arXiv:1605.03181](#)].
- [211] S. Borowka, G. Heinrich, S. Jahn, S. Jones, M. Kerner, J. Schlenk, and T. Zirke, *pySecDec: a toolbox for the numerical evaluation of multi-scale integrals*, *Comput. Phys. Commun.* **222** (2018) 313–326, [[arXiv:1703.09692](#)].
- [212] H. H. Patel, *Package-X: A Mathematica package for the analytic calculation of one-loop integrals*, *Comput. Phys. Commun.* **197** (2015) 276–290, [[arXiv:1503.01469](#)].
- [213] W. H. Furry, *A Symmetry Theorem in the Positron Theory*, *Phys. Rev.* **51** (1937) 125–129.
- [214] M. Heller and A. von Manteuffel, *MultivariateApart: Generalized Partial Fractions*, [arXiv:2101.08283](#).
- [215] D. J. Broadhurst, N. Gray, and K. Schilcher, *Gauge invariant on-shell  $Z_2$  in QED, QCD and the effective field theory of a static quark*, *Z. Phys. C* **52** (1991) 111–122.
- [216] C. A. Flett, J. A. Gracey, S. P. Jones, and T. Teubner, *Exclusive heavy vector meson electroproduction to NLO in collinear factorisation*, [arXiv:2105.07657](#).
- [217] **LHCb** Collaboration, R. Aaij et al., *Measurement of the  $\eta_c(1S)$  production cross-section in proton-proton collisions via the decay  $\eta_c(1S) \rightarrow p\bar{p}$* , *Eur. Phys. J. C* **75** (2015), no. 7 311, [[arXiv:1409.3612](#)].

- 
- [218] V. S. Fadin and L. Lipatov, *BFKL pomeron in the next-to-leading approximation*, *Phys. Lett. B* **429** (1998) 127–134, [hep-ph/9802290].
- [219] B. Geyer, D. Robaschik, M. Bordag, and J. Horejsi, *NONLOCAL LIGHT CONE EXPANSIONS AND EVOLUTION EQUATIONS*, *Z. Phys. C* **26** (1985) 591–600.
- [220] T. Braunschweig, B. Geyer, J. Horejsi, and D. Robaschik, *Hadron Operators on the Light Cone*, *Z. Phys. C* **33** (1986) 275.
- [221] F. Dittes, D. Mueller, D. Robaschik, B. Geyer, and J. Horejsi, *The Altarelli-Parisi Kernel as Asymptotic Limit of an Extended Brodsky-Lepage Kernel*, *Phys. Lett. B* **209** (1988) 325–329.
- [222] A. V. Belitsky and D. Mueller, *Next-to-leading order evolution of twist-2 conformal operators: The Abelian case*, *Nucl. Phys. B* **527** (1998) 207–234, [hep-ph/9802411].
- [223] A. V. Belitsky, D. Mueller, and A. Freund, *Reconstruction of nonforward evolution kernels*, *Phys. Lett. B* **461** (1999) 270–279, [hep-ph/9904477].
- [224] A. V. Belitsky and D. Mueller, *Exclusive evolution kernels in two loop order: Parity even sector*, *Phys. Lett. B* **464** (1999) 249–256, [hep-ph/9906409].
- [225] A. V. Belitsky, A. Freund, and D. Mueller, *Evolution kernels of skewed parton distributions: Method and two loop results*, *Nucl. Phys. B* **574** (2000) 347–406, [hep-ph/9912379].